

31 January 2014 | \$10

Science



Steering Sound

 AAAS

EDITORIAL

- 461 Visa Labyrinth
Martyn Poliakoff

NEWS OF THE WEEK

- 468 A roundup of the week's top stories

NEWS & ANALYSIS

- 471 Neandertals and Moderns Made Imperfect Mates
>> Science Express Report by B. Vernot and J. M. Akey
- 472 Ecosystems Say 'Pass the Salt!'
>> Science Podcast
- 473 Suspect Drug Research Blamed for Massive Death Toll
- 475 Online Video Game Plugs Players Into Remote-Controlled Biochemistry Lab
- 476 Editing of Targeted Genes Proved Possible in Monkeys
- 477 Antioxidants Could Spur Tumors by Acting on Cancer Gene
>> Science Translational Medicine Research Article by V. I. Sayin et al.

NEWS FOCUS

- 478 The Dangerous Professor
- 482 Quantum Spy Games
>> Science Podcast

LETTERS

- 484 Sea Turtle Funding Dries Up
P. Plotkin and J. Bernardo
- Fueling Innovation
R. W. Nichols
- Research Tax Credits: An Important Tool
D. J. Hemel and L. L. Ouellette
- The Changing Role of Medieval Women
R. E. Blanton

- 486 CORRECTIONS AND CLARIFICATIONS

BOOKS ET AL.

- 487 Consciousness and the Brain
S. Dehaene, reviewed by C. Koch
- 488 Dancing with the River
K. Lahiri-Dutt and G. Samanta, reviewed by C. W. Nuckolls

POLICY FORUM

- 489 Drug Policy as Conservation Policy: Narco-Deforestation
K. McSweeney et al.

PERSPECTIVES

- 491 Chemical Warfare in the Battle of the Sexes
D. E. L. Promislow and M. Kaeberlein
>> Reports pp. 536, 541, and 544
- 492 When Electrons Leave Holes in Organic Solar Cells
J.-L. Bredas
>> Report p. 512
- 493 Methane on the Rise—Again
E. G. Nisbet et al.
- 495 Selecting the Direction of Sound Transmission
S. A. Cummer
>> Report p. 516
- 496 Pathogen Specialization
G. Coaker
>> Report p. 552
- 497 A Unified Process for Neurological Disease
A. B. Singleton
>> Research Article p. 506
- 498 Delayed Gratification—Waiting to Terminate Stem Cell Identity
X. Zhang
>> Research Article p. 505

CONTENTS continued >>



page 482



page 488

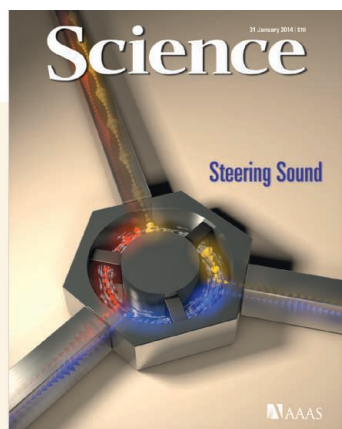
ON THE WEB THIS WEEK

>> Science Podcast

Listen to stories on the quantum cryptography arms race, salt-starved ecosystems, and more.

>> Find More Online

Check out the latest in a series of Perspectives on Challenges in Climate Science at www.sciencemag.org/extra/climate.



COVER

A circulator for sound. The arrows represent acoustic signals flowing through the device (diameter: ~20 centimeters), which circulates sound in a nonreciprocal fashion: Signals can flow from left to top, from top to right, and from right to left, but not in the opposite directions. This creates one-way communication channels for sound, allowing listeners to hear but not be heard in return. See pages 495 and 516.

Image: Erik Zumalt, Cockrell School of Engineering, The University of Texas at Austin

DEPARTMENTS

- 460 This Week in *Science*
- 462 Editors' Choice
- 466 Science Staff
- 500 AAAS News & Notes
- 557 New Products
- 558 Science Careers

REVIEW

- 504 Development-Inspired Reprogramming of the Mammalian Central Nervous System
R. Amamoto and P. Arlotta
Review Summary; for full text:
<http://dx.doi.org/10.1126/science.1239882>

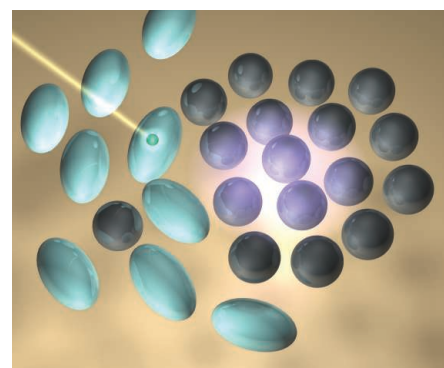
RESEARCH ARTICLES

- 505 Timing Mechanism Dependent on Cell Division Is Invoked by Polycomb Eviction in Plant Stem Cells
B. Sun et al.
A regulatory circuit controlling plant flowering genes leads the way to reconstruction of a time-delay control system.
Research Article Summary; for full text:
<http://dx.doi.org/10.1126/science.1248559>
>> Perspective p. 498
- 506 Exome Sequencing Links Corticospinal Motor Neuron Disease to Common Neurodegenerative Disorders
G. Novarino et al.
Analysis of hereditary spastic paraplegia genes identifies mutants involved in human neurodegenerative disease.
>> Perspective p. 497

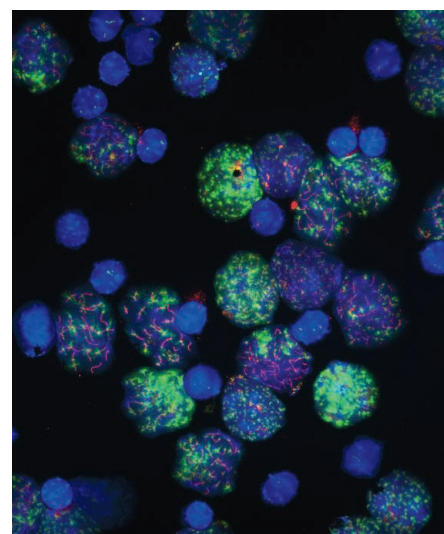
REPORTS

- 512 Ultrafast Long-Range Charge Separation in Organic Semiconductor Photovoltaic Diodes
S. Gélinas et al.
Ultrafast spectroscopy shows electrons and holes separating faster than simple diffusion would imply in organic photovoltaics.
>> Perspective p. 492
- 516 Sound Isolation and Giant Linear Nonreciprocity in a Compact Acoustic Circulator
R. Fleury et al.
Directional fluid flow is used to control and isolate the propagation of sound.
>> Perspective p. 495
- 519 Unlocking the Potential of Cation-Disordered Oxides for Rechargeable Lithium Batteries
J. Lee et al.
Cation-disordered compounds achieve high lithium (Li) storage capacity, with scope for high-energy density Li battery electrodes.
- 522 Low Core-Mantle Boundary Temperature Inferred from the Solidus of Pyrolite
R. Nomura et al.
High-pressure experiments suggest that Earth's mantle melts at lower temperatures than previously predicted.

- 525 A Mechanosensory Pathway to the *Drosophila* Circadian Clock
A. Simoni et al.
Flies use a mechanosensory organ to sense a low-frequency vibration and reset the brain's biological clock.
- 529 Marine Tubeworm Metamorphosis Induced by Arrays of Bacterial Phage Tail-Like Structures
N. J. Shikuma et al.
Benthic marine larval development is triggered by a bacterially expressed structure of phage origin.
- 533 Reversal of Female Infertility by *Chk2* Ablation Reveals the Oocyte DNA Damage Checkpoint Pathway
E. Bolcun-Filas et al.
Elucidation of a system that monitors DNA damage in both meiotic and resting oocytes in mice is shown.
- 536 Mating Induces Shrinking and Death in *Caenorhabditis* Mothers
C. Shi and C. T. Murphy
Sperm and seminal fluid cause *Caenorhabditis* mothers to die shortly after they produce offspring.
- 541 Males Shorten the Life Span of *C. elegans* Hermaphrodites via Secreted Compounds
T. J. Maures et al.
Male nematodes produce a soluble signal that shortens the life span of worms of the opposite sex.
- 544 *Drosophila* Life Span and Physiology Are Modulated by Sexual Perception and Reward
C. M. Gendron et al.
Female pheromones are bad for male flies.
>> Perspective p. 491
- 548 Savanna Vegetation-Fire-Climate Relationships Differ Among Continents
C. E. R. Lehmann et al.
Evolution cannot be overlooked when aiming to predict the potential global impacts on savanna dynamics in a warming world.
- 552 Effector Specialization in a Lineage of the Irish Potato Famine Pathogen
S. Dong et al.
A potato pathogen has changed one of its protease inhibitors that targets its new host plant protease.
>> Perspective p. 496



pages 492 & 512



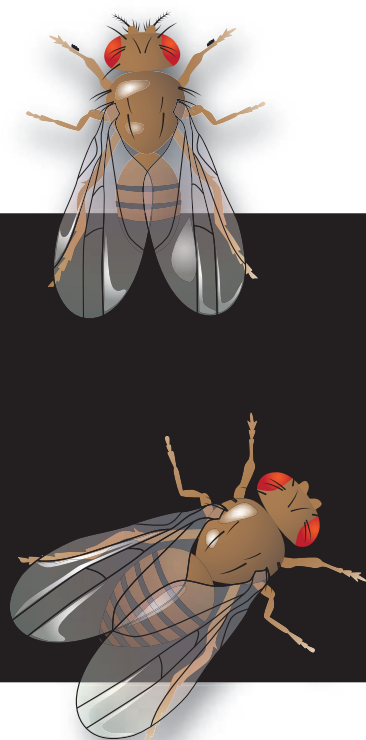
page 533

SCIENCE (ISSN 0036-8075) is published weekly on Friday, except the last week in December, by the American Association for the Advancement of Science, 1200 New York Avenue, NW, Washington, DC 20005. Periodicals Mail postage (publication No. 484460) paid at Washington, DC, and additional mailing offices. Copyright © 2014 by the American Association for the Advancement of Science. The title SCIENCE is a registered trademark of the AAAS. Domestic individual membership and subscription (51 issues): \$149 (\$74 allocated to subscription). Domestic institutional subscription (51 issues): \$990; Foreign postage extra: Mexico, Caribbean (surface mail) \$55; other countries (air assist delivery) \$85. First class, airmail, student, and emeritus rates on request. Canadian rates with GST available upon request, GST #1254 88122. Publications Mail Agreement Number 1069624. Printed in the U.S.A.

Change of address: Allow 4 weeks, giving old and new addresses and 8-digit account number. Postmaster: Send change of address to AAAS, P.O. Box 96178, Washington, DC 20090-6178. Single-copy sales: \$10.00 current issue, \$15.00 back issue prepaid includes surface postage; bulk rates on request. Authorization to photocopy material for internal or personal use under circumstances not falling within the fair use provisions of the Copyright Act is granted by AAAS to libraries and other users registered with the Copyright Clearance Center (CCC) Transactional Reporting Service, provided that \$30.00 per article is paid directly to CCC, 222 Rosewood Drive, Danvers, MA 01923. The identification code for Science is 0036-8075. Science is indexed in the Reader's Guide to Periodical Literature and in several specialized indexes.

Battle of the Sexes

In many species, males compete with one another to propagate their own DNA, often to the detriment of females (see the Perspective by Promislow and Kaeberlein). Shi and Murphy (p. 536, published online 19 December) discovered that mating in *Caenorhabditis* species causes mothers to shrink and die soon after they have ceased producing progeny. Males appear to hijack the longevity and stress resistance pathways normally employed by the mothers to slow reproduction and somatic aging in times of stress. Maures *et al.* (p. 541, published online 29 November) explored why the presence of abundant mating-competent males causes a decrease in the life span of nematodes of the opposite sex and found that a secreted substance, possibly a pheromone, reproduced the effect of the males when transferred in the culture medium. Detection of pheromones from a female fruit fly is enough to cause changes in metabolism, reduce resistance to starvation, and shorten the life span of male flies. Gendron *et al.* (p. 544, published online 29 November) report that the signals from the female appear to be recognized by sensory receptors on the legs of male flies.



Neurodegenerative Genetics

The underlying genetics of neurodegenerative disorders tend not to be well understood.

Novarino *et al.* (p. 506; see the Perspective by Singleton) investigated the underlying genetics of hereditary spastic paraplegia (HSP), a human neurodegenerative disease, by sequencing the exomes of individuals with recessive neurological disorders. Loss-of-function gene mutations in both novel genes and genes previously implicated for this condition were identified, and several were functionally validated.

Early Separation

In photovoltaic devices, electrons excited by the absorption of light must travel across a junction, while the positively charged “holes” they leave behind effectively migrate in the opposite direction. If the electrons and holes do not separate efficiently, they can recombine and fail to produce any appreciable current. Gélinas *et al.* (p. 512, published online 12 December; see the Perspective by Bredas) studied this separation process by ultrafast optical absorption spectroscopy in thiophene-derived donor-fullerene acceptor systems common in organic photovoltaics and report a rate significantly faster than simple charge diffusion would suggest. The results implicate a coherent charge delocalization process, likely to involve fullerene π -electron states.

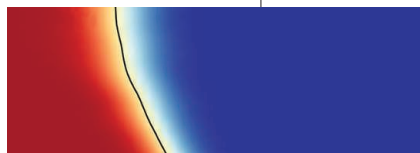
Acoustically Isolated

The control of sound transmission is desirable in a number of circumstances from noise suppression to imaging technologies. Fleury *et al.* (p. 516; see the cover; see the Perspective by Cummer) studied a subwavelength acoustic

meta-atom consisting of a resonant ring cavity biased by an internally circulating fluid. The direction of rotational flow of the fluid (air) changed the resonant properties of the ring cavity, allowing the propagation of sound waves within the cavity to be controlled. With several ports connected to the cavity, sound could be directed to a certain port while isolating transmission in another.

Disorderly Flow

Lithium batteries are becoming ever more important in society. While their application used to be confined to portable electronics, they are now becoming the enabling technology for electric vehicles and grid storage for renewables. Generally, the flow of lithium ions into and out of battery electrodes is thought to require ordered materials. Lee *et al.* (p. 519, published online 9 January) used a combination of experimental work and computations to identify disordered electrode materials with high Li diffusion. The improved energy density properties could be attributed to compositions with excess lithium beyond the stoichiometric limit, leading to intermixing between the lithium and transition metal sublattices and the formation of a percolation network providing specific lithium transport pathways.



Big MACs

Tubeworms are important marine benthic species that encrust rocks and contribute to fouling of man-made objects, such as ships’

hulls and drilling well heads. Like most marine invertebrates, the larval stages of tubeworms are free-swimming, but the cues for larval settlement and the triggers for metamorphosis are mysterious. Shikuma *et al.* (p. 529, published online 9 January) experimented on larval settlement by the tubeworm, *Hydroides elegans*, which needs to associate with a biofilm-forming bacterium, *Pseudoalteromonas luteoviolacea*, before settlement can occur. The bacterium was found to express metamorphosis-associated contractile structures (MACs) in large and structurally elaborate arrays that allow the tubeworm larvae to develop.

Surveying Savannas

Savannas are structurally similar across the three major continents where they occur, leading to the assumption that the factors controlling vegetation structure and function are broadly

similar, too. Lehmann *et al.* (p. 548) report the results of an extensive analysis of ground-based tree abundance in savannas, sampled at more than 2000 sites in Africa, Australia, and

South America. All savannas, independent of region, shared a common functional property in the way that moisture and fire regulated tree abundance. However, despite qualitative similarity in the moisture–fire–tree–biomass relationships among continents, key quantitative differences exist among the three regions, presumably as a result of unique evolutionary histories and climatic domains.

Additional summaries

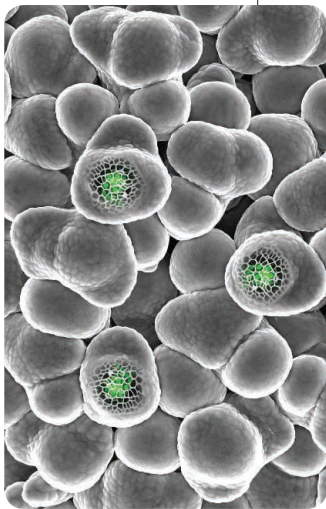
Repairing the Brain

Research with stem cells and reprogramming of cellular fates is leading to improved understanding of neurodevelopmental events, as well as opening doors to possible cellular replacement therapies. **Amamoto and Arlotta** (p. 504) review recent progress in this field and highlight the discoveries made and the remaining challenges as stem-cell technologies are applied to cells of the central nervous system.

A Matter of Timing

Plants flower only when their developmental programs give the go-ahead; otherwise floral genes remain repressed. **Sun et al.** (p. 505; see the Perspective by **Zhang**) analyzed the regulatory program that controls expression of the transcription factor KNUCKLES (KNU), which is required in the control of floral genes. KNU

expression was silenced by the presence of Polycomb group (PcG) proteins. The floral homeotic protein AGAMOUS competed for



control of KNU and activated its expression, but with a 2-day lag time. Thus, eviction of PcG by activating DNA binding proteins can insert a lag time before a switch in gene expression takes place.

Melting Moments

The boundary between Earth's core and mantle defines where the iron-rich liquid outer core meets the more chemically heterogeneous solid lower mantle and is marked by a sharp thermal gradient of nearly 1500 kelvin. The precise relationship between temperature and melting of the lowermost mantle constrains

the structure and heat flow across the core-mantle boundary. In order to identify trace amounts of liquid as melting initiates, **Nomura et al.** (p. 522, published online 16 January) performed x-ray microtomographic imaging of rocks of a primitive mantle composition that had been subjected to high pressures and temperatures in a diamond anvil cell. The experimentally determined maximum melting point of 3570 kelvin suggests that some phases typically thought to lose stability in the lowermost mantle, such as MgSiO₃-rich post-perovskite, may be more widely distributed than expected.

Coordinating the Clock

In flies, the mechanosensory chordotonal organs help to coordinate the effects of temperature on circadian cycles. **Simoni et al.** (p. 525)

provide a mechanism by which mechanosensory input is processed to help to synchronize the biological clock in *Drosophila melanogaster*. The chordotonal organs, which have similarities to the mammalian ear, were also required for sensation of a vibration stimulus and its effects on the endogenous brain clock. The chordotonal organs, present in the joints of the limbs, provide neuronal signals that allow the animal to sense its position or posture—and thus might mediate feedback of a range of behaviors onto the endogenous biological clock.

The Makings of a Choosy Pathogen

The oomycete *Phytophthora infestans* is responsible for potato blight. A closely related pathogen afflicts the 4 o'clock flower. To assess why such similar pathogens are restricted to one host or the other, **Dong et al.** (p. 552; see the Perspective by **Coaker**) analyzed similar effectors from both pathogens. The results suggest that the host specialization that led to evolutionary divergence depends on reciprocal single-amino acid changes that tailor the pathogen effector to a specific host protease that is being disabled. Thus, small changes can open the door for a pathogen to jump to another species of host and, itself, diversify into another species of pathogen.

Eggs Well Done

Germ cells can endure extensive DNA damage during their development. Programmed meiotic double-strand breaks (DSBs) are essential for proper segregation of chromosomes to oocytes and sperm. However, incomplete DSB repair by recombination activates a checkpoint that triggers cell death. Exogenous DNA damage is also lethal to oocytes via a highly sensitive checkpoint. **Bolcun-Filas et al.** (p. 533) show that the CHK2 kinase is a key component of both checkpoints in mouse oocytes. Deletion of *Chk2* restored fertility to females that would otherwise be sterile because of a meiotic recombination mutation or radiation exposure.



Martyn Poliakoff is Foreign Secretary of the Royal Society of London. E-mail: martyn.poliakoff@royalsociety.org

Visa Labyrinth

THE DATE OF AN EXCITING OVERSEAS ACADEMIC CONFERENCE IS APPROACHING, AND YOU DISCOVER that you need a visa. You have to fill out an endless form (do you really have to list every country you've visited over the past 5, or even worse 10, years?). You may need to travel to a distant town for an interview. The visa may cost as much as your airline ticket. You begin to question whether you really need to go to this conference at all. And you wonder what things are like for someone trying to get a visa to attend a conference in your own country or work in your institution.

This is a global problem. Throughout most of the developed world, governments are responding to domestic concerns over immigration by tightening entry requirements and introducing ever more complex application procedures for visas. This situation is harming science. Governments are failing to appreciate, perhaps unknowingly, that scientists and engineers across the world need to meet to carry on their business. The history of major scientific breakthroughs is littered with accounts of seminal Solvay Conferences, Faraday Discussions, Gordon Research Conferences, and so on, where key ideas were articulated for the first time. Young researchers need to travel to widen their horizons and build up their skills by experiencing the scientific cultures and approaches in different countries. Most countries, including the United Kingdom, recognize this and do welcome young scientists when they arrive. Nevertheless, the bureaucratic visa labyrinth still sends a subliminal if not explicit message of "Stay at home."

As Foreign Secretary of the Royal Society, I hear of failed visa applications and other immigration problems in the United Kingdom and across the world. Although the problems can sometimes be the fault of scientists who are not organized enough to apply for a visa in time, there is clearly a more fundamental problem with some visa systems. What can be done to fix this?

We cannot assume that all governments understand that a problem exists. Senior scientists and engineers need to explain to their governments that the movement of talented researchers is an essential prerequisite to addressing the grand challenges facing society around the globe, such as climate change, sustainability, and antibiotic resistance. Scientists also need to make it clear that overseas researchers are not economic migrants who are hell-bent on stealing jobs from locals, but an essential component of a country's scientific workforce. And scientists must emphasize to governments that international exchange is the best way of training future scientific leaders for the developing world. But more radical action is needed. The scientific community needs international recognition to legitimize the exchange of researchers and scientific dialogue across the world.

Last year, the Royal Society hosted the first of what it hopes will become regular meetings of the G8 science ministers and the presidents of their academies of science. There was constructive discussion and consensus on important issues, but visas for scientists were not discussed. Therefore, I suggest that a communique from the next meeting, provisionally scheduled for this summer, should recognize the need for free and widespread international exchange of researchers in science and engineering, especially for the younger generation. Admittedly, this would be a small step, but perhaps it might start the chain reaction that is needed to reach the ultimate goal of a single worldwide scientific community.

Local action can help too. The Royal Society and other UK academies have been steadily building a working relationship with the UK Border Agency, and we are hopeful that constructive engagement with those in the front line can help smooth the process. The simultaneous but potentially conflicting political goals of wanting to promote international scientific collaboration and being tough on immigration can lead to unintended consequences. However, when discussed constructively, such conflicts and misunderstandings can almost certainly be resolved to the benefit of global science.

— Martyn Poliakoff

10.1126/science.1250720

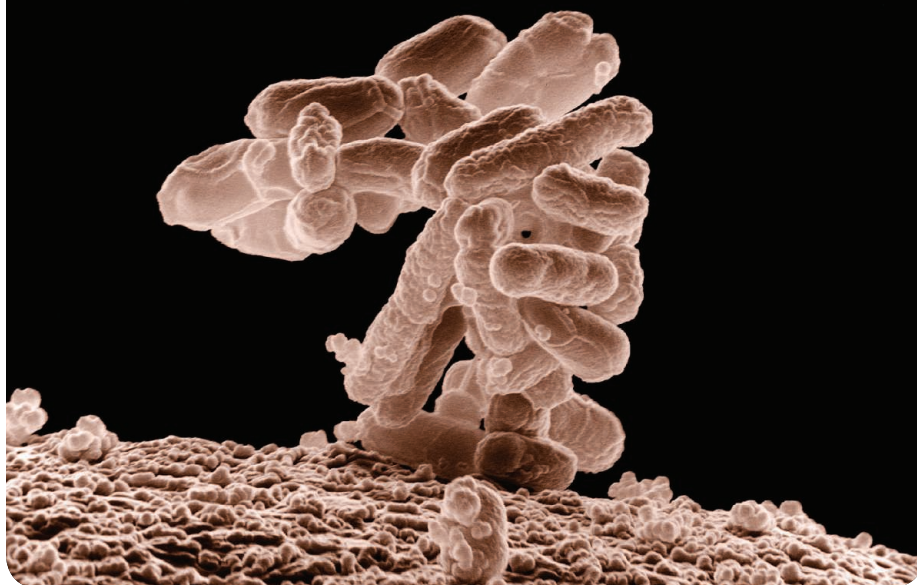


ENVIRONMENTAL SCIENCE

Recalcitrant Resistance

The increased use of antibiotics is resulting in a rise of antibiotic-resistant bacteria, and wastewater treatment plants (WWTPs) that employ biological remediation processes may provide a breeding ground for them as trace amounts of antibiotics arrive in the waste stream. Su *et al.* examined over 1000 *Escherichia coli* isolates collected from various treatment steps at two WWTPs in Guangdong Province, South China. At least 98% of the isolates were resistant to 1 of 12 screened antibiotics in either plant, and over 90% were resistant to at least three antibiotics. Plasmid-mediated quinolone resistance genes and an ampicillin resistance gene (*ampC*)—both common in clinical isolates—were found in ~43% of the isolates. Disinfection steps in the plants, including UV treatment and chlorination, reduced overall bacterial abundance; however, the percentage of antibiotic-resistant bacteria (and presence of plasmid-mediated resistance genes) was higher in effluent after various biological treatment steps. WWTPs can therefore serve as a reservoir and distribution center of antibiotic-resistant genes and bacteria. —NW

Environ. Sci. Processes Impacts 10.1039/c3em00555k (2014).

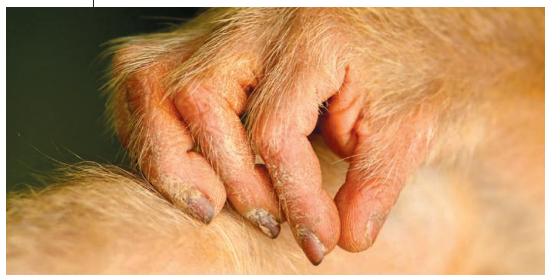


NEUROSCIENCE

Bring Up the Bodies

The physiology of face-selective cells in specialized cortical areas has been studied in great detail. We know much less about neurons in brain regions specializing in the visual representation of bodies. Functional MRI studies have identified areas that are activated by body images. Popivanov *et al.* recorded local field potentials and individual neuronal spikes from such brain scan-defined body-selective patches in the monkey superior temporal sulcus. Local field potential gamma power and neuronal population spikes were enhanced for body, compared to nonbody, images. Averaging responses from a group of individual cells caused category

selectivity in the neuronal population. Individual cells exhibited strong within-category selectivity and reacted to only a subset of bodies. A linear support vector machine classifier, trained using the spiking responses to a sample of the images, accurately classified untrained body images. Interestingly, the heterogeneous response properties of the neurons in the body patch allowed accurate classifications of all other classes,



even faces or artificial objects. The single units responded selectively to specific body parts even at different orientations. Neurons in this particular body patch thus show selectivity for both body and nonbody images, but with a stronger response to bodies. — PRS

J. Neurosci. 34, 95 (2014).

MOLECULAR BIOLOGY

Polycomb Recruitment via lncRNA

There are many protein complexes that modulate gene expression during differentiation and development. Each must be targeted to the correct regulatory sequences in the genome, to orchestrate the appropriate cell- or tissue-specific gene expression programs. Some complexes target DNA by direct binding to a specific DNA sequence. Others must be recruited by auxiliary factors to their place of action. None of the core components of the polycomb repressive complex-2 (PRC2) are able to bind DNA, yet PRC2 is targeted to, and critical for, repressing cell type-specific genes throughout development. The Jumonji family, ARID domain-containing protein JARID2, an accessory subunit of PRC2, is somehow involved in that recruitment process. Kaneko *et al.* show that JARID2 can bind to long noncoding RNAs (lncRNAs), among them Meg3, and this interaction recruits PRC2 to a subset of its target genes. Meg3 binding to JARID2 also stimulates the interaction of JARID2 with one of the core subunits of PRC2, EZH2, with which Meg3 can also interact. Binding of JARID2 to the Meg3 lncRNA thus serves both to recruit and assemble PRC2 on chromatin. — GR

Mol. Cell 53,10.1016/j.molcel.2013.11.012 (2014).

BIOMEDICINE

Interferon Boosts Efficacy

Therapeutic monoclonal antibodies, several of which have shown impressive outcomes in clinical trials, are an exciting avenue for treating cancer. Resistance to antibody treatment remains a major challenge, however, and so strategies to overcome such resistance are needed. Yang *et al.* report on one such strategy: Taking the knowledge that an increase in type I interferons (IFNs) correlates positively with clinical outcome in several cancers and that type I IFNs can enhance antitumor immunity in some models, the authors tethered IFN- β to a monoclonal antibody targeting the epithelial growth factor receptor (EGFR), which is approved for use in treating metastatic colorectal cancer and head and neck cancer. In a variety of tumor mouse models, including antibody-resistant tumor models, the antibody-

IFN therapy was more effective than antibody therapy alone. Mechanistic studies showed that IFN increases antitumor immune responses by enhancing antigen presentation to T cells by dendritic cells present in the tumor microenvironment. Delivery of the antibody-IFN therapy with an additional therapeutic monoclonal antibody enhanced the durability of the treatment, further supporting the idea that effective cancer immunotherapy will require hitting multiple targets. — KLM

Cancer Cell **25**, 37 (2014).

SOCIAL NETWORKS

Information and Freedom

There are many anecdotes linking digital media access to democracy, including the use of social media to organize and communicate information about protests. Rhue and Sundararajan col-



lected needed empirical data on 189 countries for the period 2000–2010. Democracy was measured as scores from the independent watchdog organization Freedom House on civil liberties, media freedom, and political rights. Digital access (mobile phone and Internet) was obtained from the International Telecommunication Union, an agency of the United Nations. Digital access was positively associated with civil liberties and media freedom. Mobile penetration had a greater impact on civil liberties than Internet access. Dynamic analyses revealed that greater access to mobile technology had an increased effect on civil liberties when a neighboring country (or a trade partner) scored high in civil liberties, suggesting that the diffusion of civil liberties is enhanced by digital access. — BJ

Soc. Networks **36**, 40 (2014).

APPLIED PHYSICS

Putting a Twist on Multiplexing

Light is a versatile medium for communication, with the optic fibers that span the globe forming the backbone of our Internet and communi-

cations industry. The insatiable hunger for even higher data rates and a faster Internet requires more light to be pumped along the fiber network. There is, however, a limit to how much light you can put into a fiber before optical nonlinearities are induced and the communications channel is corrupted. The traditional solution is to multiplex the various modes of light (wavelength and polarization, for instance) so the information is encoded in a number of channels (split between multiple wavelengths and polarization states) sent down the fiber in parallel, and then de-multiplexed at the other end: The aggregated data rate is boosted by the number of channels used. Recent work has explored the optical angular momentum of light, wherein the light is structured or twisted like a spiral and carries quantized units of angular momentum as it propagates. In a free-space demonstration, Huang *et al.* show that multiplexing wavelength, polarization, and optical angular momentum enables data transmission rates in excess of 100 Tbit/s. Transferring such a route of multiple multiplexing to optic fibers should stave off our hunger for faster data rates for a little while yet. — ISO

Opt. Lett. **39**, 197 (2014).

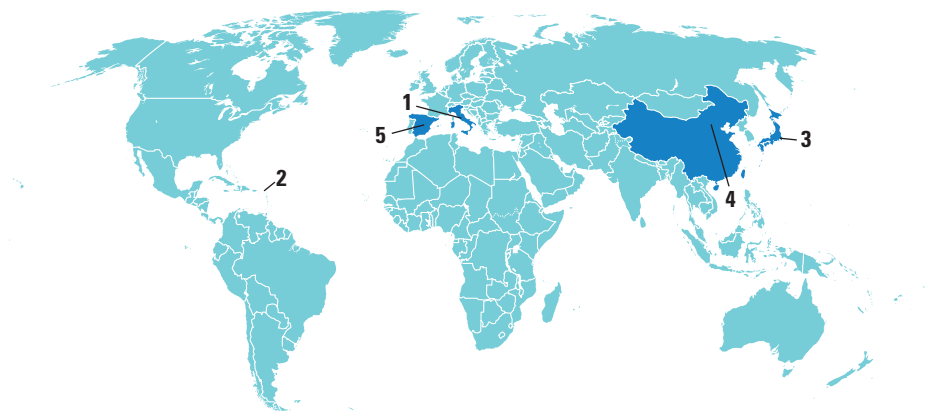
CHEMISTRY

Assembling Coated Nanocubes

For many applications of nanoparticles, it is desirable that they assemble into periodic structures or even crystallize. Knorowski and Travasset used a theoretical model to explore the effect of DNA coatings on phase diagrams for nanocube assembly. Previous studies have focused mainly on the assembly of hard cubes. The authors explored this case, as well as hard cubes (about 12 or 18 nm across) coated with single-stranded DNA strands lacking complementary ends (an f-star polymer) and pairs of nanocubes with complementary ends. The hard nanocube system evolved from a simple cubic (sc) packing to a triclinic phase for the f-star coating at isotropic pressure. For anisotropic osmotic pressures, body-centered cubic (bcc) ordering occurred, but the cubes developed a complex orientational ordering. For complementary DNA coatings, the results depended on strand length, with short strands creating face-to-face hybridization and sc lattices and longer strands creating a bcc packing. More complex ordering than the f-star system developed at high osmotic pressure. Because polymer coatings could be polymerized, it may be possible to use such phase behavior to direct nanocube assembly. — PDS

J. Am. Chem. Soc. **136**, 10.1021/ja406241n (2014).

AROUND THE WORLD



Rome 1

Italy Faces E.U. Fine Over Animal Testing Directive

A legislative stalemate over animal research could become very costly for Italy. On 23 January, the European Commission asked the E.U. Court of Justice to impose a fine of more than €4.5 million per month on the country for failing to incorporate a 2010 E.U. directive on animal testing into national laws by 10 November 2012. The directive aims to minimize the use of animals in research and standardize animal protections across the union. Six other countries are also delinquent, but so far only Italy has faced a penalty.

While Italy awaits the court's decision, a draft law is wending its way through the political system that would impose limitations well beyond those required by the European Union, but would postpone until 2017 some of the most controversial parts of the directive, including bans on drug abuse research involving animals. Scientists have spoken out against the bill, while animal rights activists have launched fierce demonstrations and even personal attacks on Italian researchers. A decision on the law is expected in March. <http://scim.ag/EUfine>

Saint Martin 2

Chikungunya Gains Foothold In the Americas

The mosquito-borne chikungunya virus appears to have established itself in the Caribbean, raising fears that the disease, which causes high fever and debilitating joint pain, will soon make its way to mainland North and South America. The outbreak represents the first time mosquitoes have spread the virus between people in the Americas. Previously, all chikungunya

patients in the region had picked up the virus while traveling in endemic areas in Africa, Europe, and Asia.

Since the first two locally acquired cases were confirmed on the French section of



Bad sign. Characteristic rash and vector (*Aedes aegypti*) of chikungunya.

Islands, according to the European Centre for Disease Prevention and Control.

The chikungunya virus, first detected in Tanzania in 1952, is primarily transmitted by *Aedes aegypti* mosquitoes, which are also responsible for spreading dengue fever. Symptoms can last for weeks or months, and there is no vaccine or cure.

Tokyo 3

Alzheimer's Researcher Strikes Back at Allegations

Scientists accused of data manipulation in a large Alzheimer's study are staunchly defending the integrity of the data, but acknowledge shortcomings in the project's management. The *Asahi Shimbun*, a Japanese newspaper, claimed in its 10 January issue that researchers behind the ongoing \$31 million Japanese Alzheimer's Disease Neuroimaging Initiative

(J-ADNI) changed details of memory tests long after data were collected and that some participants were improperly included (*Science*, 17 January, p. 234).

Neuropsychiatrist Takashi Asada of the University of Tsukuba, who oversees the study's clinical side, calls the story "completely fake." After a standard prepublication data check turned up possible inputting errors, researchers double-checked their records and made changes, but did not falsify data, Asada maintains. Patients above the study's 85-year age limit were enrolled by mistake, he says, and will be omitted from analyses and publications. Several U.S. Alzheimer's researchers have voiced support for their Japanese colleagues via Alzforum. The University of Tokyo, where an ethics committee approved the project protocol, has agreed to a health ministry request to investigate the research. <http://scim.ag/J-ADNI>

Beijing 4

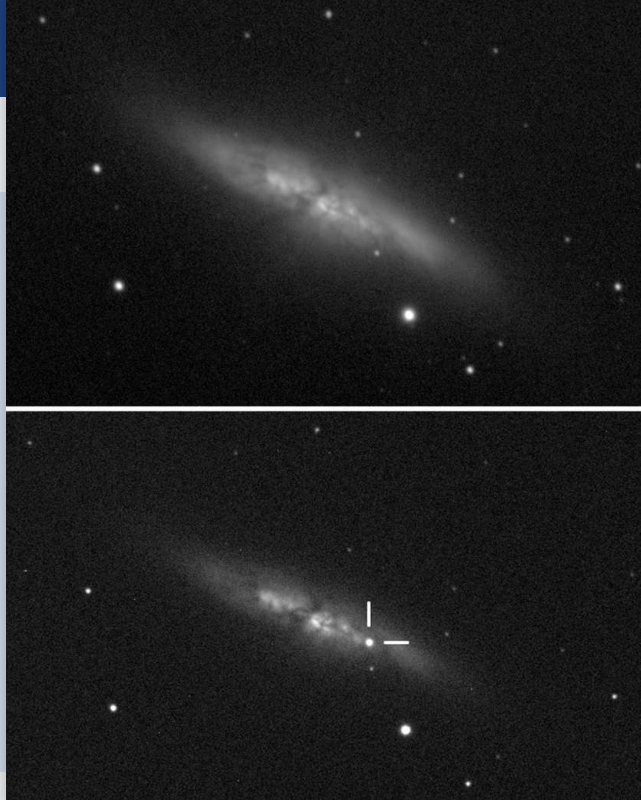
Lunar Rover in Peril

It may be curtains for China's moon rover. On 25 January, the Chinese defense science agency announced that the Jade Rabbit rover had encountered a mechanical "abnormality" just before entering hibernation mode to wait out the 2-week-long lunar night. The rover simply was unable to move, explains a mission scientist. He says that engineers are holding out hope that the frigid lunar night will "change the status a bit" and allow them to solve the problem.



Better days. Jade Rabbit on the moon last week.

A failure to rouse Jade Rabbit after the lunar day dawns next week would scuttle a big chunk of the mission's scientific program. The rover began its anticipated 3-month mission on 14 December by probing surface geochemistry and taking ground-penetrating radar images as much as 100 meters deep—a lunar first. But even if sunrise brings bad news, the Chang'e-3 lander will soldier on alone, using its ultra-



Now You See It ...

"One minute we're eating pizza then five minutes later we've helped to discover a supernova." That's how one of four undergraduate students at University College London summed up last week's chance discovery of a type Ia supernova 12 million light-years from Earth. Named SN2014J, the exploding star is the closest supernova of its kind to be spotted in 4 decades.

During an evening telescope workshop, the students' professor, Steve Fossey, noticed a bright spot in the galaxy Messier 82 (left) that he hadn't seen before. Other telescopes around the world soon confirmed that it was a type Ia—one of the brightest events of the cosmos. They arise when a white dwarf—the compact, burned-out husk of a solar-mass star—accumulates enough material from a companion star to ignite a runaway explosion. Researchers plan to collect spectral data on SN2014J that should help them better understand the origin and brightness trajectory of type Ias.

violet camera to observe Earth's plasma-sphere and a near-ultraviolet telescope to make the first detailed observations of stars and galaxies from the moon's surface.

Madrid 5

Court Upholds Fines for Unauthorized Clinical Trial

A Spanish court of appeals has upheld fines for HIV/AIDS researcher Vicente Soriano of the Hospital Carlos III in Madrid. Soriano is liable for €210,000 for three violations: conducting a clinical trial without the Spanish Agency for Medicines and Health Products' approval, failing to obtain insurance for the trial, and informing participants he had his hospital's ethical approval when he did not, according to the decision published 14 January.

The 2009 study, published in *HIV Clinical Trials* in 2010, involved 311 patients with undetectable HIV levels undergoing protease inhibitor treatment. Seeking to reduce side effects, Soriano proposed once-daily treatments with the antiretroviral drug raltegravir

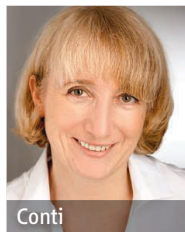
instead of the approved twice-daily protocol. He appealed the original 2011 decision by a lower court, describing his work as an observational study, not a clinical trial. He says he was the victim of "harassment" from the hospital, where he continues to work. <http://scim.ag/trialfine>

NEWSMAKERS

Brain Mapper and RNA Researcher Bag Medicine Prize



Le Bihan



Conti

This year's Louis-Jeantet Prize for Medicine goes to two researchers devoted to studying basic processes: how water moves through the brain and how cells dispose of damaged goods. The Swiss foundation, named for French businessman Louis Jeantet, gives the annual award for fundamental biological research with promising clinical implications.

It chose physicist and physician **Denis Le Bihan** for his role in developing diffusion MRI, a technique that reveals the structure of the brain by tracking how water and other molecules move within tissues. Diffusion MRI has been used to recognize signs of disease in the brain, from cancer and stroke to Alzheimer's and schizophrenia.

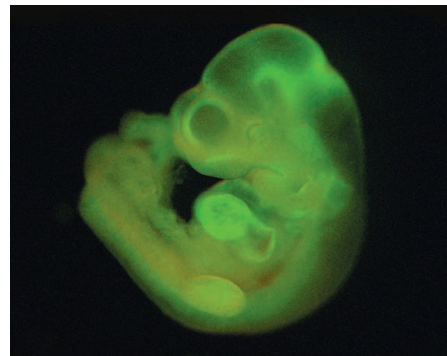
Biochemist **Elena Conti** of the Max Planck Institute of Biochemistry in Munich, Germany, studies the structure and activity of cellular mechanisms that recognize faulty RNA molecules and break them down. She will be honored alongside Le Bihan in April at an award ceremony in Geneva. Each will receive roughly \$780,000 in prize money, of which nearly \$700,000 must be devoted to future research.

FINDINGS

Acid Test Generates Stem Cells

Scientists have found yet another way of making stem cells that could have advantages over current methods. Researchers at Harvard Medical School in Boston and the RIKEN Center for Developmental Biology in Kobe, Japan, took differentiated cells from neonatal mice, subjected them to a moderately acidic environment for 25 minutes, and then returned them

>>



Restart. A mouse fetus created from STAP cells.

THEY SAID IT

"Are you going to cover the alien rock throwers?"

—Question submitted via Twitter by *Star Trek* star William Shatner to a NASA news briefing last week, regarding the mysterious "jelly doughnut" rock photographed by the Mars Opportunity rover.

>>FINDINGS

to a standard cell culture medium. A week later, cells that had survived the stress of the acid treatment had reverted to a pluripotent state—able to differentiate into nearly all cell types. Further culturing transformed what the researchers call stimulus-triggered acquisition of pluripotency (STAP) cells into self-renewing stem cells, the group reports in two papers in *Nature* this week.

Previously, researchers have created pluripotent stem cells from embryos and by introducing proteins called transcription factors. The new STAP method avoids the ethical objections of using embryos and the genetic mutations that transcription factors sometimes induce. These benefits could make STAP stem cells useful for regenerative medicine applications if the procedure proves to work for human cells.

http://scim.ag/_STAP

Science LIVE

Join us on Thursday, 6 February, at 3 p.m. EST for a live chat with experts on **combining alternative therapies with conventional medical treatments.** <http://scim.ag/science-live>

**Arizona's Grand Canyon a Patchwork of the Ages**

Is the Grand Canyon young or old, geologically speaking? A new study answers the much-debated question with a definitive ... “both.” Geologists have few clues about the shape of the land tens of millions of years ago, but they have ways to guess. Rocks deeper in the crust are hotter, and they cool as a river removes overlying rock. The decay of certain elements tells scientists when a rock cooled to a certain temperature—and therefore when the overlying rock was removed and a canyon formed.

BY THE NUMBERS

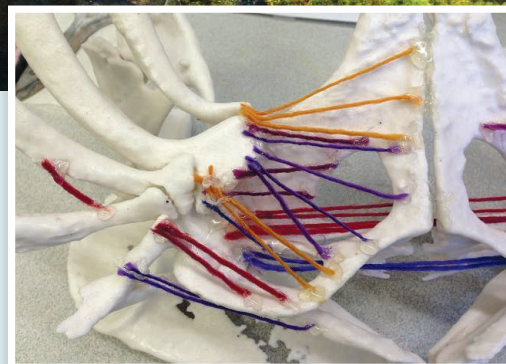
54.7 Average hours worked per week, according to an international survey of 650 early-career researchers by the Global Young Academy. <http://scim.ag/GYAsurv>

1.78 billion People breathing unhealthy air around the world, according to the latest survey by the Environmental Performance Index, up by 606 million since 2000.

A team of geologists and geochemists combined existing published data with some of their own for a new estimate: Two of the present canyon's five segments formed early on—one between 70 million and 50 million years ago, another between 25 million and 15 million years ago. But the two end segments were carved in the past 5 million to 6 million years, since the Colorado River first began flowing down the present canyon, they reported online on 26 January in *Nature Geoscience*. The nuanced view aims to put the debate to rest, but conflicting interpretations still abound. <http://scim.ag/canyonage>

Random Sample**3D Printouts Reveal How the Clingfish Clings**

While most fish use their fins to move, the aptly named clingfish also uses them to stay put on rocky Pacific shores. Its pelvic fins have formed a suction cup structure that attaches to rocks and holds the fish in place, despite breaking waves. Comparative biomechanist Adam Summers of the University of Washington's Friday Harbor Laboratories couldn't figure out how this nickel-sized structure with 211 bones and muscles generated and maintained the negative pressure needed to stay stuck. So he and Thomas Kleinteich from Kiel University in Germany turned for help to a so-called 3D printer. Based on coordinates from a CT scan of a clingfish suction disc, Kleinteich printed plaster replicas of its bones at 20 times their actual size and pieced them together. Then he recreated the connecting muscles from yarn using a second CT scan of the soft tissue as a guide. The oversized disk proved easier to analyze, revealing specific muscles that pump out water to create negative pressure and showing that the backward stroke of a single bone was enough to break the suction. Summers reported earlier this month at the annual meeting of the Society for Integrative and Comparative Biology in Austin. His team has also used the printer to shrink whale shark heads to a workable size and to create dozens of precisely sized shells to test how hermit crabs choose their homes. Once considered a luxury item in biology labs, 3D printers are “now totally in the reach of any lab,” Summers says. “Everyone is going to be using them.”



CREDITS (TOP TO BOTTOM): LAURA CROSSEY/UNM; PETRA DITSCHKE; © THOMAS KLEINTEICH



HUMAN EVOLUTION

Neandertals and Moderns Made Imperfect Mates

Tens of thousands of years ago along the balmy Mediterranean coast, or in some desert oasis in the Middle East, a hunky Neandertal male lusted after a modern human maiden. Or perhaps a sleek modern guy scored with an earthy Neandertal girl. Either way, living people in Europe and Asia still carry traces of those long-ago unions. Now two studies, the first to analyze Neandertal DNA in large numbers of living people, pinpoint genes we have inherited from our extinct cousins, including some that leave their mark on hair and skin and others implicated in disease.

The studies also show that those ancient mixed couples were not fully compatible. Both studies suggest that Neandertals and moderns came from such different genetic backgrounds that the descendants of their unions became less fertile over time, purging many Neandertal genes from modern genomes. “There were costs to interbreeding,” says population geneticist Joshua Akey of the University of Washington, Seattle, senior author of a report online this week in *Science* (<http://scim.ag/BVernot>). Population geneticist David Reich

of Harvard Medical School in Boston, who led the study reported in this week’s issue of *Nature*, agrees: “When Neandertals and modern humans mixed, they were at the edge of biological compatibility.”

To explore Neandertals’ genetic legacy, each team developed new methods that identify and precisely map Neandertal DNA in modern human genomes. Both methods use European and Asian genomes sequenced since 2008 as part of the first phase of the 1000 Genomes Project, the world’s largest data set of human genetic variation. The teams focused on the DNA of people from outside of Africa because small groups of Neandertals and moderns humans met after the moderns swept out of Africa in the past 90,000 years. Non-Africans carry the genetic legacy of those encounters.

One technique, developed by population geneticist Sriram Sankararaman in Reich’s lab, employs a software program that trains itself to recognize the signature of Neandertal DNA using a Neandertal genome as a reference. The software recognizes likely segments of Neandertal DNA based

Conditions Associated With Neandertal Alleles

Lupus

Primary biliary cirrhosis

Crohn’s disease (2 alleles)

Type 2 diabetes

Variation in keratin in skin and hair (several alleles)

Variation in interleukin-18 levels

Variation in optic disc size

Variation in smoking behavior

Great-great-great-Grandma? Living people may carry more genes from Neandertal females, like the one in this artist’s reconstruction, than from Neandertal males.

on single-nucleotide polymorphisms, or one base pair variations, found in the Neandertal genome when it is compared with the genomes of Africans. It also relies on the segments’ length, which is a clue to when they were introduced into the modern human genome. (Over time, introduced chunks of DNA are broken up by recombination.)

In more than 60% of 1004 East Asian and European genomes they studied, the team identified a Neandertal version of a particular gene that affects the function of the protein keratin in skin, nails, and hair. Keratin helps waterproof skin, makes it sensitive to heat and cold, and blocks pathogens. The team speculates that the Neandertal allele may have helped our ancestors adapt rapidly to the colder habitats in Europe and Asia. Additional Neandertal alleles that Reich’s team uncovered also affect keratin, and others seem to make modern humans more susceptible to diseases such as diabetes, lupus, and Crohn’s disease, and even to smoking addiction (see table). These alleles may not have harmed Neandertals, but Reich says they may cause disease in modern humans by interacting poorly with modern DNA.

Like Reich’s team, Akey and graduate student Benjamin Vernot developed a tool for finding archaic DNA in modern genomes—in this case 379 Europeans and 286 East Asians from the same 1000 Genomes data. Their method also relies on the length of DNA segments and their distinctness from African sequences. But it doesn’t use a Neandertal reference genome, so it can detect DNA from any kind of archaic human. This team also found Neandertal genes involved in keratin and skin pigmentation. “It’s reassuring that we’re converging on similar answers,” Akey says. Like previous studies that analyzed far fewer modern genomes (*Science*, 17 May 2013, p. 799), both teams conclude that from 1% to 3% of the genome in Europeans and East Asians comes from Neandertals.

The total amount of Neandertal genes in modern genomes is much higher than that, however, because different people carry different assortments of the ancient genes. Akey’s team recovered about 20% of the total Neandertal genome in their sample; Reich’s lab, 30%. “People say, let’s cross a Neandertal with a modern human to

understand Neandertal biology ... [but] it's already been done," Reich says. "It happened 60,000 years ago, and a lot of that Neandertal variation is still there."

But what struck the researchers most was what they didn't see. In about 20 regions of the modern human genome, both teams detected "deserts" of Neandertal genes. The starkest were on the X chromosome, which held one-fifth as much Neandertal DNA as the rest of the genome, and in genes expressed in testes. Such deserts can't be accidental, Reich says. They suggest that men carrying Neandertal genes for the testes, for example, were less likely to reproduce. "A massive process has removed at least one-third of the Neandertal ancestry that initially came into the modern human genome," he says.

In animal studies of mice, rabbits, or fruit flies, such patterns appear when two subspecies are diverging into separate species. Hybrid males eventually become infertile before females, because men carry only one X chromosome, and so become infertile if the DNA on it is incompatible with their mates' X chromosome. Women carry two Xs and so have better odds of staying fertile. Now, researchers are exploring whether we have inherited more DNA from Neandertal females than from males. In any case, "these Neandertals and humans were in the process of becoming reproductively isolated," says evolutionary geneticist Bret Payseur of the University of Wisconsin, Madison, who was not a co-author.

Finding traces of incipient speciation in human DNA is a stunning switch for biologists used to focusing on animals. "Seeing the signature of these rules of speciation in our own history is really amazing," says speciation expert Daven Presgraves of the University of Rochester in New York.

Paleoanthropologist John Hawks of the University of Wisconsin, Madison, however, notes that other evolutionary forces might have purged Neandertal genes, particularly on the X chromosome, where natural selection acts more strongly on males' single copy. Instead of biological incompatibility, he argues that DNA from a small number of Neandertal ancestors might have been swamped later by the sheer abundance of modern human DNA. "The ordinary person hearing about this is going to think of Neandertal mules," or sterile hybrids, Hawks says. "The evidence is against that because we still have a lot of their DNA."

Therein lies the mystery: Modern humans inherited key DNA from Neandertals. But much of it, like the Neandertals themselves, is long gone.

—ANN GIBBONS



ECOLOGY

Ecosystems Say 'Pass the Salt!'

After Roman troops razed and burned the city of Carthage 2000 years ago, legend has it they delivered a final blow, salting the soil so no crops could grow again. Michael Kaspari salts the ground, too, but with a different effect: His experimental plots teem with ants and other invertebrates. In sodium-poor soil, the University of Oklahoma, Norman, ecologist has found, small amounts of added salt boost biomass of these creatures and increase plant decomposition—so much so, his latest work suggests, that a lack of salt could be having a major impact on the global carbon cycle.

The finding, presented at a meeting* earlier this month, caps Kaspari's years-long campaign to persuade other researchers to pay more attention to the ecological significance of sodium, one of the two components of table salt. Not everyone accepts his claim that sodium limitation is a major factor affecting global carbon storage. But he has convinced many of his colleagues that salt is critical to the well-being of an ecosystem. "He's shed new light on the importance of sodium," says Spencer Behmer, an insect physiologist at Texas A&M University, College Station. "It will refocus people on what the consequences of salt are."

Animals use sodium in many ways, but arguably its most basic function is to help cells hold on to their contents. Bacteria and plants physically lock in nutrients and other necessary cellular components with their impermeable cell walls, but animal cells have leaky membranes that could let material inside flow out. Indeed, animal cells use up one-third of their energy budgets to prevent this loss, pumping sodium and other ions

across their cell membranes to maintain osmotic balance so that other essential molecules don't diffuse out.

But because sodium exists as a charged element, organisms can't warehouse it as they do other elements including nitrogen, carbon, and phosphorous. So they need a constant source.

Carnivores tend to have enough salt in their diets, as they consume other animals that worked hard to keep an adequate supply of salt. But herbivores, and, as Kaspari has recently shown, termites and other detritivores that depend on dead and decaying material for sustenance, require much more sodium than they can get from their primary food choices. Farmers put out salt licks for their livestock for this reason.

Many other animals go to extremes for sodium. Male butterflies lap up salts in evaporating water puddles, packaging the sodium with sperm as a gift to females they court. The salts are transferred to eggs and provide newly emerging caterpillars with a starter supply.

Moose wade into frigid waters—energetically, a costly move—to feed on submerged aquatic plants, which have more sodium than their terrestrial counterparts. And mountain gorillas like to munch on rotten wood, which is riddled with salty fungi.

Although he was aware of such observations, Kaspari didn't really begin to think about sodium as a driver of ecosystem dynamics until a field expedition to Peru in 2007. A colleague had documented that rainwater went from salty to almost distilled moving inland from the coast. The researchers wondered whether that salinity change had any effect on animals' behavior. So Kaspari and his colleagues did a simple experiment when they stopped to refuel on their cruise up the Amazon River. They put

Online

sciencemag.org

Podcast interview with Elizabeth Pennisi (http://scim.ag/pod_6170a).

* The Society for Integrative and Comparative Biology, Austin, 3–7 January.

Different place; different tastes. Typically, ants swarm sugar, but these ants living far from a coast also crave salt.

out vials containing cotton soaked in salt or sugar solutions and waited. Within minutes, ants had swarmed the sugary balls, as Kaspari had expected. But they swarmed the salty ones just as avidly.

"It was one of the greatest things I have ever seen," Kaspari says. "Deep in the tropics, the ants will crave sodium as much as they crave sugar." His team even showed that this sodium craving among ants gradually rises with distance from the ocean.

For a follow-up study, they established 70 quarter-meter-square plots in a tropical lowland forest in Peru, where the earlier work indicated ants were salt-deprived. Every other day the researchers sprinkled half the plots with stream water and the other half with a more concentrated salt solution. They subsequently harvested all the invertebrates in each plot. These creatures make up the "brown" food web that breaks down leaf litter and recycles the forest's nutrients. In the sodium-enriched plots, the number of termites and ants increased and leaf litter decomposition jumped on average by 41%, Kaspari and his colleagues reported in 2009.

The work "suggested that global carbon balance may be affected by geographical patterns of nutrient limitations," says Daniel Hahn, a comparative physiologist at the University of Florida in Gainesville. So, Kaspari and his colleagues recently tried to

estimate how much sodium influences the carbon cycle. They set up 10 pairs of 4-meter-square plots in Peru and, twice a month for a year, sprinkled half with water as salty as rain on the coast and half with river water. The plots were seeded with filter paper disks—stand-ins for leaves—and with chunks of three different types of wood. In the salted plots, termite populations increased 16-fold, leaf litter decomposition increased 26%, and wood decomposition increased by 32% to 76%, Kaspari's team reported at the meeting. (The results are also in press in *Ecology*.)



Saltshaker. Through his field studies Michael Kaspari has shown that salt can be a limiting nutrient in inland forests.

Kaspari calculates that about 80% of Earth's landmass is more than 100 kilometers from the coast, leading him to argue that the ecological effects of sodium limitation could be substantial, particularly where the natural geology fails to provide a concentrated sodium source. An estimated 30% of soil carbon is tied up in tropical forests, and Kaspari's results suggest that inland, the carbon stores build up faster and break down slower than on the coasts because of sodium limitation, a factor that researchers modeling the carbon cycle rarely consider. "Sodium can play an important role in regulating organic matter decomposition and thus terrestrial carbon storage," agrees Pablo García Palacios, a plant-soil ecologist at the Center of Evolutionary and Functional Ecology in Montpellier, France.

Not everyone is convinced. Sodium "will influence the landscape-level decomposition on the short term, but I'm not sure how it will influence the global cycle," says Michael Palace, an ecologist at the University of New Hampshire, Durham. And David Wardle, an ecologist at the Swedish University of Agricultural Sciences, Umeå, calls for more work to clarify how widespread sodium limitations are.

Still, Kaspari's colleagues say his work has given them a new appreciation for sodium's ecological and geochemical influence. "Mike takes [earlier observations] forward in a huge way," Hahn says. "He's not just looking at individual behavior and individual decisions. He's taking it to community function."

—ELIZABETH PENNISI

MEDICINE

Suspect Drug Research Blamed for Massive Death Toll

Research misconduct can ruin everything from scientific careers to institutional reputations and public confidence in science. But in a paper published 2 weeks ago, two British cardiologists claimed that misconduct in their field may have had a far greater toll. Tainted research by Don Poldermans, a disgraced cardiologist who was at Erasmus MC in the Netherlands, may have led to the deaths of 800,000 people in Europe, Darrel Francis and Graham Cole of Imperial College London wrote in a provocative article that appeared briefly in the *European Heart Journal* (*EHJ*) and was then withdrawn.

Poldermans, a prominent researcher who published more than 300 papers, was fired in November 2011 after a university investigation concluded that he had engaged

in misconduct, including data fabrication. He was the lead author on two influential trials examining whether β -blocker drugs can protect patients undergoing surgery that doesn't directly involve the heart; those studies helped shape guidelines adopted in 2009 by the European Society of Cardiology (ESC) that recommended using the drugs. (U.S. guidelines are more cautious.) When Poldermans's studies are omitted, Francis and Cole say, the evidence shows that the recommendations don't save lives but endanger them.

The accusatory paper was removed from the *EHJ*'s website less than 48 hours after it appeared. It hadn't undergone peer review, as it should have, says Thomas Lüscher of the University of Zurich in Switzerland, the

journal's editor; an official retraction was posted on 23 January, and the paper is now under review. But Cole and Francis say the staggering number of deaths they calculated was based on published data, and their claim has reignited a debate about giving β blockers to patients about to undergo surgery that might stress the heart. It is also a reminder, some scientists say, of the huge effects that a few uncertain and potentially flawed studies can have on clinical practice. "This is unfortunately what happens when you write a guideline that affects large numbers of people in a relatively common situation," Francis says.

Defenders of the guidelines counter that the estimate of 800,000 deaths is wildly inflated. It disregards explicit cautions in

the guidelines, Lüscher says. Poldermans says he has seen the paper but he declined to comment; he is waiting for the review and revision of the paper, which Francis and Cole hope will be republished shortly.

Scientists have long debated the use of β blockers during surgery in heart patients who need noncardiac surgery. The drugs, prescribed for conditions including high blood pressure, heart failure, and migraine, interfere with muscle cells' response to stress hormones such as adrenaline. That can protect the heart from the stresses of surgery. But β blockers can also exacerbate the low blood pressure that is a common and dangerous side effect of surgery. In the 1970s and '80s, doctors thought it was better to discontinue the drugs in patients who were taking them if they had an operation scheduled. But in 1996, a small clinical study suggested that the drugs could benefit patients who had heart problems by decreasing their risk of postsurgery heart attacks.

As a follow-up, Poldermans and his colleagues launched a study called DECREASE I. It enrolled only 112 patients, all with heart problems, but the results were dramatic: Only 3.4% of patients on β blockers—which they received starting 30 days before surgery—died of cardiac causes or had a nonfatal heart attack in the month after the operation, compared with 34% of controls, the team reported in *The New England Journal of Medicine* (NEJM) in 1999.

The study moved opinion toward starting β -blocker therapy in patients scheduled to have high-risk surgery. But follow-up studies had mixed results. The largest trial, published in 2008, confirmed that patients on β blockers had fewer heart attacks in the month after surgery. But the study, called POISE, also found that patients in the β -blocker group had more strokes, and more died. The POISE researchers started patients on β blockers 2 to 4 hours before surgery, however, which Poldermans and his colleagues criticized as too late; they also used a different drug, and at higher doses, than DECREASE I. (The POISE researchers responded that their trial was designed to reflect the likely real-life use of the drugs.) A year later, in 2009, Poldermans produced his second study on the topic, called DECREASE IV, which showed that β blockers were beneficial in patients at intermediate risk of heart problems.

Poldermans's view carried the day. In 2009, an ESC panel that he chaired issued guidelines concluding that β blockers were beneficial for patients undergoing high-risk surgery, and that the “weight of evidence or opinion” supported using them in patients at intermediate risk as well.

Poldermans's downfall, which began with findings of misconduct in a study that didn't involve β blockers, has called that judgment into question. In 2012, a second university panel concluded that the conduct of DECREASE IV “was in several respects negligent and scientifically incorrect.” The



Flawed advice? European recommendations for the use of β blockers before surgery that doesn't involve the heart are being revised.

committee questioned “the reliability of the findings in the publication and the validity of the conclusions.” (The paper has not yet been retracted.) In a third investigation, due to finish by early summer, Erasmus MC is examining DECREASE I, a spokesperson says.

Until that time, both DECREASE studies should be excluded as the basis for any clinical guidance, Francis says. When he and his colleagues did so in a meta-analysis of 11 trials published in July 2013, they concluded that patients who received the drugs had a 27% increased risk of dying—an increase that led to their published estimate of 800,000 additional deaths.

The paper also took aim at ESC, which publishes the journal, for being slow to react to the Poldermans affair. The society should have rescinded, or at least revised, the guidelines as soon as flaws in Poldermans's work were found in 2011, Francis says. Instead, ESC initially issued a statement saying it was “confident that our Guidelines

are supported by reliable data.” Only in March 2013 did it announce that a committee would review the guidelines; in August, ESC said that “the initiation of beta blockers ... should not be considered routine,” but should be considered on a case-by-case basis. (The review committee is expected to finish its work in August this year.). In an editorial slated for next week's issue of *EHJ*, Lüscher counters that because the validity of the *NEJM* paper on DECREASE I is still unclear, “a firm statement was intentionally avoided.”

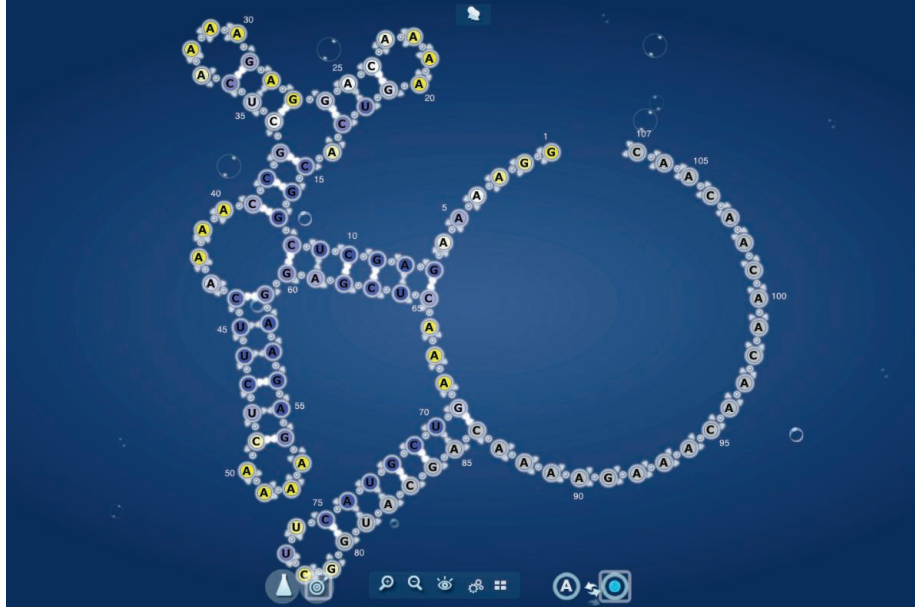
Eric Boersma, a biostatistician at Erasmus University and a co-author on both DECREASE studies and on the guidelines, disputes Francis and Cole's risk calculations. The POISE study skewed their numbers, he says, because that study's use of β blockers—in high doses and starting a few hours before an operation—is potentially dangerous. “Please don't use that technique,” he adds. If the drugs are started a week or more before surgery, “my appreciation of the literature is that that is safe, and potentially doing something good”—whether or not the DECREASE studies are included.

The only way to settle the question is a new clinical trial, says Sripal Bangalore, a cardiologist at the New York University School of Medicine in New York City who authored a 2008 meta-analysis that questioned the use of β blockers. That won't be

easy, however, Boersma says. He and his colleagues, including Poldermans, had tried to set up a larger trial, but couldn't get funding—in part, he says, because β blockers are already off-patent, so industry is not interested. Today it would be even more difficult, Boersma says, because so many people are already on β blockers that it's difficult to find enough naïve patients who meet the high-risk criteria.

Even if 800,000 deaths is a provocative exaggeration, Francis and Cole are making an important point, says biostatistician Gerd Antes, director of the German Cochrane Center in Freiburg. After misconduct, the forces slowing down any public health response often “are far stronger than those people who are brave enough to write such a provocation,” Antes says. “I know many examples where a bit more provocation would be helpful to stir things up, so they get the attention they deserve.”

—GRETCHEN VOGEL



CROWDSOURCING

Online Video Game Plugs Players Into Remote-Controlled Biochemistry Lab

Crowdsourcing is the latest research rage—Kickstarter to raise funding, screen savers that number-crunch, and games to find patterns in data—but most efforts have been confined to the virtual lab of the Internet. In a new twist, researchers have now crowdsourced their experiments by connecting players of a video game to an actual biochemistry lab. The game, called EteRNA, allows players to remotely carry out real experiments to verify their predictions of how RNA molecules fold. The first big result: a study published this week in the *Proceedings of the National Academy of Sciences*, bearing the names of more than 37,000 authors—only 10 of them professional scientists. “It’s pretty amazing stuff,” says Erik Winfree, a biophysicist at the California Institute of Technology in Pasadena.

Some see EteRNA as a sign of the future for science, not only for crowdsourcing citizen scientists but also for giving them remote access to a real lab. “Cloud biochemistry,” as some call it, isn’t just inevitable, Winfree says: It’s already here. DNA sequencing, gene expression testing, and many biochemical assays are already outsourced to remote companies, and any “wet lab” experiment that can be automated will be automated, he says. “Then the scientists can focus on the non-boring part of their work.”

EteRNA grew out of an online video game called Foldit. Created in 2008 by a team led by David Baker and Zoran Popović, a molecular biologist and computer scientist, respectively, at the University of Washington, Seattle, Foldit focuses on predicting the shape into which a string of amino acids

will fold. By tweaking virtual strings, Foldit players can surpass the accuracy of the fastest computers in the world at predicting the structure of certain proteins. Two members of the Foldit team, Adrien Treuille and Rhiju Das, conceived of EteRNA back in 2009. “The idea was to make a version of Foldit for RNA,” says Treuille, who is now based at Carnegie Mellon University in Pittsburgh, Pennsylvania. Treuille’s doctoral student Jeehyung Lee developed the needed software, but then Das persuaded them to take it a giant step further: hooking players up directly to a real-world, robot-controlled biochemistry lab. After all, RNA can be synthesized and its folded-up structure determined far more cheaply and rapidly than a protein can.

Lee went back to the drawing board, redesigning the game so that it had not only a molecular design interface like Foldit, but also a laboratory interface for designing RNA sequences for synthesis, keeping track of hypotheses for RNA folding rules, and analyzing data to revise those hypotheses. By 2010, Lee had a prototype game ready for testing. Das had the RNA wet lab ready to go at Stanford University in Palo Alto, California, where he is now a professor. All they lacked were players.

A message to the Foldit community attracted a few hundred players. Then in early 2011, *The New York Times* wrote about EteRNA and tens of thousands of players flooded in.

The game comes with a detailed tutorial and a series of puzzles involving known RNA structures. Only after winning 10,000 points do you unlock the ability to join

Game on! EteRNA players win points by submitting experiments to a real lab and using the data.

EteRNA’s research team. There the goal is to design RNA sequences that will fold into a target structure. Each week, eight sequences are chosen by vote and sent to Stanford for synthesis and structure determination. The data that come back reveal how well the sequences’ true structures matched their targets. That way, Treuille says, “reality keeps score.” The players use that feedback to tweak a set of hypotheses: design rules for determining how an RNA sequence will fold.

Two years and hundreds of RNA structures later, the players of EteRNA have proven themselves to be a potent research team. Of the 37,000 who played, about 1000 graduated to participating in the lab for the study published today. (EteRNA now has 133,000 players, 4000 of them doing research.) They generated 40 new rules for RNA folding. For example, at the junctions between different parts of the RNA structure—such as between a loop and an arm—the players discovered that it is far more stable if enriched with guanines and cytosines, the strongest bonding of the RNA base pairs. To see how well those rules describe reality, the humans then competed toe to toe against computers in a new series of RNA structure challenges. The researchers distilled the humans’ 40 rules into an algorithm called EteRNA Bot.

The human players still came out on top, solving structures more accurately than the standard software 99% of the time. The algorithmic version of their rules also outperformed the standard software, but only 95% of the time, showing that the crowdsourced human RNA-folding know-how has not been completely captured yet. The next step, Lee says, is to make the wet lab completely robotic. It still requires humans to operate some of the steps between the input of player RNA sequences and the data output.

EteRNA’s approach won’t work for every kind of science, says Shawn Douglas, a biomolecular engineer at the University of California, San Francisco, because a problem has to be “amenable to game-ification.” But he’s optimistic that there will be many more to come. “Many areas of biological research have reached a level of complexity that the mental bandwidth of the individual researcher has become a bottleneck,” Douglas says. EteRNA proves that “there are tens of thousands of people around the world with surplus mental bandwidth and the desire to participate in scientific problem solving.” The trick is to design a good game.

—JOHN BOHANNON



Living proof. These twin monkeys carry deletions in two genes, genetic changes introduced into them as one-cell embryos.

TRANSGENIC ANIMALS

Editing of Targeted Genes Proved Possible in Monkeys

A team from China has taken a precise editing pen to the genomes of monkeys, demonstrating what could be a relatively quick and cheap way to develop nonhuman primate strains tailored to mimic human diseases. Using a recently developed genome-editing technique called CRISPR, the researchers altered two target genes in twin cynomolgus monkey embryos. At 2.5 months, the twins are outwardly healthy, while carrying the new mutations in most of their cells, Sha Jiahao, a reproductive biologist at Nanjing Medical University in China, and his colleagues report this week in *Cell*.

"This is the first evidence that CRISPR can work in primates, which is very important," says Guoping Feng, a neuroscientist at the Massachusetts Institute of Technology (MIT) in Cambridge who is also trying to genetically engineer monkeys using CRISPR. CRISPR has thrilled researchers with its precision and efficiency, and it has already shown its mettle in cultured cells and in organisms from yeast to rats (*Science*, 23 August 2013, p. 833). Beyond its significance for biomedical research, the new work raises the possibility that CRISPR will one day be used to change the genetic makeup of human embryos, adds reproductive biologist Gerald Schatten of the University of Pittsburgh School of Medicine in Pennsylvania.

CRISPR's efficiency in monkeys "is not as high as [in] mouse or rat, but we believe it is good enough to do it routinely," Sha says. Still, the technique required multiple embryos, and some cells in the monkeys escaped the genetic

changes, suggesting that there is room for improvement. "They deserve a lot of credit," says Robert Desimone, Feng's colleague and a neuroscientist at the McGovern Institute for Brain Research at MIT. "That said, it's not ready for prime time quite yet."

Genetically modified monkeys are not new; the first, ANDi, was born in 2000 from an egg into which a virus had carried a gene for green fluorescent protein (GFP) (*Science*, 12 January 2001, p. 226). A few groups subsequently introduced GFP or disease

"This is the first evidence that CRISPR can work in primates."

**—GUOPING FENG,
MASSACHUSETTS INSTITUTE OF TECHNOLOGY**

genes into other monkeys and proved that the new gene passes on to recipients' offspring, a key requirement for making primate models of human disease. In each case, however, the genes were inserted at random places within the monkey genome. CRISPR, which targets specific DNA sequences through the use of matching RNA constructs, allows precise targeting of genes. In mice, it can not only add genes but also delete or modify existing ones, which should allow researchers to create a broader array of disease models in monkeys.

Sha teamed up with Huang Xingxu, a reproductive biologist at Nanjing University who specializes in genome editing, and Ji Weizhi from the Yunnan Key Laboratory of Primate Biomedical Research and Kunming

Biomed International in China, who had made a transgenic monkey in 2010 that carried the GFP gene. The team decided to try to introduce mutations in three genes: *RAG-1*, which is central to the development of B and T cells; *NR0B1*, which is important in sex determination and embryonic stem cell function; and *PPAR-γ*, which encodes a key protein in fat cell production. A monkey with a defective *RAG-1* gene, for example, should provide a valuable model of immunodeficiency.

After collecting 198 monkey eggs and fertilizing them, Sha's team added to the one-cell embryos the two components of the CRISPR system: the gene-matching RNAs and genetic instructions to make Cas9, the protein that cuts the target. They transferred the resulting 83 viable embryos to 29 surrogate mothers. Ten pregnancies ensued, producing 19 fetuses. The twins, Ningning and Mingming, were born in November; other surrogates have since miscarried and four have yet to give birth.

The monkeys haven't so far shown any ill effects from the targeted gene mutations, or from changes in untargeted genes, which didn't seem to occur, at least in the 84 potential off-target sites studied. On the other hand, the effort modified only two of the three target genes, leaving *NR0B1* untouched, and Sha and his colleagues found that different amounts of the targeted sequences were deleted in different tissues. This variation, or mosaicism, happened because the genome editing didn't occur right away in the one-cell embryo, but at later stages, so not all cells were equally modified. "If we want to build a genetic model, we have to address this mosaicism problem," says Feng Zhang, a CRISPR pioneer at the Broad Institute in Cambridge, Massachusetts.

Others are not far behind the Chinese team. Desimone, Feng, Zhang, and their collaborators have used CRISPR to try to knock out a gene called *SHANK3*, which in humans causes a genetically inherited form of autism, and have pregnant macaques in China carrying the treated embryos. In unpublished work, Japanese researchers have used a similar genome-editing technique, which involves proteins called zinc fingers, to delete the *SHANK3* gene or an immunoregulatory gene in marmosets; these smaller, faster-maturing monkeys are more budget-friendly for scientists.

Sha and his colleagues' success could convince skeptical funding agencies to take a chance on similar research. It "gives some expectation of the amount of resources that are needed and a predictable outcome," says Thaddeus Golos, a reproductive biologist at the Wisconsin National Primate Research Center in Madison whose team is seeking funding to use CRISPR to develop a marmoset model of

Parkinson's disease. "There will probably be a flurry of new grant applications."

No one expects a rapid proliferation of monkey models, which are costly and ethically fraught. But with complex disorders such as Alzheimer's and autism, there may be no other good way to understand the disease or to test potential treatments. Says John Harding, director of the National

Primate Research Center Program at the U.S. National Institutes of Health in Bethesda, Maryland: "As more of this is done—and more of it will be done—we will get a much better understanding of the nuances of this technology to see how good the technology is truly going to be."

—ELIZABETH PENNISI

With reporting by Mara Hvistendahl.

BIOMEDICAL RESEARCH

Antioxidants Could Spur Tumors by Acting on Cancer Gene

Many people take vitamins such as A, E, and C thinking that their antioxidant properties will ward off cancer. But some clinical trials have suggested that such antioxidants, which sop up DNA-damaging molecules called free radicals, have the opposite effect and raise cancer risk in certain people. Now, in a provocative study that raises unsettling questions about the widespread use of vitamin supplements, Swedish researchers have showed that moderate doses of two widely used antioxidants spur the growth of early lung tumors in mice.

Some cancer specialists caution against basing public health advice on the study, published online this week in *Science Translational Medicine*. "You can't extrapolate from this study to make a recommendation to people," says Barry Kramer, director of the Division of Cancer Prevention at the National Cancer Institute in Bethesda, Maryland. He notes that the science of antioxidants is complicated and that the results of mice studies often don't apply to humans. Still, Kramer and others say the new findings demand further exploration.

The observation decades ago that people who consumed lots of fruits and vegetables had less cancer suggested that the antioxidants in these foods might be protecting them. But in the 1980s, researchers launched two large clinical trials to test whether the antioxidants β carotene (a vitamin A precursor), vitamin A, and vitamin E protect smokers from lung cancer—and found more cases of lung cancer in volunteers taking β carotene, leading one trial to end early. A more recent trial testing vitamin E and selenium to prevent prostate cancer was stopped when prostate cancer turned out to be more common in the vitamin E group.

The Swedish researchers, led by Per Lindahl and Martin Bergö of the University of Gothenburg, studied two antioxidants: n-acetylcysteine (NAC), a water-soluble

drug used to thin mucus in people with lung disease, and fat-soluble vitamin E. They gave mice genetically engineered to develop lung tumors a dose of NAC comparable to what a patient would receive or chow containing about 10 times more vitamin E than is in ordinary mouse food. "A lot of vitamin pills contain a lot more than that. It's a conservative dose," Bergö says.

Compared with mice on a normal diet, the mice consuming the antioxidants developed more lung tumors, their tumors were more aggressive, and they lived only half as long. Follow-up studies suggested that by reducing reactive oxidative species and DNA damage in the cell, the antioxidants turn down a gene, *p53*, that is key to keeping cell growth in check and is often inactivated in cancer. For example, *p53*'s protein stops the cell cycle so enzymes can repair damaged DNA and triggers apoptosis, or self-destruction, in severely damaged cells. In cancer cells in which *p53* had been turned off, Lindahl and Bergö found, the antioxidants had no effect on cell proliferation.

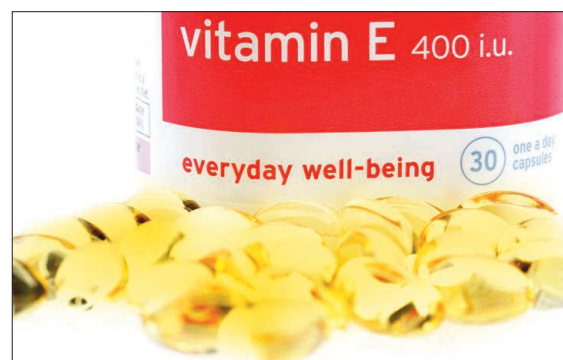
The implication, Bergö suggests, is that people at high risk of cancer—such as smokers—and others who have incipient tumors should avoid taking extra antioxidants. "In a normal cell an antioxidant might be very good. But if you have a small tumor that might become a cancer, it will reduce *p53* and the tumor will grow," Bergö says.

A clinical researcher involved with the aborted trials that tested antioxidants to prevent lung and prostate cancer says he is "thrilled" by the study. "It's the first paper I've seen that goes into some of the molecular biology to explain what we saw," says medical oncologist Gary Goodman of the Swedish Cancer Institute in Seattle, Washington. "This really shows that high doses of vitamins can be harmful."

Others are more restrained. "It's a provocative study," says cancer biologist David Tuveson of Cold Spring Harbor

Laboratory in New York. "Perhaps we should look more carefully at what's available over the counter." But he would like to see a more detailed explanation of how the cell's sensing of reactive species controls *p53* activity. Lung disease researcher Shyam Biswal of Johns Hopkins University in Baltimore, Maryland, wonders if the results would be the same in mice with cancer sparked by a carcinogen, rather than an existing mutation. "The model is great, but it's a very aggressive model," Biswal says.

Another huge caveat, Kramer adds, is that in the earlier lung cancer prevention trials, only



Risky? Consuming a moderate dose of vitamin E spurred lung tumor growth in cancer-prone mice.

the participants taking β carotene had a higher risk of lung cancer, not those on vitamin E alone. "It's not likely that all antioxidants are exactly the same," he says. He and others also emphasize that the study does not suggest that people should eat less fruit and vegetables, which provide smaller doses of antioxidants and likely have other benefits.

Bergö and Lindahl now plan to extend their mouse studies to tests of β carotene and vitamin C and to other cancer types. They also plan to comb through medical records in Sweden to see if lung disease patients receiving NAC are at higher risk for lung cancer.

—JOCELYN KAISER



The Dangerous Professor

David Nutt wants to make drug policies science-based and give the world a safe alternative to alcohol. If only politicians would listen, he says

LONDON—David Nutt is trying to develop a new recreational drug that he hopes will be taken up by millions of people around the world. No, the 62-year-old scientist isn't "breaking bad." In fact, he hopes to do good. His drug would be a substitute for alcohol, to create drinks that are just as intoxicating as beer or whiskey but less toxic. And it would come with an antidote to reverse its effects, allowing people to sober up instantly and drive home safely.

Nutt, a neuropsychopharmacologist at Imperial College London and a former top adviser to the British government on drug policy, says he has already identified a couple of candidates, which he is eager to

develop further. "We know people like alcohol, they like the relaxation, they like the sense of inebriation," Nutt says. "Why don't we just allow them to do it with a drug that isn't going to rot their liver or their heart?"

But when he presented the idea on a BBC radio program late last year and made an appeal for funding, many were appalled. A charity working on alcohol issues criticized him for "swapping potentially one addictive substance for another"; a commentator called the broadcast "outrageous." Newspapers likened his synthetic drug to soma, the intoxicating compound in Aldous Huxley's dystopian novel *Brave New World*. Some of his colleagues dismissed the idea as

scientifically unfeasible.

Nutt wasn't surprised. As a fierce advocate of what he says are more enlightened, rational drug policies, he has been a lightning rod for a long time. Politicians, in Nutt's view, make irrational decisions about drugs that help them win votes but cost society dearly. Drug policy is often based on the moral judgment that people should not use drugs, he says. Instead, it should reflect what science knows about the harms of different drugs—notably that many are far less harmful than legal substances such as alcohol, he says. The plan for a synthetic alcohol alternative is his own attempt to reduce the damage that drug use can wreak;

Outspoken. Nutt says politicians often have a “primitive, childish” way of thinking about drugs.

he believes it could save millions of lives and billions of dollars.

Such views—and the combative way in which he espouses them—frequently land Nutt in fierce disputes. Newspaper commentators have called him “Professor Nutty” or “the dangerous professor.” In 2009, he was sacked from his position as chair of the United Kingdom’s Advisory Council on the Misuse of Drugs, tasked with giving scientific advice to the home secretary, after he criticized a government decision on cannabis.

But in November 2013, he received the John Maddox Prize for standing up for science. “In circumstances that would have humiliated and silenced most people,” wrote neurobiologist Colin Blakemore, one of the judges, “David Nutt continued to affirm the importance of evidence in understanding the harms of drugs and in developing drug policy.”

Controversial comparisons

David Nutt does not look like a dangerous professor. Short and heavyset, he has a jovial, round face and an old-fashioned mustache; one could mistake him for a London taxi driver. He limps slightly, has a down-to-earth way of speaking, and laughs a lot when he talks. “He is a real personality,” says psychopharmacologist Rainer Spanagel of Heidelberg University in Germany. “You can be in a meeting and almost have a result, then he will come in an hour late, stir everything up, and in the end convince everyone of his position.”

Nutt says he realized at an early age that “understanding how the brain works is the most interesting and challenging question in the universe.” When he was a teenager, his father told him a story of how Albert Hofmann, the discoverer of LSD, took a dose of that drug and felt that the bike ride home took hours instead of minutes. “Isn’t that incredible, that a drug can change time?” he asks. On his first night as an undergraduate in Cambridge, he witnessed the powers of drugs again when he went drinking with fellow students. Two of them couldn’t stop. “I just watched them transform themselves. One of them started wailing and crying and the other became incredibly hostile.”

During his clinical training, Nutt says he treated many alcoholics but failed “to get anyone interested in how to reduce their addiction to the drug that was harming them.” He set out to answer that question, first in the United Kingdom, later as the chief of the Section of

Clinical Science at the U.S. National Institute on Alcohol Abuse and Alcoholism, a job he held for 2 years. Today, he runs the department of neuropsychopharmacology at Imperial College, using modern imaging techniques to see what happens in the brain when people take drugs or develop an addiction.

But his biggest contribution to science, he says, was a discovery he made quite early in his career: that some molecules don’t just block receptors in the brain, but actually have the opposite effect of the molecules that normally stimulate them—and in doing so shut down a brain pathway. Nutt called these molecules contragonists, and he has made a second career out of being a bit of a contragonist himself, trying to calm society’s overexcited responses to the steady stream of alarming news about drugs.

Fictional affliction

In 2009, Nutt published an article in the *Journal of Psychopharmacology* comparing the harms from ecstasy with those caused by horse riding. Every 10,000th ecstasy pill is likely to hurt someone, he calculated, while

“Because one’s illegal.”

“Why is it illegal?”

“Because it’s harmful.”

“Don’t we need to compare harms to determine if it should be illegal?”

“You can’t compare harms from a legal activity with an illegal one.”

Nutt says this kind of circular logic crops up again and again when he discusses recreational drugs with politicians. “It’s what we would call ‘splitting’ in psychiatric terms: this primitive, childish way of thinking things are either good or bad,” he says.

He’s often that outspoken. He likens the way drug laws are hampering legitimate scientific research, for instance into medical applications for psychedelic compounds, to the church’s actions against Galileo and Copernicus. When the United Kingdom recently banned khat, a plant containing a stimulant that’s popular among people from the Horn of Africa and the Arabian Peninsula, he compared the decision with banning cats. And he accuses the Russian government of deliberately using alcohol to weaken the opposition. “However miserable they are,

“You don’t get to be on the front page of *The Lancet* and *The New York Times* unless you sharpen your arguments a little bit. I can live with that.”

—Jürgen Rehm

“[Nutt] is a polarizing figure and the drug policy area is polarized enough.”

—Jonathan Caulkins

an average horse enthusiast can expect a serious accident every 350 hours of riding. The sport, he concluded, was more dangerous than the notorious party drug. That “raises the critical question of why society tolerates—indeed encourages—certain forms of potentially harmful behaviour but not others such as drug use,” he added.

Politicians were not amused, and Nutt’s whimsical reference to a fictional affliction he called equine addiction syndrome, or “equasy,” did not help. In his book *Drugs - Without the Hot Air*, Nutt provided his account of a phone conversation he had with U.K. Home Secretary Jacqui Smith after the paper was published. (Smith calls it an “embroidered version” of their talk.)

Smith: “You can’t compare harms from a legal activity with an illegal one.”

Nutt: “Why not?”

however much they hate their government and their country, they will just drink until they kill themselves, so they won’t protest,” he says.

But it’s his stance on cannabis that got him sacked. In early 2009, ignoring advice from Nutt’s advisory council, Smith upgraded cannabis from class C to class B, increasing the maximum penalty for possession from 2 to 5 years in prison. A few months later, Nutt criticized the decision in a public lecture, arguing that “overall, cannabis use does not lead to major health problems” and that tobacco and alcohol were more harmful. When media reported the remarks, Alan Johnson, who succeeded Smith as home secretary in mid-2009, asked him to resign. “He was asked to go because he cannot be both a government adviser and a campaigner against government policy,” Johnson wrote in a letter in *The Guardian*.

Nutt did not go quietly. With financial help from a young hedge fund manager, Toby Jackson, he set up a rival body, the Independent Scientific Committee on Drugs, “to ensure that the public can access clear, evidence based information on drugs without interference from political or commercial interest.” Politics have skewed not just drug laws but research itself, he argues. “If you want to get money from the U.S. government to work on a drug, you have to prove it damages the brain,” he says.

One of his favorite examples is a paper that *Science* published in September 2002. The study, led by George Ricaurte at Johns Hopkins University, seemed to show that monkeys given just two or three doses of ecstasy, chemically known as MDMA, developed severe brain damage. The finding suggested that “even individuals who use MDMA on one occasion may be at risk for

sharpen your arguments a little bit,” Rehm says. “I can live with that.”

Ranking the drugs

In 2010, Nutt sparked a new firestorm when he published another comparison: a *Lancet* paper ranking drugs according to the harm they cause. Nutt and other experts scored a long list of drugs on 16 criteria, nine related to the user, such as death from an overdose or wrecked relationships, and seven related to society, such as drug-fueled violence and economic costs. In the end, every drug was given a score between 0 and 100 to indicate its overall harm. Alcohol came out on top, ahead of heroin; mushrooms and ecstasy were at the low end (see graphic, p. 481).

Critics said the study’s methodology was flawed because it didn’t address drug interactions and the social context of drug use. “For instance, the number of fatalities caused by

they may be, would constitute a quantum leap of progress towards evidence-based and more rational drug policy in Canada and elsewhere,” two Canadian drug scientists wrote in *Addiction*. Regardless of its quality, the paper has been hugely influential, Rehm says. “Everyone in the E.U. knows that paper, whether they like it or not. There is a time before that paper and a time after it appeared.”

Nutt says his comparisons are an essential first step on the way to more evidence-based drug policies that seek to reduce harm rather than to moralize. The best option would be a regulated market for alcohol and all substances less harmful to the user than alcohol, he argues.

That scenario, under which only heroin, crack cocaine, and methamphetamine would remain illegal, seems unlikely to become a reality. But Nutt says he can already see more rational policies taking hold. Recently, Uruguay and the U.S. states of Colorado and Washington legalized the sale of recreational cannabis, going a step further than the Netherlands, which stopped enforcing laws on the sale and possession of small amounts of soft drugs decades ago. Nutt was also happy to read President Barack Obama’s recent comment that cannabis is less harmful than alcohol. “At last, a politician telling the truth,” he says. “I’ll warn him though—I was sacked for saying that.”

New Zealand, meanwhile, passed a law in 2013 that paves the way for newly invented recreational drugs to be sold legally if they have a “low risk” of harming the user. Nutt, who has advised the New Zealand government, is delighted by what he calls a “rational revolution in dealing with recreational drugs.” The main problem now, he says, is establishing new drugs’ risks—which is difficult because New Zealand does not allow them to be tested on animals—and deciding what “low risk” actually means. “I told them the threshold should be if it is safer than alcohol,” he says. “They said: ‘Oh my god, that is going to be far too dangerous.’”

Safer substitute

Nutt agrees that alcohol is now one of the most dangerous drugs on the market—which is why he’s trying to invent a safer substitute. The World Health Organization estimates that alcohol—whose harms range from liver cirrhosis, cancer, and fetal alcohol syndrome to drunk driving and domestic violence—kills about 2.5 million people annually. “When I scan the brains of people with chronic alcohol dependence, many have brains which are more damaged than those of people with Alzheimer’s,” Nutt says.

“We know people like alcohol, they like the relaxation, they like the sense of inebriation. Why don’t we just allow them to do it with a drug that isn’t going to rot their liver or their heart?”

—David Nutt

“You could come up with a drug that might make you feel good. But is it going to be the same good feeling as alcohol? I doubt that.”

—Gregg Homanics

substantial brain injury,” the authors wrote. The paper received massive media attention, but it was retracted a year later after the authors discovered that they had accidentally injected the animals not with MDMA but with methamphetamine, also known as crystal meth, which was already known to have the effects seen in the monkeys. Nutt says the mistake should have been obvious from the start because the data were “clearly wrong” and “scientifically implausible.” “If that result was true, then kids would have been dropping dead from Parkinson’s,” he says.

Some resent this combative style. “He is a polarizing figure and the drug policy area is polarized enough,” says Jonathan Caulkins, a professor of public policy at Carnegie Mellon University in Pittsburgh, Pennsylvania. But Jürgen Rehm, an epidemiologist at the Centre for Addiction and Mental Health in Toronto, Canada, says Nutt has helped stimulate debates that were long overdue. “You don’t get to be on the front page of *The Lancet* and *The New York Times* unless you

excessive alcohol use is going to depend in part on gun control laws,” says Caulkins, who calls the whole idea of expressing drug harm as a single number “embarrassing.”

Caulkins adds that even if a perfect ranking of drug harms were possible, it wouldn’t mean that politicians should put the tightest control measures on the most harmful drugs. Suppose drug A is more harmful to the individual and society than drug B, he says, but impurities in drug A, when illegally produced, can lead to potentially fatal organ failure while they just taste bad in drug B. If you were going to prohibit only one of the two drugs, it should be drug B, he says, even though it causes less harm per se, because criminalizing drug A would lead to a more dangerous product and more deaths. Nutt’s ranking of drugs, he says, is “a pseudoscientific exercise which is trying to take control of the policy process from a technocratic perspective in a way that isn’t even sound.”

Other scientists defended the paper. Using Nutt’s harm scales, “flawed and limited as

In a paper published this month in the *Journal of Psychopharmacology*, Nutt and Rehm summarize the top six interventions that governments should consider to reduce the harms of alcohol, such as minimum prices and restrictions on the places that can sell hard liquor. They also argue that governments should support the development of alternatives. Nutt points to e-cigarettes—devices that heat and vaporize a nicotine solution—as a model. “In theory, electronic cigarettes could save 5 million lives a year. That is more than [the death toll from] AIDS, malaria, tuberculosis, and meningitis put together,” he says. “I would argue that the e-cigarette is going to be the greatest health invention since vaccination.”

Can an alcohol alternative do the same? “I think that idea is utopian,” says Spanagel, the German psychopharmacologist. One reason is that researchers have recently developed a much more complex picture of what ethanol, as chemists call it, actually does. Twenty years ago, they thought that once it reached the brain, alcohol elicited its many effects by infiltrating the membranes of neurons there and changing their properties. “Now we know that’s nonsense. You would have to drink 5 liters of schnapps for that to happen,” Spanagel says.

In fact, scientists have learned that alcohol, like other drugs, interacts with the receptors for certain neurotransmitters. But unlike other drugs, it acts on a wide range of them, including receptors for GABA, NMDA, serotonin, and acetylcholine. That will make it hard to find a substance to emulate most of alcohol’s wanted effects while avoiding the unwanted ones, Spanagel predicts.

Nutt is concentrating on the GABA system—the most important inhibitory system in mammalian brains. Alcohol activates GABA receptors, effectively quieting the brain and leading to the state of relaxation many people seek. Nutt has sampled some compounds that target GABA receptors and

was pleasantly surprised. “After exploring one possible compound I was quite relaxed and sleepily inebriated for an hour or so, then within minutes of taking the antidote I was up giving a lecture with no impairment whatsoever,” he wrote in a recent article.

But he wants to go one step further. “We know that different subtypes of GABA mimic different effects of alcohol,” he says.

drug candidates precisely because they had side effects similar to alcohol intoxication.

Gregg Homanics, an alcohol researcher at the University of Pittsburgh, is skeptical that another substance could mimic all the positive effects of alcohol. “You could come up with a drug that might make you feel good. But is it going to be the same good feeling as alcohol? I doubt that.” Such a drug

might have downsides of its own, warns Andreas Heinz, an addiction researcher at Charité University Medicine Berlin. It could still turn out to be addictive or to harm a small proportion of the population. “There is an advantage when you have known drugs for hundreds of years and you know exactly what they do,” he says.

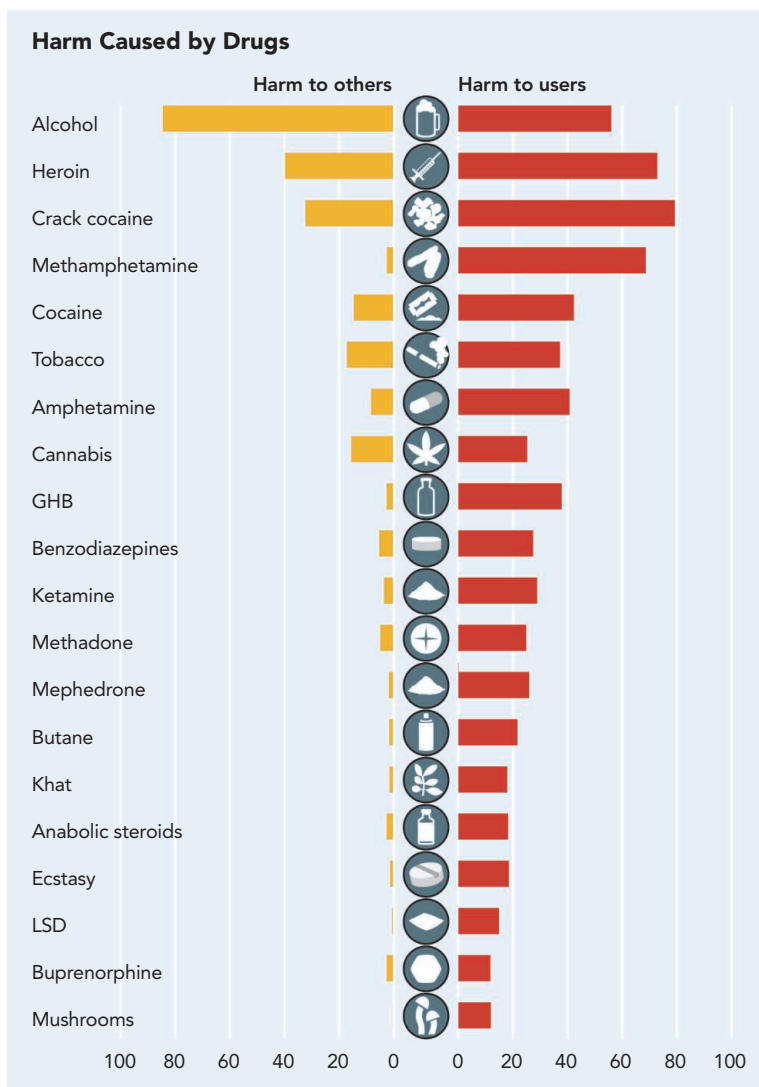
Still, Nutt’s appearance on the BBC radio program attracted new investors, ranging “from Ukrainian brewers to American hedge funds,” he says, and Imperial Innovations, a company that provides technology transfer services, is working with him “to consider a range of options for taking the research forward,” a spokesperson says. “We think we have enough funding now to take a substance all the way to the market,” Nutt says—in fact, he hopes to be able to offer the first cocktails for sale in as little as a year from now.

Even a very good alcohol substitute would face obstacles. Many people won’t forsake drinks they have long known and loved—such as beer, wine, and whiskey—for a new chemical, Spanagel says. The idea will also trigger all kinds of political and regulatory debates, Rehm says. “How

will such a new drug be seen? Will you be able to buy it in the supermarket? In the pharmacy? Will society accept it?”

Whatever the outcome, Nutt’s quest for a safer drink has already made people think about alcohol in a new way, Rehm adds. “It’s provocative in the best sense of the word.” Much the same could be said of the scientist who thought it up.

—KAI KUPFERSCHMIDT



Scoring drugs. Nutt and colleagues at the Independent Scientific Committee on Drugs in London ranked 20 drugs according to how harmful they are to the individual user and to others, expressed as a number between 0 and 100. They deemed crack cocaine the most harmful drug to the user and alcohol most harmful to U.K. society.

Nutt combed the scientific literature and patents for compounds targeting specific GABA receptors, and, in an as-yet unpublished report that he shared with *Science*, he identifies several molecules that he says fit the bill. Compounds targeting subtypes of the GABAA receptor called alpha2 and alpha3 are particularly promising, he says. Some of these molecules were dropped as therapeutic



CRYPTOGRAPHY

Quantum Spy Games

Someday a quantum computer may unlock all our secrets—if it isn't first stymied by simpler technologies

When the news broke earlier this month that the U.S. government is trying to build a super-fast quantum computer, reports suggested the demise of private information as we know it. "[T]he National Security Agency is racing to build a computer that could break nearly every kind of encryption used to protect banking, medical, business and government records around the world," *The Washington Post* said in a front-page story on 3 January.

The end may not be so nigh, however.

"People are not actually shaking in their shoes so much," says Lance Fortnow, a computer scientist and blogger at the Georgia Institute of Technology (Georgia Tech) in Atlanta. The \$80 million National Security Agency (NSA) initiative came to light in documents leaked by former NSA contractor Edward Snowden, but experts say they're not surprised that NSA is working on quantum computing. "It would be shocking if they weren't," Fortnow says. But a full-fledged quantum computer is likely decades away.

More important, even if a quantum code cracker can be built, it might be defeated by encryption algorithms already in the works—or by another technology, called quantum key distribution, that relies on quantum mechanics itself for security. "In the future, we believe

our adversaries will have better computers and better algorithms, but they won't be able to break the laws of physics," says Richard Hughes, a physicist at Los Alamos National Laboratory in New Mexico.

Which raises a practical question: If such countermeasures rob a quantum computer of its widely perceived killer app, will anybody put up the huge sums of money likely needed to make a quantum computer a reality?

The threat

Be it data file or love letter, information crosses the Internet in the form of numbers, written in binary strings of 0s and 1s. Cryptography is the mathematics of scrambling a numerical message so that it can be unscrambled only by the intended recipient, at least in a reasonable amount of time. A quantum computer could crack current algorithms for so-called asymmetric or public key encryption, the technique typically used to begin secure Internet communications.

In such schemes, a sender, Alice, scrambles a message to the recipient, Bob, using a numerical key that Bob makes public. Bob also possesses a private key that mates with

the public key to unscramble the message. In principle, an eavesdropper, Eve, could deduce the private key from the public key. In practice, that problem is so hard it would take nearly forever to solve.

For example, in the widely used RSA algorithm, the public key is a huge number that factors into two prime numbers known only to Bob. To encode a message, Alice multiplies the binary message by itself a number of times—that is, raises it to a power—that's based on those factors and specified by Bob. She divides the result by the public key and takes the remainder—an operation called modding out. (For example, $33 \bmod 15$ equals 3.) She sends the remainder to Bob as the coded message. To unscramble the message, Bob raises it to another power that depends on the two primes. That power is his private key. He then mods out by the public key. Voilà! The original message pops out.

Confusing? It's supposed to be. But basically it's as if Alice has a counter that resembles a car's odometer, except that it rolls over to zero when the count equals the public key. She dials in the original message and scrambles it by advancing the counter according to a certain recipe, letting the counter roll over however many times it will. Bob then advances the counter in a way that makes the original message roll around again.

The algorithm is secure because, without knowing how many times the counter has rolled over, Eve can't readily reverse Alice's manipulations. She may have a better shot at figuring out Bob's private key—the power to which he's going to raise the coded message. But that requires factoring the public key. As the key is huge—typically 2048 bits—that task would overwhelm an ordinary computer.

But it would be easy for a quantum computer. An ordinary computer employs "bits" that can be set to either 0 or 1; a quantum computer would use "qubits"—perhaps spinning ions or little loops of superconductor—that could be set to 0, 1,

or, thanks to the weirdness of quantum mechanics, 0 and 1 at the same time. The qubits' state would be described by quantum waves that can interfere to reinforce or cancel one another, making new algorithms possible. In 1994, Peter Shor, a computer scientist

at the Massachusetts Institute of Technology (MIT) in Cambridge, reported an algorithm that uses such "quantum interference" to factor huge numbers in far fewer steps than an ordinary computer needs. Shor's algorithm could crack not just RSA, but all current public key schemes.

Online sciencemag.org

Podcast interview with Adrian Cho (http://scim.ag/pod_6170).

Building a quantum computer, however, is easier said than done. Researchers must keep the qubits isolated enough to maintain their delicate quantum waves, yet make them interact enough to perform a calculation. That's a monumental challenge. Quantum computing has been a hot topic since the 1990s, but physicists are still struggling to manipulate a handful of qubits. The best anyone has done with Shor's algorithm has been to factor 21.

One company, D-Wave of Burnaby, Canada, sells a more limited type of supposedly quantum computer that cannot run Shor's algorithm. But for the most part, quantum computing remains a basic research subject, says Addison Snell, an industry analyst with Intersect360 Research in Mountain View, California. "If I were a big company like IBM, I'd have a couple of guys in the back room working on this," he says.

Countermeasures

Even if a quantum computer remains a remote threat, some researchers are already working to counter it. That's because it's not just future communications that might be jeopardized, but also messages we're sending today, which could be cracked after a quantum computer becomes a reality. "How do you know that somebody hasn't recorded all those communications?" says Georgia Tech's Fortnow. "The Internet doesn't forget so fast."

The easiest safeguard would be to improve cryptography. A quantum computer couldn't defeat every type of encryption. In symmetric or private key systems, Alice and Bob share a secret key and a public algorithm that, for example, makes two different chunks of coded message look like random bits when Eve compares them. In that case, Eve can't hack a transmission by looking for correlations in the stream of bits. Such schemes seem capable of withstanding a quantum attack and already encrypt most of the data transmitted in secure Internet transactions.

New public key algorithms might also fend off a quantum computer. For example, Chris Peikert, a cryptographer at Georgia Tech, and colleagues are working on so-called lattice methods. A lattice is a repeating array of dots like the atoms in a crystal. In three dimensions, each distinct crystal lattice can be characterized by three arrows or "basis vectors" that can be added to and subtracted from one another repeatedly to reconstruct the structure. Describing a lattice in 1000 dimensions requires 1000 basis vectors.

Given only the basis vectors for a 1000-dimensional lattice, which two points in the lattice are closest together? That is, what

is the shortest vector that can be made from the basis vectors? That problem appears to be hard, even for a quantum computer, Peikert says. So he's developing schemes in which the basis vectors serve as the public key to encode a message, and the shortest vector serves as the private key to decode it. "In terms of having something that is real that can be measured and optimized, we are either there or very close to there," Peikert says.

Perhaps the best defense against a quantum computer is another quantum strategy: quantum key distribution. In that technology, Alice passes Bob a secret key encoded in individual photons. The photons can be polarized—say, horizontally for 0 and vertically for 1. Thanks to quantum theory, Eve can't measure the photons without altering them and revealing herself.

A handful of companies already sell quantum key distribution systems. For example, ID Quantique in Geneva,

to make than a quantum computer, says Gregoire Ribordy, co-founder and CEO of ID Quantique: "Which is good, because it means we will be able to do [fully] quantum communications before encryption is broken."

More immediate dangers

Even without a quantum computer, public key systems are under pressure because of improvements in algorithms and increases in computing power. When RSA was invented in 1977, mathematician and writer Martin Gardner challenged readers to crack a message encoded with a 426-bit key. Ronald Rivest, a computer scientist at MIT and one of the inventors of RSA, estimated that it would take 40 quadrillion years to do so. Seventeen years later, 600 volunteers decoded the message in 8 months. To fend off such challenges, Internet companies such as Google and Microsoft are now phasing out 1024-bit RSA keys in favor of tougher 2048-bit ones.

Universal Quantum Computer vs. Quantum Key Distribution

Primarily a theoretical construct	Status	Entering market
Could crack current algorithms for public key encryption	Strength	Passes key for private key algorithms under eavesdroppers' noses
Can't break private key encryption, could be shut out by quantum key distribution	Weakness	Requires rewiring networks with optical fiber, fully quantum network not yet possible
Has been a decade away for nearly 20 years and may stay that way	Prospects	Hard and expensive, but easier and cheaper than building a quantum computer

Trumped? As a code cracker, a quantum computer might be foiled by simpler quantum key distribution.

Switzerland, has roughly 100 systems in use; its clients include the Canton of Geneva, which protects election results with the technology. Current systems cost about \$100,000 for two stations linked by an optical fiber. And they're not yet ideal: A message sent across a network must be decoded at each station along the way, where it might be intercepted.

To overcome that weakness, researchers hope to use the photons not simply to send the key, but to create a mysterious quantum connection called entanglement between qubits in 0-and-1 states at either end of a link. Alice and Bob could then generate a secret key by measuring their qubits: Alice would measure hers, causing its state to "collapse" into either 0 or 1. She'd know that Bob's had collapsed into the same state. Entanglement could be passed from node to node, so that Alice and Bob could share the key without danger of spying at the nodes between them.

That vision requires a device called a quantum repeater at each node. Such a thing does not yet exist, but it should be easier

But going further and switching to new algorithms would be hugely expensive. Widespread quantum key distribution would require rewiring networks with optical fibers. Without a dramatic threat, the technologies may not be worth the hassle. "The old joke is that one of the uses for quantum computing is to create a market for quantum key distribution," says Scott Aaronson, a theoretical computer scientist at MIT.

The economic calculus could also cut the other way, however. If quantum-proof algorithms and quantum key distribution take off, then they might blunt the desire of governments and private companies to build a quantum computer. "It could happen," Ribordy says. "It's a good argument."

Aaronson argues that a quantum computer will have other uses and that the real reason to build one is to prove it can be done. "That's a harder case to make to many business people, but I think that's the honest case," he says. It also doesn't sound like a goal that NSA would spend \$80 million to reach. **—ADRIAN CHO**



LETTERS

edited by Jennifer Sills

Sea Turtle Funding Dries Up

IN DECEMBER, AS WE CELEBRATED THE 40TH ANNIVERSARY OF THE ENDANGERED SPECIES ACT and all of its accomplishments, the U.S. Fish and Wildlife Service (USFWS) terminated support for the recovery of an icon: the Kemp's ridley sea turtle (*Lepidochelys kempii*). This sea turtle nearly slipped into oblivion in the 1980s, and controversial tactics were used to save the

species (1). The Bi-National Recovery Plan for the Kemp's Ridley Sea Turtle Program, supported largely by USFWS since 1978, worked to protect the turtles, their eggs, and their offspring at their primary nesting beaches in Mexico. As a result of these efforts, the number of nesting females increased exponentially from only a couple of hundred turtles in 1985 to nearly 10,000 turtles in 2009. This is one of USFWS's greatest conservation successes.

Unfortunately, the recovery of the Kemp's ridley has come to an abrupt halt. Since 2009, the population increase has slowed substantially (2); the slowing rate correlates spatially and temporally with multiple natural and anthropogenic stressors in the Gulf of Mexico.

Kemp's ridley requires continued monitoring and research to assess the impacts of these stressors. Calls for better science in the Gulf of Mexico in the wake of the Deepwater Horizon oil spill have highlighted the need to continue monitoring sea turtle nesting beaches to provide data such as nest counts and other demographic parameters that are essential to population assessments (3). Similar recommendations were made by a National Academy of Sciences study (4).

Scientists and leaders of nongovernmental organization and industry will meet in November 2014 to develop a plan for continued monitoring and to carry forward the efforts begun by USFWS almost 40 years ago (5).

The ridley case study exemplifies broader findings of both the efficacy of research and management funding for pulling species back from the brink of extinction (6, 7) as well as the apparent trend of stagnant or diminishing funding levels (8, 9). A recent analysis (7) shows that sadly, global expenditures on biodiversity conservation are woefully inadequate overall and uneven; nations that underfund conservation research relative to their expected capacity to do so also show a growth in the extinction status of their mammal faunas over a 12-year period beginning in 1996. International financial flows to underfunding nations are crucial to stem biodiversity loss (7), a conclusion that is highly relevant to the ridley as well.

PAMELA PLOTKIN^{1*} AND JOSEPH BERNARDO²

¹Department of Oceanography and Interdisciplinary Graduate Program in Marine Biology, Texas A&M University, College Station, TX 77843, USA. ²Department of Biology and Interdisciplinary Graduate Program in Marine Biology, Texas A&M University, College Station, TX 77843, USA.

*Corresponding author. E-mail: plotkin@tamu.edu

References

1. G. Taubes, *Science* **256**, 614 (1992).
2. B. J. Gallaway *et al.*, "Kemps' ridley stock assessment project final report" (2013); www.gsmfc.org/publications/Miscellaneous/

Kemp%20Ridley%20Stock%20Assessment%20Report%20Final%20June%202027%202013.pdf.

3. K. A. Bjørndal *et al.*, *Science* **331**, 537 (2011).
4. National Academy of Sciences, "Assessment of sea-turtle status and trends: Integrating demography and abundance" (2010); www.nap.edu/catalog/12889.html.
5. Second International Kemp's Ridley Sea Turtle Symposium, Brownsville, TX, 18 to 19 November 2014 (www.kempsridley.info).
6. P. J. Ferraro *et al.*, *J. Environ. Econ. Manage.* **54**, 245 (2007).
7. A. Waldron *et al.*, *Proc. Natl. Acad. Sci. U.S.A.* **110**, 12144 (2013).
8. V. J. Bakker *et al.*, *Conserv. Lett.* **3**, 435 (2010).
9. Anonymous, "State of financing for biodiversity: Draft global monitoring report 2012 on the strategy for resource mobilization under the Convention" (2012); www.cbd.int/doc/meetings/cop/cop-11/information/cop-11-inf-16-en.pdf.

Fueling Innovation

M. MCNUTT'S EDITORIAL "WHAT AWAITS THE new NSF director" (6 December 2013, p. 1145) highlights the high stakes in Washington's budgetary and policy cross-currents. McNutt underscores the sad fact: "Basic research" is hurting.

One crucial question is whether the National Science Foundation (NSF) can continue to hold its "basic" banner high. Recall 1965 Nobel Prize winner Richard Feynman's powerful admission: "Physics is like sex; sure, it may give some practical results, but that's not why we do it." A great country must support its geniuses, and the United States continues to thrive because we have.

NSF must foster the next generation of world-class talent and those with originality in every field. Does Congress want only practical outcomes, and right away? If so, American science may suffocate. Prioritizing mostly short-term, conventional paths is a bad national strategy for research.

As McNutt wisely argues, a second critical institutional question now is NSF's independence. Independence means selecting fertile fields and supporting the best-of-the-best investigators. NSF's quality controls, so well managed in the past, must be sustained, not undermined.

“The public interest requires doing today,” said 18th-century British statesman Edmund Burke, “those things that men [and women] of intelligence and good will would wish, 5 or 10 years hence, had been done.” At a time when spectacular research opportunities exist and when global competition rises, our engine of innovation—the science and technology that drive economic success—is sputtering. Protecting NSF’s traditional responsibility provides a major component of the fuel we need.

RODNEY W. NICHOLS

Former Executive Vice President, The Rockefeller University, President and CEO emeritus New York Academy of Sciences, S&T Consulting, New York, NY 10028, USA. E-mail: rod.nichols@verizon.net

Research Tax Credits: An Important Tool

IN HIS NEWS & ANALYSIS PIECE ON THE LAPSE of the U.S. research and experimentation (R&E) tax credit (“U.S. tax credit: Boondoggle or boon for research?” 3 January, p. 13), D. Malakoff quotes Citizens

for Tax Justice advocates who argue that we might be better off “if Congress killed the credit and used the money for targeted, direct research grants.” While we do not defend the credit in its current form, we believe (and have recently explained) that optimal innovation policy requires a mixture of financial incentives for research and development, including tax credits as well as other tools such as grants, patents, and prizes (*1*).

Targeted research grants are effective only when government decision-makers can obtain reliable information about the costs and benefits of potential research projects. For many new technologies, the government is at a comparative disadvantage when it comes to picking winners, and market signals may provide a more accurate proxy for social benefits. Under these circumstances, incentives such as tax credits may be preferable to grants. Because tax credits only refund a portion of research expenses, they are generally used in combination with private investment and do not displace the role of markets in allocating resources.

Tax credits might appear inferior to patents as a way to leverage private information

because tax credits impose a higher cost on the federal budget, but this disadvantage is illusory. The reward to innovators from patents comes from higher prices on patented products, and these higher prices impose a “shadow patent tax” on consumers comparable to the more transparent taxes that fund tax credits, grants, or prizes. This is not to say that the current implementation of the R&E tax credit is ideal, but we think that tax credits play an important role in our innovation policy portfolio.

**DANIEL J. HEMEL¹ AND
LISA LARRIMORE OUELLETTE^{2*}**

¹Washington, DC 20002, USA. ²Yale Law School Information Society Project, New Haven, CT 06511, USA.

*Corresponding author. E-mail: lisa.ouellette@aya.yale.edu

Reference

1. D. J. Hemel, L. L. Ouellette, *Texas Law Rev.* **92**, 303 (2013).

The Changing Role of Medieval Women

IN HIS PERSPECTIVE “WOMEN, FERTILITY, AND the rise of modern capitalism” (25 October 2013, p. 427), A. Alesina correctly pointed

to the importance of the Black Death, alongside new Protestant ideas, in transforming Late Medieval European economies. He and other economic historians have noted that the Black Death substantially reduced the population of rural producers, bringing better returns to labor by comparison with earlier periods. Alesina also argues that women's fertility decreased as their labor in the fields increased. Alesina did not mention the export industry or social unrest, both of which contributed to economic changes and the status of women during this time.

In the 14th century, England was becoming a major exporter of high-quality wool products. Initially, the benefits from these exports were enjoyed by the elite. However, centralized control of production was inefficient, and there was little to motivate their obligated labor force (1). Raw wool export also was increasingly supplanted by more local cloth production (2). The changing wool economy drew more female producers into the labor force. Women took jobs in weaving, basic production, and the growing service economy.

The social unrest that characterized this

period also contributed to women's changing roles. Growing commerce brought new opportunities for women, not only as producers, but also as marketers. As E. P. Thompson pointed out (3), women were often the leaders in riots in the marketplaces because they were more involved in market transactions than men, they understood market conditions in detail, and they had much to gain from institutionally improved market conditions.

RICHARD E. BLANTON

Department of Anthropology, Purdue University, West Lafayette, IN 47907, USA. E-mail: blantonr@purdue.edu

References

1. R. Hilton, *Class Conflict and the Crisis of Feudalism: Essays in Medieval Social History* (The Hambledon Press, London, 1985).
2. R. Britnell, *Britain and Ireland 1050–1530: Economy and Society* (Oxford Univ. Press, Oxford, 2004).
3. E. P. Thompson, *Past Present* **50**, 115 (1971).

CORRECTIONS AND CLARIFICATIONS

News & Analysis: "Cavefish study supports controversial evolutionary mechanism" by E. Pennisi (13 December 2013, p. 1304). The story stated that Susan Lindquist and "colleagues" were the first to propose that Hsp90 acts as an evolutionary "capacitor" by masking underlying mutations. In fact, Suzannah Rutherford was the first and only other

author on the relevant 1998 paper. The HTML and PDF versions online have been corrected.

Policy Forum: "International cooperation on human lunar heritage" by H. R. Hertzfeld and S. N. Pace (29 November 2013, p. 1049). The phrase "reinforced and formalized" was missing from the sentence: "Article II of the OST reinforced and formalized the international standard that outer space, the Moon, and other celestial bodies would not be subject to claims of sovereignty from any nation by any means, including appropriation." The HTML and PDF versions online have been corrected.

News & Analysis: "Sleep: The brain's housekeeper?" by E. Underwood (18 October 2013, p. 301). The article should have stated that amyloid plaques in Alzheimer's disease build up outside, not inside, neurons. The HTML and PDF versions online have been corrected.

Letters to the Editor

Letters (~300 words) discuss material published in *Science* in the past 3 months or matters of general interest. Letters are not acknowledged upon receipt. Whether published in full or in part, Letters are subject to editing for clarity and space. Letters submitted, published, or posted elsewhere, in print or online, will be disqualified. To submit a Letter, go to www.submit2science.org.

NEUROSCIENCE

In the Playing Ground of Consciousness

Christof Koch

Science has profited immensely from Galileo Galilei's pragmatic stance of removing subjectivity from nature in order to describe reality in an objective and quantitative manner. However, as pointed out by Galileo's near contemporary Rene Descartes, subjectivity (consciousness) is the central fact of our lived experience. It is the one undeniable fact that "I" am utterly certain of. As physics, chemistry, and biology are coming to understand the physical cosmos—including the known universe's most complex piece of organized matter, the brain—it is time to turn science's analytical lens inward, toward the mind. Or, as Oscar Wilde expressed it, "When one has weighed the sun in the balance, and measured the steps of the moon, and mapped out the seven heavens star by star, there still remains oneself. Who can calculate the orbit of his own soul?"

This was the central impulse behind the joint work that the molecular-biologist-turned-neuroscientist Francis Crick and I started in the late 1980s. At the time, there was scant experimental work that directly looked for the neuronal correlates of consciousness in people, let alone in animals. That this unfortunate state of affairs has changed dramatically is due in no small measure to Stanislas Dehaene, a mathematician and cognitive neuroscientist at the College de France in Paris. In *Consciousness and the Brain*, he summarizes the fruits of two decades of vigorous experimentation and modeling.

Dehaene has little patience with philosophy. No eristic and endless debates about whether consciousness can or cannot be explained within a reductionist framework. The book introduces the methods that acted as midwife at the birth of a science of consciousness: treating people's reports about their subjective experiences as genuine scientific data (with appropriate caveats); manipulating the visibility of briefly flashed images of faces, objects, words, or numbers so that the subject sometimes consciously sees them but sometimes not (depending on experimental conditions or uncontrolled processes in the subject's brain); and recording the associated

neural activity using functional brain imaging, electroencephalography (EEG), magnetoencephalography, or electrodes implanted into the brain of epileptic patients to monitor seizures for clinical purposes.

Dehaene is a wizard at hiding images beneath a cloak of invisibility ("masking" them, in the jargon of psychophysics) while directly or indirectly probing the subject's mind or actions by picking up vestiges that the subliminal pictures may have left behind. (For example, does a briefly flashed, "invisible" word influence the reaction time to the visible word flashed immediately afterward?) In this way, he and an entire generation of psychologists have revealed the capabilities of the unconscious mind. Dealing with the vast onslaught of sensory information impinging onto our sensors, it turns sounds into meaningful words and photons into objects and identifiable people, evaluates and weights evidence, and rapidly weaves its body through a crowd of shoppers or returns a tennis ball.

Complementing the unconscious mind, a more deliberate cognitive module places certain sensory events (typically those that have been selected when we pay "attention" to them), retrieved memories, or deliberate thoughts into a short-term scratch pad. It is the content of this short-term memory buffer that we become conscious of. Once information is loaded into this workspace—the adoption of an early computer term reveals the historical origin of this model—it can be distributed to many other processes. Data can be sent off to the language module and be identified and named so that they can be shared with other people, forwarded to the planning module to be reasoned about, and stored in long-term memory if the information is notable enough. According to this "global workspace" view, originally put forth by psychologist Bernie Baars, broadcasting information from this buffer to the rest of the brain is what renders it conscious. Consciousness is just brainwide sharing of information that is in the memory buffer. Unfortunately, this workspace has a very limited capacity. At any one time, we can only be conscious of a smithereen—in the

limit only a single item or event, although we can quickly shift things into and out of consciousness. New information will compete with the old and overwrite it.

Dehaene and molecular biologist Jean-Pierre Changeux have mapped this abstract global workspace architecture onto a dense network of interconnected brain regions in the prefrontal and parietal cortices. These are linked together by far-reaching axons of

pyramidal neurons that act as a bullhorn for the short-term memory buffer, broadcasting its content to the rest of the brain.

Dehaene devotes the book's second half to descriptions of his ongoing experimental and computational efforts to identify the neuronal footprints of conscious global workspace

processing. These cluster predominantly in frontal regions. In response to a flashed picture, the electrical activity generated by visual processing in the eyes, in primary visual cortex, and beyond peaks in the front of the brain, where it can be detected outside the skull by EEG electrodes as the "P300" wave. Becoming conscious of a sight triggers the P300 wave, igniting the prefrontal cortex. When on a different trial the image is present on the retina but remains invisible, the electrical activity moving up from the sensory periphery into the first stages of cortical processing dies out without the attendant P300 signature wave; the information fails to enter the global workspace. With this signature in hand, Dehaene infers visual awareness in infants (5 to 15 months old) and describes a detector to judge the presence or absence of consciousness in severely brain-injured patients who lack a reliable means to communicate their inner state.

Postulating that global availability of information is what we subjectively experience as a conscious state begets the question of why. Why does broadcasting information give rise to consciousness? What is the exact nature of the message that allows the system to experience it from an intrinsic point of view? Answering such questions requires an information-theoretical account of what type of data, communicated within what system, gives rise to conscious experience in biological or artificial organisms. Dehaene's well-written and well-sourced book avoids this, as he opts to restrict it to behavioral and neuronal observables. Perhaps he should heed his favorite author, Vladimir Nabokov: "The breaking of a wave cannot explain the whole sea."

Consciousness and the Brain

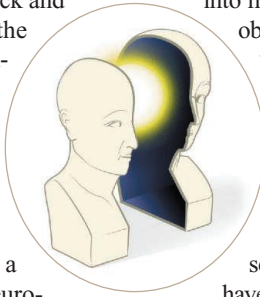
Deciphering How the Brain Codes Our Thoughts

by Stanislas Dehaene

Viking, New York, 2014.

350 pp. \$27.95, C\$32.95.

ISBN 9780670025435.



The reviewer is at the Allen Institute for Brain Science, 551 North 34th Street, Seattle, WA 98103, USA. E-mail: christofk@alleninstitute.org

10.1126/science.1248710

ANTHROPOLOGY

Life in a Fluid Landscape

Charles W. Nuckolls

Rivers do not stand alone. They are complex systems, parts of the interconnected ecological processes among which both plant and human communities live. As an introductory account of “people and life” on *chars*—small, flood-prone bits of land within the river courses of West Bengal—*Dancing with the River* provides a much-needed overview of the marginal lands where poor immigrants and refugees have settled. Poverty and political turmoil (the result of, first, India’s 1947 partition and, then, the Bangladesh war of independence in 1971) spurred successive movements of people into historically uninhabited riverine lands of West Bengal, some no more than sandy spits covered in scrub vegetation. The book touts itself as a study in “hybrid” identity formation—an overworked postmodernist concept that fortunately plays no role in subsequent chapters. Instead, geographers Kuntala Lahiri-Dutt (Australian National University) and Gopa Samanta (University of Burdwan, India) provide a richly detailed and jargon-free excursion into marginal lands and people in riparian West Bengal, not far from Kolkata and the border with Bangladesh.

The book focuses on the Damodar River area, historically associated with the erstwhile princely state of Burdwan. It begins by introducing the chars and describing their environmental uncertainties, making them, in the authors’ view, true representatives of environmental borderlands. Chars come and go, their existence dependent on seasonal floods and the buildup of sediments. The same may be said of the people, mostly landless peasants, who have settled there, either as immigrants from elsewhere in India (mostly the poor state of Bihar) or as undocumented refugees

from Bangladesh. Many stay permanently, while others move off the chars and onto the “mainland” once their fortunes improve. The chars were, until recently, one of the few remaining wild areas available for settlement to economically dispossessed and politically displaced people.

After describing the geomorphological environment of the area, the authors review the tactics and strategies (some deliberate, others accidental) to control the Damodar River and its floodplains from colonial times to the present. They next discuss the relationship between the chars and the mainland, showing that as the latter became more prosperous the chars served increasingly as overflow territories largely inhabited by the dispossessed.

The first of the ethnographic chapters sketches the history of the successive waves of immigration into the chars. Lahiri-Dutt and Samanta then explore the dimensions of vulnerability and security. Biharis and Bangladeshis have adjusted to the chars of the Damodar in different ways. The former generally grow wheat and the latter rice, reflecting the agricultural habits of their homelands. One might have thought that because both groups come from flood-prone areas, the differences between them would be slight. It turns out, however, that the Biharis have found it harder to cope with the changing ecology and therefore tend to move out when they are able. The largely undocu-

mented Bangladeshis, by contrast, have flourished by manipulating their land- and water-based livelihoods in an area still largely beyond government control.

The penultimate, and strongest, chapter examines the fine points of everyday economic life, giving special attention to the multifaceted earning strategies of the marginal population. It includes small case studies that allow the voices of the char-dwellers to be heard.

Peculiarly absent is any substantial attention to caste. Perhaps the Damodar is the exception to the rule everywhere else in India that caste is always a first-order consideration in local social relations. “Caste differences,” we are told, “are not much pronounced in the chars, since most households are from lower-caste and lower economic classes.” This, however, seems unlikely, because even “lower” castes are acutely conscious of their positions—all the more so if

their economic status is precarious and weak. It is hardly a coincidence that most economically marginal groups in South Asia are also, generally, the lowest in the caste hierarchy. What accounts for the authors’ neglect? The reader cannot know. The same is true of marriage and kinship relations, despite the fact that Lahiri-Dutt and Samanta acknowledge that family is the primary resource for people who otherwise would be extremely vulnerable to the vicissitudes of nature and economy. But we are told almost nothing about marriage systems, sibling relations, and descent patterns. Instead, the authors devote most of the last chapter to the role of women—an important consideration, to be sure, but not as useful as it would have been if set within the larger context of kinship structure.

Dancing with the River offers a richly panoramic study of a unique geographical context. It will be indispensable to scholars of marginality, poverty, and vulnerability, as well as to geographers, historians, and anthropologists of South Asia.

10.1126/science.1245713

Dancing with the River People and Life on the Chars of South Asia

by Kuntala Lahiri-Dutt
and Gopa Samanta

Yale University Press,
New Haven, CT, 2013. 296 pp.
\$65, £40. ISBN 9780300188301.
Yale Agrarian Studies.



Shyamal Baran Saha's *Impression of Chars* (2008).

The reviewer is at the Department of Anthropology, Brigham Young University, Provo, UT 84602, USA. E-mail: charles_nuckolls@byu.edu

CONSERVATION

Drug Policy as Conservation Policy: Narco-Deforestation

Kendra McSweeney,^{1*} Erik A. Nielsen,² Matthew J. Taylor,³ David J. Wrathall,⁴ Zoe Pearson,¹ Ophelia Wang,² Spencer T. Plumb⁵

The watershed 2013 report, *The Drug Problem in the Americas* (1), highlights a shift toward multilateral support for hemispheric drug policy reform. This report by the Organization of American States (OAS) reviews failures of the U.S.-led prohibitionist “war on drugs” and urges states to reconsider orthodox “supply-side” strategies (including interdiction and drug crop eradication), and to focus more on demand-side policy experimentation. In Central America, a key zone of drug transit that is being ripped apart by narco-fueled violence and corruption (2, 3), the push for reform signals hope that the conditions fueling drug traffickers’ profits and corrosive political influence may eventually be dismantled (4).

Seemingly far from the world of conservation science, drug policy reform could also alleviate pressures on Central America’s rapidly disappearing forests. Mounting evidence suggests that the trafficking of drugs (principally cocaine) has become a crucial—and overlooked—accelerant of forest loss in the isthmus. A better understanding of this process is essential for anticipating how it might be mitigated by specific drug policy reforms.

Overlapping Traffic and Deforestation

Since 2000, deforestation rates in Honduras, Guatemala, and Nicaragua have been among the highest in Latin America and the world; after 2005, the rates increased (5). Forest loss is concentrated in the Caribbean lowlands of the Mesoamerican Biological Corridor, a globally important region



Clandestine landing strip in a protected area in eastern Honduras. This is used and maintained exclusively for drug planes from South America (23 May 2011).

of exceptional biological diversity (6).

Forest loss in the corridor has long been driven by multiple interacting forces: weak governance, conflicting property regimes, high poverty, climate change, illegal logging, infrastructure megaprojects, and agribusiness expansion (6, 7). But a compelling case can be made for the ways in which the trafficking of drugs has intensified these processes and has become a powerful deforestation driver in its own right.

One clue to this connection lies in the close correlation between the timing and location of forest loss and drug transit. Central America has long been a conduit for U.S.-bound cocaine from South America. But the isthmus’ importance as a “bridge” exploded after 2006–07, as Mexican drug-trafficking organizations (DTOs) moved their smuggling operations southward (2, 8). Porous borders, corruption, and weak public institutions made Guatemala and Honduras especially attractive to DTOs (3, 8), who increasingly routed “primary” cocaine shipments (i.e., boats or planes carrying cocaine directly from South America) into Guatemala’s Petén and eastern Honduras (2, 9). Thinly populated and with little state presence, these remote forest frontiers offer ideal conditions for traffickers evading interdiction (9).

As more cocaine flowed through eastern Honduras’ forest, loss rose apace (see the graph); the large size of new patches of detected deforestation (>5.29 ha) relative to

indigenous agricultural plots (<2 ha) (10) points to the presence of unusually well-capitalized agents on the ground. Similarly, in Guatemala’s Petén, an unprecedented number of primary cocaine flows into the region coincided with a period of extensive forest loss (2006–10) (2, 11).

“Hot spots” of deforestation often overlap spatially with trafficking nodes, especially near primary drug-transfer hubs in eastern Nicaragua and eastern Honduras (6, 9). For example, in 2011, Honduras’ Río Plátano Biosphere Reserve was listed by UNESCO as “World Heritage in Danger” because of alarming rates of forest loss attributed to the presence of narco-traffickers—as signaled by multiple clandestine landing strips throughout the reserve.

In the contested rural landscapes of the Petén (7), newer sites of primary drug transfer combine with established secondary transshipment routes into Mexico. In Laguna del Tigre National Park and protected areas in the municipality of Sayaxché, the intensification of drug trafficking has been concurrent with annual forest loss rates there of 5% and 10%, respectively (8, 11, 12). Cadastral analyses confirm that narco-traffickers own large ranches within Laguna del Tigre and other protected areas (13, 14).

Landing Planes, Laundering Money

What explains the spatial and temporal overlap of drug trafficking and deforestation? Strong causal evidence remains scarce, limited by classified data on traffickers’ illegal activities and the hazards of in situ research. Nevertheless, a growing number of studies identify three interrelated mechanisms by which forest loss follows the establishment of a drug transit hub.

¹Department of Geography, Ohio State University, Columbus, OH 43210, USA. ²School of Earth Sciences and Environmental Sustainability, Northern Arizona University, Flagstaff, AZ 86011, USA. ³Department of Geography and the Environment, University of Denver, Denver, CO 80208, USA. ⁴Institute for Environment and Human Security, United Nations University, 53113 Bonn, Germany. ⁵College of Natural Resources, University of Idaho, Moscow, ID 83844, USA. *Corresponding author. mcsweeney.14@osu.edu

First, forests are cut for clandestine roads and landing strips (15) (see the photo). Second, drug trafficking intensifies preexisting pressures on forests by infusing already weakly governed frontiers with unprecedented amounts of cash and weapons. When resident ranchers, oil-palm growers, land speculators, and timber traffickers become involved in drug trafficking, they are narco-capitalized and emboldened (13, 14) and so greatly expand their activities—typically at the expense of the (indigenous) smallholders who are often key forest defenders (7, 13, 16).

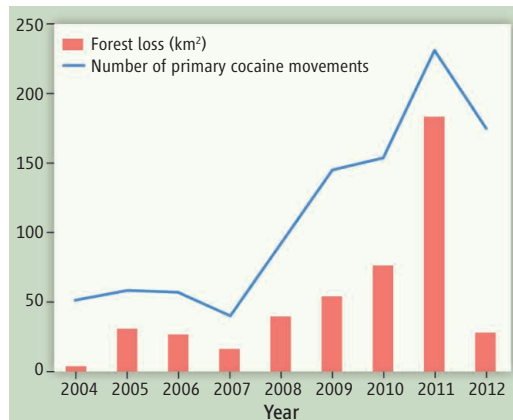
Indigenous and peasant groups report being powerless against the bribes, property fraud, and brutality dispossessing them of their lands (13, 14, 16). Forest governance at higher levels is also eroded by violence and corruption: Conservation groups have been threatened and fear entering “narco-zones” (15), while state prosecutors are bribed to look away (3).

Third, the vast profits that traffickers earn from moving drugs (8) appear to create powerful new incentives for DTOs themselves to convert forest to agriculture (usually pasture or oil-palm plantation). Profits must be laundered. Buying and “improving” remote land (by clearing it) allows dollars to be untraceably converted into private assets, while simultaneously legitimizing a DTO’s presence at the frontier (e.g., as a ranching operation). Large “narco-estates” also serve to monopolize territory against rival DTOs and to maximize traffickers’ range of activity (12–16).

In most cases, the purchase and conversion of forests within protected areas and indigenous territories is illegal. But traffickers have enough political influence to ensure their impunity and, where necessary, to falsify land titles (14, 16). They can then profit from land speculation when they sell to criminal organizations—domestic and foreign—who are increasingly diversifying into rural enterprise (12, 14). These actors may in turn sell to legitimate corporate interests looking to invest in Central American agribusiness (7, 12, 16). The result is permanent conversion of forests to agriculture.

Drug Policies Are Conservation Policies

In contexts of drug crop cultivation—particularly in the Andes—analysts have long noted that eradication policies often push coca (and opium poppy and marijuana) growers into ever more ecologically sensitive zones, with substantial environmental impacts (1,



Deforestation and drug trafficking in eastern Honduras. Deforested area is the sum of new clearings >5.29 ha detected by the Moderate Resolution Imaging Spectroradiometer (MODIS). For materials and methods, see the supplementary materials.

17). Relatively little attention, however, has focused on how the same “balloon effect” is operating further up the drug commodity chain, in the countries through which drugs are being moved: Interdiction programs push traffickers into remote spaces where they exacerbate existing pressures on forests and find new opportunities for money laundering and illegal enrichment through forest conversion. For example, “successful” interdiction efforts in Honduras in 2012 (see graph) appear to be encouraging traffickers to shift operations and ecological impacts to new areas in eastern Nicaragua (18).

Ultimately, intensified ecological devastation across trafficking zones should be added to the long list of negative unintended consequences borne by poor countries as a result of the overwhelming emphasis on supply-side drug reduction policies (4).

For the international conservation community, this is an important reminder that drug policy is conservation policy. Careful interdisciplinary research is now needed to address empirical uncertainties regarding the magnitude and dynamics of the narco-trafficking–deforestation relation, especially how narco-capital (especially via money laundering and bribery) influences environmental governance, agrarian futures, and ecosystem services. Such research will inform not only conservation policy but evidence-based drug policy, too (1, 4). For example, recognizing the ecological costs of drug trafficking in transit countries would improve full-cost pricing analyses of the drug policy scenarios explored by the OAS.

Of course, drug policy innovations alone will never end deforestation in Central America. But well-targeted drug policy reforms could mitigate a compounding pressure on

these biodiverse forests and buy time for states, conservationists, and rural communities to renew protected area governance and enforcement. Rethinking the war on drugs could yield important ecological benefits.

References and Notes

1. A. Briones *et al.*, Eds., *The Drug Problem in the Americas* (General Secretariat, OAS, Washington, DC, 2013).
2. United Nations Office on Drugs and Crime, *Transnational Organized Crime in Central America and the Caribbean: A Threat Assessment* (UNODC, Vienna, 2012).
3. J. M. Bunck, M. R. Fowler, *Bribes, Bullets, and Intimidation: Drug Trafficking and the Law in Central America* (Pennsylvania State Univ. Press, University Park, PA, 2012).
4. Global Commission on Drug Policy, *War on Drugs: Report of the Global Commission on Drug Policy* (Global Commission on Drug Policy, 2011).
5. Food and Agriculture Organization of the United Nations, “Global forest resources assessment 2010” (FAO, Rome, 2010).
6. D. J. Redo, H. R. Grau, T. M. Aide, M. L. Clark, *Proc. Natl. Acad. Sci. U.S.A.* **109**, 8839 (2012).
7. N. Cuéllar *et al.*, *Territorial Dynamics in Central America: Context and Challenges for Rural Communities* (Fundación PRISMA, San Salvador, 2011).
8. C. J. Arnason, E. L. Olson, Eds., *Organized Crime in Central America: The Northern Triangle* (Woodrow Wilson International Center for Scholars, Washington, DC, 2011).
9. Bureau of International Narcotics and Law Enforcement Affairs, “2013 International Narcotics Control Strategy Report” (Department of State, Washington, DC, 2013).
10. S. T. Plumb, E. A. Nielsen, Y.-S. Kim, *Forests* **3**, 244 (2012).
11. O. Regalado *et al.*, “Mapa de cobertura forestal de Guatemala 2010 y dinámica de la cobertura forestal 2006–2010” [National Forestry Institute (INAB), National Council for Protected Areas (CONAP), Universidad del Valle de Guatemala, Universidad Rafael Landívar, Guatemala City, 2012].
12. L. Grandia, *Dev. Change* **44**, 233 (2013).
13. J. Grüberg, L. Grandia, B. Milian and team, *Tierra y Igualdad: Desafíos para la Administración de Tierras en Petén, Guatemala* (Agriculture and Rural Development, World Bank, Washington, DC, 2012).
14. InSight Crime, *Grupos de Poder en Petén: Territorio, Política y Negocios* (Insight Crime, Medellín, Colombia, and American Univ., Washington, DC, 2011); www.libertopolis.com/wp-content/files/REPORTE_PETEN_DE_InSightCrime_Parte_1.pdf.
15. W. Allen, *Yale Environment* **360**, 8 October 2012.
16. K. McSweeney, Z. Pearson, “Prying native people from native lands: Narco business in Honduras” *NACLA Report on the Americas*, 7 January 2014.
17. A. V. Bradley, A. C. Millington, *Ecol. Soc.* **13**, 31 (2008).
18. H. Stone, “Nicaragua coast becomes gateway for Honduras drug flights” (Insight Crime, Medellín, Colombia, and American Univ., Washington, DC, 2012); www.insight-crime.org/news-analysis/nicaragua-coast-becomes-gateway-for-honduras-drug-flights.

Acknowledgments: Portions of this work were supported by grants to K.M. from the National Geographic Society, Ohio State University’s (OSU’s) Mershon Center for International Security Studies, OSU’s Office of International Affairs, and the Association of American Geographers and by faculty grants to E.A.N. from Northern Arizona University (NAU). Planet Action, the Landscape Conservation Initiative at NAU, and the Science Foundation of Arizona provided support to O.W. We thank S. Sesnie, reviewers, and Terra-i.org.

Supplementary Materials

www.sciencemag.org/content/343/6170/489/suppl/DC1

DEVELOPMENT

Chemical Warfare in the Battle of the Sexes

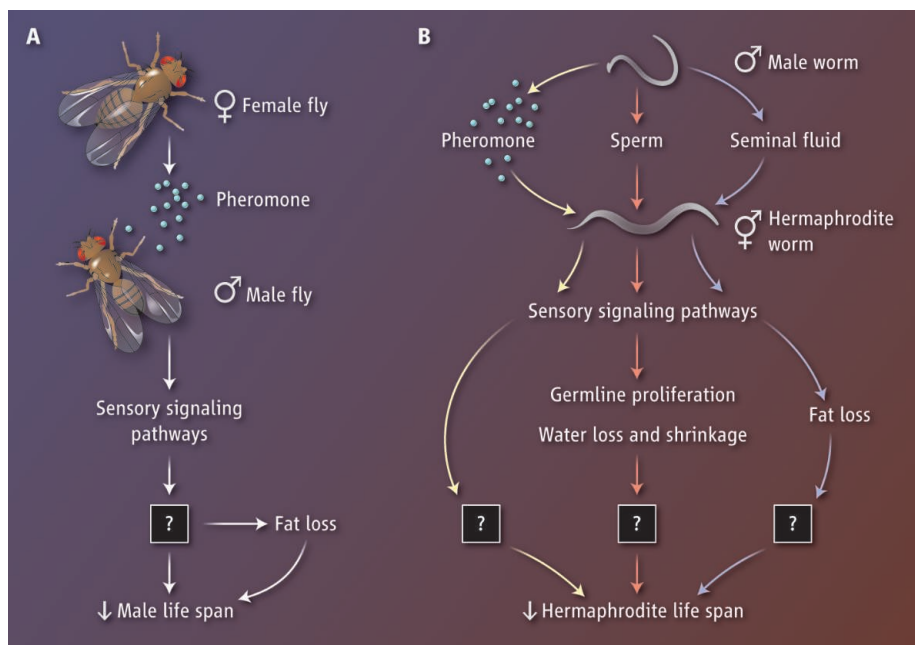
Daniel E. L. Promislow^{1,2} and Matt Kaeberlein¹

It may not be a complete surprise to learn that prolonged exposure to the opposite sex could be detrimental to your health. This is certainly true for some invertebrates, such as nematode worms and fruit flies (1, 2). In this issue, Shi *et al.* (3) on page 536 and Maures *et al.* (4) on page 541 provide important new insights into the genetic and molecular processes that account for “male-induced demise” in worms. The battle of the sexes goes both ways, however, and on page 544, Gendron *et al.* (5) report that female-produced pheromones in the fruit fly can have similar detrimental effects on longevity and other age-related traits in male flies. Together, these studies pose some interesting evolutionary questions that touch on sex, death, and aging.

It has long been known that having the opposite sex around can reduce fitness in some species. Fitness is determined by the number of offspring an individual produces, but is limited by costs of reproduction (6). The costs of courtship, mating, and offspring production are paid in higher mortality, reduced immunity, loss of future reproduction, and many other traits.

The studies of Shi *et al.*, Maures *et al.*, and Gendron *et al.* take this idea to a new level by showing that costs of reproduction can be incurred just by perceiving the opposite sex. This is sufficient to decrease fat stores, increase mortality, and as demonstrated by Shi *et al.*, shrink an animal's overall size. Interestingly, a similar importance for sensory perception of food has been observed. In both fruit flies and worms, just the smell of a rich diet is enough to increase mortality rate and prevent many of the benefits of a low-calorie diet (7, 8). Gendron *et al.* show that the scent of a female fruit fly (*Drosophila melanogaster*), even when that smell comes from another male fruit fly genetically altered to produce female pheromones, is sufficient to shorten the male's life span substantially. Similarly, in the worm *Caenorhabditis elegans*, a species in which the vast majority of animals are self-fertilizing hermaphrodites,

Merely perceiving the opposite sex can shorten an animal's life span.



Mating and mortality. (A) Female fruit flies can shorten the life span of males through a pheromone pathway and unknown downstream mechanisms. (B) Signals from male worms can shorten the life span of recipient hermaphroditic worms through various pathways that are not yet fully understood.

exposure to medium that was once exposed to males causes hermaphrodites to die faster. This effect is seen even in sterile mutants, distinguishing it from direct energetic costs of reproduction.

These new observations raise two related questions: What are the proximate mechanisms that reduce life span (and in the case of the study by Shi *et al.*, shrink females)? That is, what lies in the “black box” between the sensory input that turns on these pathways, and the anatomical, physiological, and demographic consequences that lie downstream (see the figure)? And, why, from an evolutionary perspective, does the presence of the opposite sex shorten life span? The answer to the first question will come from additional mechanistic studies. But answers to both questions will also benefit from an evolutionary perspective.

Previous studies suggest that the relationship between mating and mortality could have been shaped by sexually antagonistic coevolution (9). According to this concept, the behaviors by which a female can maximize her evolutionary fitness are often in conflict

with those of her male partner and vice versa. Research suggests that in the fruit fly, sexually antagonistic coevolution has led male *Drosophila* to evolve ejaculate proteins that manipulate female behavior and physiology in ways that increase the male's fitness (1). And to counter the ways that males reduce female fitness, selection acts on females to evolve mechanisms to mitigate the male's effects (10). The two sexes are in a continuous arms race, both trying to maximize their own fitness, even if at the expense of the other sex.

Despite their different mating systems, flies and worms are likely to have been influenced by sexually antagonistic coevolution. For example *C. elegans* are female hermaphrodites that can self-fertilize their own eggs. Males are rare, typically less than 1% in nature and can only reproduce by mating with hermaphrodites. Hermaphrodites will generally avoid outcrossing with males, which dilutes their genetic contribution to offspring by half. While selection should favor females that use their own sperm, at the same time it should select for males that do everything possible to mate, even if that means coercing females,

¹Department of Pathology, University of Washington, Seattle, WA 98195 USA. ²Department of Biology, University of Washington, Seattle, WA 98195, USA. E-mail: promislo@uw.edu

chemically if not physically, to fertilize their eggs using the male's sperm. In this scenario, selection could well have led to the evolution of male pheromones that alter female physiology in a way that enhances male fitness, even if they shorten female life span. Given that males are rare and do not know which female in their environment they might mate with, releasing pheromones that influence all females in their vicinity might be the best way to maximize fitness.

But why don't female worms evolve ways to avoid such costly consequences of perceiving males? This might be a case of the "rare enemy" effect. If males are seldom encountered by hermaphrodites, then selection might be too weak to favor what could be costly measures for hermaphrodites to fight off male attempts at manipulation.

What about the observation that male mortality in flies increases merely by perceiving the presence of females? Here, too, sexual conflict might be the proximate explanation. Interestingly, the detrimental effects

from exposure to female pheromones can be largely alleviated by allowing the male fruit fly to mate with multiple females (5). Is this a cost of false expectations? An alternative possibility is that the very traits that males have evolved to manipulate females can be costly to the male. Males produce toxic proteins in their seminal fluid that promote egg-laying in the female but also reduce her life span (1). It may be that perceiving females are sufficient to drive production of these or other toxic molecules, and failure to ejaculate them during mating could result in deleterious consequences for the male flies—the evolutionary equivalent of friendly fire.

Perhaps sexually antagonistic coevolution has shaped sensory pathways—the signals produced by one sex, and the receptors and neural pathways that transduce these signals in the other sex. Although additional studies are needed to definitively test this idea, these same pathways have evolved to modulate longevity and fecundity in response to subtle and complex changes in a multitude of envi-

ronmental parameters, including nutrients, temperature, pathogens, and population density. How humans age might thus be a consequence not only of the way we treat our body, and the genetic lottery handed to us by our parents; it might also be affected by the social interactions—some cooperative, some conflictual—played out by males and females over millions of years.

References

1. T. Chapman *et al.*, *Nature* **373**, 241 (1995).
2. D. Gems, D. L. Riddle, *Nature* **379**, 723 (1996).
3. C. Shi, C. T. Murphy, *Science* **343**, 536 (2014); 10.1126/science.1242958.
4. T. J. Maures *et al.*, *Science* **343**, 541 (2014); 10.1126/science.1244160.
5. C. M. Gendron *et al.*, *Science* **343**, 544 (2014); 10.1126/science.1243339.
6. L. Partridge, P. Harvey, *Nature* **316**, 20 (1985).
7. S. Libert *et al.*, *Science* **315**, 1133 (2007).
8. E. D. Smith *et al.*, *BMC Dev. Biol.* **8**, 49 (2008).
9. G. Arnqvist, L. Rowe, *Sexual Conflict. Monographs in Behavior and Ecology*, J. Krebs, T. H. Clutton-Brock, Eds. (Princeton Univ. Press, Princeton, NJ, 2005).
10. W. R. Rice, *Nature* **381**, 232 (1996).

10.1126/science.1250174

APPLIED PHYSICS

When Electrons Leave Holes in Organic Solar Cells

Jean-Luc Bredas^{1,2}

Organic solar cells convert sunlight into electricity by exploiting the electronic properties of electrically and optically active organic materials. Since the initial report of an organic solar cell reaching a power conversion efficiency near 1% (1), many efforts have brought the efficiency of carefully optimized devices in the 10 to 12% range (2). These efficiencies remain, however, well below the thermodynamic limit for single-junction organic solar cells, estimated to be >20% (3). Part of the failure in reaching the full potential of these devices is the lack of a comprehensive mechanistic picture of energy harvesting and carrier generation, transport, and recombination, particularly as a function of materials properties and active-layer morphology. On page 512 of this issue, Gélinas *et al.* (4) present a major step forward in the characterization of the charge-separation mechanism in organic solar cells.

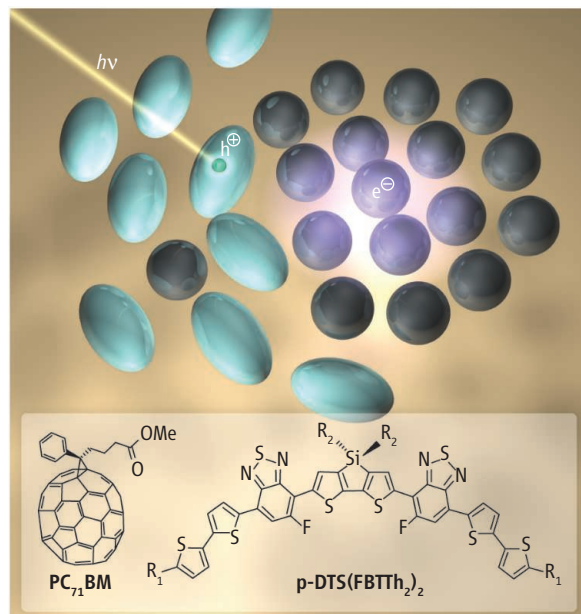
¹School of Chemistry and Biochemistry, and Center for Organic Photonics and Electronics, Georgia Institute of Technology, Atlanta, GA 30332-0400, USA. ²Department of Chemistry, King Abdulaziz University, 21589 Jeddah, Saudi Arabia. E-mail: jean-luc.bredas@chemistry.gatech.edu

An established view of organic π -conjugated materials is that the primary photoexcitations are excitonic in nature. The photoexcited electron is not free to move on

its own; it remains bound to the hole (positive charge carrier) that forms on the molecular orbital from which the electron was excited. The binding energies of these electron-hole

pairs, or excitons, are generally more than one order of magnitude greater than the thermal energy at room temperature. The formation of strongly bound excitons is in contrast to the situation in inorganic materials, such as crystalline silicon, where photoexcitations lead to immediate separation of elec-

Charges at the interface. In this illustration of the donor-acceptor interface and the ultrafast process of charge separation of hole and electron probed by Gélinas *et al.*, the ovals represent the donor molecules [p-DTS(FBTTh₂)₂] and the circles the fullerene acceptor molecules (PC₇₁BM). The modeling carried out by Gélinas *et al.* suggests that the electron wave function is delocalized over several fullerene molecules.



tron and hole at room temperature and generation of free charge carriers.

The large exciton binding energies in π -conjugated materials are related not only to their low dielectric constants (which offer less screening between charges and lead to stronger interactions) but also to the presence of strong electron-vibration and electron-electron interactions (5). Because excitons are neutral species unable to carry a current, the efficiency of organic solar cells depends critically on charge-separation processes at heterojunctions between an electron donor (D; typically a π -conjugated polymer or molecule) and acceptor (A; typically a fullerene derivative), such as those displayed in the figure. These D-A heterojunctions are required to produce a driving force to dissociate excitons into spatially separated charges and are generally considered as an important factor limiting efficiency compared to inorganic p-n junction solar cells [the efficiency of crystalline silicon solar cells is on the order of 25% (2)]. Understanding the energy-harvesting mechanisms in organic solar cells, thus requires the ability to characterize the elementary charge-generating processes as a function of materials choice and in the presence of multiple nano- and mesoscale morphological variations.

From an electronic-structure standpoint, when an exciton appears at the D-A interface, the exciton state can evolve into a charge-transfer (CT) state and eventually into a charge-separated state (5). A CT state is a D-A interfacial state for which a hole on a donor molecule or polymer segment is located next to an electron on an acceptor (fullerene) molecule. In the CT state, the electron and hole are still electrostatically bound to one another; as a result, there is limited electronic polarization of the surrounding molecules because the CT exciton is neutral. For the electron and hole to separate, they have to overcome their Coulomb attraction; this is facilitated by an increased electronic polarization of the surrounding molecules, which stabilizes the separated charges.

Gélinas *et al.* developed ultrafast spectroscopic tools that resolve the electron-hole separation in the femtosecond regime. They exploit the signature of the electric field that is generated between the electron and the hole as they separate. This field alters the molecular orbital energies of the surrounding molecules and thus their optical transition energies, i.e., it leads to an electro-absorption (EA) signal (6). Gélinas *et al.* could measure the EA signals with <30-fs precision and quantify the electrostatic energy stored in the electric field. In this way, they could characterize the initial

steps of electron-hole separation as they occur in the tens of femtoseconds regime (4). The authors measured two model systems, consisting of a small molecule–fullerene blend (illustrated in the figure) and a polymer–fullerene blend, and varied the D-A compositions. In the blends with compositions leading to high power conversion efficiencies, there appears a clear EA signal indicative of long-range separation of electrons and holes. For the polymer–fullerene blend, the electrostatic energy between electron and hole reaches up to ~0.2 eV (about eight times the thermal energy at room temperature) within 40 fs of excitation, at which time the electron has left the hole some 4 to 5 nm behind and the charges can move apart freely. Efficient separation is accomplished without requiring excess energy beyond that needed to overcome Coulomb attraction, which is in line with recent results from Vandewal *et al.* (7).

Although providing a much needed characterization of the charge-separation process as it occurs at D-A interfaces, the work of Gélinas *et al.* opens up many intriguing questions, particularly with regard to the nature

of the interfacial morphology and electronic structure that enables ultrafast charge separation. The authors suggest that relatively ordered domains of fullerenes at the D-A interface allow the electrons to access delocalized “bandlike” states. It remains to be seen what happens in the regions where donors and acceptors are mixed and disordered, which are often invoked as a key component of efficient solar cells (8). Also, most of the energetic analyses to date have focused on enthalpy considerations. Reaching a complete picture will require including the role of entropy (9), in addition to obtaining an accurate description of the polarization effects.

References

1. C. W. Tang, *Appl. Phys. Lett.* **48**, 183 (1986).
2. See www.nrel.gov/ncpv/images/efficiency_chart.jpg.
3. R. A. J. Janssen, J. Nelson, *Adv. Mater.* **25**, 1847 (2013).
4. S. Gélinas *et al.*, *Science* **343**, 512 (2014); 10.1126/science.1246249.
5. J. L. Brédas *et al.*, *Acc. Chem. Res.* **42**, 1691 (2009).
6. L. Sebastian *et al.*, *Chem. Phys.* **61**, 125 (1981).
7. K. Vandewal *et al.*, *Nat. Mater.* **13**, 63 (2014).
8. P. Westacott *et al.*, *Energy, Environ. Sci.* **6**, 2756 (2013).
9. B. A. Gregg, *J. Phys. Chem. Lett.* **2**, 3013 (2011).

10.1126/science.1249230

ATMOSPHERIC SCIENCE

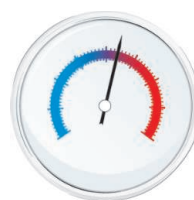
Methane on the Rise—Again

Euan G. Nisbet,¹ Edward J. Dlugokencky,² Philippe Bousquet³

Atmospheric concentrations of the greenhouse gas methane are rising, but the reasons remain incompletely understood.

Roughly one-fifth of the increase in radiative forcing by human-linked greenhouse gases since 1750 is due to methane. The past three decades have seen prolonged periods of increasing atmospheric methane, but the growth rate slowed in the 1990s (1), and from 1999 to 2006, the methane burden (that is, the total amount of methane in the air) was nearly constant. Yet strong growth resumed in 2007.

The reasons for these observed changes remain poorly understood because of limited knowledge of what controls the global methane budget (2).



Challenges in
**CLIMATE
SCIENCE**
scim.ag/climatechall

Estimates of methane emissions vary widely. Global estimates derived from process studies of sources (termed “bottom-up”) are generally much larger than those from direct observation of the air (“top-down”) (2). Local industrial emissions may be far underestimated (3). The renewed rise in the methane burden prompts urgent questions about the causes, but globally, in situ

monitoring to track atmospheric methane is very limited outside the major nations.

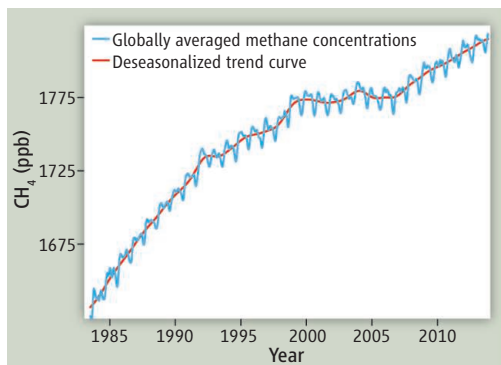
Methane sources and sinks vary with latitude. Overall, about two-thirds of the emissions are caused by human activities; the remaining third is from natural sources. At polar latitudes, methane sources include wetlands, natural gas wells and pipelines, thawing permafrost, and methane hydrate associated with decaying offshore permafrost. In

¹Department of Earth Sciences, Royal Holloway, University of London, Egham TW20 0EX, UK. ²National Oceanic and Atmospheric Administration, Earth System Research Laboratory, Boulder, CO 80305, USA. ³Laboratoire des Sciences du Climat et de l'Environnement, CEA-CNRS-UVSQ, Saclay, 91191, Gif-sur-Yvette, France. E-mail: e.nisbet@es.rhul.ac.uk

the heavily populated northern mid-latitudes, the main sources are the gas and coal industries, agriculture, landfills, and biomass fires. Tropical wetlands are the world's largest natural source of methane (4). Emissions from equatorial and savanna wetlands, ruminants, and biomass burning are increased further by tropical anthropogenic inputs. The main methane sink is reaction with hydroxide radicals (OH), especially in the tropical mid-troposphere. Minor sinks include soil oxidation, reaction with marine chlorine, and reactions in the stratosphere.

From the 1980s until about 1992, atmospheric methane was rising sharply by about 12 parts per billion (ppb) per year (see the first figure). Then came a decade of much slower growth (by about 3 ppb/year) coupled to a sudden decrease in the north-south inter-polar difference (1). In the early 2000s, growth almost ceased; for short periods, the total methane burden even declined. For the “stagnation” period from 1999 to 2006, these top-down findings from atmospheric data differ markedly (5) from bottom-up inventories, which detail strong growth in anthropogenic emissions. Yet the main sink—oxidation by OH—sees little changed (4). This discrepancy between top-down and bottom-up budgets remains unresolved.

In 2007, just when scientists thought the methane concentration had stabilized, it rose again. Since then, global average growth has been ~6 ppb/year. Considering the latitudinal zones in more detail (see the second figure),



Methane ups and downs. Globally averaged atmospheric methane concentrations rose quickly before 1992. The rise then slowed and almost stopped between 1999 and 2006, but resumed in 2007. Data from <ftp://ftp.cmdl.noaa.gov/ccg/ch4/flask/event/>.

Arctic methane rose more than the global growth rate in 2007, but since then Arctic growth has tracked global trends. Large emissions attributed to decaying methane hydrates have been reported from the East Siberian Arctic Shelf (6) but are not apparent in NOAA atmospheric observations, nor are they detected in isotopic measurements from surface and aircraft sampling in the European Arctic (7), which point to wetlands as a major Arctic source in summer and industrial gas leaks in winter. Long-term release of methane from hydrate is probable (8), but catastrophic hydrate emission scenarios (9, 10) are unlikely.

In the southern tropics, growth has been above global trends since 2007 (see the second figure). For example, at Ascension Island (8°S), sampling the tropical South Atlantic,

growth was >10 ppb per year in 2009 and 2010, when wet regional summers would have led to expanded wetland areas. This was part of a regional 5-year rise in natural emissions that may give insight into past glacial terminations and initiations, when the methane burden changed sharply, perhaps from similar processes.

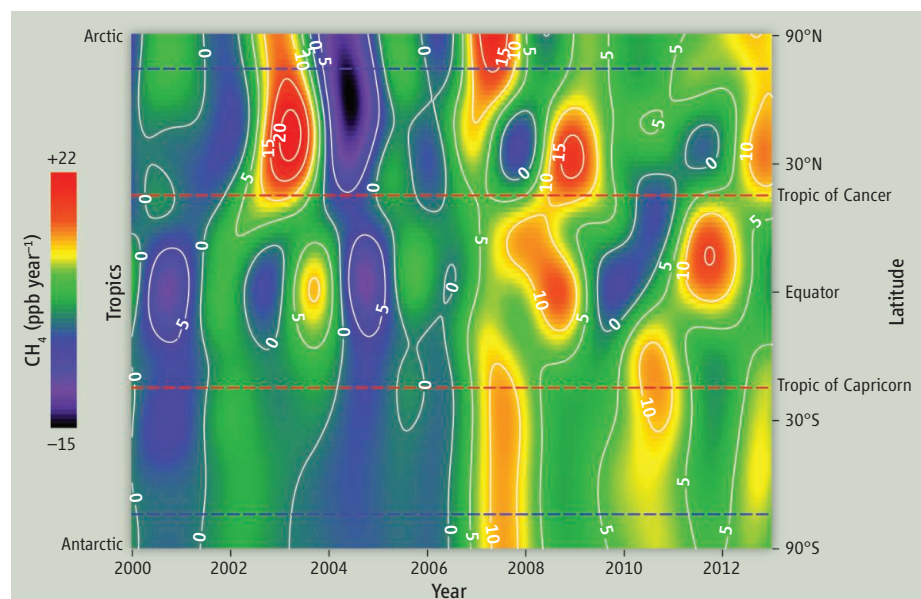
Atmospheric data show that global emissions were ~15 to 22 Tg (million tons) CH₄ per year greater in 2010 than in 2005. Global-scale modeling of these methane observations (4, 5, 11) suggests that in 2007, tropical wetland emissions dominated growth, with output from high northern latitudes also important. Since then, the increase has mostly been driven by the tropics (9 to 14 Tg/year) and northern mid-latitudes (6 to 8 Tg/year) (11).

There is much to suggest that emissions from human activities have also increased since 2007. In the United States, which has overtaken Russia as the largest gas producer (12), hydraulic fracturing is increasingly important. In Utah, fracking may locally leak 6 to 12% of gas production to the air (13). A full understanding of the greenhouse impact of fracking requires monitoring over the gas-well lifetime and analysis of the transport distribution system. Global coal mining has also expanded dramatically (12), especially in China. Rising energy production suggests increased emission from these human activities, but this inference needs to be reconciled with observations on ¹³C in methane; since 2007, atmospheric methane has become more depleted in ¹³C (14), an indication that growth is dominated by ¹²C-rich wetland and ruminant emissions.

More data are needed to resolve the divergence between top-down and bottom-up estimates, but the measurement network for methane concentration and isotopes is very thin. At a meeting of the European Pergamon Arctic methane group in Kiel, Germany, in November 2013, Crill commented that “data without models are chaos, but models without data are fantasy.” Spatially and temporally, better measurement is essential to identify and quantify methane sources (3, 4, 12), but long-term data gathering is in trouble. Despite methane’s attractiveness as a cost-effective greenhouse reduction target, budgets for greenhouse gas monitoring are contracting. Somewhere, perhaps in the tropics or East Asia, unwelcome methane surprises may lurk, but watchers are few.

References and Notes

1. E. J. Dlugokencky, E. G. Nisbet, R. Fisher, D. Lowry, *Philos. Trans. R. Soc. London Ser. A* **369**, 2058 (2011).



Methane growth rate by latitude. Contours of methane growth rate with sine of latitude. Plotting by sine of degree of latitude equally weights the results for surface area with latitude. Data from www.esrl.noaa.gov/gmd/ccgg/mb/.

2. S. Kirschke *et al.*, *Nat. Geosci.* **6**, 813 (2013).
3. S. M. Miller *et al.*, *Proc. Natl. Acad. Sci. U.S.A.* **10**, 10731 (2013).
4. P. Bousquet *et al.*, *Atmos. Chem. Phys.* **11**, 3689 (2011).
5. I. Pison *et al.*, *Atmos. Chem. Phys.* **13**, 11609 (2013).
6. N. Shakhova *et al.*, *Nat. Geosci.* **7**, 64 (2014).
7. R. E. Fisher *et al.*, *Geophys. Res. Lett.* **38**, L21803 (2011).
8. A. Biastoch *et al.*, *Geophys. Res. Lett.* **38**, L08602 (2011).
9. G. Whiteman *et al.*, *Nature* **499**, 401 (2013).
10. See also http://equianos.com/wordpress/wp-content/uploads/Response-to-Whiteman_et-al-Comment.pdf.
11. P. Bergamaschi *et al.*, *J. Geophys. Res.* **118**, 7350 (2013).
12. BP Statistical Review of World Energy 2013; www.bp.com/statisticalreview.
13. A. Karion *et al.*, *Geophys. Res. Lett.* **40**, 4393 (2013).
14. See ftp://ftp.cmdl.noaa.gov/data/trace_gases/ch4c13/flask/.

Acknowledgments: Supported in part by the UK Natural Environment Research Council MAMM and Tropical Methane projects, the European Union's Ingos project, and Royal Holloway.

10.1126/science.1247828

APPLIED PHYSICS

Selecting the Direction of Sound Transmission

Steven A. Cummer

Structures that admit flow in only one direction are commonplace—consider one-way streets, insect traps, and the staple of the police procedural story, the one-way mirror. However, creating a device that allows waves to pass in only one direction, termed an isolator, is challenging because of the inherently symmetric physics of wave phenomena. On page 516 of this issue, Fleury *et al.* (1), taking inspiration from a natural electromagnetic phenomenon, designed and demonstrated an engineered structure that allows one-way transmission of sound waves.

Creating a one-way, or nonreciprocal, structure for general wave flow is more challenging than one might think. The one-way mirror, for example, is not truly a nonreciprocal optical wave device, as the effect is created primarily by a trick of unequal lighting. True nonreciprocity in linear materials is tied to breaking of time-reversal symmetry (2). A system exhibits time-reversal symmetry if one solution of the entire system, but run backward in time, is a second solution. This condition is equivalent to interchanging the source and receiver sides of the problem, as illustrated in panel A of the figure. Wave phenomena by their nature generally exhibit time-reversal symmetry (consider how circular ripples on a pond surface can be either outwardly expanding or inwardly converging), so creating a nonreciprocal device or medium takes something special.

Engineering wave propagation nonreciprocity into materials is an area of substantial recent research. There are several different ways to do this, which are summarized in clear and thorough reviews in the context of

acoustic (3) and electromagnetic (4) waves. Interestingly, many efforts that have demonstrated asymmetric power transmission for specific input and output field distributions are not truly nonreciprocal and cannot be used to create general nonreciprocal devices (3, 4). Carefully designed nonlinear structures can exhibit nonreciprocity without time-reversal asymmetry (3, 4), but this approach results in constraints like amplitude dependence that limit its value in wave isolator applications.

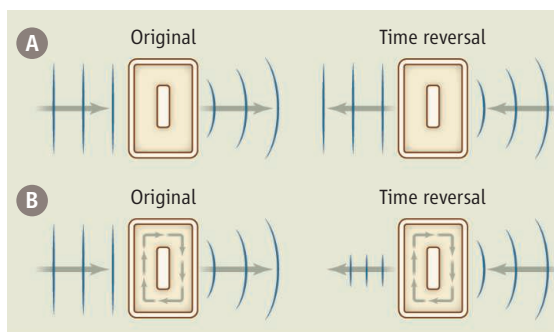
It turns out that linear systems that contain a directional bias that is defined by some form of internal motion (a so-called odd vector under time reversal) can be made nonreciprocal (2). In such a system, strict time reversal reverses the direction of that internal motion and reverses the bias direction as well. Such systems would be reciprocal if the internal motion, and thus the directional bias, is also reversed when the input and outputs are

swapped, in accord with time reversal. Interchanging the input and output ports without reversing the direction of the bias creates a nonreciprocal device by breaking time-reversal symmetry, as illustrated in panel B of the figure.

Some materials naturally contain this kind of directional bias and are inherently nonreciprocal—for example, the ionized gas of Earth's upper atmosphere permeated by the directional bias of the steady geomagnetic field (5). An external magnetic field can also be applied to magnetically active materials, such as ferrites to create nonreciprocity. This approach is used in many practical nonreciprocal optical or radio-frequency isolators (6).

In contrast, linear acoustic nonreciprocity had not, until now, been demonstrated except in weak or large-scale forms not suitable for compact applications. Fleury *et al.* have now done precisely that by borrowing

the basic physics of the Zeeman effect, in which a biasing magnetic field creates a strongly birefringent medium in which different polarization states interact with different medium resonances. Because this is an effect created by a fixed bias field, such a medium is nonreciprocal. Fleury *et al.* (1) create analogous acoustic resonance splitting in a compact circular cell that contains a rotational mean air flow. Counterpropagating acoustic waves in this cell experience different resonant frequencies, an effect that can be derived both from the basics of acoustic wave propagation in a steady mean flow and from a quantum-mechanical operator approach [see the supplementary materials of (1)].



Obeying and breaking time-reversal symmetry. (A) In a material or device without a preferred direction, the fundamentally symmetric behavior of waves means that a solution runs backward in time and is still a solution. This condition is equivalent to interchanging the input and output waves in the system. (B) However, if the system contains a flow-based directional bias, and that bias is not flipped when the input and output waves are interchanged, then time-reversal symmetry is broken. Wave transmission through such a system can be dramatically different when the input and outputs are interchanged, and thus nonreciprocal.

Department of Electrical and Computer Engineering, Duke University, Durham, NC 27708, USA. E-mail: cummer@duke.edu

Critically, the mean fluid flow provides the fixed-direction bias field that breaks the time-reversal invariance of the system. The two resonant modes of the system are unequally excited by an input, despite the symmetric port configuration. Careful design, by tuning of the mean fluid flow, enables the interference of these two modes to create a sound null at one of the ports, resulting in complete transmission to the other port.

In this case, the three-port device that was fabricated functions as a circulator, in which an input signal on one port at the design frequency transmits all of its acoustic energy to its neighbor port in the direction of the mean flow, and none to its neighbor port opposite the flow. The resulting nonreciprocity is easily seen: An input signal on port 1 is transmitted fully to port 2, whereas the same input

signal on port 2 is fully transmitted to port 3 (not port 1, as would happen in a reciprocal device). A circulator like this can easily be converted into a two-port isolator with a matched termination on one port. The measured sample exhibits an impressive 30 dB of sound isolation in a device built from simple, off-the-shelf components.

A one-way device for sound and vibrations has broad implications. Unidirectional acoustic wave propagation has obvious uses in noise control, acoustic sensors, and manipulation of acoustic scattering. At smaller spatial scales, mechanical vibrations (called phonons in their quantum-mechanical form) are responsible for heat transport in solid materials as well. The work of Fleury *et al.* adds to the bank of ideas that can be applied to manipulating heat flow in a nonreciprocal

fashion (although still subject to the laws of thermodynamics) in what is called a thermal diode (7, 8). Challenges in device scaling and bandwidth control remain in applying the mean-flow-based concept demonstrated here to more specific scenarios, but that all-important first step toward general-purpose linear acoustic nonreciprocity has now been taken.

References

1. R. Fleury *et al.*, *Science* **343**, 516 (2014).
2. H. B. G. Casimir, *Rev. Mod. Phys.* **17**, 343 (1945).
3. A. A. Maznev *et al.*, *Wave Motion* **50**, 776 (2013).
4. D. Jalas *et al.*, *Nat. Photonics* **7**, 579 (2013).
5. K. G. Budden, *Radio Waves in the Ionosphere* (Cambridge Univ. Press, Cambridge, UK, 1961).
6. D. M. Pozar, *Microwave Engineering* (Wiley, Hoboken, NJ, ed. 4, 2012).
7. N. A. Roberts, D. G. Walker, *Int. J. Therm. Sci.* **50**, 648 (2011).
8. N. Li *et al.*, *Rev. Mod. Phys.* **84**, 1045 (2012).

10.1126/science.1249616

BOTANY

Pathogen Specialization

Gitta Coaker

Plants can be attacked by a vast range of pathogen classes, causing substantial agricultural losses. The *Phytophthora* (meaning “plant killer”) genus is a particularly destructive pathogen that causes root and stem base decay in a wide range of plants. *Phytophthora infestans*, which precipitated the Irish potato famine, originated in Central Mexico and is closely related to other *Phytophthora* species with distinct host ranges (1, 2). Pathogen effectors that are secreted during infection play a key role in disease biology, but effector-induced adaptation to new hosts is an understudied topic. On page 552 of this issue, Dong *et al.* investigate how *Phytophthora* effector proteins evolve the ability to specialize on new hosts (see the figure) (3).

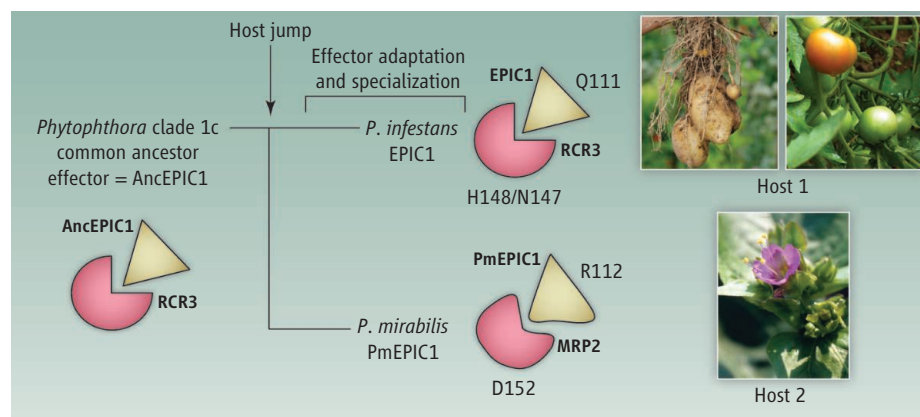
Phytophthora is a genus of oomycetes that exhibit filamentous growth on plants. Oomycetes share some phenotypes with fungi, but are phylogenetically related to photosynthetic brown algae and are thought to have initially emerged from marine environments. The *Phytophthora* genus comprises 10 main lineages designated as clades 1 to 10. Clade 1c, a subdivision of clade 1, includes *P. infestans* (infecting potato and tomato) and *P. mirabilis* (infecting 4 o'clock weeds), indicating that these species share a recent common ancestor

(2). Genome comparisons between *P. infestans* and *P. mirabilis* highlight alterations and patterns of selection in repetitive DNA containing rapidly evolving families of virulence genes (such as effectors) (4).

The 82 effectors undergoing positive selection between *P. infestans* and *P. mirabilis* are promising candidates shaping host specialization (4). Dong *et al.* focused their efforts on the EPIC1 effector, which is abundantly secreted during infection of tomato and inhibits extracellular papain-like proteases (including RCR3) that are involved in plant immune perception (5).

The ability to infect new hosts can drive the evolution and specialization of secreted pathogen proteins.

Dong *et al.* now report that the *P. mirabilis* *epiC1* ortholog (*PmepiC1*) shows signatures of positive selection, suggesting that this effector has evolved to function in *Mirabilis jalapa*, the 4 o'clock plant, following the split between *P. mirabilis* and *P. infestans*. Using activity-based profiling with a probe that targets papain proteases, the authors demonstrate that recombinant EPIC1 from *P. infestans* effectively inhibits tomato and wild potato RCR3 proteases, whereas PmEPIC1 does not. The authors identify two PmEPIC1 *M. jalapa* targets with homology to RCR3 (MRP1 and MRP2). Subsequent experi-



Route to specialization. A host jump within *Phytophthora* 1c led to the emergence of *P. mirabilis*, which can infect *M. jalapa*. Dong *et al.* show that effector specialization following the host jump is associated with the R112 mutation in PmEPIC1, enabling effective inhibition of the *M. jalapa* MRP2 protease. Polymorphic residues controlling specificity for the host and pathogen are highlighted. Adapted from fig. S18 in (3).

Department of Plant Pathology, University of California, Davis, Davis, CA 95616, USA. E-mail: gcoaker@ucdavis.edu

ments confirmed that MRP2 is an active protease and can be effectively inhibited only by PmEPIC1. Thus, EPIC1 effectors function more effectively on their respective hosts, supporting the hypothesis of effector specialization after a host jump.

To define the biochemical basis of EPIC1 host specialization, Dong *et al.* inferred the ancestral allele of *epiC1* using maximum likelihood methods. Ancestral EPIC1 had similar specificity as *P. infestans* EPIC1 for RCR3. Thus, the ability of PmEPIC1 to function more effectively on MRP2 was likely acquired after host jumping.

Surprisingly, both EPIC1 and PmEPIC1 can bind MRP2 using co-immunoprecipitation. Competition experiments show that binding likely occurs at the active site of MRP2 for both EPIC1 and PmEPIC1. How can two similar EPIC1 effectors exhibit different target specificity while still binding to both effective and ineffective targets? Analyses of variant amino acid residues superimposed on an existing structure of tarocystatin in complex with papain protease (6)

indicate that EPIC1 effectors have similar folds and likely bind proteases at three sites, two of which are polymorphic. A single amino acid polymorphism in PmEPIC1 and its corresponding protease, MRP2, determine specificity.

Future experiments are needed to determine whether PmEPIC1 provides a fitness advantage. If it does, then this would validate the importance of effector specialization for disease biology. These experiments are possible but likely to be difficult to interpret. Oomycete genomes contain large effector arsenals, with ~563 cell-entering effectors in *P. infestans* (7). Collectively, effectors are critical virulence factors, but each individual effector typically provides a minor fitness advantage for the pathogen (8). It is likely that numerous effectors together rather than individual effectors are crucial for fitness.

By exploring both evolutionary pressures and biochemical adaptation of EPIC1 and corresponding host proteases, Dong *et al.* reveal that selection for single amino acid polymorphisms can significantly affect effec-

tor specialization. These findings open an exciting new door to understanding the role effectors play in shaping pathogen adaptation. Conserved core effectors undergoing positive selection could be promising targets for disease control. Nature's ability to select for biochemical specialization has implications for engineering enzymes and their corresponding targets for enhanced specificity. Undoubtedly, many important secrets remain to be discovered.

References and Notes

1. N. J. Grünwald, W. G. Flier, *Annu. Rev. Phytopathol.* **43**, 171 (2005).
2. J. E. Blai *et al.*, *PLOS ONE* **7**, e37003 (2012).
3. S. Dong *et al.*, *Science* **343**, 552 (2014).
4. S. Raffaele, S. Kamoun, *Nat. Rev. Microbiol.* **10**, 417 (2012).
5. J. Song *et al.*, *Proc. Natl. Acad. Sci. U.S.A.* **106**, 1654 (2009).
6. M. H. Chu *et al.*, *Planta* **234**, 243 (2011).
7. B. J. Haas *et al.*, *Nature* **461**, 393 (2009).
8. G. Fabro *et al.*, *PLOS Pathog.* **7**, e1002348 (2011).

Acknowledgments: G. C. is funded by the NIH and NSF. I regret not being able to cite some work due to space limitations.

10.1126/science.1250171

GENETICS

A Unified Process for Neurological Disease

Andrew B. Singleton

The perennial promise of human disease genetics is the delivery of etiology-based therapies. This rests on the notion that identifying disease-causing mutations will provide a basis for determining the molecular networks that constitute the disease process—an understanding that is critical for the development of such therapies. On page 506 of this issue, Novarino *et al.* (1) perform what is perhaps the most complete genetic analysis of the neurological disorder hereditary spastic paraplegia (HSP), and deliver on part of this promise by creating an “HSPome,” a plausible network of proteins involved in this disease.

In many fields, the hard-won discoveries linking mutations to diseases are the foundation for investigations into molecular pathogenesis. In rare instances, mutation detection has provided immediate insight into the disease process. Usually, however, moving from gene to pathogenesis has been exceptionally

difficult. Functional and mechanistic work on the molecular etiology of disease remains one of the major challenges in modern biology; this is quite understandable given the inherent limitations of traditional reductionist functional work. There have been successes, however, and these have helped form the dominant theories of pathogenesis for many diseases, including Alzheimer's disease (2). An increasingly popular intermediate step between genetics and function is the use of pathways-based analysis. Such an approach attempts not only to produce a refined list of potential functional interactions to investigate at the bench, but also to provide a global snapshot of the landscape of a particular disease's etiology.

Novarino *et al.* have executed this approach with compelling results. The underlying strategy of their study involved the identification of disease-causing mutations using the power of small, inbred families. HSPs represent a class of inherited progressive neurodegenerative disorders that manifest with stiffness and contraction in

The discovery of mutations associated with disease pathogenesis does not have to rest solely on genetic evidence.

the lower limbs—a feature believed to be the result of corticospinal tract dysfunction. These diseases are extremely genetically heterogeneous. Novarino *et al.* examined the autosomal recessive form (AR-HSP), which was already linked to mutation of more than 20 genes (3). The authors expand this list by means of an iterative set of analyses on an initial set of 55 AR-HSP families. Using a straightforward genetic strategy of segregation, they show that disease in one-third of the families is linked to genes previously implicated in AR-HSP, but they also identify new candidate gene mutations in more than half of the remaining families. Additional mutations were identified in one-third of these new genes, providing substantive genetic support for causality. Functional analysis showed that candidate gene mutations cause a locomotor deficit in an animal model (zebrafish) of HSP, consistent with what has been described in previous HSP modeling efforts, thus further supporting pathogenicity.

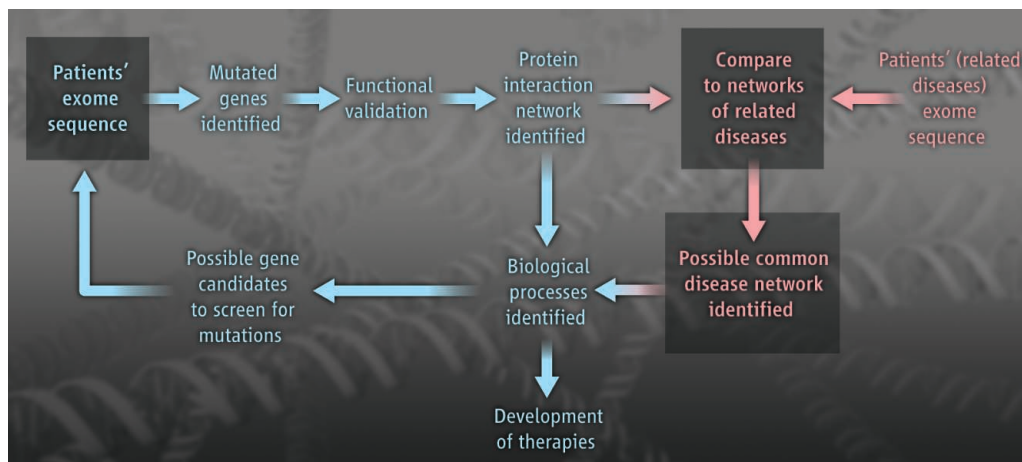
Beyond identifying new genes associated with HSP, Novarino *et al.* constructed a pro-

Laboratory of Neurogenetics, National Institute on Aging, Bethesda, MD 20892, USA. E-mail: singleton@mail.nih.gov

A global view of disease pathogenesis. The scheme illustrates an investigative approach that connects gene mutations in one disease through protein networks. This network can be used to nominate additional candidate genes and infer mechanistic overlap with other diseases. It may be possible to derive a core network that can guide the development of therapeutics.

teome network for HSP from information available in protein interaction databases. They observed that candidate genes and known HSP genes were more highly connected within this network than expected by chance. The authors then created a network of proteins encoded by known HSP genes, their nominated candidate genes, and proximal interactors, naming this expanded network the “HSPome.” This not only provides a global view of the processes and proteins underlying HSP, but also identifies genes as new candidates to bear disease-causing mutations. Novarino *et al.* validated this last point by returning to genetics. They identified likely pathogenic variants in three new genes mined from the HSPome, one of which was independently implicated in HSP (4).

Novarino *et al.* illustrate a subtle and perhaps necessary shift in genetics work. The burden of proving mutation pathogenicity has traditionally rested on the shoulders of genetics alone, relying on association of mutations with disease, segregation of mutations within families, and independent replication of results. Given the pace and nature of genetic mutation discovery, these proofs are no longer always tenable. Instead, genetics increasingly relies on functional and bioinformatics work. This change has been contentious among those who believe that genetic evidence should be the foundation of functional work. There is admittedly potential danger in using functional work to identify candidate genes—most important is the inevitable issue of circularity where studies are limited to what investigators believe to be biologically plausible genes and proteins. This runs the risk not only of incorrectly self-affirming hypotheses, but also of ignoring new and critically important pathways because they don’t fit into a current understanding of the disease process. This is not the case in the study by Novarino *et al.* The authors have been careful to question the significance of their observations, and they have in some instances the reassurance of independent replication. It is exactly this type of care that the field needs to take.



Novarino *et al.* also examined the relationship of the HSPome to genes implicated in other diseases, and found significant overlap with gene sets linked to Alzheimer’s disease, Parkinson’s disease, and amyotrophic lateral sclerosis. If this fascinating observation holds true, it raises a critical question: If varied neurodegenerative disorders are linked by a common pathway, what is the underlying cause of the distinct cellular vulnerability seen in these disorders? One might predict that identifying disease-linked protein networks is a key step toward understanding this phenomenon. In this regard, the type of work described by Novarino *et al.* shows not only the power of comprehensive genetic analysis in identify-

ing the pathogenic networks involved in that disease but also the potential of such work to inform outside of the disease in question (see the figure).

This study clearly adds another dimension to our understanding of HSP. With this knowledge, we can turn toward fulfilling the ultimate promise of genetics: translating this understanding into etiology-based therapies.

References

1. G. Novarino *et al.*, *Science* **343**, 506 (2014).
2. J. Hardy, D. J. Selkoe, *Science* **297**, 353 (2002).
3. J. K. Fink, *Acta Neuropathol.* **126**, 307 (2013).
4. E. C. Oates *et al.*, *Am. J. Hum. Genet.* **92**, 965 (2013).

10.1126/science.1250172

PLANT SCIENCE

Delayed Gratification—Waiting to Terminate Stem Cell Identity

Xiaoyu Zhang

A cell-cycle timing mechanism in *Arabidopsis* is critical for flower development through the staggered expression of two transcription factors.

In *Arabidopsis*, a small group of undifferentiated stem cells in the center of the floral meristem give rise to the flower. These stem cells produce daughter cells that differentiate into the four whorls of organs (sepals, petals, stamens, and carpels) underlying the basic flower structure. The different organ identities are determined by the complex interplay of floral organ identity genes, most of which are transcription factors. On page 505 in this issue, Sun *et al.* (1) describe an elegant timing mechanism that allows tran-

scriptional changes specified in the stem cells to be executed only in daughter cells and only after a predefined number of cell divisions.

The meristem identity gene *WUSCHEL* (*WUS*) is required to maintain the stem cell population in the floral meristem. The transcription factor *AGAMOUS* (*AG*) drives differentiation of the stem cells into stamens and carpels and is induced by both the floral activator *LEAFY* (*LFY*) and *WUS* in early flowerers (stage 3). At a later stage (stage 6), *AG* represses *WUS* in a negative feedback loop to convert the stem cells to organ primordia (2) (see the figure). Although *AG* induction by *WUS*, and *WUS* repression by *AG*, both

Department of Plant Biology, University of Georgia, Athens, GA 30602, USA. E-mail: xiaoyu@plantbio.uga.edu

CREDIT: C. BICKEL/SCIENCE

occur in the same stem cell population, the two events are temporally separated, with *WUS* being completely repressed ~2 days after *AG* induction. The precise timing of *WUS* repression allows the correct number of cells to be produced for reproductive organ formation. Too early and flowers have fewer stamens and no carpel; one day too late and flowers become partially indeterminate with additional and abnormal organs (3). Sun *et al.* now explain how the 2-day delay is achieved, through linking cycles of cell division to transcriptional derepression.

A key component in the *WUS-AG* pathway is the transcriptional repressor *KNUCKLES* (*KNU*), which represses *WUS* in stage 6 flowers (2). *KNU* is repressed by histone H3 lysine 27 trimethylation (H3K27me3), a repressive modification established by the Polycomb repressive complex 2 (PRC2). In

Sun *et al.* show that *AG* binding leads to the immediate eviction of FIE.

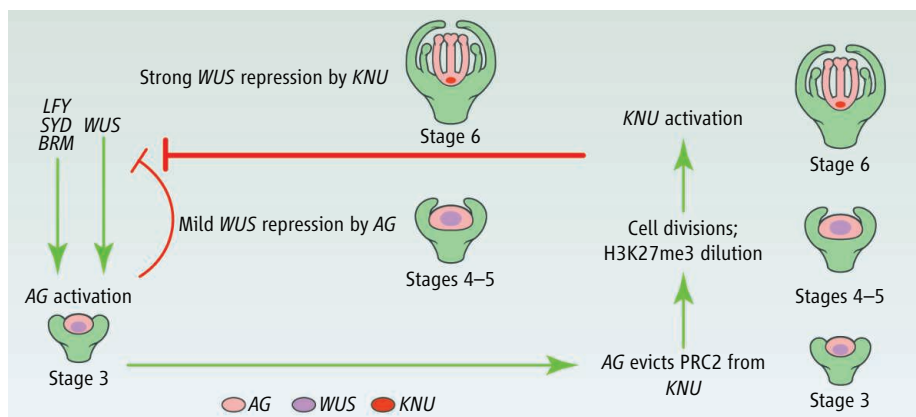
AG also directly binds to the *WUS* gene to repress *WUS* expression in an H3K27me3-dependent manner (4) (see the figure). The two independent modes of *WUS* repression by *AG* likely have different consequences. Whereas the direct repression of *WUS* by *AG* is relatively mild but immediate (in stage 4 to 6 flowers), the repression of *WUS* through *KNU* is more complete but temporally delayed (at stage 6) (4). How *AG* recruits PRC2 to repress some genes but evicts the same complex to activate other genes remains an open question.

Despite the importance of H3K27me3 in regulating plant development (targeting ~4000 to 5000 *Arabidopsis* genes) (5), relatively little is known about the mechanisms responsible for the establishment, maintenance

in plants characterized by continued growth and differentiation from small populations of stem cells.

The *KNU* PRE is located in the promoter, but FIE binding and H3K27me3 extend downstream to cover the entire transcribed region of *KNU*. The absolute requirement of the *KNU* PRE for FIE binding suggests that PRC2 is initially recruited to the PRE and then spreads unidirectionally to the remainder of *KNU*, establishing H3K27me3 along the way. In addition, the cell-cycle-dependent loss of H3K27me3 after FIE is displaced by *AG* indicates that PRC2 needs to be constantly recruited to the *KNU* PRE to maintain H3K27me3 after cell divisions. It is not yet clear whether additional factors facilitate the spreading and maintenance of H3K27me3.

The repressive H3K27me3 mark can be removed enzymically by the REF6 family of JmjC-domain-containing H3K27me3 demethylases (10). The repressive state associated with H3K27me3 can also be overcome by strong transcription activators and/or chromatin-remodeling factors, with H3K27me3-containing histones being subsequently lost during active transcription. For example, *AG* itself is repressed by H3K27me3 during vegetative growth, and LFY recruits the SWI2/SNF2 chromatin-remodeling adenosine triphosphatases *SPLAYED* (*SYD*) and *BRAHMA* (*BRM*) to *AG* for transcriptional activation (11). LFY binding sites frequently colocalize with PRE-like sequences, indicating that LFY binding may also displace PRC2 (12). Finally, when PRC2 is displaced from the chromatin, H3K27me3 can be gradually diluted by the incorporation of unmodified histones during chromatin replication. Sun *et al.* not only provide a clear example of this scenario, but also reveal its biological function in specifying delayed and cell-cycle-dependent transcriptional activation.



A timed transcription circuit makes flowers. A network of transcription factors act in *Arabidopsis* flower development to balance stem cell maintenance and cellular differentiation.

developing flowers, *AG* activates *KNU* by binding to its promoter, but *KNU* expression only becomes detectable ~2 days after the initial *AG* binding, resulting in a substantial decrease in *WUS* expression. The delay in *KNU* activation is likely caused by the gradual loss of the repressive H3K27me3 mark at the *KNU* gene (3).

Sun *et al.* observed that the ~2-day delay depends on cell-cycle progression, suggesting that the “timer” may be a “counter” that monitors the number of cell divisions. The authors hypothesized that *AG* binding interferes with the maintenance of H3K27me3 at *KNU*: Incorporation of unmodified H3 after roughly two rounds of cell divisions sufficiently dilutes the preexisting H3K27me3 to allow *KNU* expression. Indeed, a short region in the *KNU* promoter immediately adjacent to the *AG* binding site was found to be necessary and sufficient for recruiting a core component of the PRC2, FERTILIZATION-INDEPENDENT ENDOSPERM (FIE). Critically,

and removal of H3K27me3. In the fruit fly *Drosophila*, PRC2 is targeted to specific sites called Polycomb response elements (PREs) by the Pho-repressive complex (PhoRC) (6). Genome-wide analysis of FIE binding sites in *Arabidopsis* identified several motifs, including a GA-repeat motif frequently found in *Drosophila* PREs (7). However, because plants do not have Rho homologs, whether these motifs are involved in targeting PRC2 is not fully understood. The FIE binding site at *KNU* adds to a short but growing list of functional PREs in plants (8). Notably, the *KNU* PRE also contains GA-repeats, suggesting that similar motifs found in FIE binding sites may indeed function as PREs. However, several different motifs are present at distinct subsets of FIE binding sites (7, 9), suggesting that PRC2 recruitment in *Arabidopsis* is likely carried out by many different factors (8). Such a “recruiting by committee” approach may provide more versatility during the predominantly postembryonic devel-

References

1. B. Sun *et al.*, *Science* **343**, 1248559 (2014); 10.1126/science.1248559.
2. J. U. Lohmann *et al.*, *Cell* **105**, 793 (2001).
3. B. Sun, Y. Xu, K. H. Ng, T. Ito, *Genes Dev.* **23**, 1791 (2009).
4. X. Liu *et al.*, *Plant Cell* **23**, 3654 (2011).
5. X. Zhang *et al.*, *PLOS Biol.* **5**, e129 (2007).
6. J. Müller, J. A. Kassiss, *Curr. Opin. Genet. Dev.* **16**, 476 (2006).
7. W. Deng *et al.*, *BMC Genomics* **14**, 593 (2013).
8. C. He, H. Huang, L. Xu, *Front. Plant Sci.* **4**, 454 (2013).
9. N. Berger, B. Dubreucq, F. Roudier, C. Dubos, L. Lepiniec, *Plant Cell* **23**, 4065 (2011).
10. F. Lu, X. Cui, S. Zhang, T. Jenuwein, X. Cao, *Nat. Genet.* **43**, 715 (2011).
11. M. F. Wu *et al.*, *Proc. Natl. Acad. Sci. U.S.A.* **109**, 3576 (2012).
12. C. M. Winter *et al.*, *Dev. Cell* **20**, 430 (2011).

10.1126/science.1249343



ASSOCIATION AFFAIRS

Gerald Fink: Global Challenges Require Sustained Support

Gerald Fink has learned to love a good experiment. And while the geneticist doesn't expect everyone to share his passion for elegant experimental designs or effective controls, he believes the general public does respect and depend on the solutions that science provides.

"Most Americans are very practical people, and they are also kind of amateur scien-

people, for solutions to these problems, and the policy-makers. AAAS is the voice of American science to the world, and it's not just scientists who listen to this voice."

Climate warming, communicable diseases, and food and energy demand are among the enormous challenges facing the global community, he noted. "Everyone talks about these, but the solutions to these problems demand an investment in science. And I think in the 21st century, we need to listen to scientists and support them to attack these very difficult problems."

There "probably isn't a 'eureka experiment' that can solve them," he added, "but they require dedication, a long-term dedication, to their solution."

This long-term, sustained support of science is one that Fink hopes AAAS can continue to foster in Washington, D.C., with programs such as the R&D Budget and Policy Program and the AAAS Science & Technology Policy Fellowships. But he also cautioned that the recent battles over sequestration have had "a very damaging effect on science, particularly on young scientists."

"When I was a student, I didn't worry that I wouldn't be able to get a grant or have my education supported. The government was forthcoming at every point," he said. "I don't know that we can look forward to that commitment, and more importantly, without it our young scientists cannot be optimistic about

a career in science. The challenge is to reinvigorate our economy by investing in education and science so that the best minds of the next generation will have the support of their nation."

Fink turned to science in high school after reading Paul de Kruif's *Microbe Hunters*, about pioneering scientists like Louis Pasteur and Walter Reed, who built the germ theory of disease and developed the first vaccinations. "It was so exciting to me," he recalled, "but I went to a public high school that was not particularly good, and most people were interested in sports instead." So he and his best friend—now a mathematician—thought mostly about winning their next basketball game.

The successful launching of the Sputnik satellite by the Soviet Union in 1957 changed everything, however. Like many scientists his age, Fink remembers Sputnik as the impetus for an entirely new and exciting emphasis on science education. Spurred by this challenge, engineers and scientists began visiting schools to teach classes and to encourage students to choose a career in research.

Inspired by these examples, Fink went on to receive his Ph.D. in genetics from Yale University. His 1977 discovery of a technique to introduce DNA into living yeast cells paved the way for genetic engineering in this organism and others and helped establish yeast as "factories" for producing new vaccines and other medicines. Now, as a professor of biology and a founding member of the Whitehead Institute at MIT, Fink has focused his research on the molecular underpinnings of fungal infections.

His work with infectious agents also led to a stint as chair of the National Academy of Sciences Committee on Research Standards and Practices to Prevent the Destructive Application of Biotechnology, from 2002 to 2003. The committee's 2004 report has yielded a "very good public discourse" on the potential for misuse of scientific findings, one that has guided policies at *Science* and other research journals, Fink said.

Fink will succeed Phillip A. Sharp as president at the close of the 180th AAAS Annual Meeting in Chicago on 18 February. Sharp will become chairman of the AAAS Board of Directors.

—Carla Schaffer, Linda Hosler, and Becky Ham



tists," Fink said in a recent interview. "They want these problems like energy and global warming solved and know that they can only be solved by scientists."

As the incoming AAAS president, Fink believes that the organization is a vital "connection between the wishes of the American

ASSOCIATION AFFAIRS

Call for Nomination of 2014 Fellows

AAAS Fellows who are current members of the Association are invited to nominate members for election as Fellows. A member whose efforts on behalf of the advancement of science or its applications are scientifically or socially distinguished, and who has been a continuous member for the 4-year period leading up to the year of nomination, may by virtue of such

meritorious contribution be elected a Fellow by the AAAS Council.

A nomination must be sponsored by three previously elected AAAS Fellows (who are current in their membership), two of whom must have no affiliation with the nominee's institution.

Nominations undergo review by the steering groups of the Association's sections (the chair, chair-elect, retiring chair, secretary, and four members-at-large of each section). Each steering group reviews only those nominations designated for its section.

Names of Fellow nominees who are approved by the steering groups are presented to the Council in the fall for election.

Nominations with complete documentation must be received by 16 April 2014. Nominations received after that date or nominations that are incomplete as of the deadline will not move forward.

Complete instructions and a copy of the nomination form are available at www.aaas.org/page/aaas-fellows. Questions may be directed to fellownomination@aaas.org.

Results of the 2013 Election of AAAS Officers

Following are the results of the 2013 election. Terms begin on 18 February 2014.

General Election

President-Elect: Geraldine (Geri) Richmond, Univ. of Oregon

Board of Directors: Carlos J. Bustamante, Univ. of California, Berkeley; Laura H. Greene, Univ. of Illinois at Urbana-Champaign

Committee on Nominations: Sylvia T. Ceyer, Massachusetts Institute of Technology; Susan M. Fitzpatrick, James S. McDonnell Foundation; Alice Petry Gast, Lehigh Univ.; Susan Gottesman, National Cancer Institute/NIH

Section Elections

Agriculture, Food, and Renewable Resources

Chair Elect: Michael F. Thomashow, Michigan State Univ.

Member-at-Large of the Section Committee: Elizabeth E. Hood, Arkansas State Univ.

Electorate Nominating Committee: Sheila McCormick, USDA-ARS; Esther van der Knaap, Ohio State Univ.

Anthropology

Chair Elect: Robert W. Sussman, Washington Univ. in St. Louis

Member-at-Large of the Section Committee: Margaret C. Nelson, Arizona State Univ.

Electorate Nominating Committee: Patricia M. Lambert, Utah State Univ.; Lisa J. Lucero, Univ. of Illinois at Urbana-Champaign

Astronomy

Chair Elect: Stefi Alison Baum, Rochester Institute of Technology

Member-at-Large of the Section Committee: Jean L. Turner, Univ. of California, Los Angeles

Electorate Nominating Committee: Neil Gehrels, NASA/Univ. of Maryland; Michael Werner, Jet Propulsion Laboratory/Caltech

Atmospheric and Hydrospheric Sciences

Chair Elect: Michael J. Prather, Univ. of California, Irvine

Member-at-Large of the Section Committee: Soroosh Sorooshian, Univ. of California, Irvine

Electorate Nominating Committee: Anthony J. Broccoli, Rutgers Univ.; James A. Yoder, Woods Hole Oceanographic Institution

Council Delegate: David Halpern, Jet Propulsion Laboratory

Biological Sciences

Chair Elect: Steve Henikoff, Fred Hutchinson Cancer Research Center

Member-at-Large of the Section Committee: Susan R. Wentz, Vanderbilt Univ. School of Medicine

Electorate Nominating Committee: Vicki L. Chandler, Gordon and Betty Moore Foundation; Claire M. Fraser, Univ. of Maryland School of Medicine

Chemistry

Chair Elect: Bruce E. Bursten, Univ. of Tennessee, Knoxville

Member-at-Large of the Section Committee: Mark Thompson, Univ. of Southern California

Electorate Nominating Committee: Katrina M. Miranda, Univ. of Arizona; Galen D. Stucky, Univ. of California, Santa Barbara

Dentistry and Oral Health Sciences

Chair Elect: Mina Mina, Univ. of Connecticut Health Center

Member-at-Large of the Section Committee: Van P. Thompson, King's College London Dental Institute (UK)

Electorate Nominating Committee: Pamela K. Den Besten, UC San Francisco School of Dentistry; Mark C. Herzberg, Univ. of Minnesota School of Dentistry

Council Delegate: Linda C. Niessen, Nova Southeastern Univ.

Education

Chair Elect: Jay B. Labov, National Academy of Sciences/National Research Council

Member-at-Large of the Section Committee: Tamara Shapiro Ledley, TERC

Electorate Nominating Committee: Margaret R. Caldwell, Center for Ocean Solutions/Stanford Law School; Kristin P. Jenkins, Univ. of Wisconsin-Madison/BioQUEST Curriculum Consortium

Council Delegate: Elizabeth K. Stage, UC Berkeley Lawrence Hall of Science

Engineering

Chair Elect: W. Kent Fuchs, Cornell Univ.

Member-at-Large of the Section Committee: Nicholas L. Abbott, Univ. of Wisconsin-Madison

Electorate Nominating Committee: Linda Broadbelt, Northwestern Univ.; David B. Williams, Ohio State Univ.

continued >

General Interest in Science and Engineering

Chair Elect: Dominique Brossard, Univ. of Wisconsin-Madison

Member-at-Large of the Section Committee: Carol Lynn Alpert, Museum of Science, Boston

Electorate Nominating Committee: Robert Lee Hotz, Wall Street Journal; Lisa M. Van Pay, George Washington Univ.

Council Delegate: Sharon M. Friedman, Lehigh Univ.

Geology and Geography

Chair Elect: Maureen E. Raymo, Lamont-Doherty Earth Observatory

Member-at-Large of the Section Committee: Dennis V. Kent, Rutgers Univ.

Electorate Nominating Committee: Jennifer R. Marlon, Yale Univ.; Konrad (Koni) Steffen, Swiss Federal Research Institute/ETH Zürich (Switzerland)

History and Philosophy of Science

Chair Elect: Elliott Sober, Univ. of Wisconsin-Madison

Member-at-Large of the Section Committee: Roberta L. Millstein, Univ. of California, Davis

Electorate Nominating Committee: Heather Douglas, Univ. of Waterloo (Canada); Kristine C. Harper, Florida State Univ.

Industrial Science and Technology

Chair Elect: Sharon C. Glotzer, Univ. of Michigan

Member-at-Large of the Section Committee: Harold H. Kung, Northwestern Univ.

Electorate Nominating Committee: Isaac Cann, Univ. of Illinois at Urbana-Champaign; Michael Tsapatsis, Univ. of Minnesota

Information, Computing, and Communication

Chair Elect: Carla P. Gomes, Cornell Univ.

Member-at-Large of the Section Committee: Justine Cassell, Carnegie Mellon Univ.

Electorate Nominating Committee: Bonnie C. Carroll, Information International Associates (IIa)/CENDI; Susan Landau, Google

Council Delegate: Karen R. Sollins, Massachusetts Institute of Technology

Linguistics and Language Science

Chair Elect: Keren Rice, Univ. of Toronto (Canada)

Member-at-Large of the Section Committee: David Poeppel, New York Univ.

Electorate Nominating Committee: Cecile McKee, Univ. of Arizona; Shari R. Speer, Ohio State Univ.

Council Delegate: Joan Maling, National Science Foundation

Mathematics

Chair Elect: Martin Golubitsky, Ohio State Univ.

Member-at-Large of the Section Committee: Irene Fonseca, Carnegie Mellon Univ.

Electorate Nominating Committee: Harvey Thomas Banks, North Carolina State Univ.; James (Mac) Hyman, Tulane Univ.

Medical Sciences

Chair Elect: Pamela B. Davis, Case Western Reserve Univ. School of Medicine

Member-at-Large of the Section Committee: David M. Sabatini, Massachusetts Institute of Technology

Electorate Nominating Committee: Lisa M. Coussens, Oregon Health & Science Univ.; Jules L. Dienstag, Massachusetts General Hospital/Harvard Medical School

Neuroscience

Chair Elect: Marie-Françoise Chesselet, Univ. of California, Los Angeles

Member-at-Large of the Section Committee: Allan Basbaum, Univ. of California, San Francisco

Electorate Nominating Committee: Diane O'Dowd, Univ. of California, Irvine; Phyllis M. Wise, Univ. of Illinois at Urbana-Champaign

Pharmaceutical Sciences

Chair Elect: Jeanette C. Roberts, Univ. of Wisconsin School of Pharmacy

Member-at-Large of the Section Committee: Donald P. McDonnell, Duke Univ. School of Medicine

Electorate Nominating Committee: Barbara S. Beckman, Tulane Univ. School of Medicine; Melanie S. Joy, Univ. of Colorado School of Medicine and School of Pharmacy

Council Delegate: Barbara N. Timmermann, Univ. of Kansas

Physics

Chair Elect: Eva Andrei, Rutgers Univ.

Member-at-Large of the Section Committee: Lene Vestergaard Hau, Harvard Univ.

Electorate Nominating Committee: Marcela Carena, Univ. of Chicago/Fermilab; John M. Tranquada, Brookhaven National Laboratory

Psychology

Chair Elect: Susan Goldin-Meadow, Univ. of Chicago

Member-at-Large of the Section Committee: Barbara A. (Bobbie) Spellman, Univ. of Virginia/Univ. of Virginia School of Law

Electorate Nominating Committee: Charles A. Nelson III, Harvard Medical School/Boston Children's Hospital; Elizabeth Phelps, New York Univ.

Social, Economic, and Political Sciences

Chair Elect: Maryann P. Feldman, Univ. of North Carolina at Chapel Hill

Member-at-Large of the Section Committee: Paula Stephan, Georgia State Univ.

Electorate Nominating Committee: Stephanie Shipp, Virginia Tech; Howard J. Silver, Consortium of Social Science Associations

Societal Impacts of Science and Engineering

Chair Elect: Francesca T. Grifo, Union of Concerned Scientists

Member-at-Large of the Section Committee: Gerald L. Epstein, U.S. Department of Homeland Security

Electorate Nominating Committee: Maryann P. Feldman, Univ. of North Carolina at Chapel Hill; Tobin L. Smith, Association of American Universities

Council Delegate: Susan Sauer Sloan, National Academies

Statistics

Chair Elect: Sallie Ann Keller, Virginia Tech

Member-at-Large of the Section Committee: Karen Kafadar, Indiana Univ.

Electorate Nominating Committee: Michael Boehnke, Univ. of Michigan; M. Elizabeth (Betz) Halloran, Univ. of Washington/Fred Hutchinson Cancer Research Center

Council Delegate: Linda J. Young, Univ. of Florida/USDA-NASS

Development-Inspired Reprogramming of the Mammalian Central Nervous System

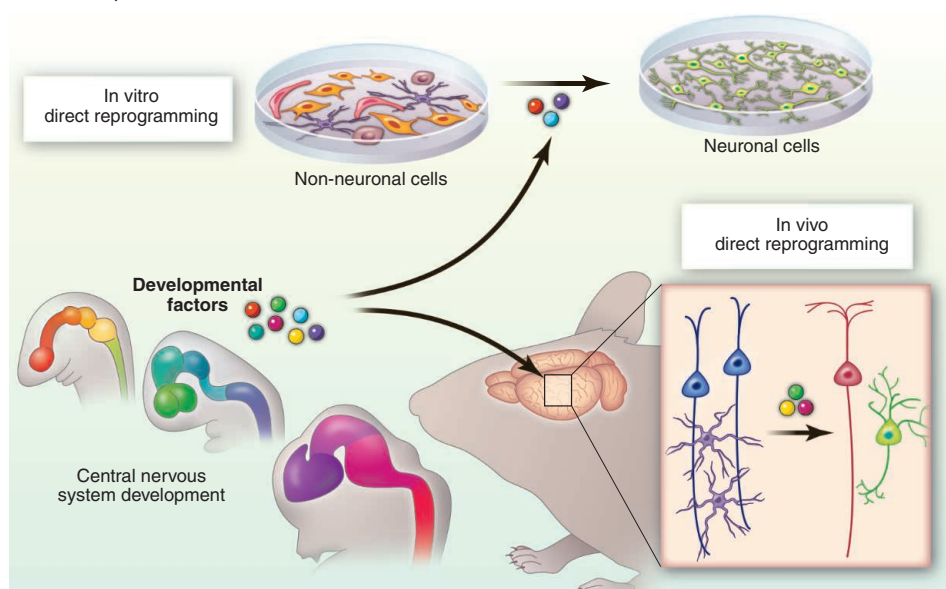
Ryoji Amamoto and Paola Arlotta*

Background: Differentiated cells can be reprogrammed to switch identities from one cell type to another under the direction of powerful transcription factors. In the mammalian central nervous system, this approach has been used experimentally to generate new categories of neuronal cells. The protocols are inspired by what we have learned from normal development, but the applications lie outside of normal embryogenesis. The research is changing how scientists think about regeneration of lost neurons and modeling of neuronal function in the central nervous system. The approaches also allow for new ways to study human neuronal development, a process that cannot be studied *in vivo*.

Advances: Neurons are a highly specialized cell type, with their ability to transmit electrical signals. Beyond that, though, neurons also specialize into an astonishing diversity of classes. Although reprogramming with known transcription factors is a comparatively blunt tool, researchers have used knowledge of normal neuronal development to identify suites of factors that can convert mouse or human non-neuronal cells into induced neuronal cells showing class-specific features. These protocols have provided a renewable source of neuronal cells for high-throughput studies, which is particularly useful when source tissue is rare or unavailable. One exciting application of lineage reprogramming has been the generation of new neurons *in situ* by the direct conversion of other cell types already resident within the brain. Astrocytes have been converted into neurons *in vivo*. Even neurons have been changed from one subtype to another in young animals, indicating that postmitotic neurons may not be as immutable as once thought. These provocative results may foster the development of strategies for neuronal replacement that rely on “code-switching” of neuronal identity on the spot.

Outlook: Direct lineage reprogramming is a nascent but promising field. Although both unspecialized and specialized neuronal cells have already been generated by these methods, we still need more refined understanding of how reprogramming works, how the cellular context constrains reprogramming routes, and what synergistic effects arise with various reprogramming factors. Better-defined criteria are needed to classify neurons obtained by reprogramming and to determine how they differ from their endogenous counterparts. Functional analyses are also necessary to clarify when a new neuron achieves the needed function, even if its other features do not match endogenous neurons. The challenge requires collaborative expertise in stem cell biology, embryology, and fundamental neuroscience. Future ability to reprogram postmitotic neurons in the adult brain will be important for the growth of this field and likely influence the way we think about neuronal stability, regeneration, and function.

Development-inspired signals directly reprogram non-neuronal cells into induced neuronal cells. Pools of transcription factors initially selected based on functional roles during developmental neurogenesis have been reduced to “modules” able to promote the conversion of differentiated cells into neuronal cells. Non-neuronal cells—including astrocytes, fibroblasts, pericytes, and hepatocytes—have been converted into neuronal cells. Young postmitotic neurons and astrocytes have been reprogrammed from one class into another from within the brain.



READ THE FULL ARTICLE ONLINE

<http://dx.doi.org/10.1126/science.1239882>



Cite this article as R. Amamoto and P. Arlotta, *Science* **343**, 1239882 (2014). DOI: 10.1126/science.1239882

ARTICLE OUTLINE

Generation of Development-Inspired Neurons

Potency of Developmental Transcription Factor Modules to Generate Neurons

Inducing Neuronal Diversity

Challenges of Generating Neuronal Diversity

In Vivo Neuronal Reprogramming

Looking into the Future of Induced Neuronal Cells

ADDITIONAL RESOURCES

T. Vierbuchen, Direct conversion of fibroblasts to functional neurons by defined factors. *Nature* **463**, 1035–1041 (2010). DOI:10.1038/nature08797 Medline

C. Rouaux, P. Arlotta, Direct lineage reprogramming of post-mitotic callosal neurons into corticofugal neurons *in vivo*. *Nat. Cell Biol.* **15**, 214–221 (2013). DOI:10.1038/ncb2660 Medline

N. Heins, Glial cells generate neurons: the role of the transcription factor Pax6. *Nat. Neurosci.* **5**, 308–315 (2002). DOI:10.1038/nn828 Medline

Department of Stem Cell and Regenerative Biology, Sherman Fairchild Building 7 Divinity Avenue, Harvard University, Cambridge, MA 02138, USA.

*Corresponding author. E-mail: paola_arlotta@harvard.edu

Development-Inspired Reprogramming of the Mammalian Central Nervous System

Ryoji Amamoto and Paola Arlotta*

In 2012, John Gurdon and Shinya Yamanaka shared the Nobel Prize for the demonstration that the identity of differentiated cells is not irreversibly determined but can be changed back to a pluripotent state under appropriate instructive signals. The principle that differentiated cells can revert to an embryonic state and even be converted directly from one cell type into another not only turns fundamental principles of development on their heads but also has profound implications for regenerative medicine. Replacement of diseased tissue with newly reprogrammed cells and modeling of human disease are concrete opportunities. Here, we focus on the central nervous system to consider whether and how reprogramming of cell identity may affect regeneration and modeling of a system historically considered immutable and hardwired.

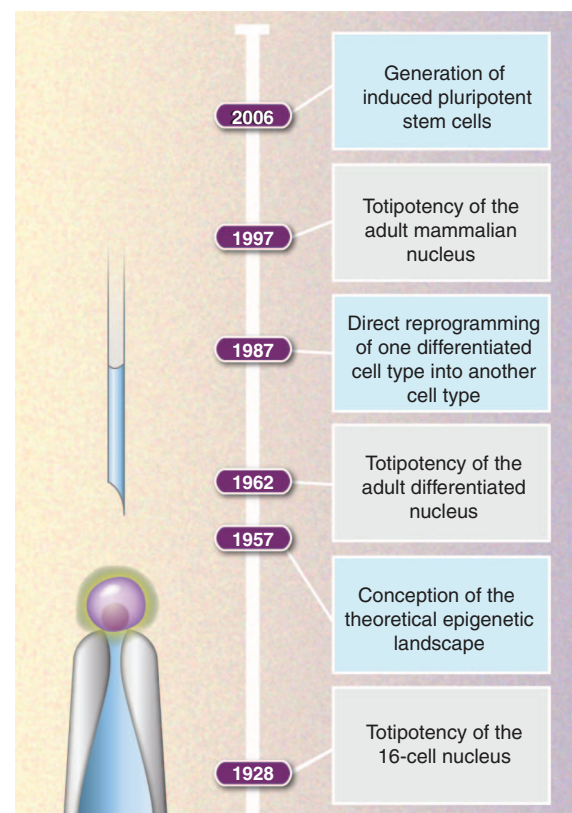
In the earliest stages of embryonic development, a handful of uncommitted cells possess the potential to differentiate into any cell type if given the right cues. During the first half of the 20th century, a major question in developmental biology was whether permanent genomic changes accompany differentiation and are in place to enable such pluripotent cells to attain and maintain terminal, cell-type-specific characteristics (1). In 1962, Gurdon first published the results of seminal experiments that challenged the commonly held belief that differentiation was unidirectional and irreversible (2, 3). He used somatic cell nuclear transfer, a technique developed a decade earlier by Briggs and King (4), to transplant the nucleus of a differentiated tadpole intestinal cell into an irradiated egg and showed that normal adult frogs could develop from these eggs. This groundbreaking work provided the first proof-of-principle demonstration that it is indeed possible to reprogram differentiated cells back to pluripotency. More recently, similar conclusions were extended to mammalian cells (5).

These experiments indicate that barriers that lock these cells into their differentiated state do not involve permanent genomic changes and that there are factors in the egg's cytoplasm that enable fully differentiated cells to "reverse development" and regain pluripotency. One set of such factors was revealed when Yamanaka's group successfully converted fibroblasts into pluripotent stem cells with a cocktail of transcription factors. The resulting cells were thereby named induced pluripotent stem cells (iPSCs) (6). Along with Gurdon, Yamanaka received the Nobel Prize for this work, and these findings, more than 40 years apart, contributed to establishing that nuclear

reprogramming is possible across a spectrum of organisms, including mammals [see (7) for an in-depth review on iPSCs and mechanisms of induced pluripotency] (Fig. 1).

Waddington famously likened the process of cellular differentiation and its associated epigenetic changes during development to a marble traveling along a downward slope and ending up in one of many valleys surrounded by impassable hills (8). Reverting differentiated cells back

Fig. 1. Historical perspective on nuclear reprogramming. Selected milestone findings from experiments in amphibians first demonstrated that the nucleus of cells at the 16-cell stage (63) and differentiated adult cells (2) are plastic and capable of generating full organisms. Waddington is credited for theoretically conceiving the epigenetic landscape (8). More recent evidence indicates that differentiated mammalian cells are equally able to reprogram to either a pluripotent state (6, 64) or to a new differentiated cell state (65).



to pluripotency through nuclear reprogramming is comparable to forcibly pushing a marble from a valley back to the starting point, also known as the developmental "ground state." However, it has become evident that it is also possible to push the marble from valley to valley in a process that turns one differentiated cell type directly into another without transitioning through a pluripotent cell state. This process has been termed transdifferentiation or direct lineage reprogramming, and various cell types have been directly reprogrammed to acquire a new differentiated identity, across organ systems and in different species (9). Direct lineage reprogramming has several attractive features, including low likelihood of tumor formation and increased speed and efficiency of conversion if starting from a related cell type (10). Most notably, this approach carries great potential for applicability in vivo, a key advantage when aiming to rebuild cells of a tissue as complex as the central nervous system. Here, we examine direct lineage reprogramming into neurons and discuss the developmental programs that facilitate conversion of cell identity in the central nervous system.

Generation of Development-Inspired Neurons

In *The Greatest Show on Earth*, Dawkins likened embryology to a concerted, graceful flight murmuration of starling birds, each individual starling in the flock following its own local rules, with no overall goal or blueprint for what the flock

Department of Stem Cell and Regenerative Biology, Sherman Fairchild Building, 7 Divinity Avenue, Harvard University, Cambridge, MA 02138, USA.

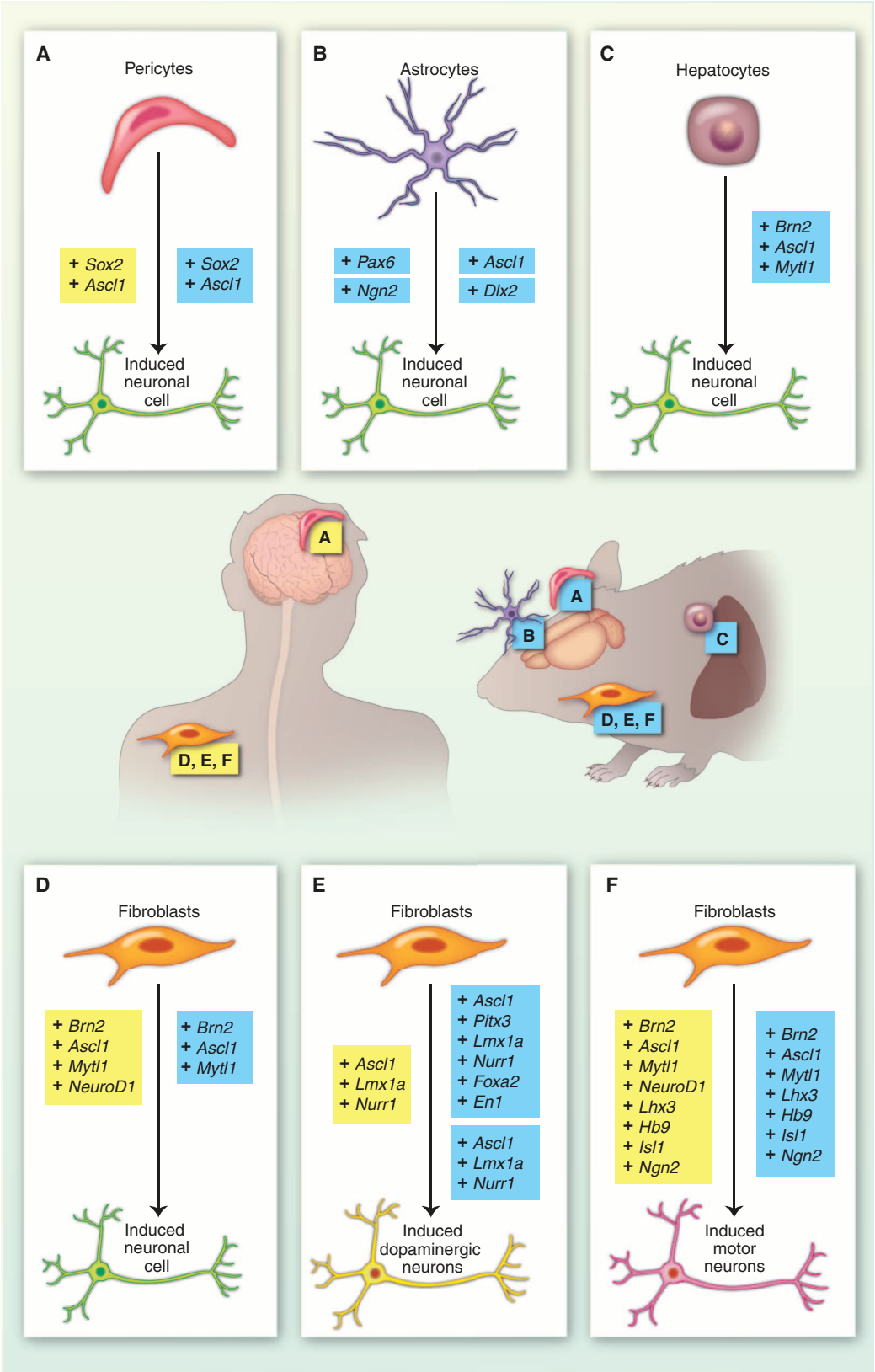
*Corresponding author. E-mail: paola_arlotta@harvard.edu

should ultimately resemble (11). Like starlings in a flock, during development, cells interact according to local guidance cues that converge on the activation of intrinsic programs and ultimately allow

for a collection of low-level unspecified units to self-assemble into a high-level configuration. Development is a bottom-up process that requires highly orchestrated and complex signaling mech-

anisms to produce a whole tissue and organism. Several studies have highlighted the similarities in self-organizing properties between organogenesis in embryos and generation of complex tissues

Fig. 2. Direct reprogramming of various cell types into induced neuronal cells in vitro. (A) Cultured pericytes (20), (B) astrocytes (15–18), (C) hepatocytes (19), and (D) fibroblasts (22, 23) are reprogrammed into induced neurons by defined factors. (E) Fibroblasts are reprogrammed into iDA neurons (38, 39) and (F) iMNs (34). Selected methods for the direct conversion into these neuronal subtypes are illustrated. Blue box, mouse reprogramming factors; yellow box, human reprogramming factors.



from pluripotent stem cells in a dish. In the nervous system, investigators have demonstrated that a three-dimensional (3D) culture of pluripotent stem cells in defined differentiation media could induce self-directed organization of complex tissues (“organoids”), which developed into structures highly similar to the optic cup (12, 13) and the cerebral cortex (14). Such an approach may become a useful strategy to generate the complexity of neural tissue beyond individual neurons.

Developmental studies have also identified master transcription factors that alone are able to instruct signature features of neuronal classes as they develop in the central nervous system. This has fueled top-down experiments in which researchers dictate the use of a handful of master regulators to generate specific neurons from other types of cells. Scientists are venturing into daring territories where neuronal cells in their own brand-new category are generated outside the context of embryogenesis following development-inspired protocols. For the first time, protocols to generate predefined neuronal classes from human embryonic stem cells (ESCs), fibroblasts, and other cell types are rapidly expanding, and this progress is likely to have a major impact not only in the clinics but also on our understanding of human

neural development, a process that cannot be studied *in vivo*.

Potency of Developmental Transcription Factor Modules to Generate Neurons

The idea of direct lineage reprogramming with transcription factors is not new, and over the years, overexpression of key transcription factors has been used to successfully convert the identity of various cell types, both *in vitro* and *in vivo* (9). One of the first indications that intrinsic modulation of transcription factors may be sufficient to generate neurons from non-neuronal cells came from experiments in which *Pax6* was overexpressed in young glial cells isolated from the early postnatal brain (15). These results are in line with the known developmental role of *Pax6* in the cerebral cortex, where its loss results in reduced numbers of neurons generated from radial glia cells (15). Subsequent studies have demonstrated that other neurogenic factors, namely *Ngn2*, *Ascl1*, and *Dlx2*, can also reprogram early-postnatal astrocytes into neurons *in vitro* (16–18). Neurons have been subsequently produced from many differentiated cell types, including hepatocytes (19), pericytes (20), adult astrocytes (21) and, most often, fibroblasts (22) (Fig. 2).

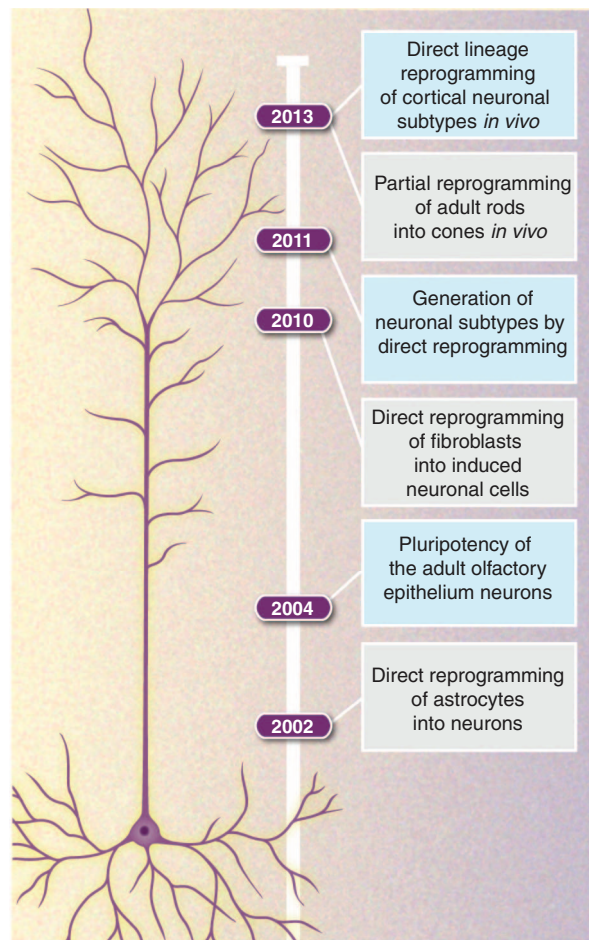
Fibroblasts have been extensively used for reprogramming experiments. In a first ground-

breaking study, a module of three factors—*Brn2*, *Ascl1*, and *Myt1l*—collectively known as the BAM factors, has been used successfully to reprogram mouse embryonic fibroblasts (MEFs) and tail-tip fibroblasts into induced neuronal cells (iN cells), albeit at a low efficiency (<20%) (22). iN cells generated by these methods display neuronal morphology and gene expression, as well as functional electrophysiological properties. Integration of the BAM module with NeuroD1 extended this reprogramming capacity to human fibroblasts (23). Each of the BAM factors has demonstrated functions in neuronal development. *Ascl1* in particular is necessary for neuronal differentiation in the ventral telencephalon, neurogenesis in the olfactory epithelium, and development of the sympathetic ganglia (24). In line with such a powerful developmental role, *Ascl1* has also been shown to be the primary driver, among the BAM factors, of the MEFs to iN cell conversion (25). Notably, the presence of a specific trivalent chromatin signature at *Ascl1* binding sites on the genome appears to alone predict the capability of different cell types to reprogram into iN cells (25). How these mechanisms relate to *Ascl1* function during normal development is not known; however, it is interesting that *Ascl1* DNA binding sites in MEFs and ESC-derived neural progenitor cells largely overlap. This data suggests that *Ascl1* may instruct neuronal reprogramming of MEFs by binding to the same genomic loci that it occupies in neural progenitor cells during development, which in turn would make this reprogramming protocol a useful platform to explore principles of developmental neurogenesis.

Fibroblast-to-neuron conversion has enabled subsequent studies aimed at improving the efficiency and precision by which iN cells are generated. A long road lies ahead; however, it seems that manipulation of transcription factors may be combined with extrinsic, development-inspired cues to enhance direct reprogramming. Overexpression of *Ascl1* and *Ngn2* or *Ngn2* alone was combined with small-molecule inhibitors of pathways normally repressed during developmental neurogenesis to generate iN cells at a high efficiency (26, 27). The mechanisms by which patterning signals modify the fate of a differentiated cell remain unexplained. During development, these signals act at early stages of neural induction on progenitors that are in a plastic epigenetic state. Therefore, it is plausible that *Ascl1* and *Ngn2* might synergistically facilitate the process of direct reprogramming of differentiated cells by inducing chromatin remodeling. Such a role in chromatin remodeling by master regulators might result in the establishment of a plastic cellular environment in fibroblasts, which in turn makes them sensitive to extracellular patterning signals. In line with this concept, it was shown that *Pax6* directly interacts with the chromatin remodeler Brg1-containing BAF complex to regulate a transcriptional cross-regulatory network that can reprogram glia into neurons (28). Interestingly, ectopic expression of brain-enriched microRNAs that promote the

Fig. 3. Historical perspective on neuronal reprogramming and reprogramming into neurons.

Selected milestone experiments that collectively supported the view that neurons are amenable to be reprogrammed and that non-neuronal cell types can be reprogrammed into neurons. Neurons could be generated from non-neuronal cells *in vitro* (15), and successive studies have shown that lineage-distant fibroblasts could be used as the starting cells for direct reprogramming into generic neurons (22) and specific neuronal subtypes (34, 38). Somatic cell nuclear transfer experiments have determined that adult neurons can undergo nuclear reprogramming (51, 52). Studies have induced neuronal class switch *in vivo* (58–60), suggesting that some neurons can undergo lineage reprogramming, although this capacity drastically decreases with neuronal age.



assembly of neuron-specific BAF complexes has successfully converted fibroblasts into neurons, indicating that active alteration of the epigenetic landscape of non-neuronal cells can be sufficient to generate neuron-like cells (29).

Inducing Neuronal Diversity

The human brain consists of ~100 billion neurons, which are grouped in a large number of neuronal classes (30). Classification of neuronal diversity in the mammalian brain is far from complete, but it is clear that defined differences exist among different classes of neurons and that susceptibility to neurological conditions is strongly neuronal class-specific. Therefore, generation of specific neuronal subtypes for the purpose of cell replacement therapy or in vitro disease modeling becomes important.

Progress has been made to generate a small number of neuronal classes by direct reprogramming. These classes were typically chosen based on contribution to disease and knowledge of the factors controlling their neuron class-specific development. Spinal motor neurons are a notable example. They are susceptible to selective degeneration in pathologies like spinal muscular atrophy and amyotrophic lateral sclerosis (ALS) (31), and several of the transcription factors govern-

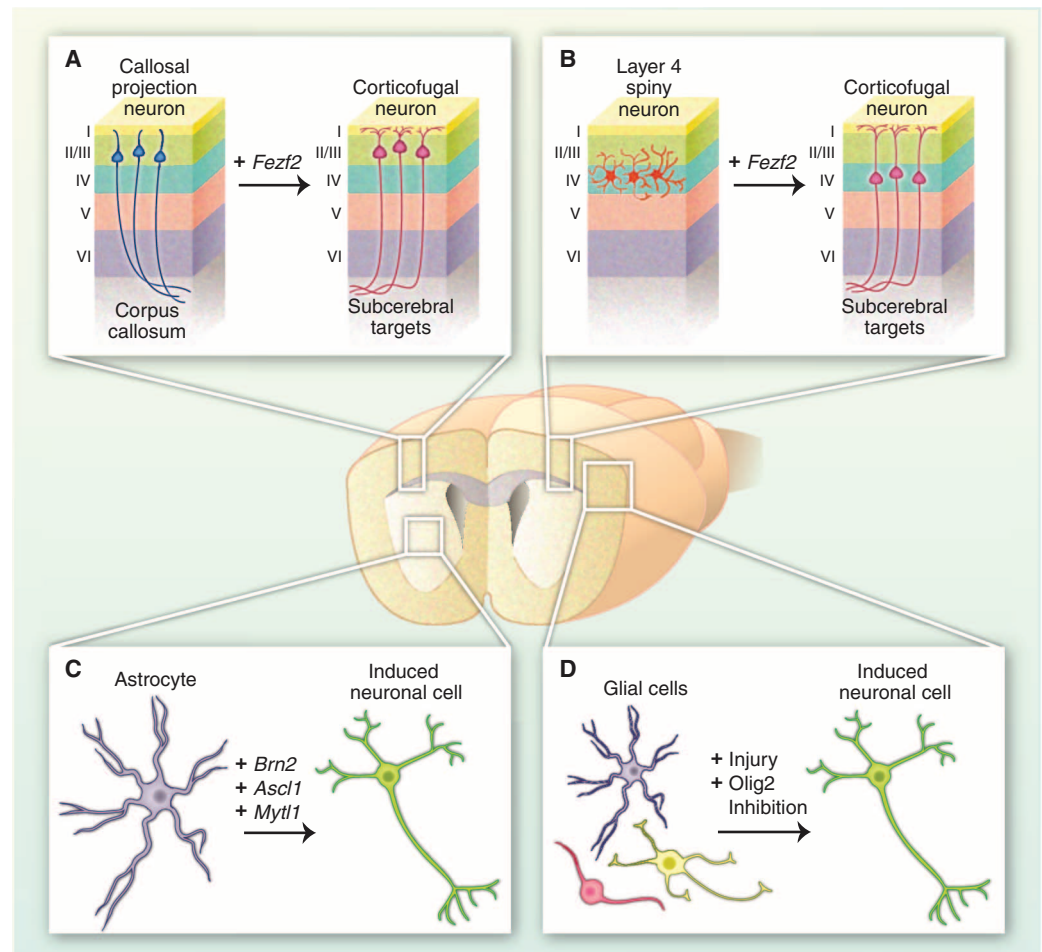
ing spinal motor neuron development are known (32). In 2002, a pioneering study provided proof-of-principle evidence that spinal motor neurons can be made from ESCs using developmental patterning signals (33). Subsequently, a cocktail of transcription factors made of BAM and motor neuron transcription factors (*Brn2*, *Ascl1*, *Myt1l*, *Lhx3*, *Hb9*, *Isl1*, and *Ngn2*) reprogrammed mouse fibroblasts into induced motor neurons (iMNs) (34). Although these iMNs did not show clear anterior-posterior (A-P) motor neuron identities, two different sets of programming factors—NIL (*Ngn2*, *Isl1*, and *Lhx3*) and NIP (*Ngn2*, *Isl1*, and *Phox2a*)—succeeded at differentiating ESCs into two groups of motor neurons with spinal and cranial identity, respectively. Interestingly, by performing chromatin immunoprecipitation sequencing analysis of *Isl1* genome binding in NIL- and NIP-programmed neurons, it was shown that *Isl1* binds to different genomic loci depending on whether *Lhx3* or *Phox2a* are coexpressed, indicating that synergistic binding of programming factors may be crucial to drive the generation of different types of motor neurons (35). Indeed, during the MEF to iMN conversion, application of *Lhx3*, *Hb9*, *Isl1*, and *Ngn2* enhanced efficiency, whereas the addition of *Sox1*, *Pax6*, *Nkx6.1*, and *Olig2* decreased the efficiency rather than being neutral. These data

suggest that the composition of each transcription factor module is critical to the success of reprogramming and that the most effective modules may be those composed of transcription factors that are expressed synchronically within the desired cell lineage in the embryo. In the future, deeper understanding of the synergism between individual transcription factors will clarify the mechanisms of reprogramming into specific neuronal cells. This knowledge should lead to a more informed choice of transcription factors and better predictions of reprogramming outcome to ultimately replace the current candidate screening approach.

Researchers have also extensively invested in generating midbrain dopaminergic (mDA) neurons because of their degenerative phenotype in patients with Parkinson's disease (36). *Nurr1* and *Lmx1a*, transcription factors necessary to generate mDA neurons during development (37), were coexpressed with *Ascl1* in mouse and human fibroblasts in an attempt to generate induced dopaminergic (iDA) neurons in vitro (38). Since then, several different combinations of factors have also been used to reprogram fibroblasts to a similar neuronal fate (39–41). Notably, the resulting neuronal cells displayed functional characteristics of endogenous dopaminergic neurons, including

Fig. 4. In vivo direct reprogramming of various cell types into neurons.

(A) Endogenous callosal projection neurons of early postnatal mice are directly reprogrammed into corticofugal projection neurons (58). (B) Layer IV spiny neurons are reprogrammed into neurons with electrophysiological properties of corticofugal neurons (59). (C) Adult striatal astrocytes are reprogrammed into induced neuronal cells by overexpression of the BAM factors (48). (D) Cortical OLIG2⁺ glial cells give rise to neuronal cells upon injury, combined with either inhibition of *Olig2* or overexpression of *Pax6* (47).



the ability to release dopamine and class-specific electrophysiological properties. Moreover, although additional work will be required to determine the clinical utility of these iDA neurons, encouragingly, transplantation experiments showed integration into mouse striatum and a mild amelioration of Parkinsonian symptoms (39). It should be noted, however, that cells generated by these methods did not acquire a distinct midbrain dopaminergic neuron identity. Clear persistence of epigenetic memory of fibroblast origin was observed, and subtype-specific markers of mDA neurons were not present to the extent observed in the endogenous counterparts (38, 39). This result highlights that, despite the necessary role of the reprogramming transcription factors during mDA development, these modules were not sufficient to impart the cells with class-specific traits of mDA neurons. However, the data also suggest that, even if lacking lineage-specific features, iDA neuronal cells may mimic key functional features of mDA neurons and therefore be clinically relevant. The fact that different combinations of factors lead to neuronal cells with similar functional properties may reflect the fundamental nature of such induced traits, which in vivo are shared by most types of dopaminergic neurons, not only mDA neurons. Alternatively, different molecular pathways may direct reprogramming to the same final cellular identity.

Considerable questions and challenges remain; nonetheless, pioneering studies in both direct lineage reprogramming and directed differentiation of defined neuronal classes indicate that production of patient-specific, defined classes of human neurons with clinical value is becoming a reality.

Challenges of Generating Neuronal Diversity

Direct lineage reprogramming is a nascent, but promising, field. Although both unspecialized and specialized neuronal cells have been generated, the extent of reprogramming is largely undefined, and this young field is collectively in need of better-defined criteria to classify the neurons obtained by these approaches. Some broad questions remain unanswered. How similar are reprogrammed neurons to their endogenous counterparts? Or, perhaps more relevantly, how close do these neurons need to be for applications such as disease modeling and cell replacement therapy? Do neurons obtained by direct reprogramming always maintain a memory of their original identity, and how does that influence their functionality? Some of these questions are beginning to be answered, whereas others remain a challenge for the future. We propose that some criteria for classifying reprogrammed neurons may be universal; however, others should take into account the intended use of the neurons.

Guidelines for defining neurons derived from non-neuronal cells in vitro have been suggested (10). The criteria include acquisition of neuronal morphology, expression of pan-neuronal markers, and functional synaptic inputs and outputs (10).

We agree that these criteria are well suited to broadly define iN cells as they test the acquisition of fundamental, basic traits that distinguish all neurons from fibroblasts and other non-neuronal cells. iN cells with these properties are valuable cells for a variety of applications, including disease modeling and therapeutic screening. For example, direct reprogramming of fibroblasts into “generic” populations of induced neuronal cells through overexpression of the BAM factors may be sufficient to model pathologies that affect a broad spectrum of neurons, with limited class specificity. In one example, fibroblasts isolated from human patients with a familial form of Alzheimer’s disease have been used to generate iN cells, which in turn could model some features of the disease, including modified amyloid precursor protein processing (42).

However, within the brain and spinal cord, neurons differ greatly from each other, and numerous subtypes can be recognized. Neuronal classification is based on many distinguishing features, which include global molecular identity, morphology, ultrastructural traits, electrophysiological properties, and connectivity. All of these traits collectively (and not in isolation) allow class distinction. Some neuronal subtype-specific traits—most prominently morphology, target-specific connectivity, and the ability to functionally integrate into circuitry—can only be examined in vivo and remain largely untested for reprogrammed neurons. Transplantation into developing or early postnatal brain, when the corresponding endogenous neuronal classes are acquiring defining traits, should allow for a clean assessment of the true potential of reprogrammed neurons to acquire class-specific features and developmentally “behave” like their endogenous counterparts. In particular, axonal connectivity to specific targets is a key, defining feature of many classes of neurons in the central nervous system and a prime predictor of functional integration. The trajectory of axons of reprogrammed neurons could easily be determined in vivo using genetic labels and standard retrograde tracing experiments. Reporter labeling of reprogrammed neurons would also allow for morphological measurements, including the establishment of stereotyped dendritic trees, which differ in shape, size, complexity, and position among different neuronal classes. Finally, modulation and recording of neuronal activity, facilitated by the use of optogenetic tools, could clarify the functional contribution of reprogrammed cells within a network of neurons.

Comparative analysis of the transcriptomes among reprogrammed neuron classes, endogenous neurons of the same class, and the starting non-neuronal cells (e.g., fibroblasts) has been initiated for iDA neurons and iMNs (34, 38). Transcriptional profiling and hierarchical clustering of fibroblast-derived spinal motor neurons showed that they cluster more closely to endogenous motor neurons than fibroblasts or ESCs (34). Similarly, iDA neurons resemble to some extent endogenous dopaminergic neurons (38). However,

notable differences exist. The iDA neurons obtained in vitro exhibited expression profiles that were distinguishable from those of endogenous mDAs (38, 39). Furthermore, expression of several fibroblast genes was retained after reprogramming into dopaminergic neurons. It is unclear how this memory affects the functionality of iN cells, and mechanistic studies are necessary to understand how fibroblast identity is maintained in order to inform the development of more complete reprogramming strategies. It is likely that, within a dish, neurons have achieved distinct levels of reprogramming. Induced neuronal cells have thus far been profiled as populations, which may have led to underestimating differences and similarities present at the single-neuron level. Major technological progress now enables single-cell RNA sequencing (43), and these methods are being rapidly interfaced with high-throughput platforms to allow the automatic sequencing of large numbers of individual cells. Single-cell molecular profiling of reprogrammed neurons should in the near future help define the molecular underpinnings that drive the acquisition of neuronal subtype-specific identity by these methods and allow the selection of better reprogrammed cells for downstream applications.

For the first time, neuroscientists and stem cell biologists alike are faced with the notable challenge of classifying an ever-growing number of “man-made,” reprogrammed neurons that did not exist a mere 5 years ago. It is possible that incompletely reprogrammed neurons of a specific class might be functionally equivalent to their endogenous neuronal subtypes. However, when aiming to generate neurons for goals as ambitious as neurological disease modeling and circuit replacement, we propose that a useful starting point would be to determine how iN cells relate to “nature-made” neurons and, further, that the endogenous neuronal complexity should be respected and emulated to a feasible extent.

In Vivo Neuronal Reprogramming

In organs and tissues such as the blood, the heart, and the pancreas, it is possible to directly reprogram one cell type into another in vivo by overexpression of defined factors (44–46). However, researchers have questioned whether all cells are endowed with such plasticity.

Resident non-neuronal cells of the central nervous system have been reprogrammed into induced neuronal cells in vivo. Due to the ability to divide, abundance in the brain, and proximity in lineage distance, astrocytes have been the ideal starting candidate cell type to generate new neurons. Early work showed that, in the adult mouse neocortex, OLIG2⁺ cells (which include oligodendrocytes, their progenitors, and astrocytes) could give rise to neurons upon injury, combined with either overexpression of *Pax6* or inhibition of *Olig2* (47). Since then, glial fibrillary acidic protein-positive (GFAP⁺) cells could be tuned into morphologically identifiable neurons in the adult striatum upon expression of the BAM cocktail

(48), and overexpression of *Sox2* was sufficient to reprogram adult striatal astrocytes into neuroblasts, which in turn were able to form neurons (21). These studies illustrate the feasibility of directly reprogramming non-neuronal cells into neurons in situ, which may become a therapeutic option in the future.

In addition to non-neuronal cells, an important question in the field has been whether neurons themselves could be turned from one class into another and whether this could become an optimal strategy to generate neuronal subtypes susceptible to disease with enhanced precision. The plasticity of neurons has been the subject of much debate. Once generated, neurons become postmitotic and do not change their identity for the life span of the organism, suggesting that neurons cannot be converted into other cell types. Much effort has been directed to generate live mice using somatic cell nuclear transfer from primary neurons, with varying results. Some studies led to conclude that postmitotic neurons may indeed have largely lost their developmental pluripotency (49, 50). However, a first sign that neurons may be capable of reprogramming their identity came from pioneering experiments in which a live mouse was obtained from the nucleus of an olfactory epithelium neuron (51, 52). Using a similar approach, viable mice were subsequently produced by somatic cell nuclear transfer using the nuclei of postmitotic neurons from the cerebral cortex of juvenile mice (53). These experiments provided a proof-of-principle demonstration that the nucleus of at least some classes of neurons is plastic and that no irreversible genetic or epigenetic changes have taken place that preclude the acquisition of a new cellular identity. For a historical perspective on neuronal reprogramming and on reprogramming into neurons, see Fig. 3.

If neurons retain the capability to reprogram their identity, could neurons then be converted from one class into another within the central nervous system? This field is only emerging, but some studies have begun to explore this strategy to build new neurons and circuits, in vivo (Fig. 4). Similar to the work on reprogramming non-neuronal cells, master selector genes able to drive the acquisition of class-specific neuronal identity can be powerful tools to instruct neuronal class switch in vivo. In a first application to neurons of the cerebral cortex, we have used the transcription factor *Fezf2*, a master gene capable of instructing multiple features of identity of corticospinal motor neurons (CSMN), to investigate whether reprogramming other cortical neurons to become CSMN is possible within the brain. *Fezf2* is developmentally required for the birth of CSMN, and in its absence all CSMN fail to generate (54–56). In agreement, *Fezf2* alone can cell-autonomously instruct the acquisition of CSMN-specific features when expressed in a permissive cellular context in vivo (57). We have demonstrated that overexpression of *Fezf2* is sufficient to directly reprogram embryonic and early postnatal callosal

projection neurons (CPN), a class of cortical neurons making interhemispheric connections via the corpus callosum, into corticofugal neurons, including CSMN. Reprogrammed callosal neurons acquire molecular properties of CSMN and change their axonal connectivity from interhemispheric intracortical projections to corticofugal projections directed below the cortex, including to the spinal cord (58). In line with these findings, endogenous electrophysiological features of CSMN were induced when *Fezf2* was force-expressed in layer IV stellate interneurons of the cortex (59).

What is notable about callosal neuron reprogramming is that postmitotic neuronal identity could be changed at postmitotic day 3 (P3) and P6 when callosal neurons have already reached their layer location, have connected to their targets in contralateral cortex, and have acquired defined, class-specific features. The data indicate that young neurons retain some ability to change and that the postmitotic nature of the cell does not per se preclude reprogramming. However, neuronal plasticity progressively declines, and reprogramming capabilities in response to *Fezf2* have been exhausted by P21 (58).

These results indicate that mechanisms are in place postmitotically to progressively restrict neuronal fate potential and reprogramming capabilities as neurons age. Molecular studies are now needed to extend the critical period of postmitotic neuron reprogramming to the mature brain, and this will be an important challenge for the growth of this field. To this end, one long-term goal will be to investigate the mechanisms that contribute in the first place to maintaining neuron class-specific identity during brain development and maturation. Such studies will help understand normal mechanisms used by neurons to refrain from changing but also will inform strategies to facilitate direct reprogramming of neuronal identity in the adult. It is likely that, beyond fate specifying transcription factors, “opening” the permissive temporal window of neuronal reprogramming will require additional manipulations. Epigenetic status, one of the major barriers to reprogramming somatic cells, may be modulated by chemical and genetic approaches. These manipulations may increase the plasticity of the target neurons and enable fate-specifying transcription factors to reprogram neuronal identity at later developmental stages.

In support for the existence of epigenetic blocks to neuronal reprogramming in vivo, work in the retina demonstrates that failure of reprogramming of adult rods into cone photoreceptors may be at least partly due to DNA methylation at key, class-specific loci (60). This study is notable, as the authors were able to induce several molecular, ultrastructural, and physiological properties of cones upon conditional removal of the rod-specifying transcription factor *Nrl* from adult rods. Although the cells retained some rod-specific traits, the work suggests that partial conversion of diseased rods into cones may be feasible in adults.

There are advantages to neuron-to-neuron conversion that make this approach worth pursuing. Closely related neurons could be chosen that share some pan-neuronal features, most prominently the use of the same neurotransmitter, ability to send long-distance axons, similar morphology, and location into circuit. This method is likely to facilitate the generation of highly specialized neurons, ease their integration into circuitry, and possibly reduce off-target connectivity. Because neurons do not divide, this process is also unlikely to become tumorigenic. It is generally accepted that a small percentage of new neurons of a given class can be sufficient to regain some functionality without visible effects on the behavior mediated by the starting neuronal population. Should in vivo reprogramming of adult neurons become a reality, this approach could be used to generate neurons that are affected by disease by the conversion, in situ, of a small percentage of neighboring neurons that are naturally resistant to the same pathology.

Looking into the Future of Induced Neuronal Cells

This is an exciting time for the field of cellular reprogramming in the central nervous system. Generation of neurons by direct reprogramming holds great promise for both cell replacement therapy and disease modeling. However, challenges remain. This field is just beginning to understand how differentiated cells are turned into neuronal cells. Mechanistic studies will be of fundamental importance to be able to predict the effect of different transcription factors and of the starting cellular context on the success of direct reprogramming into neuronal cells. This knowledge should help the field move away from current strategies that screen multiple-factor permutations. In addition, better criteria to classify induced neuronal cells are needed, especially when aiming to obtain specific classes of neurons. We propose that as more “realistic” and complex replicas of endogenous central neurons and tissue are generated, successful reprogramming in the central nervous system will require that expertise in reprogramming and embryology meet those in fundamental neuroscience to drive the choice of neurons to generate and to classify and functionally test the final neuronal products.

Given the speed of reprogramming and the ease of access to patient-derived fibroblasts, direct reprogramming of neurons is a manageable, alternative approach to generating neurons by directed differentiation of human iPSCs. We foresee that comparative characterization of neuronal cells obtained by these two methods will soon define similarities and differences between these sources. Newer approaches to achieve genome editing have also emerged over the past few years that will enable large-scale genome modification of different cell types to insert (or repair) disease-associated mutations (61, 62). These state-of-the-art technologies allow for scalable, highly specific insertion of somatic mutations in the

genome and could ultimately add a new dimension to modeling and understanding human disease using iN cells. For neuroscientists in particular, generation of an unlimited supply of human neuronal cells (neurons are notoriously difficult to obtain from patients and cannot be expanded in culture) was merely an ambition, far from reality until this opportunity emerged a few years ago. It is now possible to design clinical trials in the dish that may revolutionize preclinical screening of therapeutic compounds by testing them in a high-throughput manner on human neuronal cells, in parallel to mouse modeling.

One application of direct lineage reprogramming in the nervous system is the generation of new neurons in situ by the direct conversion of cells that are resident within the central nervous system. Given the highly specialized nature of neurons and the complexity of the connections they make and receive, it may be advantageous to generate new neurons by direct conversion of other classes of neurons. The starting neurons may have already acquired basic pan-neuronal features that are functionally critical. However, a major challenge will be to identify and overcome barriers that currently hamper reprogramming of neurons in the adult nervous system. The mechanisms that maintain neuronal class-specific identity throughout the life span of an organism are largely unknown. Although it is speculative at this stage, we propose that neurons might maintain their identity using unique mechanisms. It is intriguing that the closure of the temporal window of nuclear plasticity of neurons loosely corresponds to their integration into circuit. This suggests the provocative possibility that elements of neuronal identity are sustained by the network in which each neuron integrates.

It remains to be determined whether and how local (or even long-distance) circuitry would react in response to a change in neuronal class-specific identity induced by reprogramming. Should adult neuronal reprogramming become a reality, this in vivo application could be informative in elucidating aspects of circuit plasticity and understanding some of the rules that shape circuit maintenance in vivo. With the knowledge of development and cell identity of all neurons present in the nervous system of *Caenorhabditis elegans*, this organism may be a perfect first model system to determine whether circuit remodeling accompanies the process of direct reprogramming in vivo. Investigation of invertebrate organisms that are endowed with natural reprogramming capabilities will also facilitate understanding of reprogramming in mammals.

As evidenced by the presentation of the Nobel Prize in 2012, nuclear reprogramming is an exciting, rapidly growing field with the potential to transform basic science and clinical research. Direct reprogramming from one cell into another may be particularly advantageous for the central nervous system because of its in vivo applicability, in addition to neuronal production in the dish. Although the progress in the field has gen-

erated as many unresolved questions as answers, direct reprogramming has shown promise to revolutionize the way the field thinks about neuronal stability and repair.

References and Notes

- J. B. Gurdon, From nuclear transfer to nuclear reprogramming: The reversal of cell differentiation. *Annu. Rev. Cell Dev. Biol.* **22**, 1–22 (2006). doi: [10.1146/annurev.cellbio.22.090805.140144](#); pmid: [16704337](#)
- J. B. Gurdon, Adult frogs derived from the nuclei of single somatic cells. *Dev. Biol.* **4**, 256–273 (1962). doi: [10.1016/0012-1606\(62\)90043-X](#); pmid: [13903207](#)
- J. B. Gurdon, V. Uehlinger, "Fertile" intestine nuclei. *Nature* **210**, 1240–1241 (1966). doi: [10.1038/2101240a0](#); pmid: [5967799](#)
- R. Briggs, T. J. King, Transplantation of living nuclei from blastula cells into enucleated frogs' eggs. *Proc. Natl. Acad. Sci. U.S.A.* **38**, 455–463 (1952). doi: [10.1073/pnas.38.5.455](#); pmid: [16589125](#)
- K. Hochedlinger, R. Jaenisch, Nuclear reprogramming and pluripotency. *Nature* **441**, 1061–1067 (2006). doi: [10.1038/nature04955](#); pmid: [16810240](#)
- K. Takahashi, S. Yamanaka, Induction of pluripotent stem cells from mouse embryonic and adult fibroblast cultures by defined factors. *Cell* **126**, 663–676 (2006). doi: [10.1016/j.cell.2006.07.024](#); pmid: [16904174](#)
- M. Stadtfeld, K. Hochedlinger, Induced pluripotency: History, mechanisms, and applications. *Genes Dev.* **24**, 2239–2263 (2010). doi: [10.1101/gad.1963910](#); pmid: [20952534](#)
- C. Waddington, *The Strategy of the Genes* (Allen and Unwin, London, 1957).
- J. Ladewig, P. Koch, O. Brüstle, Leveling Waddington: The emergence of direct programming and the loss of cell fate hierarchies. *Nat. Rev. Mol. Cell Biol.* **14**, 225–236 (2013). doi: [10.1038/nrm3543](#)
- N. Yang, Y. H. Ng, Z. P. Pang, T. C. Südhof, M. Wernig, Induced neuronal cells: How to make and define a neuron. *Cell Stem Cell* **9**, 517–525 (2011). doi: [10.1016/j.stem.2011.11.015](#); pmid: [22136927](#)
- R. Dawkins, *The Greatest Show on Earth: The Evidence for Evolution* (Simon and Schuster, New York, 2009).
- H. Aoki, A. Hara, M. Niwa, Y. Yamada, T. Kunisada, In vitro and in vivo differentiation of human embryonic stem cells into retina-like organs and comparison with that from mouse pluripotent epiblast stem cells. *Dev. Dyn.* **238**, 2266–2279 (2009). doi: [10.1002/dvdy.22008](#); pmid: [19544586](#)
- M. Eiraku *et al.*, Self-organizing optic-cup morphogenesis in three-dimensional culture. *Nature* **472**, 51–56 (2011). doi: [10.1038/nature09941](#); pmid: [21475194](#)
- M. A. Lancaster *et al.*, Cerebral organoids model human brain development and microcephaly. *Nature* **501**, 373–379 (2013). doi: [10.1038/nature12517](#); pmid: [23995685](#)
- N. Heins *et al.*, Glial cells generate neurons: The role of the transcription factor Pax6. *Nat. Neurosci.* **5**, 308–315 (2002). doi: [10.1038/nn828](#); pmid: [11896398](#)
- B. Berninger *et al.*, Functional properties of neurons derived from in vitro reprogrammed postnatal astroglia. *J. Neurosci.* **27**, 8654–8664 (2007). doi: [10.1523/JNEUROSCI.1615-07.2007](#); pmid: [17687043](#)
- C. Heinrich *et al.*, Directing astroglia from the cerebral cortex into subtype specific functional neurons. *PLOS Biol.* **8**, e1000373 (2010). doi: [10.1371/journal.pbio.1000373](#); pmid: [20502524](#)
- C. Heinrich *et al.*, Generation of subtype-specific neurons from postnatal astroglia of the mouse cerebral cortex. *Nat. Protoc.* **6**, 214–228 (2011). doi: [10.1038/nprot.2010.188](#); pmid: [21293461](#)
- S. Marro *et al.*, Direct lineage conversion of terminally differentiated hepatocytes to functional neurons. *Cell Stem Cell* **9**, 374–382 (2011). doi: [10.1016/j.stem.2011.09.002](#); pmid: [21962918](#)
- M. Karow *et al.*, Reprogramming of pericyte-derived cells of the adult human brain into induced neuronal cells. *Cell Stem Cell* **11**, 471–476 (2012). doi: [10.1016/j.stem.2012.07.007](#); pmid: [23040476](#)
- W. Niu *et al.*, In vivo reprogramming of astrocytes to neuroblasts in the adult brain. *Nat. Cell Biol.* **15**, 1164–1175 (2013). doi: [10.1038/ncb2843](#); pmid: [24056302](#)
- T. Vierbuchen *et al.*, Direct conversion of fibroblasts to functional neurons by defined factors. *Nature* **463**, 1035–1041 (2010). doi: [10.1038/nature08797](#); pmid: [20107439](#)
- Z. P. Pang *et al.*, Induction of human neuronal cells by defined transcription factors. *Nature* **476**, 220–223 (2011). pmid: [21617644](#)
- N. Bertrand, D. S. Castro, F. Guillemot, Proneural genes and the specification of neural cell types. *Nat. Rev. Neurosci.* **3**, 517–530 (2002). doi: [10.1038/nrn874](#); pmid: [12094208](#)
- O. L. Wapinski *et al.*, Hierarchical mechanisms for direct reprogramming of fibroblasts to neurons. *Cell* **155**, 621–635 (2013). doi: [10.1016/j.cell.2013.09.028](#); pmid: [24243019](#)
- J. Ladewig *et al.*, Small molecules enable highly efficient neuronal conversion of human fibroblasts. *Nat. Methods* **9**, 575–578 (2012). doi: [10.1038/nmeth.1972](#); pmid: [22484851](#)
- M.-L. Liu *et al.*, Small molecules enable neurogenesis 2 to efficiently convert human fibroblasts into cholinergic neurons. *Nat. Commun.* **4**, 2183 (2013). pmid: [23873306](#)
- J. Ninkovic *et al.*, The BAF complex interacts with Pax6 in adult neural progenitors to establish a neurogenic cross-regulatory transcriptional network. *Cell Stem Cell* **13**, 403–418 (2013). doi: [10.1016/j.stem.2013.07.002](#); pmid: [23933087](#)
- A. X. Sun, G. R. Crabtree, A. S. Yoo, MicroRNAs: Regulators of neuronal fate. *Curr. Opin. Cell Biol.* **25**, 215–221 (2013). doi: [10.1016/j.ceb.2012.12.007](#); pmid: [23374323](#)
- A. R. Muotri, F. H. Gage, Generation of neuronal variability and complexity. *Nature* **441**, 1087–1093 (2006). doi: [10.1038/nature04959](#); pmid: [16810244](#)
- K. C. Kanning, A. Kaplan, C. E. Henderson, Motor neuron diversity in development and disease. *Annu. Rev. Neurosci.* **33**, 409–440 (2010). doi: [10.1146/annurev.neuro.051508.135722](#); pmid: [20367447](#)
- T. M. Jessell, Neuronal specification in the spinal cord: Inductive signals and transcriptional codes. *Nat. Rev. Genet.* **1**, 20–29 (2000). doi: [10.1038/35049541](#); pmid: [11262869](#)
- H. Wichterle, I. Lieberam, J. A. Porter, T. M. Jessell, Directed differentiation of embryonic stem cells into motor neurons. *Cell* **110**, 385–397 (2002). doi: [10.1016/S0092-8674\(02\)00835-8](#); pmid: [12176325](#)
- E. Y. Son *et al.*, Conversion of mouse and human fibroblasts into functional spinal motor neurons. *Cell Stem Cell* **9**, 205–218 (2011). doi: [10.1016/j.stem.2011.07.014](#); pmid: [21852222](#)
- E. O. Mazzoni *et al.*, Synergistic binding of transcription factors to cell-specific enhancers programs motor neuron identity. *Nat. Neurosci.* **16**, 1219–1227 (2013). doi: [10.1038/nn.3467](#); pmid: [23872598](#)
- D. Sulzer, D. J. Surmeier, Neuronal vulnerability, pathogenesis, and Parkinson's disease. *Mov. Disord.* **28**, 41–50 (2013). doi: [10.1002/mds.25095](#); pmid: [22791686](#)
- K. N. Alavian, C. Scholz, H. H. Simon, Transcriptional regulation of mesencephalic dopaminergic neurons: The full circle of life and death. *Mov. Disord.* **23**, 319–328 (2008). doi: [10.1002/mds.21640](#); pmid: [18044702](#)
- M. Caiazzo *et al.*, Direct generation of functional dopaminergic neurons from mouse and human fibroblasts. *Nature* **476**, 224–227 (2011). doi: [10.1038/nature10284](#); pmid: [21725324](#)
- J. Kim *et al.*, Functional integration of dopaminergic neurons directly converted from mouse fibroblasts. *Cell Stem Cell* **9**, 413–419 (2011). doi: [10.1016/j.stem.2011.09.011](#); pmid: [22019014](#)
- X. Liu *et al.*, Direct reprogramming of human fibroblasts into dopaminergic neuron-like cells. *Cell Res.* **22**, 321–332 (2012). doi: [10.1038/cr.2011.181](#); pmid: [22105488](#)
- U. Pfisterer *et al.*, Direct conversion of human fibroblasts to dopaminergic neurons. *Proc. Natl. Acad.*

- Sci. U.S.A.* **108**, 10343–10348 (2011). doi: [10.1073/pnas.1105135108](https://doi.org/10.1073/pnas.1105135108); pmid: [21646515](https://pubmed.ncbi.nlm.nih.gov/21646515/)
42. L. Qiang *et al.*, Directed conversion of Alzheimer's disease patient skin fibroblasts into functional neurons. *Cell* **146**, 359–371 (2011). doi: [10.1016/j.cell.2011.07.007](https://doi.org/10.1016/j.cell.2011.07.007); pmid: [21816272](https://pubmed.ncbi.nlm.nih.gov/21816272/)
 43. F. Tang, K. Lao, M. A. Surani, Development and applications of single-cell transcriptome analysis. *Nat. Methods* **8** (suppl.), S6–S11 (2011). pmid: [21451510](https://pubmed.ncbi.nlm.nih.gov/21451510/)
 44. L. Qian *et al.*, In vivo reprogramming of murine cardiac fibroblasts into induced cardiomyocytes. *Nature* **485**, 593–598 (2012). doi: [10.1038/nature11044](https://doi.org/10.1038/nature11044); pmid: [22522929](https://pubmed.ncbi.nlm.nih.gov/22522929/)
 45. H. Xie, M. Ye, R. Feng, T. Graf, Stepwise reprogramming of B cells into macrophages. *Cell* **117**, 663–676 (2004). doi: [10.1016/S0092-8674\(04\)00419-2](https://doi.org/10.1016/S0092-8674(04)00419-2); pmid: [15163413](https://pubmed.ncbi.nlm.nih.gov/15163413/)
 46. Q. Zhou, J. Brown, A. Kanarek, J. Rajagopal, D. A. Melton, In vivo reprogramming of adult pancreatic exocrine cells to beta-cells. *Nature* **455**, 627–632 (2008). doi: [10.1038/nature07314](https://doi.org/10.1038/nature07314); pmid: [18754011](https://pubmed.ncbi.nlm.nih.gov/18754011/)
 47. A. Buffo *et al.*, Expression pattern of the transcription factor Olig2 in response to brain injuries: Implications for neuronal repair. *Proc. Natl. Acad. Sci. U.S.A.* **102**, 18183–18188 (2005). doi: [10.1073/pnas.0506535102](https://doi.org/10.1073/pnas.0506535102); pmid: [16330768](https://pubmed.ncbi.nlm.nih.gov/16330768/)
 48. O. Torper *et al.*, Generation of induced neurons via direct conversion in vivo. *Proc. Natl. Acad. Sci. U.S.A.* **110**, 7038–7043 (2013). doi: [10.1073/pnas.1303829110](https://doi.org/10.1073/pnas.1303829110); pmid: [23530235](https://pubmed.ncbi.nlm.nih.gov/23530235/)
 49. H. Makino *et al.*, Mouse embryos and chimera cloned from neural cells in the postnatal cerebral cortex. *Cloning Stem Cells* **7**, 45–61 (2005). doi: [10.1089/clo.2005.7.45](https://doi.org/10.1089/clo.2005.7.45); pmid: [15996117](https://pubmed.ncbi.nlm.nih.gov/15996117/)
 50. Y. Yamazaki *et al.*, Assessment of the developmental totipotency of neural cells in the cerebral cortex of mouse embryo by nuclear transfer. *Proc. Natl. Acad. Sci. U.S.A.* **98**, 14022–14026 (2001). doi: [10.1073/pnas.231489398](https://doi.org/10.1073/pnas.231489398); pmid: [11698647](https://pubmed.ncbi.nlm.nih.gov/11698647/)
 51. K. Eggan *et al.*, Mice cloned from olfactory sensory neurons. *Nature* **428**, 44–49 (2004). doi: [10.1038/nature02375](https://doi.org/10.1038/nature02375); pmid: [14990966](https://pubmed.ncbi.nlm.nih.gov/14990966/)
 52. J. Li, T. Ishii, P. Feinstein, P. Mombaerts, Odorant receptor gene choice is reset by nuclear transfer from mouse olfactory sensory neurons. *Nature* **428**, 393–399 (2004). doi: [10.1038/nature02433](https://doi.org/10.1038/nature02433); pmid: [15042081](https://pubmed.ncbi.nlm.nih.gov/15042081/)
 53. T. Osada *et al.*, Developmental pluripotency of the nuclei of neurons in the cerebral cortex of juvenile mice. *J. Neurosci.* **25**, 8368–8374 (2005). doi: [10.1523/JNEUROSCI.1591-05.2005](https://doi.org/10.1523/JNEUROSCI.1591-05.2005); pmid: [16162918](https://pubmed.ncbi.nlm.nih.gov/16162918/)
 54. B. Chen, L. R. Schaefer, S. K. McConnell, Fezl regulates the differentiation and axon targeting of layer 5 subcortical projection neurons in cerebral cortex. *Proc. Natl. Acad. Sci. U.S.A.* **102**, 17184–17189 (2005). doi: [10.1073/pnas.0508732102](https://doi.org/10.1073/pnas.0508732102); pmid: [16284245](https://pubmed.ncbi.nlm.nih.gov/16284245/)
 55. J.-G. Chen, M.-R. Rasin, K. Y. Kwan, N. Sestan, Zfp312 is required for subcortical axonal projections and dendritic morphology of deep-layer pyramidal neurons of the cerebral cortex. *Proc. Natl. Acad. Sci. U.S.A.* **102**, 17792–17797 (2005). doi: [10.1073/pnas.0509032102](https://doi.org/10.1073/pnas.0509032102); pmid: [16314561](https://pubmed.ncbi.nlm.nih.gov/16314561/)
 56. B. J. Molyneaux, P. Arlotta, T. Hirata, M. Hibi, J. D. Macklis, Fezl is required for the birth and specification of corticospinal motor neurons. *Neuron* **47**, 817–831 (2005). doi: [10.1016/j.neuron.2005.08.030](https://doi.org/10.1016/j.neuron.2005.08.030); pmid: [16157277](https://pubmed.ncbi.nlm.nih.gov/16157277/)
 57. C. Rouaux, P. Arlotta, Fezf2 directs the differentiation of corticofugal neurons from striatal progenitors in vivo. *Nat. Neurosci.* **13**, 1345–1347 (2010). doi: [10.1038/nn.2658](https://doi.org/10.1038/nn.2658); pmid: [20953195](https://pubmed.ncbi.nlm.nih.gov/20953195/)
 58. C. Rouaux, P. Arlotta, Direct lineage reprogramming of post-mitotic callosal neurons into corticofugal neurons in vivo. *Nat. Cell Biol.* **15**, 214–221 (2013). doi: [10.1038/ncb2660](https://doi.org/10.1038/ncb2660); pmid: [23334497](https://pubmed.ncbi.nlm.nih.gov/23334497/)
 59. A. De la Rossa *et al.*, In vivo reprogramming of circuit connectivity in postmitotic neocortical neurons. *Nat. Neurosci.* **16**, 193–200 (2013). doi: [10.1038/nn.3299](https://doi.org/10.1038/nn.3299); pmid: [23292682](https://pubmed.ncbi.nlm.nih.gov/23292682/)
 60. C. L. Montana *et al.*, Reprogramming of adult rod photoreceptors prevents retinal degeneration. *Proc. Natl. Acad. Sci. U.S.A.* **110**, 1732–1737 (2013). doi: [10.1073/pnas.1214387110](https://doi.org/10.1073/pnas.1214387110); pmid: [23319618](https://pubmed.ncbi.nlm.nih.gov/23319618/)
 61. L. Cong *et al.*, Multiplex genome engineering using CRISPR/Cas systems. *Science* **339**, 819–823 (2013). doi: [10.1126/science.1231143](https://doi.org/10.1126/science.1231143); pmid: [23287718](https://pubmed.ncbi.nlm.nih.gov/23287718/)
 62. F. Zhang *et al.*, Efficient construction of sequence-specific TAL effectors for modulating mammalian transcription. *Nat. Biotechnol.* **29**, 149–153 (2011). doi: [10.1038/nbt.1775](https://doi.org/10.1038/nbt.1775); pmid: [21248753](https://pubmed.ncbi.nlm.nih.gov/21248753/)
 63. H. Spemann, *Embryonic Development and Induction* (Yale Univ. Press, New Haven, CT, 1938).
 64. I. Wilmut, A. E. Schnieke, J. McWhir, A. J. Kind, K. H. Campbell, Viable offspring derived from fetal and adult mammalian cells. *Nature* **385**, 810–813 (1997). doi: [10.1038/385810a0](https://doi.org/10.1038/385810a0); pmid: [9039911](https://pubmed.ncbi.nlm.nih.gov/9039911/)
 65. R. L. Davis, H. Weintraub, A. B. Lassar, Expression of a single transfected cDNA converts fibroblasts to myoblasts. *Cell* **51**, 987–1000 (1987). doi: [10.1016/0092-8674\(87\)90585-X](https://doi.org/10.1016/0092-8674(87)90585-X); pmid: [3690668](https://pubmed.ncbi.nlm.nih.gov/3690668/)

Acknowledgments: We thank B. Berninger, M. Stadtfeld, H. Wichterle, and members of the Arlotta laboratory for their valuable comments on the manuscript. We apologize to colleagues whose work we could not include due to space limitations. Work in the Arlotta laboratory is funded by the U.S. National Institutes of Health. P.A. is a New York Stem Cell Foundation Robertson Investigator.

[10.1126/science.1239882](https://doi.org/10.1126/science.1239882)

Timing Mechanism Dependent on Cell Division Is Invoked by Polycomb Eviction in Plant Stem Cells

Bo Sun, Liang-Sheng Looi, Siyi Guo, Zemiao He, Eng-Seng Gan, Jiangbo Huang, Yifeng Xu, Wan-Yi Wee, Toshiro Ito*

Introduction: In plants, leaves and flowers originate from the shoot apical meristem. In an indeterminate shoot apical meristem, stem cells persist for the life of the plant. In a determinate meristem, a certain number of organs are produced before the meristem is terminated; this characterizes the floral meristem derived from the shoot apical meristem. In *Arabidopsis*, stem cell identity is sustained by expression of the gene *WUSCHEL*. Expression of *WUSCHEL* can be terminated by the zinc finger protein *KNUCKLES* (*KNU*), with the result that stem cell identity is inactivated. *KNU* expression is induced by the floral homeotic protein *AGAMOUS* (*AG*), but that induction process requires ~2 days and invokes modification of histones resident at the *KNU* locus. Here, we show that the 2-day time lag is a consequence of a regulated molecular mechanism and that this mechanism can be embedded in a synthetic regulatory system to invoke a similar time lag.

Methods: For transgenic *Arabidopsis* plants, we accelerated or inhibited cell cycles with pharmacological agents and studied the resulting *KNU* expression in response to *AG* induction. We used chromatin immunoprecipitation to study the presence of Polycomb proteins on the *KNU* locus at specific times during flower development. We used insertional mutagenesis to alter the function of the Polycomb response element (PRE) and analyzed the response from a heterologous promoter in *Arabidopsis* cell cultures. We constructed a synthetic mimic in *Arabidopsis* floral buds of the *AG* function by using the DNA binding domain of the lactose operon repressor (*lacI*) with its cognate binding sites. To test the logic that the delay in downstream gene induction was caused by the need to evict Polycomb group (PcG) proteins from their residence, we simulated the competition between PcG proteins and DNA binding proteins by using *lacI*, designed transcription activator–like effector DNA binding proteins, and synthesized promoters in *Arabidopsis* cell lines.

Results: *AG* induces *KNU* with a time delay regulated by epigenetic modification. In wild-type plants, *KNU* expression begins in the center of the floral meristem and follows cell cycle progression. The binding sites for *AG* in the *KNU* upstream region are located within the PRE sequences required for the repressive histone modification. Binding of *AG* displaces PcG proteins, leading to the failure to maintain the repressive histone methylation. The combination of *lacI* operator sequences with a chimeric protein that contained the *lacI* DNA binding domain but lacked the activation domain was able to mimic the *AG* activity in *Arabidopsis* floral buds. We also reconstituted the cell division–dependent delayed-induction circuit in cell lines.

Discussion: Our results indicate that flower development in *Arabidopsis* employs cell division to provide stem cells with a window of opportunity to change fate. The competition we observed between repressive PcG proteins and an activating transcription factor may reflect a general mechanism. The logic of the molecular circuit we have uncovered here may impose timing control on diverse growth and differentiation pathways in plants and animals.

READ THE FULL ARTICLE ONLINE

<http://dx.doi.org/10.1126/science.1248559>



Cite this article as B. Sun *et al.*, *Science* **343**, 1248559 (2014). DOI: 10.1126/science.1248559

FIGURES IN THE FULL ARTICLE

Fig. 1. *KNU* induction timing is cell division–dependent.

Fig. 2. Polycomb group protein binding on *KNU* and *cis* activities.

Fig. 3. Polycomb response element and simulation of *AG*.

Fig. 4. Synthetic epigenetic timer and eviction model.

SUPPLEMENTARY MATERIALS

Supplementary Text

Figs. S1 to S21

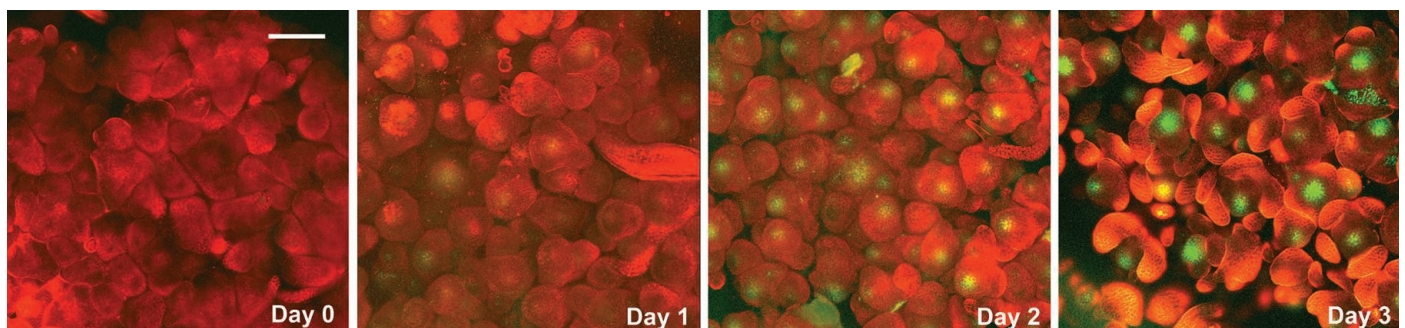
Tables S1 to S4

Full Reference List

RELATED ITEMS IN SCIENCE

X. Zhang, Delayed gratification—Waiting to terminate stem cell identity. *Science* **343**, 498–499 (2014). DOI: 10.1126/science.1249343

Induction of *KNU* in *Arabidopsis* floral meristems. Synchronized inflorescences imaged by confocal microscopy and reconstructed into three-dimensional projections (red stains by a fluorescence dye show the shapes of developing flowers). In an *Arabidopsis* line that has been engineered so that its floral development is both inducible and synchronized, *KNU* expression (green) begins 1 to 3 days after the activation of flower development. The delay is mediated by repressive histone methylation at the *KNU* locus. Upon activation, the transcription factor *AG* displaces Polycomb proteins, and the repressive histone marks are lost with cell cycle progression. Scale bar, 100 μ m.



The list of author affiliations is available in the full article online.

*Corresponding author. E-mail: itot@tll.org.sg

Timing Mechanism Dependent on Cell Division Is Invoked by Polycomb Eviction in Plant Stem Cells

Bo Sun,¹ Liang-Sheng Looi,^{1,2} Siyi Guo,¹ Zemiao He,^{1,2} Eng-Seng Gan,^{1,2} Jiangbo Huang,^{1,2} Yifeng Xu,¹ Wan-Yi Wee,¹ Toshiro Ito^{1,2*}

Plant floral stem cells divide a limited number of times before they stop and terminally differentiate, but the mechanisms that control this timing remain unclear. The precise temporal induction of the *Arabidopsis* zinc finger repressor KNUCKLES (*KNU*) is essential for the coordinated growth and differentiation of floral stem cells. We identify an epigenetic mechanism in which the floral homeotic protein AGAMOUS (*AG*) induces *KNU* at ~2 days of delay. *AG* binding sites colocalize with a Polycomb response element in the *KNU* upstream region. *AG* binding to the *KNU* promoter causes the eviction of the Polycomb group proteins from the locus, leading to cell division-dependent induction. These analyses demonstrate that floral stem cells measure developmental timing by a division-dependent epigenetic timer triggered by Polycomb eviction.

Multicellular developmental processes require the precise coordination of growth and differentiation. The growth and development of the aerial part of the plant depends on the continuous activity of stem cells that are maintained at the growing tips called the shoot apical meristem (SAM) (1). After floral transition, the SAM usually becomes an inflorescence meristem (IM) that generates floral meristems (FMs). In contrast to the continuous SAM and IM, the FM gives rise to a certain number of organs and loses its pool of stem cells during differentiation. Thus, in the vast majority of land plants, FMs are considered determinate meristems. However, the mechanisms that control when the cells stop dividing and terminally differentiate remain largely mysterious. In *Arabidopsis*, the homeodomain protein WUSCHEL (*WUS*) is expressed in a small group of cells at the center of the meristems (SAMs, IMs, and FMs) and is essential for maintenance of the stem cell pool (2). *WUS* expression is repressed by the C2H2-type zinc finger protein KNUCKLES (*KNU*) in the FM (3, 4). The floral homeotic protein AGAMOUS (*AG*), which is directly induced by *WUS* in young floral buds, directly induces *KNU* ~2 days later to terminate FMs at the precise timing (Fig. 1, A and B) (4–8). Delayed or precocious *KNU* expression leads to the formation of extra or fewer organs, respectively (4). Here, we study the molecular mechanisms of these time-regulated delays in developmental programs.

KNU Induction Is Cell Division-Dependent

To examine the basis of the 2-day delay between *AG* and *KNU* induction, we used *ag-1 35S::AG-GR*

pKNU::KNU-GUS, a *KNU* reporter line that expresses an *AG* construct that can be induced posttranslationally with dexamethasone (DEX) in the *ag-1* mutant (4). Roscovitine and olomoucine (cyclin-dependent kinase inhibitors) block cell cycle progression at the G₁-S and G₂-M phases, whereas aphidicolin (an inhibitor of DNA polymerase) blocks the cell cycle at the early S phase (9). Whereas the *KNU-GUS* reporter was induced ~2 days after DEX treatment in the *AG* inducible line, addition of cell cycle inhibitors prevented the *KNU* induction on day 2 (Fig. 1, C and D, and fig. S1). *AG* also induces *SPOROCTELESS* (*SPL/NOZZLE*) at about the same developmental stage when *KNU* starts to express (10). However, *SPL* reporter expression was unaffected by olomoucine treatment (which had the strongest effect to *KNU*) in the *AG* inducible line (figs. S1 and S2). Thus, division-dependent time lag is required for *AG*'s induction of *KNU* but not of *SPL*.

Phytohormones gibberellin and cytokinin, which accelerate cell cycle progression (11), increased the expression of a cyclin reporter construct in developing flowers (11) (fig. S3, A to C). In the inducible line of *AG*, treatment with these phytohormones alone did not induce the *KNU* reporter (fig. S3, D to F), but *AG* induction (through DEX) combined with phytohormone treatment showed precocious *KNU-GUS* activity within 24 to 36 hours (Fig. 1, E and F, and fig. S4).

To visualize *KNU* expression at the cellular level, we established a *KNU* fluorescence reporter in the inducible line of flower development, *ap1 cal 35S::API-GR pKNU::KNU-VENUS* (12), which enabled us to synchronize flower development of multiple floral buds. After the induction of flower development, *KNU* started to be expressed only in a limited number of cells with a time window of 1 and 3 days (fig. S5). The treatment with olomoucine or gibberellin to this line delayed or accelerated the induction timing

of *KNU*, respectively, in a way that correlated with cell cycle progression (fig. S6). Cellular-level observation showed that *KNU* was induced in more cells by gibberellin treatment than the control on days 2 and 3, whereas no (on day 2) or fewer cells (on day 3) showed *KNU* induction when treated with olomoucine (Fig. 1, G to I, and fig. S7). Although we did not see any obvious phenotypic differences by the cell cycle manipulation until day 2, olomoucine and gibberellin delayed or accelerated the emergence of floral organ primordia on day 3, suggesting that cell division plays an important role in morphological changes in flower development (fig. S8; see supplementary text for details). The cell division of floral stem cells is not synchronized and occurs once in 18 to 36 hours in most of the cells (13). Together, these data indicate that *KNU* regulation may be controlled by an intrinsic cell division-based timer.

AG Displaces Polycomb Group Proteins from *KNU*

The *KNU* transcribed region carries the repressive histone modification trimethylation of lysine 27 of histone H3 (H3K27me3), which is established and maintained by Polycomb group (PcG) proteins (14, 15). *KNU* activation by *AG* is associated with the loss of H3K27me3 (4). In PcG mutants, *KNU* is precociously expressed, and so is the *KNU* reporter line with a deletion in the *KNU* coding region carrying H3K27me3, suggesting that the mark has the commanding role for temporal regulation (4). Furthermore, the reduction of the H3K27me3 levels is *AG*-dependent (4), and the above-mentioned truncated reporter is expressed in *ag-1* (fig. S9). Thus, *AG* appears to temporally-specifically remove H3K27me3. To examine the mechanism underlying how *AG* affects the repressive marks on *KNU* in a cell division-dependent manner, we created tagged lines for the essential components of PcG, the ESC homolog FERTILIZATION-INDEPENDENT ENDOSPERM (*FIE*) and the structural homolog of Su(z)12, EMBRYONIC FLOWER2 (*EMF2*) (16, 17). We first transformed the *pFIE::FIE-VENUS* and *pEMF2::EMF2-VENUS* constructs into the *fie-11/+* and *emf2-1/+* heterozygous mutant lines, respectively, and obtained the rescued lines in the homozygous background for each mutation. Next, we introduced them into *ap1 cal 35S::API-GR* (12), which enabled us to harvest stage-specific floral buds (fig. S10, A to C). After one time of DEX treatment, floral buds were harvested to perform chromatin immunoprecipitation (ChIP) assays for *FIE*, *EMF2*, and *AG* [with an *AG* antibody (4)] at days 0, 1, and 2. We detected *AG* binding in the samples on days 1 and 2 at a region ~900 base pairs (bp) from the transcriptional start site, but not on day 0 (4) (fig. S11). In contrast, we detected moderate binding of *FIE* and *EMF2* around a wider region of the *KNU* locus, including the *AG* binding sites on day 0 (Fig. 2, A and B, and fig. S12, A and B). From day 1 when *AG* binding started to be detected, the relative binding levels of *FIE* and *EMF2* decreased to

¹Temasek Life Sciences Laboratory, 1 Research Link, National University of Singapore, Singapore 117604, Republic of Singapore.

²Department of Biological Sciences, National University of Singapore, Singapore 117543, Republic of Singapore.

*Corresponding author. E-mail: itot@tll.org.sg

the basal levels (Fig. 2B and figs. S11 and S12B). In the backgrounds containing the *ag-1* mutation, we detected continuous binding of FIE and EMF2 (Fig. 2C and fig. S12C). These results suggest that AG binds to the upstream region of *KNU* in a competitive manner with PcG proteins, evicting them from the locus, which would lead to the loss of H3K27me3 at the coding region.

KNU Upstream Regions Contain a Polycomb Response Element

PcG proteins are recruited to a specific site of target gene loci and then mediate the spread of H3K27me3 (18, 19). Originally found in *Drosophila*, the Polycomb response element (PRE) is responsible for the recruitment of PcG to specific genes, possibly through DNA binding proteins or noncoding RNAs (14, 15). The antagonistic localization of AG and PcG proteins on the same upstream region of *KNU* indicates that the region is necessary for the initial recruitment of PcG and, thus, for the prevention of ectopic *KNU* expression. To examine the function of PcG binding, we performed insertional mutagenesis of the PcG binding region of the *KNU-GUS* reporter construct (Fig. 2, D to H). When we inserted 6-bp unrelated nucleotide sequences immediately upstream of the first AG half-binding consensus sequence, the *KNU* reporter was ectopically expressed in the IMs of most of the independent transgenic lines (Fig. 2F and table S1). However, we observed no effects by the insertion of the same 6-bp fragment in 10- or 100-bp upstream regions (Fig. 2, G and H, and table S1). These results indicate that the region immediately adjacent to the first AG binding site may contain a PRE-like activity, which was at least partially perturbed by the insertion.

To further characterize the PRE-like activity of the *KNU* locus, we cloned the *KNU* upstream region containing the AG binding sites into a heterologous promoter, *pF3H*, with ubiquitous activity (20) and transformed the resulting constructs into *Arabidopsis* cultured cells (Fig. 3A). The shortest 153-bp fragment containing three AG binding sites retained the ability to almost fully silence the reporter expression, as did a longer fragment in the *KNU* upstream and the positive control *LEAFY COTYLEDON2* (*LEC2*) upstream region containing PRE-like activity (20) (Fig. 3, A to C, and fig. S13, A and B). High levels of H3K27me3 were deposited at the reporter coding region in transgenic lines containing the *KNU* 153-bp fragment but not in the negative control lines without any inserts (fig. S13C). These results suggest that the 153-bp fragment containing AG binding sites is sufficient to silence the heterologous promoter through the recruitment of PcG and deposition of H3K27me3 at the reporter coding region. Furthermore, the disruptive insertion, which caused the ectopic expression of the *KNU* reporter in plants, abolished the PRE activity in the cell line (Fig. 3, A and D).

To test whether the *KNU* PRE activity is transcription-dependent, we deleted the core pro-

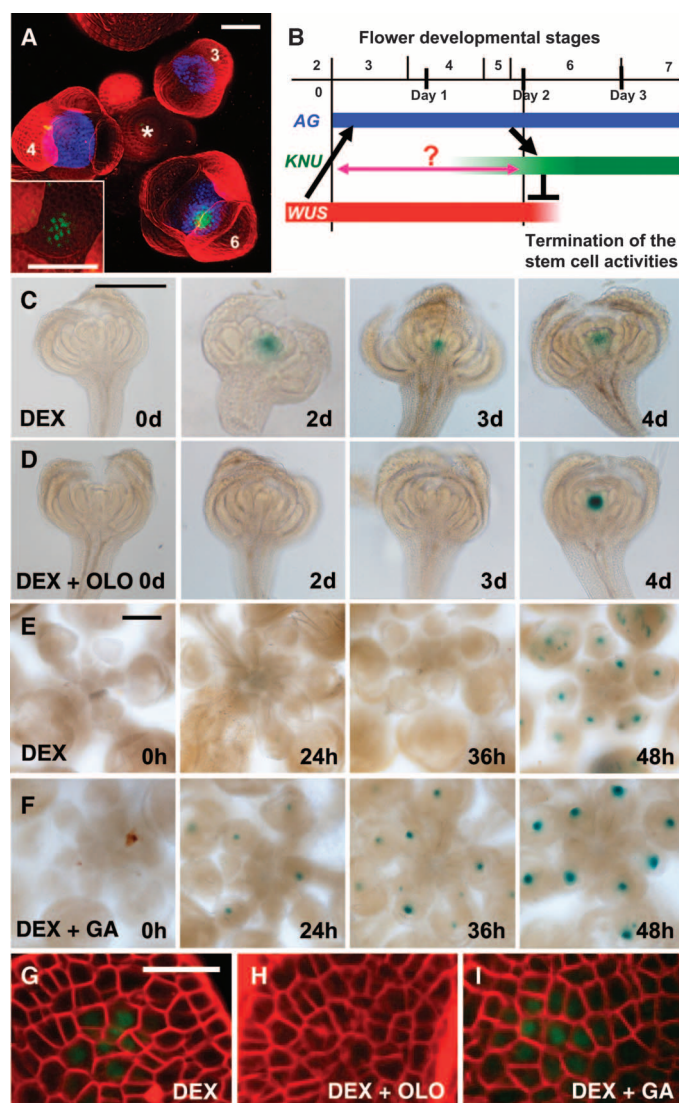
motor from the original constructs, abolishing the reporter expression regardless of the *KNU* PRE (fig. S13, D and E). Then, we tested the accumulation of the repressive marks by ChIP assay. We detected PRE-dependent accumulation of H3K27me3 in the reporter coding region (fig. S13F). This result indicates that the *KNU* PRE may have a transcription-independent activity in this context to recruit PcG and deposit the repressive marks.

Mimicking AG Functions by an Artificial Protein

The *KNU* PRE contains AG binding sites, and the binding of PcG and AG are complementary in flower development (Figs. 2, A to D, and 3A and figs. S11 and S12), leading to the AG-dependent reduction of the H3K27me3 marks (4). The Trithorax group (TrxG) transcriptional activator complexes counteract PcG activity and mediate the active H3K4 methylation marks (14). We examined the active marks at *KNU* in flower de-

velopment by ChIP assays using the *ap1 cal 35S::AP1-GR* inflorescences. The *KNU* coding region contains both the H3K4me2 and H3K4me3 marks, and our sequential ChIP assays with antibodies for H3K27me3 and H3K4me3 showed that the *KNU* locus contains the bivalent marks (fig. S14). During flower development, we noticed a progressive decrease in the H3K27me3 levels consistent with *KNU* activation (4), whereas the H3K4me2 and H3K4me3 levels remained unchanged (fig. S14, B and C). Therefore, AG does not affect H3K4me2 and H3K4me3, but H3K27me3. The simplest explanation for these results may be that the AG functions to physically block the binding of the PcG proteins from PRE, causing the dilution of the epigenetic repressive status through cell division. A similar sustained silencing by PcG has been suggested in assays of the *Drosophila* heat shock-induced clonal analysis of PcG (21, 22). Deletion of *Enhancer of Zeste* showed 2 to 3 days of delay

Fig. 1. *KNU* induction timing is cell division-dependent. (A) Confocal observations of the inflorescence doubly transgenic for *pAG::GFP* (blue) (8) and *pKNU::KNU-VENUS* (green), which rescues *knu-1*. *, SAM. Numbers, floral stages (39). (Inset) A higher magnification of the *KNU-VENUS* signal in a stage 5 to 6 floral bud. (B) Schematic diagram showing the developmental expression patterns of AG, *KNU*, and *WUS* in different floral stages. (C to F) GUS staining in *ag-1 35S::AG-GR pKNU::KNU-GUS* flowers at 0, 2, 3, and 4 days (C and D) or 0, 24, 36, and 48 hours (E and F) after treatment with 10 μ M DEX alone (C and E), 10 μ M DEX and 100 μ M olomoucine (OLO) (D), or 10 μ M DEX and 50 μ M gibberellic acid 3 (GA) (F). For better penetration of the cell cycle inhibitors and phytohormones, we pretreated the lines with these compounds twice in total, 1 day before the DEX treatment and again in combination with DEX. (G to I) Confocal observation of *ap1 cal 35S::AP1-GR pKNU::KNU-VENUS*, 2 days after treatment with 1 μ M DEX (G), 1 μ M DEX and 100 μ M OLO (H), or 1 μ M DEX and 50 μ M GA (I). Cells were stained with FM4-64 dye in (A) and (G) to (I). Scale bars, 50 μ m (A and inset), 100 μ m (C and D), 200 μ m (E and F), and 20 μ m (G to I).



before *HOX* misexpression was detected (22). To further examine the nature of the competitive binding between AG and PcG on the *KNU* locus, we tried to mimic the behavior of AG in vivo using an artificial protein (LacI-GR), which has the lactose operon repressor (lacI) DNA binding domain and a glucocorticoid hormone binding domain but no detectable transactivation activity (23–25) (Fig. 3E). In particular, two of the three AG half-binding consensus sequences on the *KNU* promoter were replaced by two *lac* operator (op) sequences, and the remaining one was mutated to prevent AG binding (Fig. 3E). We detected a clear DEX-dependent induction of *KNU* expression with a time lag of 3 days in most of the primary T1 transgenic plants and in selected T2 plants (Fig. 3, F to M, and tables S2 and S3). We noticed a weak basal level of expression without DEX treatment (Fig. 3, F and H to J), which may be caused by the weaker PRE-like activity due to the mutagenesis and/or the leaky effect of *35S::LacI-GR*. We further detected high levels of H3K27me3 on the coding region of the *GUS* reporter gene before the DEX treatment, and this level dropped on day 3 after the treatment (fig. S15). These results suggest that binding of the chimeric protein on the 2× op sequences can block the PcG complex binding and enable the

expression of *KNU* through the removal of the repressive marks, which mimics the endogenous function of AG in *KNU* induction.

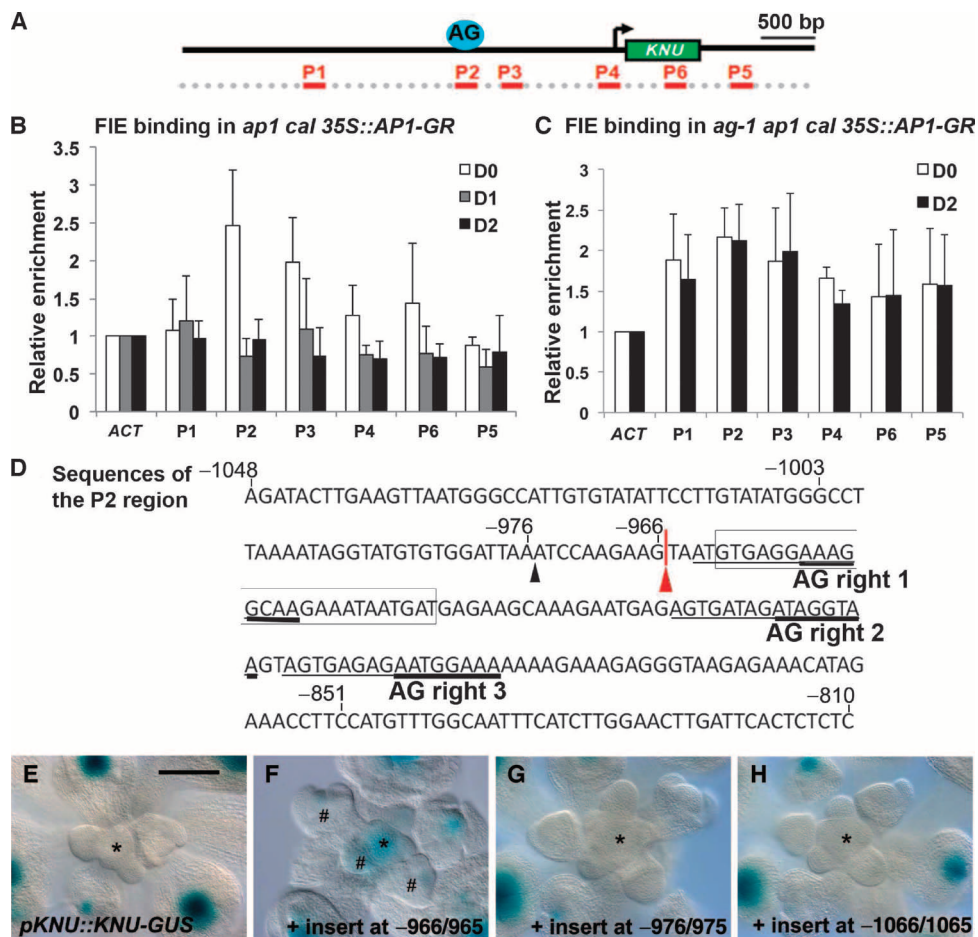
Creation of Cell Division–Dependent Epigenetic Timers

To test the logic of the timed induction of *KNU* based on the eviction of PcG proteins, we decided to reconstitute the “epigenetic timer” by simplifying the systems. We created a synthetic promoter combining the ubiquitous *pF3H* promoter and the short 50-bp PRE-like element of *LEC2* (20) (Fig. 3A) conjugated with two copies of op sequences in the 5′ and 3′ ends (fig. S16A). This chimeric reporter was silenced because of the PRE-like activity, but when the LacI-GR was induced, it should bind to the op sequences and physically interfere with factors binding to the PRE-like element, leading to their eviction and the subsequent induction of the reporter. After the DEX treatment, the fluorescence reporter was induced by 18 hours in the culture cells (fig. S16B). The reporter was resiled in 24 hours after a single DEX treatment. When the cells were pretreated with olomoucine, the induction was delayed and observed by 24 hours (fig. S16C).

We further tested the inducibility of the silenced reporter containing the *KNU* PRE (Fig. 3,

A to C) by cotransforming the AG protein, or a TAL (transcription activator–like) effector–based synthetic DNA binding protein (26), that is designed to recognize the sequences around the first AG binding site. Overexpression of AG by *35S::AG-GR* in the cultured cells could not activate the reporter (fig. S17), possibly because of the low binding affinity of the ectopically expressed AG to the *KNU* promoter. We then created and assayed the specific binding of the designer TAL by fusing the TAL DNA binding domain with a transcriptional activation domain (AD) and nuclear localization signal (NLS) (26). The transient assay in the leaf protoplasts revealed the specific induction of the endogenous *KNU*, showing that the TAL protein can bind to the upstream target sequence of *KNU* in vivo (fig. S18). We next induced the fusion protein between the TAL DNA binding domain, NLS, and the GR domain (which has no transcriptional activation domain) in the cultured cell lines containing the silenced reporter by *KNU* PRE (Fig. 4A). After a single DEX treatment, the reporter started to be induced in 20 hours, reached higher levels in 40 hours, and was resiled in 60 hours (Fig. 4B). The induction was clearly delayed by the olomoucine pretreatment and observed by 60 to 70 hours (Fig. 4C). Accordingly, the ChIP assay in these cells showed

Fig. 2. Polycomb group protein binding on *KNU* and cis activities. (A) Schematic diagram of the *KNU* locus and primer sets P1 to P6 used for the ChIP assays in (B) and (C). (B and C) ChIP assays using *ap1 cal 35S::AP1-GR pFIE::FIE-VENUS* (B) and *ag-1 ap1 cal 35S::AP1-GR pFIE::FIE-VENUS* (C) inflorescences harvested 0, 1, and 2 days after a single 1 μ M DEX treatment. Nuclear protein complexes were immunoprecipitated with an anti-GFP antibody, and the enriched DNA was used for quantitative PCR analysis. The y axis shows the relative enrichment with immunoglobulin G (IgG) as a control. The error bars represent SD based on three biological replicates. *ACTIN* (*ACT*) was used as a control gene for calibration. (D) Sequences of the *KNU* promoter, encompassing the P2 region from –1048 to –810 from the transcription start site (+1), which is bound by AG and PcG proteins. The 6-bp fragment (CATATG) was inserted at the position –966/–965 on the *KNU* promoter (red arrowhead). The three AG half-perfect binding consensus sequences are underlined (the full-length sequences are marked by thin lines). The boxed sequences show the target site for the TAL designer protein shown in Fig. 4. (E to H) *GUS* staining of the wild-type *pKNU::KNU-GUS* (E). The 6-bp insertion at the position –966/–965 caused ectopic and precocious *KNU* expression (shown by #) (F), whereas the same insertion at the –976/–975 [a small black arrowhead in (D)], 10 bp upstream (G) and –1066/–1065, 100 bp upstream sites (H) showed the same *KNU* expression pattern as the wild-type *pKNU::KNU-GUS* plants. *, IMs. Scale bar, 100 μ m.

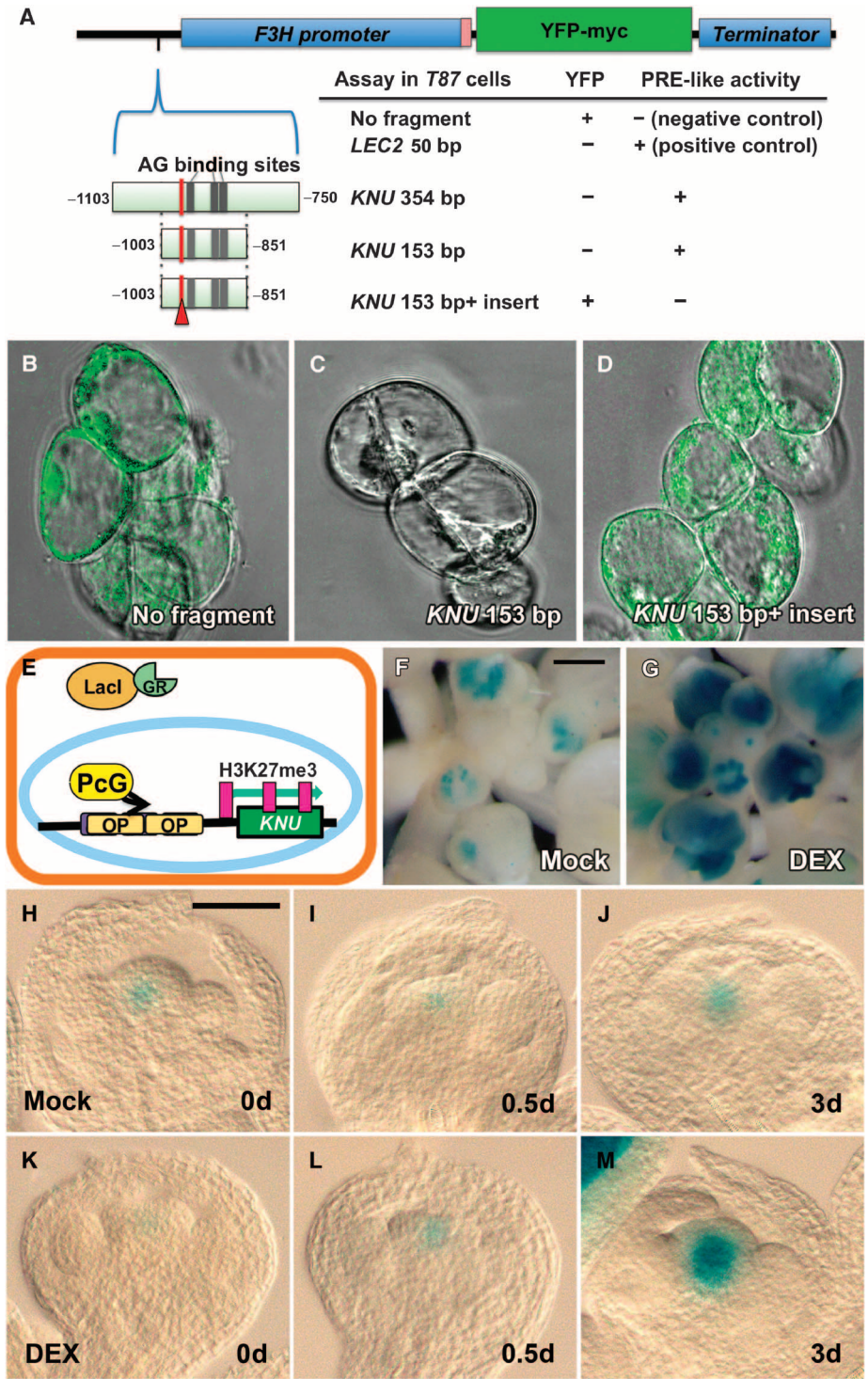


that H3K27me3 was reduced by 72 hours in the reporter coding region (fig. S19). When we fully blocked the cell cycle progression by the continuous olomoucine treatment, we did not observe the reporter induction (fig. S20). These results indicate that competitive eviction of PcG from PREs by DNA binding proteins leads to cell division-dependent delayed induction (Fig. 4D). The different timing in induction and resilencing

in these two systems may be due to the different PRE-like elements and different affinities of LacI and TAL DNA binding domains to the target sites. In *Drosophila* flp-mediated recombination assay of PREs in different transgenes, excision of PREs from the reporter genes led to loss of silencing at various timing from 12 hours to 2 to 3 days of considerable longer delay (27, 28). In *Arabidopsis*, LEAFY induces *AG* concomitantly

through the recruitment of chromatin-remodeling adenosine triphosphatase by antagonizing PcG activities (29). Thus, the displacement of PcG proteins by competitive transcription factor binding may be a general mechanism with different cell division dependence (see supplementary text for PcG and cell division). An interesting future subject would be to determine the factors controlling the duration of this epigenetic timer and link with

Fig. 3. Polycomb response element and simulation of AG. (A) Schematic diagram of the constructs to test the PRE activity of the fragment containing three AG binding sites (gray bars) on the *KNU* promoter and the disruptive insertion site that caused ectopic expression of the reporter in Fig. 2D (red arrowhead) and the summary of the assay in the *Arabidopsis* T87 culture cells. (B to D) T87 cells transgenic for the construct of *pF3H::YFP* alone (B) and the *pF3H::YFP* constructs conjugated with the 153-bp fragment, *pF3H-KNU PRE 153 bp::YFP* (C), and with the 153-bp fragment with the disruptive 6-bp insert, *pF3H-KNU PRE 153 bp+6 bp::YFP* (D). (E) Schematic diagram of the experiment to show that a chimeric protein with the lacI DNA binding domain (LacI) and glucocorticoid hormone binding domain (GR) partially mimics the function of AG to induce *KNU* expression by binding to the operator sequences (OP) upon DEX treatment and eviction of the PcG proteins. (F and G) GUS reporter staining 3 days after a single DEX treatment in T1 transgenic plants of *35S::LacI-GR pKNU-OP::KNU-GUS* treated with mock (F) and 10 μ M DEX (G). (H to M) Time course observation of T2 *35S::LacI-GR pKNU-OP::KNU-GUS* flowers treated with mock (H to J) or DEX (K to M) harvested at days 0 (H and K), 0.5 (I and L), and 3 (J and M) after a single 10 μ M DEX treatment. Scale bars, 25 μ m (B to D), 200 μ m (F and G), and 50 μ m (H to M).



cell cycle phase. This epigenetic timer can be used as a module to build time-responsive molecular circuits in synthetic biology.

Materials and Methods

Plant Materials and Chemical Treatments

All plants had the Landsberg *erecta* (Ler) background and were grown at 22°C under continuous light. Plant photographs were taken with a stereomicroscope (Carl Zeiss MicroImaging GmbH).

DEX (Sigma) treatments were conducted by inverting the plants and submerging the inflorescences for 1 min in a solution containing either 1 μ M DEX (for 35S::AP1-GR) or 10 μ M DEX (for 35S::AG-GR, 35S::LacI-GR and 35S::TAL-GR) together with 0.015% Silwet L-77. The time of the initial DEX treatment was taken as day 0 or 0 hour. Cell cycle inhibitors and phytohormones, applied at final concentrations of 50 μ M for roscovitine, 100 μ M for olomoucine, 35 μ M for aphidicolin, 500 μ M for cytokinin [benzylami-

nopurine (BAP)], and 50 μ M for gibberellic acid 3 (GA), were treated one time 24 hours before the DEX treatment for better penetration, as well as in combination with DEX at 0 hour. The mock treatments were conducted using the same method with the dipping solution without the chemicals.

For cultured cells, 10 μ M DEX was applied directly into the liquid cell culture medium at 0 hour. For cell cycle manipulation, the cells were pretreated with dimethyl sulfoxide for mock or 50 μ M olomoucine 1 day before the DEX treatment. Olomoucine was washed away at the time of DEX treatment or kept in the cultured medium for continuous treatment.

GUS Staining

GUS staining was performed as previously described (30) and observed in whole-mount samples in clearing solution with a Carl Zeiss MicroImaging stereomicroscope, or in paraffin sections with a Carl Zeiss Axioplan 2 microscope.

ChIP Assay

The ChIP experiments were performed as previously described (31) with slight modification. Inflorescences from *ap1 cal 35S::AP1-GR* were ground in liquid nitrogen and postfixed with 1% formaldehyde for 10 min. The chromatin was isolated and solubilized by sonication to generate DNA fragments with an average length of 400 bp. After incubation with salmon sperm DNA–protein A (for polyclonal antibody) or sperm DNA–protein G (for monoclonal antibody) agarose beads (Millipore), the solubilized chromatin was incubated overnight with anti-GFP (green fluorescent protein) antibody (Santa Cruz Biotechnology or Invitrogen), normal rabbit IgG (Santa Cruz Biotechnology), or anti-H3K27me3 antibody (Millipore or Abcam). The DNA fragments were recovered from the purified DNA–protein complexes and then used for enrichment tests by real-time polymerase chain reaction (PCR) analysis in triplicate. For the H3K27me3 ChIP, the ratio between the bound DNA after immunoprecipitation and the input DNA before immunoprecipitation was calculated for all the representative primer sets spanning the *KNU* genomic region, or for the primer sets on *GUS* or *yellow fluorescent protein* (YFP) reporters, and the ratios were plotted to show the relative changes in the levels of epigenetic marks. The relative enrichment for FIE and EMF2 proteins on the *KNU* locus was the ratio between the bound DNA after immunoprecipitation by anti-GFP over that by IgG. For sequential ChIP assay, cross-linked chromatin from the inflorescences was immunoprecipitated with monoclonal anti-H3K27me3 antibody (Abcam) as described above, except that chromatin was eluted in a solution of 30 mM dithiothreitol, 500 mM NaCl, and 0.1% SDS at 37°C (32). Eluted chromatin was subject to a second immunoprecipitation with monoclonal anti-H3K4me3 antibody (Abcam). In addition, a reversed sequential ChIP assay was performed in the sequence of application of anti-H3K4me3 antibody first, followed

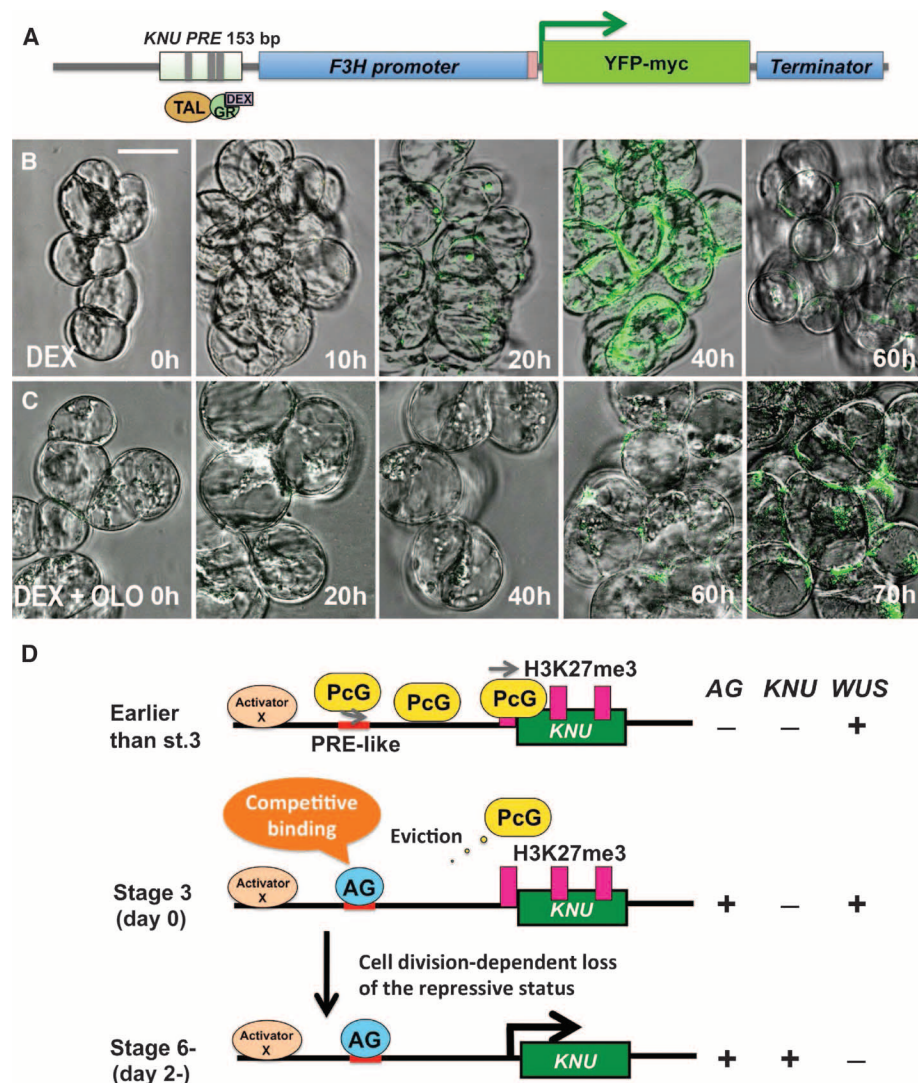


Fig. 4. Synthetic epigenetic timer and eviction model. (A) Schematic diagram of a synthetic epigenetic timer. *pF3H-KNU PRE 153 bp::YFP* was cotransformed with the 35S::TAL DNA binding domain-GR (TAL-GR) construct, which targets the region around the first AG binding site (boxed sequences in Fig. 2D) in the *Arabidopsis* T87 culture cells. (B and C) Time course confocal microscopy observation of the T87 cells transgenic for the constructs shown in (A). The cells were observed at 0, 10, 20, 40, 60, and 70 hours after a single 10 μ M DEX treatment. The cells were pretreated with mock (B) or 50 μ M olomoucine (OLO) (C) 1 day before the DEX treatment, and the inhibitor was washed away at the time of the DEX treatment. Scale bar, 25 μ m. (D) Schematic diagram of the *KNU* regulation. Earlier than stage 3 (corresponding to day 0 of *ap1 cal 35S::AP1-GR* floral buds), the *KNU* locus is covered by the H3K27me3 repressive mark, which is maintained by PcG. The *KNU* transcript cannot be induced because of the repressive marks. At stage 3, the AG protein, which is induced by WUS (6, 7), directly binds to the *KNU* promoter competitively with PcG, leading to eviction of PcG from the *KNU* locus. The eviction of PcG leads to cell division-dependent loss of the repressive status of *KNU* and the timed induction. Subsequently, WUS transcription is repressed by *KNU* (4), and floral stem cell activity is terminated with perfect timing.

by immunoprecipitation with anti-H3K27me3 antibody. For all ChIP experiments, the primers for the *Mu-like* transposon or the *ACT* gene were included as negative controls.

Vector Construction and Transgenic Selection

1) *pEMF2::EMF2-VENUS*, *pFIE::FIE-VENUS*, and *pKNU::KNU-VENUS* (fig. S21A) were produced as follows: The *EMF2* and *FIE* genomic regions were amplified from Col wild-type genomic DNA with the primer sets PSOKK131EMF2F/PSOKK132EMF2R and PSOKK162FIEF/PSOKK165FIER, respectively. The amplified *EMF2* and *FIE* genomic fragments were TA-cloned into pENTR-D TOPO vectors (Invitrogen). Subsequently, an Sfo I restriction site was introduced immediately before the stop codons of *EMF2* and *FIE* with the QuikChange Site-Directed Mutagenesis Kit (Stratagene). The *VENUS* fragment was generated by digestion of the vector *pRS316-VENUS* (33) with Sfo I. Then, the *VENUS* fragment flanked by Sfo I was introduced into the Sfo I sites in the above-mentioned *EMF2* or *FIE* genomic region, or Sfo I-digested *pKNU::KNU-GUS* (4) to replace the *GUS* fragment, to generate *pEMF2::EMF2-VENUS*, *pFIE::FIE-VENUS*, or *pKNU::KNU-VENUS*. Through LR reaction by Gateway LR Clonase II (Invitrogen), *pEMF2::EMF2-VENUS* or *pFIE::FIE-VENUS* was exchanged from the pENTR-D TOPO backbone to the destination vector pKGW (Invitrogen). *pKNU::KNU-VENUS* was exchanged from the pCR8 backbone to the destination vector CD3-694, pEarlyGate 303 (4).

2) Three *pKNU::KNU-GUS* lines with the 6-bp insertion at three different positions (fig. S21B) were produced as follows: First, a 996-bp *KNU* promoter fragment (from −1249 to −253 bp) flanked by Nde I sites, which contains the three AG binding sites, was cloned with the primer set PSOXYF68-KNU-NdeI-FP/PSOXYF69-KNU-NdeI-RP into pCR8 GW TOPO vector by TA cloning (Invitrogen). To test the positional effect of 6-bp insertion, PCR mutagenesis using the primer sets PSOXYF393/394, PSOXYF397/398, and PSOZM204/205 were performed to introduce one extra Nde I site at three different positions inside the above-mentioned 996-bp *KNU* promoter fragment and named *pKNUM3* (−966/−965), *pKNUM5* (−976/−975), and *pKNUM7* (−1066/−1065), respectively. The resulting 1002-bp promoter fragments were digested from *pKNUM3*, *pKNUM5*, and *pKNUM7* by partial digestion with Nde I (to keep the internal Nde I site intact but not the flanking ones) and introduced into a pCR8-based modified *pKNU::KNU-GUS* vector (by Nde I) (4) to replace the specific endogenous *KNU* promoter region. Subsequently, the entire cassettes of *pKNUM3::KNU-GUS*, *pKNUM5::KNU-GUS*, and *pKNUM7::KNU-GUS* were recombined into the destination vector pKGW by the LR reaction (Invitrogen).

3) *35S::LacI-GR pKNU-OP::KNU-GUS* (fig. S21C) was constructed as follows: To prevent AG binding, a 996-bp *KNU* promoter fragment (from −1249 to −253 bp) flanked by Nde I sites

was cloned from *pMutated KNU* with all three AG half binding sites mutated (from part ii) (4) into pCRII GW/TOPO vector and named *pCRII pMutated KNU NdeI*. Two copies of the op sequences were introduced to replace the second and third mutated AG half binding sites on pCRII *pMutated KNU NdeI* by four rounds of PCR mutagenesis with the primer sets PSOXYF399-OP1-F/PSOXYF400-OP1-R, PSOXYF401-OP2-F/PSOXYF402-OP2-R, PSOZM8MOP3_F/PSOZM9MOP3_R, and PSOZM10MOP4_F/PSOZM11 MOP4-R. Subsequently, the Nde I-flanked fragment harboring two copies of the op sequences was digested with Nde I and introduced into an Nde I-digested pCR8 *pKNU::KNU-GUS* to form the pCR8-based *pKNU-OP::KNU-GUS*. The resulting construct was further mutated by PCR with PSOZM50 KNUGUS NotI F/PSOZM51 KNUGUS NotI R to create a Not I site after the *KNU* 3' untranslated region for further cloning. The *35S::LacI-GR* fragment was obtained as follows: *LacI-GR* flanked by Sal I and Spe I was amplified by PCR with PSOZM12 LhGR_F/PSOZM13 LhGR_DB_R from vector pBJ36 (34). The *LacI-GR* was later introduced into the modified pGreen binary vector 0280 (35) with the same sites. The resulting pGreen-based product with a promoter and a terminator was further digested by Not I to obtain the Not I-flanked *35S::LacI-GR* fragment. Subsequently, the fragment was introduced into the Not I-digested vector pCR8 *pKNU-OP::KNU-GUS*, resulting in the entry vector pCR8 *35S::LacI-GR pKNU-OP::KNU-GUS*. The whole cassette was then recombined into pEarlygate303 CD3-694 (36) by the LR reaction (Invitrogen).

4) *pF3H::YFP* and *pF3H-RLE::YFP* (*RLE* from *LEC2*) (fig. S21D) were constructed as follows: The *YFP* fragment and terminator (*YFP CDS* followed by the *3myc* and *CaMV ter* fragments) was amplified by the primer set PSOZM161-YFP-F/PSOZM133-CaMV-terR from *p1002-35S-YFP-3myc-CaMV* to generate the cassette *35S-YFP-3myc-CaMV*. The resulting cassette was then digested with Asc I and introduced into the modified pENTR-D TOPO p1002 to create the *p1002-YFP*. The *F3H* fragment was amplified from *Arabidopsis Ler* genomic DNA by PSOZM153 F3HpF/PSOZM154 F3Hp-35SR, which contains the sequences for the *35S* core promoter. The fragment was then digested with Bgl II and Xho I and introduced into the *p1002-YFP* vector to create *pF3H::YFP* (fig. S21D), and *F3H* is followed by the *35S* core promoter *pF3H-RLE::YFP* (fig. S21D) was constructed by one round of PCR mutagenesis based on the template of *pF3H::YFP* with the primer set PSOZM159 F3H_iRLE F/PSOZM160 F3H_iRLE R, resulting in the insertion of an *RLE* fragment (20) into *pF3H::YFP* to generate *pF3H-RLE::YFP*.

pF3H-KNU PRE 354bp::YFP and *pF3H-KNU PRE 153bp::YFP* were constructed based on *pF3H::YFP* as follows: To create *pF3H-KNU PRE 354bp::YFP* (fig. S21E), the 354-bp fragment flanked by Bgl II was first amplified with

PSOZM142 KNU pro BglII F/PSOZM206 KNU pro BglII R from *pKNU::KNU-GUS* (4). Then, the fragment was introduced into *p1002 pF3H::YFP* to generate *pF3H-KNU PRE 354bp::YFP*. To create *pF3H-KNU PRE 153bp::YFP* (fig. S21E), the 153-bp fragment flanked by Bgl II was first amplified with PSOZM142 KNU pro BglII F/PSOZM143 KNU pro XhoI R from *pKNU::KNU-GUS* (4). Then, the fragment was introduced into *p1002 pF3H::YFP* to generate *pF3H-KNU PRE 153bp::YFP*.

5) *pF3H-KNU PRE 153bp+6bp insert::YFP*; *pOp-RLE-Op-F3H::YFP 35S::Lac-GR* (fig. S21F) were constructed as follows: For the *pF3H-KNU PRE 153bp+6bp insert::YFP* (fig. S21E), the 153-bp fragment was amplified from *pKNUM7*, which had an Nde I site at −1066/−1065. The fragment was introduced into *p1002 pF3H::YFP* to generate *pF3H-KNU PRE 153bp+6bp insert::YFP*. *pOp-RLE-Op-F3H::YFP* (fig. S21F) was created by two rounds of PCR mutagenesis with primer sets PSOZM175 F3H SopL F/PSOZM176 F3H SopL R and PSOZM177 F3H SopR F/PSOZM178 F3H SopR R sequentially to insert 1× op each into the 5' and 3' ends of the RLE sequences of *pF3H-RLE::YFP* to generate *pOp-RLE-Op-F3H::YFP*. *35S::LacI-GR* was constructed as follows: First, the *35S::LacI-GR-CaMVter* fragment was amplified by the primer set PSOZM187_35S F/PSOZM133CaMVter with pCR8 *pKNU-Op::KNU-GUS 35S::LacI-GR-CaMVter* as the template. Subsequently, the amplified fragment was digested with Asc I and introduced into pENTR-D TOPO p1002. The *CaMV* terminator was then replaced with the *Nos* terminator by mega-primer mutagenesis with the primer set PSOZM195_CaMV_NosF/PSOZM196_CaMV_NosR, resulting in the construct *p1002 35S::LacI-GR-Nos ter*. Next, the *pOp-RLE-Op-F3H::YFP* fragment was amplified with the primer set PSOZM153_F3Hp_F/PSOZM193_CaMV_ter NotIR. The fragment was later introduced into *p1002 35S::LacI-GR-Nos ter* through Bgl II and Not I sites to generate *pOp-RLE-Op-F3H::YFP 35S::LacI-GR* (fig. S21F).

6) *35S::TAL-GR* and *35S::TAL-AD* (fig. S21G) were created as follows: The *KNU* promoter 996-bp fragment, −1249 to −253 bp with an Nde I site on both ends, containing the three AG half binding sites, was input into an online tool (TAL Effector-Nucleotide Targeter, TALE-NT; <http://boglabx.plp.iastate.edu/TALENT/>). A 25-bp TALE sequence targeting the first AG half binding site was chosen as a good target site (Fig. 2D). TALC of pTAL1 vector (Addgene) contains NLSs and transactivation domain VP64 (AD). To create *35S::TAL-GR* (fig. S21G), a GR fragment including a hemagglutinin (HA) tag (861 bp) was first amplified from pGreen0281 plasmid (35) with the primer set PSOWY66_talBglIINdeI/GR/PSOZM192_talAscIHA. Subsequently, the amplified fragment was used as a primer to anneal to pTAL1 vector (Addgene), amplifying the whole plasmid, resulting in replacement of the 105-bp transactivation domain VP64 (AD) with GR to generate the *pTAL1-NLS-GR*. Next, the chosen 25-bp TALE sequence was created by golden gate reaction (Addgene) into the *pTAL1-NLS-GR* destination

vector to generate *pTAL1-TALE-NLS-GR*, followed by exchanging the cassette of *TALE-NLS-GR* into binary vector pMDC32 by LR reaction (Invitrogen) to generate *35S::TAL-GR* (fig. S21G). *35S::TAL-AD* was constructed by using golden gate reaction (Addgene) of the chosen 25-bp TALE sequence into pTAL1 (Addgene) to generate *pTAL1-25bpTALE-NLS-AD*, followed by exchanging the cassette of *25bpTALE-NLS-AD* into binary vector pMDC32 by LR reaction (Invitrogen) to generate *35S::TAL-AD* (fig. S21G).

7) *35S* core promoter deletion (*Acore promoter*) (fig. S21H) was created as follows: Both *pF3H::YFP* and *pF3H-KNU PRE 153bp::YFP* constructs were mutated by the KAPA PCR mutagenesis kit to delete 10 bp in the *35S* core promoter sequence using the PSOLS257-35sdel F/ PSOLS258-35sdelR primers. Subsequently, the transgenes were recombined into the destination vector KGW.

All clones from 1) to 7) (fig. S21) were fully sequenced for confirmation, and all the primers used for construction are listed in table S4. *pEMF2::EMF2-VENUS* and *pFIE::FIE-VENUS* (fig. S21A) were introduced into *ap1 cal 35S::API-GR*. All the *GUS* constructs from 2) and 3) (fig. S21, B and C) were introduced into wild-type *Ler* plants using the floral dipping method mediated by *Agrobacterium*. *pEMF2::EMF2-VENUS* and *pFIE::FIE-VENUS* T1 transgenic plants were selected on an MS solid medium plate with the antibiotic kanamycin at a concentration of 50 µg/ml. All the *GUS* reporter transgenic plants were selected on soil with the herbicide Basta 15 (Bayer; 0.2% of the commercial solution). Constructs from 4) to 7) (fig. S21, D to H) were introduced into T87 cultured cells, and transformation was performed as described below.

Arabidopsis Protoplast and Culture Cell Assay

The transient gene expression assay using *Arabidopsis* mesophyll protoplasts was performed as previously described (37). The stable *Arabidopsis* transgenic culture cells were established using T87 suspensions cells (38). Briefly, the cells were maintained in JPL3 medium under continuous illumination at 22°C with rotary shaking at 120 rpm as previously described (38). To generate transgenic lines, 2-week-old T87 cells were sieved through a 500-µm stainless mesh and resuspended in B5 medium supplemented with 1 µM 1-naphthaleneacetic acid and sucrose (30 g/liter). Cell suspension was cultured under continuous illumination at 22°C with shaking at 120 rpm for 1 day. Then, 2.5 µl of overnight cultured *Agrobacterium* transformed with the appropriate vectors was added to the cell suspension and cultured for a further 2 days. After cocultivation, the cell suspension was washed twice with 10 ml of JPL3 medium supplemented with carbenicillin (200 µg/ml) by centrifugation at 100g for 2 min. Finally, cells were resuspended in 3 ml of JPL3 medium and spread over a selection JPL3 agar plate supplemented with carbenicillin (250 µg/ml) and selection drugs. After 2 weeks of culture,

drug-resistant calli were transferred to fresh selection medium and maintained by subculture fortnightly. Kanamycin (30 µg/ml) and/or hygromycin B (12 µg/ml) were used for single/cotransformation on a plate. Kanamycin (25 µg/ml) and/or hygromycin B (7.5 µg/ml) were used for single/cotransformation in liquid medium. For reverse transcription PCR and ChIP assays, we used 1- to 2-week-old transgenic T87 suspension lines and collected ~0.2 ml of dry weight pellet by centrifugation at 100g for 2 min. For expression assay of the reporter lines, confocal microscopy images were taken with a Leica SP5 (as described below).

Confocal Microscopy Imaging

For the observation of the reporter lines in *Arabidopsis* inflorescences, the transgenic seeds were sowed on soil, and inflorescences were plucked and mounted on slides. The older floral buds were then carefully removed or spaced out to expose the SAM and early-stage floral buds. Dissected inflorescence was incubated with FM4-64 dye (50 µg/ml) for ~45 min on slides. Plants were imaged using a Zeiss LSM 510 upright (with motorized stage) confocal microscope with EC Plan-Neofluar 40×/1.30 oil differential interference contrast or Plan-Apochromat 20×/0.8 objective lens. GFP was stimulated with an argon laser at 488 nm at 60 to 70% of its output, with emission filtered using a 505- to 530-nm band-pass filter. VENUS was stimulated with an argon laser at 514 nm at 65 to 80% of its output, with emission filtered using a 530- to 600-nm band-pass filter. FM4-64 dye emission was filtered with a 585-nm long-pass filter. The z-stack was acquired using a 512-by-512-pixel frame, and the three-dimensional projections of the obtained z-stacks were then made with Zeiss LSM Image Browser version 4 and adjusted with Adobe Photoshop.

For the observation of T87 transgenic lines, 10 µl of cell suspension was mounted on slides and imaged using a Leica SP5 inverted confocal microscope with HCX PL APO 40×/1.25 objective lens. YFP was stimulated with an argon laser at 514 nm at 80% of its output, with emission filtered using a 520- to 550-nm band-pass filter. Images were acquired using 512 pixels by 512 pixels. Subsequently, images were made with Leica Application Suite Advanced Fluorescence v2.6.0 and adjusted with ImageJ v1.44 and Adobe Photoshop.

References and Notes

1. T. A. Steeves, I. M. Sussex, *Patterns in Plant Development* (Cambridge Univ. Press, Cambridge, ed. 2, 1989).
2. K. F. Mayer *et al.*, Role of *WUSCHEL* in regulating stem cell fate in the *Arabidopsis* shoot meristem. *Cell* **95**, 805–815 (1998). doi: [10.1016/S0092-8674\(00\)81703-1](https://doi.org/10.1016/S0092-8674(00)81703-1); pmid: [9865698](https://pubmed.ncbi.nlm.nih.gov/9865698/)
3. T. Payne, S. D. Johnson, A. M. Koltunow, *KNUCKLES (KNU)* encodes a C2H2 zinc-finger protein that regulates development of basal pattern elements of the *Arabidopsis* gynoecium. *Development* **131**, 3737–3749 (2004). doi: [10.1242/dev.01216](https://doi.org/10.1242/dev.01216); pmid: [15240552](https://pubmed.ncbi.nlm.nih.gov/15240552/)
4. B. Sun, Y. Xu, K. H. Ng, T. Ito, A timing mechanism for stem cell maintenance and differentiation in the *Arabidopsis* floral meristem. *Genes Dev.* **23**, 1791–1804 (2009). doi: [10.1101/gad.1800409](https://doi.org/10.1101/gad.1800409); pmid: [19651987](https://pubmed.ncbi.nlm.nih.gov/19651987/)
5. M. F. Yanofsky *et al.*, The protein encoded by the *Arabidopsis* homeotic gene *agamous* resembles transcription factors. *Nature* **346**, 35–39 (1990). doi: [10.1038/346035a0](https://doi.org/10.1038/346035a0); pmid: [1973265](https://pubmed.ncbi.nlm.nih.gov/1973265/)
6. J. U. Lohmann *et al.*, A molecular link between stem cell regulation and floral patterning in *Arabidopsis*. *Cell* **105**, 793–803 (2001). doi: [10.1016/S0092-8674\(01\)00384-1](https://doi.org/10.1016/S0092-8674(01)00384-1); pmid: [11440721](https://pubmed.ncbi.nlm.nih.gov/11440721/)
7. M. Lenhard, A. Bohnert, G. Jürgens, T. Laux, Termination of stem cell maintenance in *Arabidopsis* floral meristems by interactions between *WUSCHEL* and *AGAMOUS*. *Cell* **105**, 805–814 (2001). doi: [10.1016/S0092-8674\(01\)00390-7](https://doi.org/10.1016/S0092-8674(01)00390-7); pmid: [11440722](https://pubmed.ncbi.nlm.nih.gov/11440722/)
8. S. L. Urbanus *et al.*, In planta localisation patterns of MADS domain proteins during floral development in *Arabidopsis thaliana*. *BMC Plant Biol.* **9**, 5 (2009). doi: [10.1186/1471-2229-9-5](https://doi.org/10.1186/1471-2229-9-5); pmid: [19138429](https://pubmed.ncbi.nlm.nih.gov/19138429/)
9. S. Planchais, N. Glab, D. Inzé, C. Bergounioux, Chemical inhibitors: A tool for plant cell cycle studies. *FEBS Lett.* **476**, 78–83 (2000). doi: [10.1016/S0014-5793\(00\)01675-6](https://doi.org/10.1016/S0014-5793(00)01675-6); pmid: [10878255](https://pubmed.ncbi.nlm.nih.gov/10878255/)
10. T. Ito *et al.*, The homeotic protein AGAMOUS controls microsporogenesis by regulation of *SPOROCTELESS*. *Nature* **430**, 356–360 (2004). doi: [10.1038/nature02733](https://doi.org/10.1038/nature02733); pmid: [15254538](https://pubmed.ncbi.nlm.nih.gov/15254538/)
11. H. Stals, D. Inzé, When plant cells decide to divide. *Trends Plant Sci.* **6**, 359–364 (2001). doi: [10.1016/S1360-1385\(01\)00216-7](https://doi.org/10.1016/S1360-1385(01)00216-7); pmid: [11495789](https://pubmed.ncbi.nlm.nih.gov/11495789/)
12. F. Wellmer, M. Alves-Ferreira, A. Dubois, J. L. Riechmann, E. M. Meyerowitz, Genome-wide analysis of gene expression during early *Arabidopsis* flower development. *PLoS Genet.* **2**, e117 (2006). doi: [10.1371/journal.pgen.0020117](https://doi.org/10.1371/journal.pgen.0020117); pmid: [16789830](https://pubmed.ncbi.nlm.nih.gov/16789830/)
13. G. V. Reddy, M. G. Heisler, D. W. Ehrhardt, E. M. Meyerowitz, Real-time lineage analysis reveals oriented cell divisions associated with morphogenesis at the shoot apex of *Arabidopsis thaliana*. *Development* **131**, 4225–4237 (2004). doi: [10.1242/dev.01261](https://doi.org/10.1242/dev.01261); pmid: [15280208](https://pubmed.ncbi.nlm.nih.gov/15280208/)
14. R. Sawarkar, R. Paro, Interpretation of developmental signaling at chromatin: The Polycomb perspective. *Dev. Cell* **19**, 651–661 (2010). doi: [10.1016/j.devcel.2010.10.012](https://doi.org/10.1016/j.devcel.2010.10.012); pmid: [21074716](https://pubmed.ncbi.nlm.nih.gov/21074716/)
15. J. A. Simon, R. E. Kingston, Occupying chromatin: Polycomb mechanisms for getting to genomic targets, stopping transcriptional traffic, and staying put. *Mol. Cell* **49**, 808–824 (2013). doi: [10.1016/j.molcel.2013.02.013](https://doi.org/10.1016/j.molcel.2013.02.013); pmid: [23473600](https://pubmed.ncbi.nlm.nih.gov/23473600/)
16. A. Katz, M. Oliva, A. Mosquera, O. Hakim, N. Ohad, FIE and CURLY LEAF polycomb proteins interact in the regulation of homeobox gene expression during sporophyte development. *Plant J.* **37**, 707–719 (2004). doi: [10.1111/j.1365-3113X.2003.01996.x](https://doi.org/10.1111/j.1365-3113X.2003.01996.x); pmid: [14871310](https://pubmed.ncbi.nlm.nih.gov/14871310/)
17. N. Yoshida *et al.*, EMBRYONIC FLOWER2, a novel polycomb group protein homolog, mediates shoot development and flowering in *Arabidopsis*. *Plant Cell* **13**, 2471–2481 (2001). doi: [10.2307/3871588](https://doi.org/10.2307/3871588); pmid: [11701882](https://pubmed.ncbi.nlm.nih.gov/11701882/)
18. Y. B. Schwartz *et al.*, Genome-wide analysis of Polycomb targets in *Drosophila melanogaster*. *Nat. Genet.* **38**, 700–705 (2006). doi: [10.1038/ng1817](https://doi.org/10.1038/ng1817); pmid: [16732288](https://pubmed.ncbi.nlm.nih.gov/16732288/)
19. D. Schubert *et al.*, Silencing by plant Polycomb-group genes requires dispersed trimethylation of histone H3 at lysine 27. *EMBO J.* **25**, 4638–4649 (2006). doi: [10.1038/sj.emboj.7601311](https://doi.org/10.1038/sj.emboj.7601311); pmid: [16957776](https://pubmed.ncbi.nlm.nih.gov/16957776/)
20. N. Berger, B. Dubreucq, F. Roudier, C. Dubos, L. Lepiniec, Transcriptional regulation of *Arabidopsis* *LEAFY* *COTYLEDON2* involves *RLE*, a cis-element that regulates trimethylation of histone H3 at lysine-27. *Plant Cell* **23**, 4065–4078 (2011). doi: [10.1105/tpc.111.087866](https://doi.org/10.1105/tpc.111.087866); pmid: [22080598](https://pubmed.ncbi.nlm.nih.gov/22080598/)
21. D. Beuchle, G. Struhl, J. Müller, Polycomb group proteins and heritable silencing of *Drosophila* Hox genes. *Development* **128**, 993–1004 (2001). pmid: [11222153](https://pubmed.ncbi.nlm.nih.gov/11222153/)
22. J. Müller *et al.*, Histone methyltransferase activity of a *Drosophila* Polycomb group repressor complex. *Cell* **111**, 197–208 (2002). doi: [10.1016/S0092-8674\(02\)00976-5](https://doi.org/10.1016/S0092-8674(02)00976-5); pmid: [12408864](https://pubmed.ncbi.nlm.nih.gov/12408864/)

23. S. M. Hollenberg, R. M. Evans, Multiple and cooperative *trans*-activation domains of the human glucocorticoid receptor. *Cell* **55**, 899–906 (1988). doi: [10.1016/0092-8674\(88\)90145-6](https://doi.org/10.1016/0092-8674(88)90145-6); pmid: [3191531](https://pubmed.ncbi.nlm.nih.gov/3191531/)
24. A. M. Lloyd, M. Schena, V. Walbot, R. W. Davis, Epidermal cell fate determination in *Arabidopsis*: Patterns defined by a steroid-inducible regulator. *Science* **266**, 436–439 (1994). doi: [10.1126/science.7939683](https://doi.org/10.1126/science.7939683); pmid: [7939683](https://pubmed.ncbi.nlm.nih.gov/7939683/)
25. L. Swint-Kruse, K. S. Matthews, Allosteric in the LacI/GalR family: Variations on a theme. *Curr. Opin. Microbiol.* **12**, 129–137 (2009). doi: [10.1016/j.mib.2009.01.009](https://doi.org/10.1016/j.mib.2009.01.009); pmid: [19269243](https://pubmed.ncbi.nlm.nih.gov/19269243/)
26. T. Cermak *et al.*, Efficient design and assembly of custom TALEN and other TAL effector-based constructs for DNA targeting. *Nucleic Acids Res.* **39**, e82 (2011). doi: [10.1093/nar/gkr218](https://doi.org/10.1093/nar/gkr218); pmid: [21493687](https://pubmed.ncbi.nlm.nih.gov/21493687/)
27. A. Busturia, C. D. Wightman, S. Sakonju, A silencer is required for maintenance of transcriptional repression throughout *Drosophila* development. *Development* **124**, 4343–4350 (1997). pmid: [9334282](https://pubmed.ncbi.nlm.nih.gov/9334282/)
28. A. K. Sengupta, A. Kuhrs, J. Müller, General transcriptional silencing by a Polycomb response element in *Drosophila*. *Development* **131**, 1959–1965 (2004). doi: [10.1242/dev.01084](https://doi.org/10.1242/dev.01084); pmid: [15056613](https://pubmed.ncbi.nlm.nih.gov/15056613/)
29. M. F. Wu *et al.*, SWI2/SNF2 chromatin remodeling ATPases overcome polycomb repression and control floral organ identity with the LEAFY and SEPALLATA3 transcription factors. *Proc. Natl. Acad. Sci. U.S.A.* **109**, 3576–3581 (2012). doi: [10.1073/pnas.1113409109](https://doi.org/10.1073/pnas.1113409109); pmid: [22323601](https://pubmed.ncbi.nlm.nih.gov/22323601/)
30. T. Ito, H. Sakai, E. M. Meyerowitz, Whorl-specific expression of the *SUPERMAN* gene of *Arabidopsis* is mediated by *cis* elements in the transcribed region. *Curr. Biol.* **13**, 1524–1530 (2003). doi: [10.1016/S0960-9822\(03\)00612-2](https://doi.org/10.1016/S0960-9822(03)00612-2); pmid: [12956955](https://pubmed.ncbi.nlm.nih.gov/12956955/)
31. T. Ito, N. Takahashi, Y. Shimura, K. Okada, A serine/threonine protein kinase gene isolated by an in vivo binding procedure using the *Arabidopsis* floral homeotic gene product, AGAMOUS. *Plant Cell Physiol.* **38**, 248–258 (1997). doi: [10.1093/oxfordjournals.pcp.a029160](https://doi.org/10.1093/oxfordjournals.pcp.a029160); pmid: [9150601](https://pubmed.ncbi.nlm.nih.gov/9150601/)
32. B. E. Bernstein *et al.*, A bivalent chromatin structure marks key developmental genes in embryonic stem cells. *Cell* **125**, 315–326 (2006). doi: [10.1016/j.cell.2006.02.041](https://doi.org/10.1016/j.cell.2006.02.041); pmid: [16630819](https://pubmed.ncbi.nlm.nih.gov/16630819/)
33. M. G. Heisler *et al.*, Patterns of auxin transport and gene expression during primordium development revealed by live imaging of the *Arabidopsis* inflorescence meristem. *Curr. Biol.* **15**, 1899–1911 (2005). doi: [10.1016/j.cub.2005.09.052](https://doi.org/10.1016/j.cub.2005.09.052); pmid: [16271866](https://pubmed.ncbi.nlm.nih.gov/16271866/)
34. Y. Eshed, S. F. Baum, J. V. Perea, J. L. Bowman, Establishment of polarity in lateral organs of plants. *Curr. Biol.* **11**, 1251–1260 (2001). doi: [10.1016/S0960-9822\(01\)00392-X](https://doi.org/10.1016/S0960-9822(01)00392-X); pmid: [11525739](https://pubmed.ncbi.nlm.nih.gov/11525739/)
35. R. P. Hellens, E. A. Edwards, N. R. Leyland, S. Bean, P. M. Mullineaux, pGreen: A versatile and flexible binary Ti vector for *Agrobacterium*-mediated plant transformation. *Plant Mol. Biol.* **42**, 819–832 (2000). doi: [10.1023/A:1006496308160](https://doi.org/10.1023/A:1006496308160); pmid: [10890530](https://pubmed.ncbi.nlm.nih.gov/10890530/)
36. K. W. Earley *et al.*, Gateway-compatible vectors for plant functional genomics and proteomics. *Plant J.* **45**, 616–629 (2006). doi: [10.1111/j.1365-3113X.2005.02617.x](https://doi.org/10.1111/j.1365-3113X.2005.02617.x); pmid: [16441352](https://pubmed.ncbi.nlm.nih.gov/16441352/)
37. S. D. Yoo, Y. H. Cho, J. Sheen, *Arabidopsis* mesophyll protoplasts: A versatile cell system for transient gene expression analysis. *Nat. Protoc.* **2**, 1565–1572 (2007). doi: [10.1038/nprot.2007.199](https://doi.org/10.1038/nprot.2007.199); pmid: [17585298](https://pubmed.ncbi.nlm.nih.gov/17585298/)
38. Y. Ogawa *et al.*, Efficient and high-throughput vector construction and *Agrobacterium*-mediated transformation of *Arabidopsis thaliana* suspension-cultured cells for functional genomics. *Plant Cell Physiol.* **49**, 242–250 (2008). doi: [10.1093/pcp/pcm181](https://doi.org/10.1093/pcp/pcm181); pmid: [18178967](https://pubmed.ncbi.nlm.nih.gov/18178967/)
39. D. R. Smyth, J. L. Bowman, E. M. Meyerowitz, Early flower development in *Arabidopsis*. *Plant Cell* **2**, 755–767 (1990). doi: [10.2307/3869174](https://doi.org/10.2307/3869174); pmid: [2152125](https://pubmed.ncbi.nlm.nih.gov/2152125/)

Acknowledgments: We thank H. Li and K. Kanehara for their experimental help, G. C. Angenent for the *pAG::GFP* seeds, D. Voytas for Golden Gate TAL effector kit (through Addgene), and RIKEN BRC for the *Arabidopsis* T87 culture cells. We thank H. Yu and F. Berger for their comments on the manuscript. This work was supported by a research grant to T.I. from Temasek Life Sciences Laboratory (TLL), PRESTO (Japan Science and Technology Agency, 4-1-8 Honcho Kawaguchi, Saitama, Japan), and the National Research Foundation Singapore under its Competitive Research Programme (CRP Award NRF-CRP001-108). All the constructs made in this work are available from T.I. under a material transfer agreement with TLL.

Supplementary Materials
www.sciencemag.org/content/343/6170/1248559/suppl/DC1
 Supplementary Text
 Figs. S1 to S21
 Tables S1 to S4
 References (40–44)

15 November 2013; accepted 6 December 2013
[10.1126/science.1248559](https://doi.org/10.1126/science.1248559)

Exome Sequencing Links Corticospinal Motor Neuron Disease to Common Neurodegenerative Disorders

Gaia Novarino,^{1*†} Ali G. Fenstermaker,^{1*} Maha S. Zaki,^{3*} Matan Hofree,² Jennifer L. Silhavy,¹ Andrew D. Heiberg,¹ Mostafa Abdellateef,¹ Basak Rosti,¹ Eric Scott,¹ Lobna Mansour,⁴ Amira Masri,⁵ Hulya Kayserili,⁶ Jumana Y. Al-Aama,⁷ Ghada M. H. Abdel-Salam,³ Ariana Karminejad,⁸ Majdi Kara,⁹ Bulent Kara,¹⁰ Bitu Bozorgmehri,⁸ Tawfeq Ben-Omran,¹¹ Faezeh Mojahedi,¹² Iman Gamal El Din Mahmoud,⁴ Naima Bouslam,¹³ Ahmed Bouhouche,¹³ Ali Benomar,¹³ Sylvain Hanein,¹⁴ Laure Raymond,¹⁴ Sylvie Forlani,¹⁴ Massimo Mascaro,¹ Laila Selim,⁴ Nabil Shehata,¹⁵ Nasir Al-Allawi,¹⁶ P.S. Bindu,¹⁷ Matloob Azam,¹⁸ Murat Gunel,¹⁹ Ahmet Caglayan,¹⁹ Kaya Bilguvar,¹⁹ Aslihan Tolun,²⁰ Mahmoud Y. Issa,³ Jana Schroth,¹ Emily G. Spencer,¹ Rasim O. Rosti,¹ Naiara Akizu,¹ Keith K. Vaux,¹ Anide Johansen,¹ Alice A. Koh,¹ Hisham Megahed,³ Alexandra Durr,^{14,21} Alexis Brice,^{14,21,22} Giovanni Stevanin,^{14,21,22,23} Stacy B. Gabriel,²⁴ Trey Ideker,² Joseph G. Gleeson^{1‡}

Hereditary spastic paraplegias (HSPs) are neurodegenerative motor neuron diseases characterized by progressive age-dependent loss of corticospinal motor tract function. Although the genetic basis is partly understood, only a fraction of cases can receive a genetic diagnosis, and a global view of HSP is lacking. By using whole-exome sequencing in combination with network analysis, we identified 18 previously unknown putative HSP genes and validated nearly all of these genes functionally or genetically. The pathways highlighted by these mutations link HSP to cellular transport, nucleotide metabolism, and synapse and axon development. Network analysis revealed a host of further candidate genes, of which three were mutated in our cohort. Our analysis links HSP to other neurodegenerative disorders and can facilitate gene discovery and mechanistic understanding of disease.

Hereditary spastic paraplegias (HSPs) are a group of genetically heterogeneous neurodegenerative disorders with prevalence between 3 and 10 per 100,000 individuals (*1*). Hallmark features are axonal degeneration and progressive lower limb spasticity resulting from a loss of corticospinal tract (CST) function. HSP is classified into two broad categories, uncomplicated and complicated, on the basis of the presence of additional clinical features such as intellectual disability, seizures, ataxia, peripheral neuropathy, skin abnormalities, and visual defects. The condition displays several distinct modes of inheritance, including autosomal dominant, autosomal recessive, and X-linked. Several loci have been linked to autosomal recessive HSP (AR-HSP), from which 22 genes with mutations have been cloned. However, most of the underlying causes of HSP remain unidentified.

We analyzed 55 families displaying AR-HSP by whole-exome sequencing (WES). We identified the genetic basis in about 75% of the cases, greatly increasing the number of mutated genes in HSP; functionally validated many of these genes in zebrafish; defined new biological processes underlying HSP; and created an “HSPome” interaction map to help guide future studies.

Multiple Genes Are Implicated in HSP

We used WES to identify the genetic causes of AR-HSP in families with documented consanguinity. Selecting from these families without

congenital malformations referred for features of either complicated or uncomplicated HSP (table S1), we performed WES on 93 individuals typically from two affected siblings or cousins where possible, for multiplex families, or one affected and one unaffected sibling or both parents, for simplex families. We prioritized predicted protein frame shift, stop codon, splice defects, and conserved nonsynonymous amino acid substitution mutations [Genomic Evolutionary Rate Profile (GERP) score > 4 or phastCons (genome conservation) score > 0.9]. We excluded variants with an allele frequency of greater than 0.2% in our internal exome database of over 2000 individuals. We genotyped each informative member from the majority of families with a 5000 single-nucleotide polymorphism (SNP) panel and generated genome-wide parametric multipoint linkage plots or used WES data to generate homozygosity plots (*2*). We excluded variants falling outside of homozygous intervals <2.0 Mb threshold (fig. S1).

We tested segregation of every variant meeting these criteria (table S2). We report a candidate HSP gene only if there was a single deleterious variant that segregated in the family or if the gene was identified as mutated in multiple families (*3*). For 15 families, a single genetic cause could not be identified. We identified mutations in 13 genes known to be mutated in HSP (33% of the cases in our cohort) (table S3 and fig. S2), supporting the methodology. These include *EIF2B5*, associated with vanishing white-matter disease [Online Men-

delian Inheritance in Man (OMIM) no. 603896]; *CLN8*, associated with ceroid lipofuscinosis (OMIM 600143); and *ARG1*, which causes arginase deficiency (OMIM 207800). The diversity of genes identified speaks to the heterogeneity of HSP presentations. *ALS2* (OMIM 205100) was mutated in four different families presenting with uncomplicated HSP, and *ATL1* (OMIM 182600) was mutated in three different families, some displaying partial penetrance (*4*).

We identified 14 candidate genes not previously implicated in disease (Table 1), accounting for 42% of the cases in our cohort. We also evaluated five non-consanguineous families by WES, implicating one additional candidate gene. We estimated, on the basis of our false discovery rate (FDR), that fewer than 0.1 alleles per family should pass this threshold randomly, dependent on the number of informative meioses, suggesting that fewer than 1:10 genes identified with this method should prove false positive (i.e., identify by chance) (*3*).

The mutations in the 15 novel genes were identified in patients presenting with a spectrum of HSP phenotypes. Three of these genes, *ERLIN1*,

¹Howard Hughes Medical Institute, University of California, San Diego, La Jolla, CA 92093, USA. ²Department of Computer Science and Engineering and Department of Medicine, University of California, San Diego, La Jolla, CA 92093, USA. ³Clinical Genetics Department, Human Genetics and Genome Research Division, National Research Center, Cairo 12311, Egypt. ⁴Department of Pediatric Neurology, Neurometabolic Unit, Cairo University Children's Hospital, Cairo 406, Egypt. ⁵Division of Child Neurology, Department of Pediatrics, University of Jordan, Amman 11942, Jordan. ⁶Istanbul University, Istanbul Medical Faculty, Medical Genetics Department, 34093 Istanbul, Turkey. ⁷Department of Genetic Medicine, King Abdulaziz University, Jeddah, Kingdom of Saudi Arabia. ⁸Kariminejad-Najmabadi Pathology and Genetics Center, Tehran, Iran. ⁹Department of Pediatrics, Tripoli Children's Hospital, Tripoli, Libya. ¹⁰Kocaeli University, Medical Faculty, Department of Pediatric Neurology, 41380 Umuttepe, Kocaeli, Turkey. ¹¹Clinical and Metabolic Genetics Division, Department of Pediatrics, Hamad Medical Corporation, Doha 3050, Qatar. ¹²Mashhad Medical Genetic Counseling Center, 91767 Mashhad, Iran. ¹³Université Mohammed V Souissi, Equipe de Recherche de Maladies Neuro-dégénératives (ERMN) and Centre de Recherche en Épidémiologie Clinique et Essais Thérapeutiques (CRECET), 6402 Rabat, Morocco. ¹⁴Centre de Recherche de l'Institut du Cerveau et de la Moelle épinière, INSERM U1127, CNRS UMR7225; UPMC Univ Paris VI UMR S975, 75013 Paris, France. ¹⁵Department of Pediatrics and Neonatology, Saudi German Hospital, Post Office Box 84348, Riyadh, Kingdom of Saudi Arabia. ¹⁶Department of Pathology, School of Medicine, University of Dohuk, Dohuk, Iraq. ¹⁷Department of Neurology, National Institute of Mental Health and Neurosciences, Bangalore, India. ¹⁸Department of Pediatrics and Child Neurology, Wah Medical College, Wah Cantt, Pakistan. ¹⁹Department of Genetics and Neurosurgery, Yale University School of Medicine, New Haven, CT 06510, USA. ²⁰Department of Molecular Biology and Genetics, Bogazici University, 34342 Istanbul, Turkey. ²¹Assistance Publique—Hôpitaux de Paris, Fédération de Génétique, Pitié-Salpêtrière Hospital, 75013 Paris, France. ²²Institut du Cerveau et de la Moelle épinière, 75013 Paris, France. ²³Laboratoire de Neurogénétique, Ecole Pratique des Hautes Etudes, Institut du Cerveau et de la Moelle épinière, 75013 Paris, France. ²⁴Broad Institute of Harvard and Massachusetts Institute of Technology, Cambridge, MA 02142, USA.

*These authors contributed equally to this work.

†Present address: IST Austria (Institute of Science and Technology Austria), Klosterneuburg, Austria.

‡Corresponding author. E-mail: jogleeson@ucsd.edu

KIF1C, and *NT5C2*, were found independently mutated in more than one family, and all mutations were predicted to be highly deleterious. All but one was homozygous, whereas the non-consanguineous family 787, with four affected and six healthy children, displayed a compound heterozygous mutation. This approach thus identified a host of novel candidate genes for further investigation.

Extending Results to Larger HSP Cohort

An additional cohort of 200 patients diagnosed with HSP (5) were screened for mutations in these genes with exome sequencing or microfluidic polymerase chain reaction (PCR) followed by sequencing (3). Additional mutations in *ERLIN1*, *ENTPD1*, *KIF1C*, *NT5C2*, and *DDHD2* were identified (Table 1), thus validating these in the pathogenesis of HSP. Microfluidic PCR provided threshold coverage of only 68% of the targeted exons, suggesting that improved methods will be required to fully evaluate this second cohort. While this paper was in preparation, *DDHD2* was published as mutated in complicated HSP, cross-validating results (6).

Functional Testing Candidates with Expression and Zebrafish

To understand the potential role of these disease genes in HSP, we profiled their expression across multiple human tissues with reverse transcription PCR. Expression was specific to neural tissue for

the genes *FLRT1* and *ZFR*, suggesting a neuronal function (fig. S3). For most, however, we noted broadly distributed expression patterns, suggesting functions in other tissues but that neurons show increased susceptibility to genetic mutations.

To functionally validate the private genes (i.e., those mutated in a single family), we performed knockdown modeling in zebrafish. Phylogenetic analysis indicated a single zebrafish ortholog for the private genes *ARL6IP1*, *MARS*, *PGAP1*, and *USP8*. Morphants were phenotyped for lethality and defects in body axis (Fig. 1 and fig. S4), motor neuron morphology (fig. S5), and evoked and spontaneous swimming behavior, all relevant to HSP. Except for *mars* morphants, which were too severe to be analyzed completely, we identified phenotypes for all morphants in both touch-induced and spontaneous locomotion behavior, as previously reported for other HSP candidate genes (7). Although more work is warranted to conclusively uncover the role of the tested genes in CST degeneration, our in vivo functional validation supports the genetic data.

HSP-Related Proteins Interact Within a Network

To generate an HSPome containing all known and candidate genes as well as proximal interactors, we first created a protein network of all known human genes and/or proteins. We then extracted the subnetwork containing all previously published HSP mutated genes (seeds, table S4) to

derive the HSP seeds network and then extracted the subnetwork containing all seed genes plus candidate HSP genes (from Table 1) to derive the HSP seed + candidates network (Fig. 2A).

We tested whether the HSP seeds network was more highly connected than expected by chance. We compared the connectivity of the network comparing the 43 seeds to a background network generated by 10,000 permutations of randomly selected sets of 43 seeds from the global network using three different measures of connectivity: (i) the number of edges within the query set (within group edge count), (ii) the mean overlap in interaction neighborhoods between pairs of proteins in the query set (Jaccard similarity), and (iii) the mean random walk similarity (i.e., the expected “time” it takes to get from one protein to another when performing a random walk on the network) (8). By all three measures, we found the HSP seed proteins were more cohesive than expected at random ($P = 2.0 \times 10^{-04}$, $P = 1.3 \times 10^{-03}$, and $P = 1.5 \times 10^{-05}$) (Fig. 2B and supplementary data 1).

We also examined whether the HSP seed + candidates network, containing 43 seeds plus 15 candidates, was more highly connected than expected in a background of 10,000 random permutations (Fig. 2C). The addition of the candidates to the HSP seeds network resulted in a set significantly more highly connected than expected by chance ($P = 3.1 \times 10^{-02}$, $P = 1.2 \times 10^{-03}$, $P = 4.8 \times 10^{-04}$, respectively). We conclude that these newly

Table 1. Novel candidate HSP genes. List of novel candidate HSP genes identified through WES, divided into major functional modules (ERAD, etc.). OMIM nomenclature refers to established or new (beginning with SPG58) locus. Position refers to the Genome Browser release 19 map. Family 787 has a compound heterozygous mutation in the *MARS* gene. C, complicated; U, uncomplicated forms

Gene Symbol	Locus Nomenclature	Entrez Gene ID	Gene Name	Putative Biological Function	Family #	Position (hg19)	Nucleotide Change	Deduced Protein Change	Effect on Protein	Phenotype
Endoplasmic reticulum and ER-associated degradation (ERAD)										
<i>ARL6IP1</i>	<i>SPG61</i>	23204	ADP-ribosylation factor-like 6 interacting protein 1	Protein transport	827	chr16:18804609 TGTTT>T	c.576_579delAAAC	p.K193Ffs36X	Frameshift	C
<i>ERLIN1</i>	<i>SPG62</i>	10613	ER lipid raft associated 1	ER-associated degradation	786 1098 1598	chr10:101914679 G>A chr10:101943559 C>A chr10:101912067 CCTGGTA>C	c.C763T c.G149T c.862_868delACCAGG	p. R255X p. G50V p.del203-204YQ	Stop codon Missense Frameshift	U U
Endosome and membrane trafficking										
<i>KIF1C</i>	<i>SPG58</i>	10749	Kinesin family member 1C	Retrograde Golgi to ER transport	789 803 RBT53	chr17:4904143 G>A chr17:4925567 C>T Del	c.G183A c.C2191T -	Splice p.R731X -	N/A Stop codon Absent protein	C U C
<i>USP8</i>	<i>SPG59</i>	9101	Ubiquitin specific peptidase 8	Deubiquitinating enzyme	882	chr15:50769124 C>A	c.C928A	p.Q310K	Missense	C
<i>WDR48</i>	<i>SPG60</i>	57599	WD repeat domain 48	Regulator of deubiquitination	910	chr3:39135498 AAAG>A	c.1879_1881delAAG	p.del628E	Amino acid del	C
Nucleotide metabolism										
<i>AMPD2</i>	<i>SPG63</i>	271	Adenosine monophosphate deaminase 2	Deaminates AMP to IMP in purine nucleotide metabolism	1526	chr1:110167989 CT>C	c.318delT	p.C107Afs365X	Frameshift	C
<i>ENTPD1</i>	<i>SPG64</i>	953	Ectonucleoside triphosphate diphosphohydrolase 1	Hydrolyzes ATP and other nucleotides to regulate purinergic transmission	1242 1800	chr10:97605168 G>A chr10:97604339 G>T	c.G649A c.G719T	p.G217R p.E181X	Missense Stop codon	C C
<i>NT5C2</i>	<i>SPG65</i>	22978	5'-nucleotidase, cytosolic II	Preferentially hydrolyzes IMP, in both purine/pyrimidine nucleotide metabolism	659 1290 1549 NGT2 1829	chr10:104899162 C>T chr10:104850739 CT>C chr10:104853067 C>A chr10:104894653 C>T chr10:104861028 T>A	c.175+1G>A c.1225delA c.988-1G>T c.G86A c.A445T	Splice p.S409Vfs436X Splice p.R29X p.R149X	N/A Frameshift N/A Stop codon Stop codon	U C U U C
Lipid/Myelination related										
<i>ARSI</i>	<i>SPG66</i>	340075	Arylsulfatase family, member I	Hydrolyze sulfate esters Hormone biosynthesis	1349	chr5:149676845 A>AT	c.1641insA	p.C548Mfs559X	Frameshift	C
<i>DDHD2</i>	<i>SPG54</i>	23259	DDHD domain-containing protein 2	Phospholipase preferentially hydrolyzes phosphatidic acid	1675 1314	chr8:38103473 C>G chr8:38103270 C>T	c.1057+5C>G c.C859T	Splice p.R287X	N/A Stop codon	C C
<i>PGAP1</i>	<i>SPG67</i>	80055	Post-GPI attachment to proteins 1	GPI biosynthesis	1241	chr2:197712670 C>A	c.1952+1G>T	Splice	N/A	C
Axon guidance/synapse related										
<i>FLRT1</i>	<i>SPG68</i>	23769	Fibronectin leucine rich transmembrane protein 1	Cell adhesion and receptor signaling	709	chr11:63885762 T>C	c.T2023C	Stop-loss	Stop-loss	C
<i>RAB3GAP2</i>	<i>SPG69</i>	25782	RAB3 GTPase activating protein subunit 2	Exocytosis of neurotransmitters and hormones	738	chr1:220357421 A>C	c.T1955G	p.L252X	Stop codon	C
Other										
<i>MARS</i>	<i>SPG70</i>	4141	Methionyl-tRNA synthetase	Cytosolic methionyl-tRNA synthetase	787	chr12:57881886 G>A chr12:57908741 C>T	c.G13A;c.C2104T	p.V5M;p.R702W	Missense Missense	C
<i>ZFR</i>	<i>SPG71</i>	51663	Zinc finger RNA binding protein	RNA localization?	1611	chr5:32406955 A>G	c.T956C	p.L319P	Missense	U

of HSP. ADP, adenosine diphosphate; IMP, inosine monophosphate; ATP, adenosine triphosphate; DDHD, Asp-Asp-His domain; GPI, glycosyl phosphatidylinositol; GTPase, guanosine triphosphatase; tRNA, transfer RNA. N/A, not applicable. Single-letter amino acid abbreviations are as follows: C, Cys; E, Glu; F, Phe; G, Gly; I, Ile; K, Lys; L, Leu; P, Pro; Q, Gln; R, Arg; S, Ser; T, Thr; V, Val; and X, termination.

identified genes are more cohesive than would be expected with candidates selected at random.

To identify proximal interactors, we expanded the global network by including HumanNet protein interaction database (9) and literature-curated interactions from STRING (10) to derive an expanded global network (fig. S6). This network propagation method assigns a priority score to each protein within the network (11). From this expanded network, we extracted the expanded HSP seeds network and found that 7 of the 15 newly identified candidates have significant support in the network (*ARSI*, *DDHD2*, *ERLIN1*, *FLRT1*, *KIF1C*, *PGAP1*, and *RAB3GAP2*, FDR < 0.1). Genes involved in biochemical pathways, such as *NT5C2*, *AMPD2*, and *ENTPD1*, did not emerge from this analysis, probably because of a lack of metabolic network edges in the input networks. Proteins that were not well characterized or represented in public databases also did not show enrichment.

We next expanded the HSP seed + candidate network to derive the HSPome (i.e., HSP seeds + candidates + proximal interactors network), allowing a global view of HSP and flagging other potential genes that may be mutated in HSP patients. The HSPome contains 589 proteins (i.e., potential HSP candidates) (supplementary data 2 and table S5).

Implied Causal Genes Suggest Modules of HSP Pathology

Studies in HSP consistently report an ascending axonal CST degeneration (12), but the processes modulating this degeneration are not well defined. Supporting the hypothesis that individual rare mutations in distinct genes may converge on specific biological pathways, we identified major modules involved in the pathophysiology of HSP. Several HSP genes have previously implicated endoplasmic reticulum (ER) biology (i.e., *ATL1*, *REEP1*, *RTN2*, and *SPAST*) and the ER-associated

degradation (ERAD) pathway (i.e., *ERLIN2*) (13–15). From the HSPome, we focused on this ER subnetwork containing the newly identified genes *ARL6IP1* and *ERLIN1* (fig. S7). *ARL6IP1* encodes a tetraspan membrane protein localized to the ER, composed of highly conserved hydrophobic hairpin domains implicated in the formation of ER tubules (16). We overexpressed *ARL6IP1* in cells and noted dramatically altered ER shape (fig. S7). The ERAD system controls protein quality control, critical for cellular adaptation to stress and survival. *ERLIN1* encodes a prohibitin-domain-containing protein localized to the ER that forms a ring-shaped complex with *ERLIN2*, further implicating defective ERAD in HSP etiology.

We identified an endosomal and membrane-trafficking subnetwork composed of seeds and candidates *KIF1C*, *USP8*, and *WDR48*, implicating the endosomal sorting complexes required for transport (ESCRT) pathway (fig. S8). *USP8*

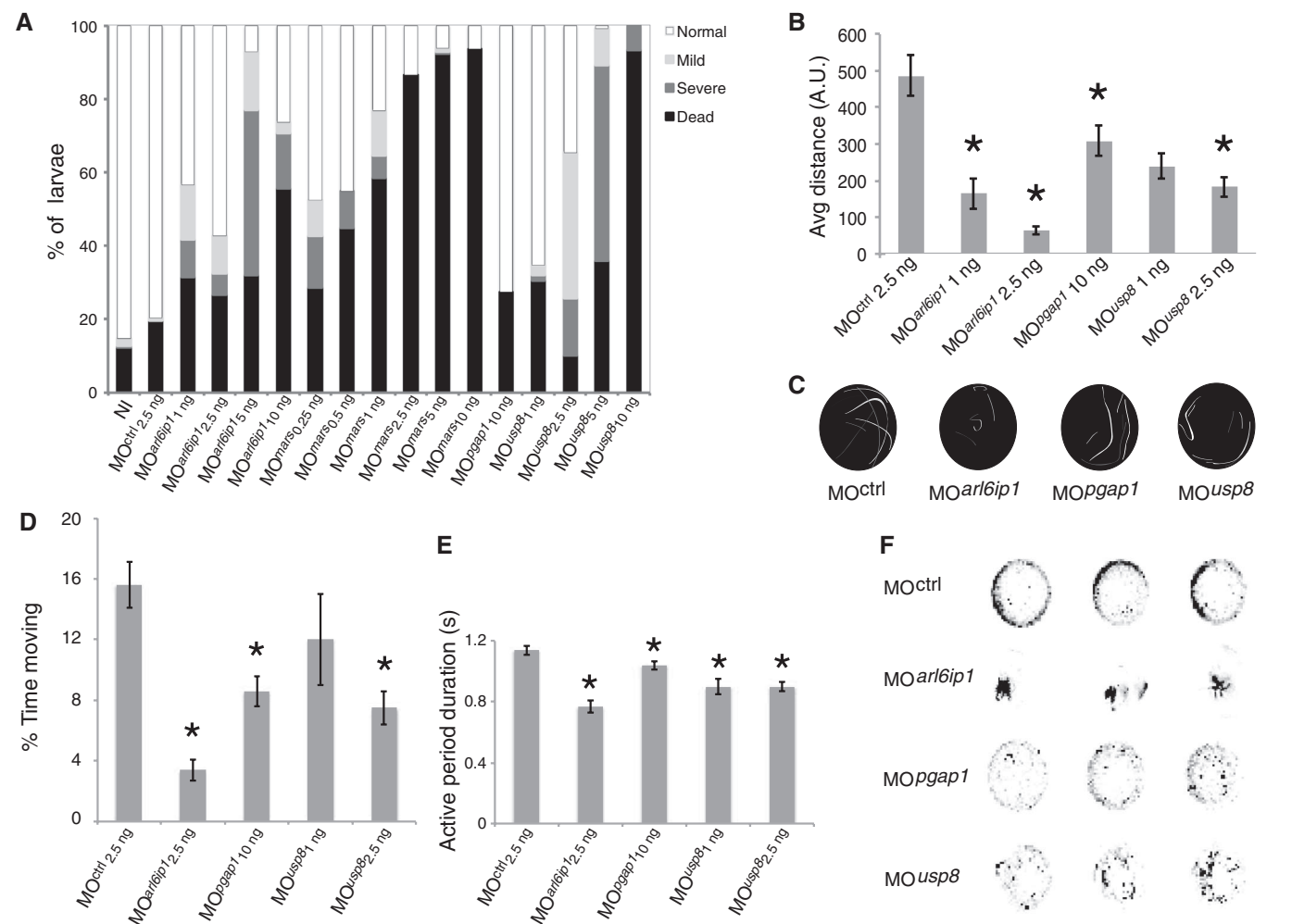


Fig. 1. Functional validation of private HSP genes in zebrafish. (A) Quantification of 24-hours-post-fertilization (hpf) embryos mortality (black) and curly-tail (gray) phenotypes for noninjected (NI), scrambled, and morphants (MO) at stated nanogram concentrations. Overt phenotypes were observed for all MOs except MO^{pgap1}. (B) Average touch-response distance (in arbitrary units, A.U.) in 72-hpf larvae, showing blunted response for all MOs. (C) Immediate touch-response trajectory of example larvae, each shaded uniquely. *Mars2* MO was too severe to be tested, whereas others showed reduced response.

(D to F) Spontaneous locomotion at 6 days post fertilization. (D) Average percent of time spent moving over a 30-min window showed a reduction for all for at least one dose. (E) Average active period duration, showing reduction for all. (F) Representative kymographs recording fish position (black dot) over 30-min recording. MOs showed either short distance traveled (MO^{ar6ip1}) or reduced movements per recording (MO^{pgap1} and MO^{usp8}). **p* < 0.01 (t test). *N* > 2 experiments with *n* > 20 animals per experiment. Error bars indicate standard error.

encodes a deubiquitinating enzyme (DUB) in the ESCRT pathway (17). The *WDR48*-encoded protein forms stable complexes with multiple DUBs, such as USP1, USP12, and USP46, and is required for enzymatic activity and linked to lysosomal trafficking (18, 19). *KIF1C* encodes a motor protein localized to the ER/Golgi complex, suggesting a role in trafficking (20). To validate the effect of the putative splicing mutation in family 789, we obtained fibroblasts and confirmed skipping of exon 4 (fig. S9). Defects in ESCRT are linked to neurodegenerative disorders such as frontotemporal dementia, Charcot Marie Tooth disease, and recently AR-HSP (21–23). Additionally, the HSP gene products SPG20, SPAST, and ZFYVE26 interact with components of this complex (24–26). Taken together, this suggests that disruptions in ESCRT and endosomal function can lead to HSP and other forms of neurodegeneration.

AMPD2, *ENTPD1*, and *NT5C2* are involved in purine nucleotide metabolism (fig. S10). Nucleotide metabolism is linked to the neurological disorder Lesch-Nyhan disease, among others (27), but was not previously implicated in HSP. *AMPD2*

encodes one of three adenosine monophosphate (AMP) deaminase enzymes involved in balancing purine levels (28). Mutations in *AMPD2* have been recently linked to a neurodegenerative brainstem disorder (28). In addition, the deletion we have identified in this study affects just the longest of the three *AMPD2* isoforms, indicating that the most N-terminal domain of *AMPD2* is important to prevent motor neuron degeneration. *ENTPD1* encodes an extracellular ectonuclease hydrolyzing adenosine nucleotides in the synaptic cleft (29). *NT5C2* encodes a downstream cytosolic purine nucleotide 5' phosphatase. Purine nucleotides are neuroprotective and play a critical role in the ischemic and developing brain (29); thus, alterations in their levels could sensitize neurons to stress and insult. *ENTPD1* was recently identified as a candidate gene in a family with nonsyndromic intellectual disability, but *HSP* was not evaluated (30).

Candidate HSP Genes Identified by Network Analysis

For families that were not included in our initial analysis, we interrogated our exome database for

variants in genes emerging from the extended HSPome network. By using this method, we identified potentially pathogenic variants in *MAG*, *BICD2*, and *REEP2*, found in homozygous intervals in three families (Fig. 3), validating the usefulness of the HSPome to identify new HSP genes. Interacting with *KIF1C* in the HSPome is *CCDC64*, encoding a member of the Bicaudal family (31), a paralog of the *BIC2* gene that emerged in the HSPome (FDR < 0.05, table S5). Family 1370 displays a homozygous Ser⁶⁰⁸→Leu⁶⁰⁸ missense change in the *BIC2* gene within a homozygous haplotype. The *Drosophila* bicaudal-D protein is associated with Golgi-to-ER transport and potentially regulates the rate of synaptic vesicle recycling (32). Coimmunoprecipitation confirmed that *BICD2* physically interacts with *KIF1C* (fig. S11). Recently, a mutation in *BICD2* was implicated in a dominant form of HSP (33).

MAG was identified as a significant potential HSP candidate (FDR < 0.05) from the HSPome, interacting with *PLP1*, the gene product mutated in *SPG2*. *MAG* is a membrane-bound adhesion protein implicated in myelin function, and knockout

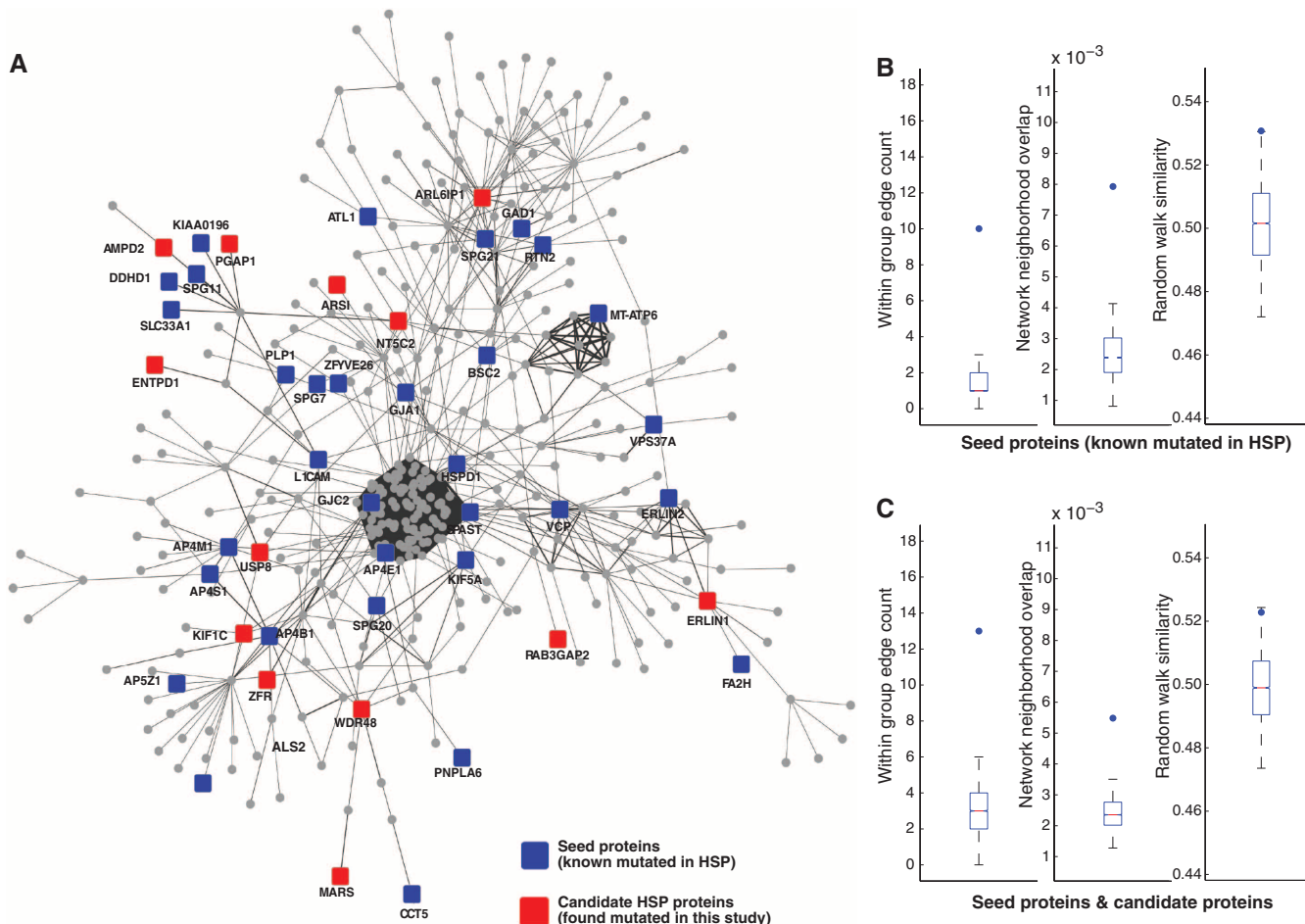


Fig. 2. Hereditary spastic paraplegia interactome. (A) HSP seeds + candidate network (edge-weighted force-directed layout), demonstrating many of the genes known to be mutated in HSP (seeds, blue) and new HSP candidates (red), along with others (circles) constituting the network. (B and C) Comparison of statistical strength of HSP subnetworks with 10,000 permutations of randomly selected proteins. Dots denote the value of the metric on the true set (i.e., seeds

or seeds + candidates). Box and whisker plots denote matched null distributions (i.e., 10,000 permutations). (B) Seed (known mutated in HSP) versus random proteins drawn with the same degree distribution. (C) Seed plus candidate HSP versus a matching set of proteins. (Left) Within group edge count (i.e., number of edges between members of the query set). (Middle) Interaction neighborhood overlap (i.e., Jaccard similarity). (Right) Network random walk similarity.

mice display defects of the periaxonal cytoplasmic collar in the spinal cord with later oligodendrocyte degeneration (34). MAG was found mutated in family 1226, displaying a homozygous Cys⁴³⁰→Gly⁴³⁰ missense mutation. *REEP2* encodes the receptor expression-enhancing protein 2, a paralog of *REEP1*, mutated in *SPG31* (35). Family 1967 displays a homozygous Met¹→Thr¹ mutation in *REEP2* removing

the canonical start codon and is mutated in a second recessive HSP family in an independent cohort (36). All of these gene mutations segregated with the phenotype in the family according to recessive inheritance and were not encountered in our exome database, consistent with pathogenicity. Although further validation of these three candidates is necessary in larger cohorts, the data suggest the HSPome can be

useful to identify HSP-relevant pathways and genes.

Link Between HSP and Neurodegenerative Disease Genes

Some of the genes we identified in this cohort have been previously associated with other neurodegenerative disorders (e.g., *CLN8*, *EIF2B5*, and *AMPD2*) primarily affecting areas of the nervous system other than the corticospinal tract. Prompted by this observation, we used the network to examine the similarity of HSP genes (seed + candidates) to other common neurological disorders. By using the random walk distance, we found that the set of HSP seeds plus candidates is significantly overlapping with sets of genes previously implicated in three neurodegenerative disorders, amyotrophic lateral sclerosis (ALS), Alzheimer’s disease, and Parkinson’s disease ($P = 1.1 \times 10^{-02}$, $P = 7.6 \times 10^{-03}$, $P = 1.6 \times 10^{-02}$, respectively) (Fig. 4). In contrast, we did not find a similar association with sets for representative neurodevelopmental disorders such as autism spectrum disorders and epilepsy ($P = 0.49$ and $P = 0.51$, respectively; fig. S12), nor with nonneurological disorders represented by heart and pulmonary disorders.

Discussion

By using WES, we identified 18 previously unknown candidates for AR-HSP (fig. S13), three of which (*ERLIN1*, *KIF1C*, and *NT5C2*) alone explain almost 20% of this cohort. These new candidates are predicted to display near 100% risk of HSP when mutated (37). All mutations were predicted as damaging to protein function, probably resulting in null or severely reduced function, consistent with the recessive mode of inheritance. In about 25% of the families a single candidate gene mutation could not be identified, probably a result of two factors: (i) Some mutations are in noncoding regions. (ii) Some causative mutations within the exome do not stand out more than other variants.

Four of our candidate HSP genes are located within previously identified loci for AR-HSP for which genes were not known: *ENTPD1*, *NT5C2*, *ERLIN1*, and *MARS*. Both *ERLIN1* and *NT5C2* are in the *SPG45* locus (38) and *ENTPD1* resides in *SPG27* (39). Recently, the *MARS2* gene, encoding a methionyl-tRNA synthetase, was implicated in the spastic ataxia 3 (*SPAX3*) phenotype (40). *KIF1C* is within the spastic ataxia 2 (*SAX2*) locus (41). On the basis of our findings, we returned to the original *SPAX2* family and identified a homozygous deletion of exons 14 to 18, confirming *KIF1C* as the *SPAX2* gene (fig. S14).

Our data support the idea that rare genetic mutations may converge on a few key biological processes, and our HSP interactome demonstrates that many of the known and candidate HSP genes are highly connected. This highlights important biological processes, such as cellular transport, nucleotide metabolism, and synapse and axon development. Some of the HSP gene modules suggest potential

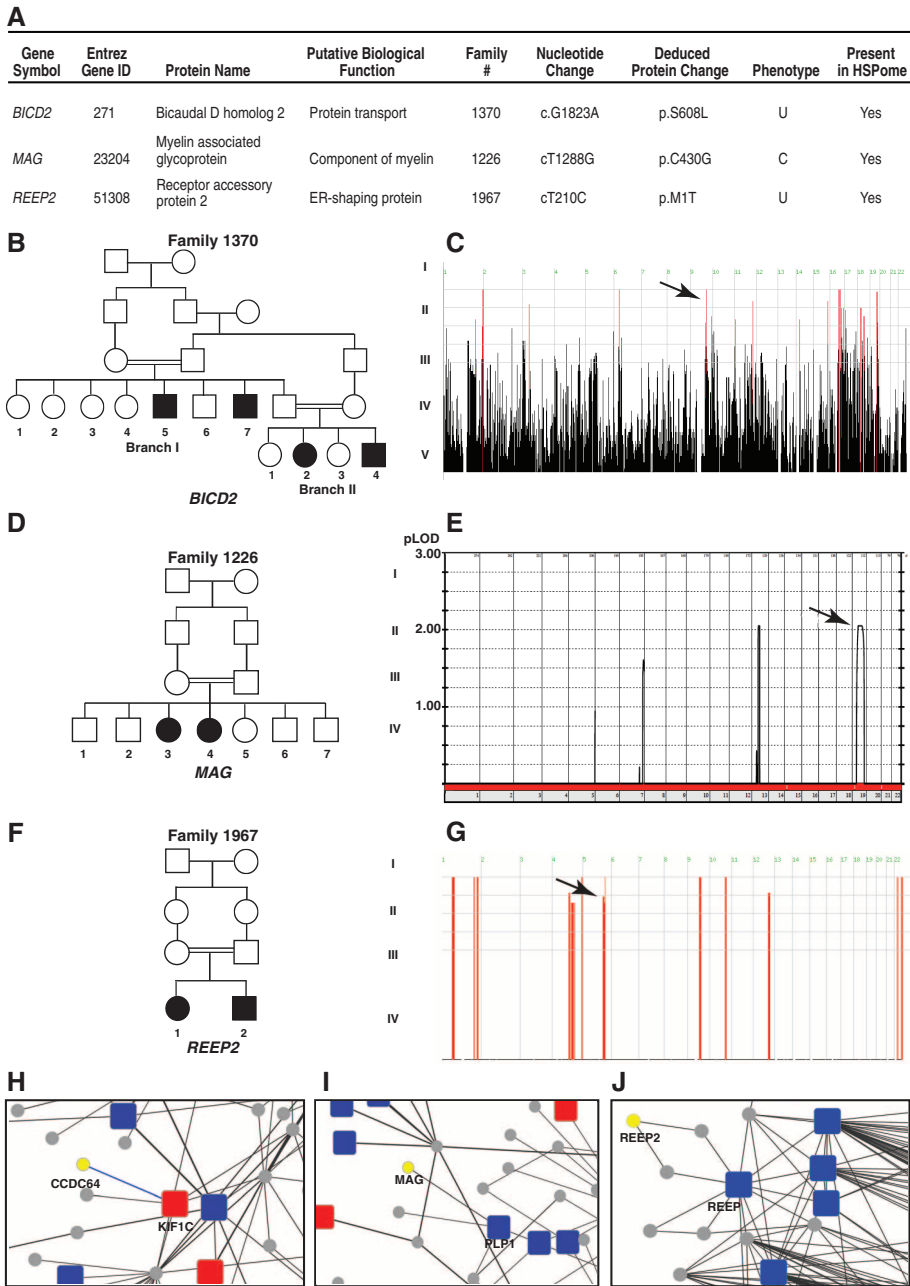


Fig. 3. Genes from HSP networks found mutated in HSP. (A) HSP candidate genes predicted from the HSPome found mutated in the HSP cohort. *BICD2*, *MAP*, and *REEP2* were subsequently found mutated in HSP families 1370 (B), 1226 (D), and 1967 (F), respectively. (C) Homozygosity plot from family 1370. Red bars, regions of homozygosity; arrow, homozygous block containing *BICD2*. (E) Linkage plot of family 1226; arrow, *MAG* locus. (G) Homozygosity plot; arrow, *REEP2* locus. (H to J) Zoom in from HSPome for specific interaction identifying candidates CCDC64 (a paralog of *BIC2D*), *MAG*, and *REEP2* (yellow) with previously published (blue) and newly identified (red) genes mutated in HSP. Blue lines denote manually curated interactions.

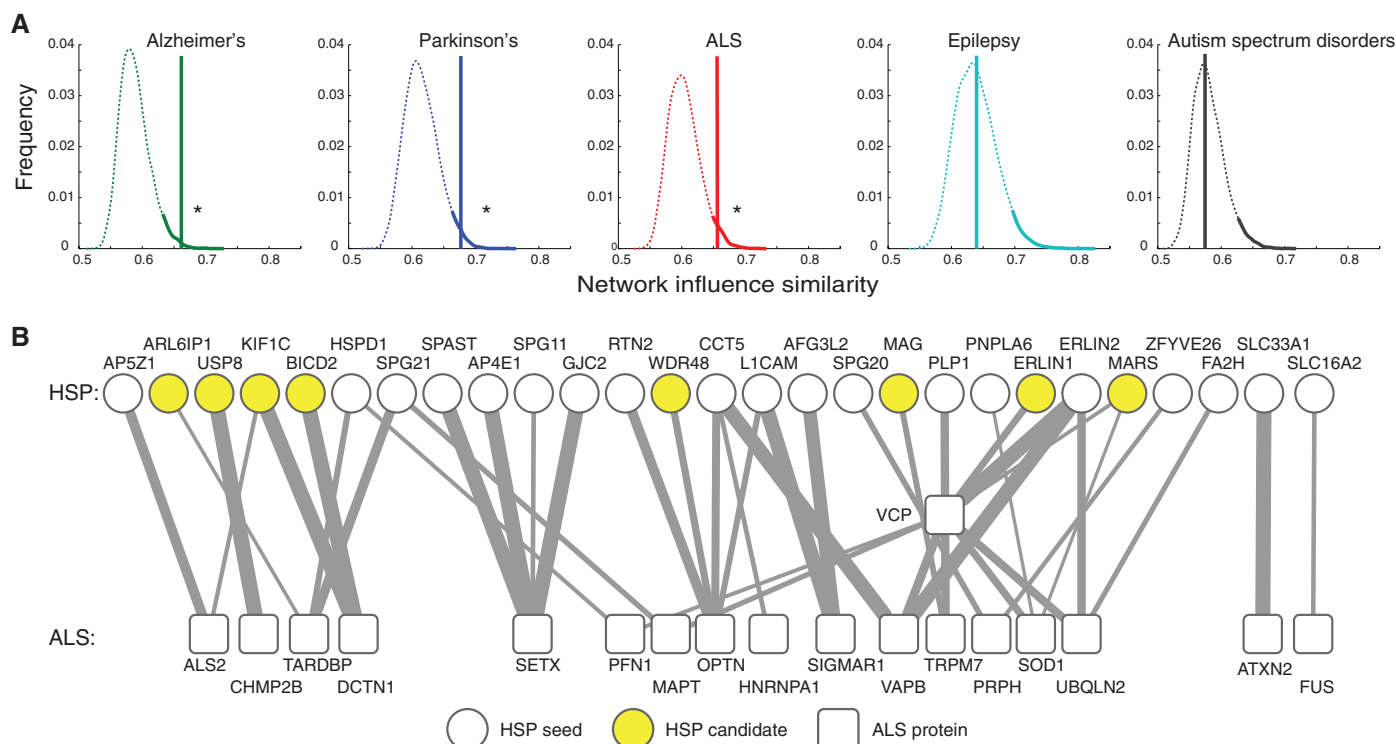


Fig. 4. Functional link between HSP genes and genes of other neurodegenerative conditions. (A) Density distribution representing random walk distances of OMIM-derived neurodegeneration gene networks along with 10,000 permutations of randomly selected protein pools compared with the HSP seeds plus candidates pool. The top 5%ile distance is shaded. Only for Parkinson's, Alzheimer's,

and ALS do the HSP seeds plus candidates fall within this 5%, whereas epilepsy and autism spectrum disorder show no statistical overlap. (B) Bipartite network showing the top links between the set of HSP and ALS proteins. Clear circles, HSP seeds; yellow circles, HSP candidates; boxes, ALS genes (VCP and ALS2 are implicated as causative of both HSP and ALS); line thickness, diffusion similarity between the two proteins.

points of treatment; for example, the nucleotide metabolism module or the lipid metabolism module could be targeted by bypassing specific metabolic blocks. Our HSPome ranked list of genes also provides candidates for unsolved cases of HSP. In addition to our analysis, we were able to link HSP with more common neurodegenerative disorders, indicating that the study of one disorder might advance the understanding of other neurodegenerative disorders as well.

Our study supports the principle that integrating family-based gene discovery together with prior knowledge (represented here as known causative genes and pathways) can facilitate the identification of biological pathways and processes disrupted in disease. Furthermore, this mode of analysis should be highly useful in the future to aid in the validation of private mutations in genes found in single families, to identify novel candidate genes and pathways, and for the discovery of potential therapeutic targets.

References and Notes

1. C. Blackstone, *Annu. Rev. Neurosci.* **35**, 25–47 (2012).
2. D. Seelow, M. Schuelke, F. Hildebrandt, P. Nürnberg, *Nucleic Acids Res.* **37**, W593–W599 (2009).
3. See supplementary text available on Science Online.
4. A. D'Amico *et al.*, *Neurology* **62**, 2138–2139 (2004).
5. C. Tesson *et al.*, *Am. J. Hum. Genet.* **91**, 1051–1064 (2012).
6. J. H. Schuurs-Hoeijmakers *et al.*, *Am. J. Hum. Genet.* **91**, 1073–1081 (2012).
7. C. Fassier *et al.*, *Nat. Neurosci.* **13**, 1380–1387 (2010).
8. F. Vandin, E. Upfal, B. J. Raphael, *J. Comput. Biol.* **18**, 507–522 (2011).
9. I. Lee, U. M. Blom, P. I. Wang, J. E. Shim, E. M. Marcotte, *Genome Res.* **21**, 1109–1121 (2011).
10. D. Szklarczyk *et al.*, *Nucleic Acids Res.* **39**, D561–D568 (2011).
11. O. Vanunu, O. Magger, E. Ruppin, T. Shlomi, R. Sharan, *PLOS Comput. Biol.* **6**, e1000641 (2010).
12. G. C. DeLuca, G. C. Ebers, M. M. Esiri, *Neuropathol. Appl. Neurobiol.* **30**, 576–584 (2004).
13. N. Rismanchi, C. Soderblom, J. Stadler, P. P. Zhu, C. Blackstone, *Hum. Mol. Genet.* **17**, 1591–1604 (2008).
14. G. Montenegro *et al.*, *J. Clin. Invest.* **122**, 538–544 (2012).
15. Y. Yildirim *et al.*, *Hum. Mol. Genet.* **20**, 1886–1892 (2011).
16. G. K. Voeltz, W. A. Prinz, Y. Shibata, J. M. Rist, T. A. Rapoport, *Cell* **124**, 573–586 (2006).
17. M. H. Wright, I. Berlin, P. D. Nash, *Cell Biochem. Biophys.* **60**, 39–46 (2011).
18. J. Park *et al.*, *Immunity* **17**, 221–233 (2002).
19. M. A. Cohn, Y. Kee, W. Haas, S. P. Gygi, A. D. D'Andrea, *J. Biol. Chem.* **284**, 5343–5351 (2009).
20. C. Dörner *et al.*, *J. Biol. Chem.* **273**, 20267–20275 (1998).
21. S. M. Lee, L. S. Chin, L. Li, *J. Cell Biol.* **199**, 799–816 (2012).
22. G. Skibinski *et al.*, *Nat. Genet.* **37**, 806–808 (2005).
23. Y. Zivony-Elboum *et al.*, *J. Med. Genet.* **49**, 462–472 (2012).
24. B. Renvoisé *et al.*, *Mol. Biol. Cell* **21**, 3293–3303 (2010).
25. J. H. Lumb, J. W. Connell, R. Allison, E. Reid, *Biochim. Biophys. Acta* **1823**, 192–197 (2012).
26. A. P. Sagona *et al.*, *Nat. Cell Biol.* **12**, 362–371 (2010).
27. H. A. Jinnah, R. L. Sabina, G. Van Den Berghe, *Handb. Clin. Neurol.* **113**, 1827–1836 (2013).
28. N. Akizu *et al.*, *Cell* **154**, 505–517 (2013).
29. B. Thauerer, S. Zur Nedden, G. Baier-Bitterlich, *J. Neurochem.* **121**, 329–342 (2012).
30. H. Najmabadi *et al.*, *Nature* **478**, 57–63 (2011).
31. M. A. Schlager *et al.*, *EMBO J.* **29**, 1637–1651 (2010).
32. X. Li *et al.*, *EMBO J.* **29**, 992–1006 (2010).
33. E. C. Oates *et al.*, *Am. J. Hum. Genet.* **92**, 965–973 (2013).
34. Z. Cai *et al.*, *J. Peripher. Nerv. Syst.* **7**, 181–189 (2002).
35. S. Züchner *et al.*, *Am. J. Hum. Genet.* **79**, 365–369 (2006).
36. T. Esteves *et al.*, *Am. J. Hum. Genet.*, published online 31 December 2013 (10.1016/j.ajhg.2013.12.005).
37. J. R. Lupski, J. W. Belmont, E. Boerwinkle, R. A. Gibbs, *Cell* **147**, 32–43 (2011).
38. U. Dursun, C. Koroglu, E. Kocayog Orhan, S. A. Ugur, A. Tolun, *Neurogenetics* **10**, 325–331 (2009).
39. I. A. Meijer *et al.*, *Ann. Neurol.* **56**, 579–582 (2004).
40. V. Bayat *et al.*, *PLOS Biol.* **10**, e1001288 (2012).
41. N. Bouslam *et al.*, *Hum. Genet.* **121**, 413–420 (2007).

Acknowledgments: We are grateful to the participating families. Supported by the Deutsche Forschungsgemeinschaft (G.N.); the Brain and Behavior Research Foundation (A.G.F.); NIH R01NS041537, R01NS048453, R01NS052455, P01HD070494, and P30NS047101 (J.G.G.); French National Agency for Research (G.S., A.D.); the Verum Foundation (A.B.); the European Union (Omics call, “Neuromics” A.B.); Fondation Roger de Spoelberch (A.B.); P41GM103504 (T.I.); “Investissements d’avenir” ANR-10-IAIHU-06 (to the Brain and Spine Institute, Paris); and Princess Al Jawhara Center of Excellence in Research of Hereditary Disorders. Genotyping services provided in part by Center for Inherited Disease Research contract numbers HHSN268200782096C, HHSN268201100011, and N01-CO-12400. We thank the Broad Institute (U54HG003067 to E. Lander), the Yale Center for Mendelian Disorders (U54HG006504 to R. Lifton and M. Gunel), M. Liv for technical expertise, and E. N. Smith, N. Schork, M. Yahyaoui, F. Santorelli, and F. Darios for discussion. Data available at dbGaP (accession number phs000288). UCSD Institutional Review Board (070870) supervised the study. The authors declare no competing financial interests.

Supplementary Materials

www.sciencemag.org/content/343/6170/506/suppl/DC1
Materials and Methods
Supplementary Text
Figs. S1 to S15
Tables S1 to S6
References (42–52)

18 October 2013; accepted 11 December 2013
10.1126/science.1247363

Ultrafast Long-Range Charge Separation in Organic Semiconductor Photovoltaic Diodes

Simon Gélinas,¹ Akshay Rao,¹ Abhishek Kumar,¹ Samuel L. Smith,¹ Alex W. Chin,¹ Jenny Clark,¹ Tom S. van der Poll,² Guillermo C. Bazan,² Richard H. Friend^{1*}

Understanding the charge-separation mechanism in organic photovoltaic cells (OPVs) could facilitate optimization of their overall efficiency. Here we report the time dependence of the separation of photogenerated electron hole pairs across the donor-acceptor heterojunction in OPV model systems. By tracking the modulation of the optical absorption due to the electric field generated between the charges, we measure ~200 millielectron volts of electrostatic energy arising from electron-hole separation within 40 femtoseconds of excitation, corresponding to a charge separation distance of at least 4 nanometers. At this separation, the residual Coulomb attraction between charges is at or below thermal energies, so that electron and hole separate freely. This early time behavior is consistent with charge separation through access to delocalized π -electron states in ordered regions of the fullerene acceptor material.

Organic photovoltaic cells (OPVs) consist of a nanostructured blend of donor (D) and acceptor (A) semiconductors (1, 2). Photons absorbed in either material create molecular excitons, which can dissociate at the D-A heterojunction into holes on D and electrons on A (3, 4). The hole and electron are still subject to their mutual Coulomb interaction and can self-trap at the heterojunction (5–8), giving rise to charge transfer (CT) excitons. However, in efficient OPV blends that use fullerenes as the acceptor, electron and hole escape from the heterojunction and

long-range charge separation is efficient (9, 10) (Fig. 1A). The motion of charges away from the heterojunction had been generally attributed to diffusion (11, 12); however, recent results have suggested that delocalized states may play a role in this process (9). Here we directly measure the electron-hole separation process at the heterojunction and find that the Coulomb barrier is surmounted at times as short as 40 fs, suggesting that rapid charge motion away from the interface through delocalized band states is necessary for long-range charge separation.

To temporally resolve the electron-hole separation process, we require a probe that is sensitive to the distance between these charges. The electric field generated as the charges separate (Fig. 1A) (13–15) serves this purpose by shifting the energy levels of neighboring molecules,

causing a change in their electronic transition energies and an associated optical electro-absorption (EA) (16) signature, represented schematically in Fig. 1B (17). We measured these EA signals with sub-30 fs precision, using transient absorption (TA) spectroscopy. This allows us to calculate the energy stored in the electric field as the charges separate and hence the mean electron-hole distance as a function of time, as we can calibrate the time-resolved data against steady-state EA measurements.

We studied two high-efficiency model systems. The first consists of blends of a solution-processable small molecule (18), p-DTS(FBTTh₂)₂, ((7,7'-(4,4-bis(2-ethylhexyl)-4H-silolo[3,2-b:4,5-b']dithiophene-2,6-diyl)bis(6-fluoro-4-(5'-hexyl-[2,2'-bithiophen]-5-yl)benzo[c][1,2,5]thiadiazole))), as electron donor with PC₇₁BM, (phenyl-C71-butyric acid methyl ester), as acceptor (19). The second system consists of blends of the polymer PCDTBT (20), (poly[N-11"-henicosanyl-2,7-carbazole-alt-5,5-(40, 70-di-2-thienyl-20, 10, 30-benzothiadiazole)]), as electron donor with PC₆₁BM, (phenyl-C61-butyric acid methyl ester), as acceptor. Figure 1, C to E, shows their molecular structure and absorption spectra.

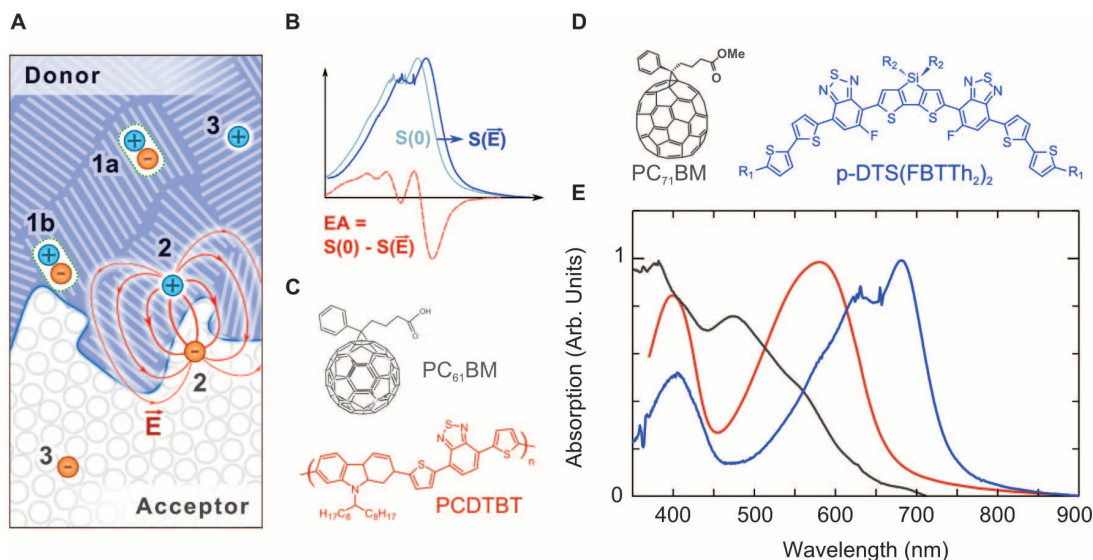
The small-molecule fullerene blend system [p-DTS(FBTTh₂)₂:PC₇₁BM] was chosen as it exhibits sharper optical transitions than literature-standard polymer-fullerene blends. As we develop below, this property leads to a strong EA response that enables us to separate this feature from the other excited-state absorption features. We investigated two blends with different donor/acceptor composition, 60:40 and 90:10. Blends containing a 60:40 weight ratio of p-DTS(FBTTh₂)₂:PC₇₁BM, processed from chlorobenzene with 0.4% diiodooctane (DIO) as a solvent additive, achieve very high internal quantum efficiency (IQE) and power-conversion efficiencies (PCEs) above 7% (19, 21). They

¹Cavendish Laboratory, University of Cambridge, Cambridge, UK. ²Center for Polymers and Organic Solids, University of California, Santa Barbara, CA, USA.

*Corresponding author. E-mail: rhf10@cam.ac.uk

Fig. 1. Schematics of interfacial photophysical processes in OPVs (and molecules studied).

(A) Overview of charge photogeneration at a heterojunction. Light absorption generates excitons in the bulk (1a) and at interfaces (1b). When next to an interface, excitons undergo rapid charge transfer into an electron-hole pair (2), generating a dipole-like electric field in its surroundings (E). The electron and hole then separate further and form free charges (3). (B) Stark shift of the absorption spectrum (S) due to an electric field E (dark blue) and the resulting electro-absorption signature (red) calculated from the difference between the shifted and unshifted spectra. The EA amplitude is proportional to $|E|^2$. (C) Chemical structure of PC₆₁BM (gray) and PCDTBT (red). (D) Chemical structure of PC₇₁BM (gray) and p-DTS(FBTTh₂)₂ (blue). (E) Absorption spectra of the molecules presented in (D).



have been shown to comprise crystalline regions of p-DTS(FBTTh₂)₂ and PC₇₁BM aggregates (27). We contrast this system with the 90:10 blend, processed from chloroform, which shows much lower quantum efficiency and for which the low-fullerene fraction precludes aggregation of the fullerene (see supplementary materials) (22–24).

PCDTBT is a widely studied noncrystalline polymer, which when blended with PCBM gives IQEs close to 100% and PCEs as high as 7% (25, 26). As has been discussed previously, PCBM effectively intercalates into the polymer side chains. Thus, at low fullerene loading the PCBM is mainly unaggregated, forming a mixed phase with the polymer (23). As the fullerene content is increased, the excess fullerene begins to form aggregates (27). Here we contrast a low PCBM loading, 20% (4:1), which does not show fullerene aggregation, to the optimized 80% (1:4) loading that shows high quantum efficiencies and gives rise to aggregated fullerene domains.

Figure 2, A to C, shows TA data for the 90:10 and 60:40 p-DTS(FBTTh₂)₂:PC₇₁BM blends covering the visible and near-infrared spectrum from 100 fs to 2 ns. The positive features between 600 and 700 nm are due to bleaching of the ground-state absorption features. The negative signal peaking at 1230 nm (extending up to 1500 nm) is due to the photoinduced absorption (PIA) of singlet excitons, in agreement with mea-

surements on pristine films of p-DTS(FBTTh₂)₂ (fig. S2). The negative signal that peaks at 800 nm is due to the PIA from positive charges (polarons) on the donor. Its amplitude is similar for both blends, indicating that the density of photogenerated holes is comparable. However, the subsequent behavior is very different. In comparison to the 90:10 blend, the 60:40 blend shows a more complex behavior around 710 nm. The strength of the bleach is reduced at early times, and a negative response is observed beyond 10 ps. This is clearly seen (Fig. 2D) in the spectra at 100-ps delay of the two blends, of a neat film of p-DTS(FBTTh₂)₂ (100:0), and of the steady-state EA spectra of p-DTS(FBTTh₂)₂ (measured independently; see fig. S7). When compared to the neat film, the 90:10 blend shows a reduction in stimulated emission at wavelengths >720 nm, indicating efficient exciton quenching. In addition, the 60:40 blend also shows a large negative signal peaking at 710 nm, which matches the measured steady-state EA spectrum in this region.

From the data presented in Fig. 2, we identify two time scales for charge generation. We consider that the early subpicosecond dynamics are due to the dissociation of excitons photogenerated at the heterojunction, whereas the later evolution is due to excitons photogenerated in bulk p-DTS(FBTTh₂)₂ domains that diffuse before reaching heterojunctions where they dissociate. We use a

global analysis to separate spectral features that have different time evolutions (see supplementary materials). Figure 3A shows the separation of the different features in the 60:40 blend over the time range 30 to 2500 fs. The evolution of the singlet exciton and hole absorption spectra is described by two time constants of 82 ± 5 fs and 22 ± 0.1 ps (with 70% weight to the 82-fs component); the exciton component decreases and the charge component grows with time (Fig. 3B). Our global analysis reveals a third feature with distinct temporal dynamics. This feature closely resembles the steady-state EA spectrum (Fig. 3A), confirming the presence of an EA signature in the 60:40 blend. The singlet spectrum in Fig. 3A is in good agreement with that of neat p-DTS(FBTTh₂)₂ films in Fig. 2D, where the signal is due only to singlet excitons. The signature of the hole polaron matches the spectrum of the 90:10 blend (Fig. 2D) but differs substantially from the 60:40 blend, where features due to both holes and EA are present. This comparison indicates that charge generation occurs in the 90:10 blend without inducing an EA signature, in contrast to the 60:40 blend.

Turning to the dynamics of the EA feature (Fig. 3B), we note that some oscillations are present within the first picosecond, which are due to a nonresonant artefact, and this limits our reconstruction of the EA kinetics to delays ≥ 300 fs. At 300 fs, we already observe a large signal, more than half of the value at 2 ps, beyond which the signal saturates. At low temperatures (4 K), the early time response is the same, but the later growth is delayed (fig. S4). As noted above, the EA feature is absent from the 90:10 blends where charges are generated efficiently but are unable to separate away from the heterojunction. This implies that the EA of a barely separated charge pair is negligible, and hence the large EA signal occurs due to longer-range charge separation. The EA signature in the 60:40 blend thus allows us to resolve the separation of electron-hole pairs.

Figure 3D shows the spectral signatures of singlet and charge features in 4:1 and 1:4 blends of PCDTBT:PCBM. The spectral signatures of charges in the two blends differ substantially, with the 1:4 blend having a more pronounced negative feature at 640 nm. This is qualitatively similar to the behavior of the p-DTS(FBTTh₂)₂:PC₇₁BM blends where the 60:40 blend, which shows EA, has a more pronounced negative feature at 710 nm than the 90:10 blend, which does not show EA. Using the difference between the 4:1 and 1:4 PCDTBT:PCBM blends allows us to extract a third spectral component for the 1:4 blend (purple line in Fig. 3D; see supplementary materials for details) that matches the steady-state EA spectrum. The dynamics of the blends are shown in Fig. 3C: The singlet exciton is rapidly quenched (86 fs) by charge transfer in both the 4:1 and 1:4 blends, with corresponding growth in the charge population. There is no EA response for the 4:1 blend (Fig. 3D), but the 1:4 blend shows a large EA signal at 40 fs. For

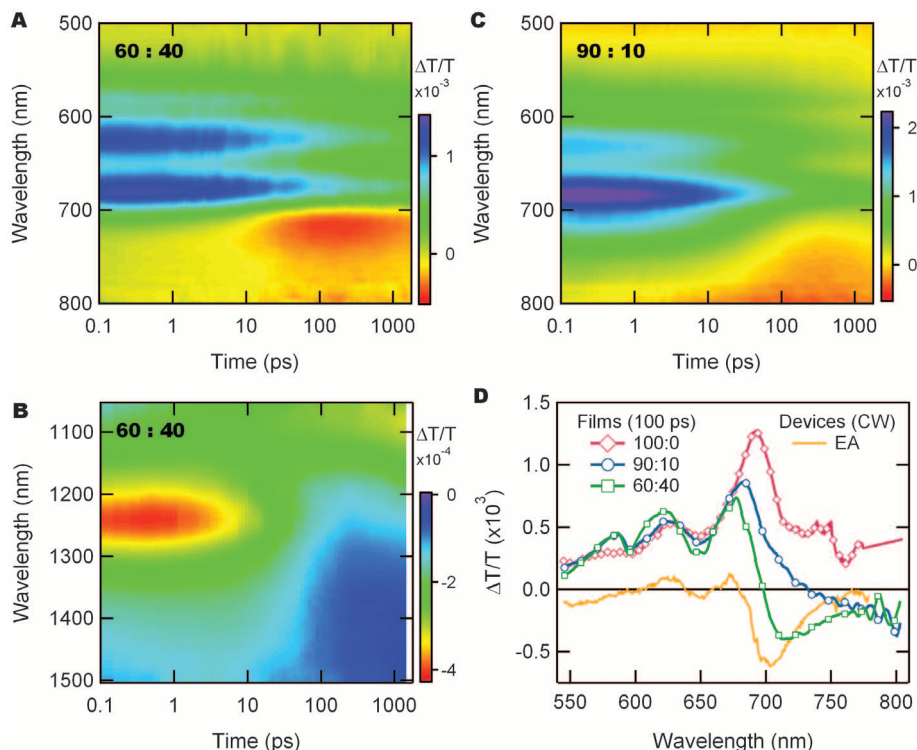


Fig. 2. Transient absorption spectra of excited states in p-DTS(FBTTh₂)₂:PC₇₁BM films. (A and B) Visible and near-infrared measurements of a 60:40 film prepared identically to the active layer of an efficient OPV device. The samples were excited with 700-nm laser pulses at a fluence of $2 \mu\text{J}/\text{cm}^2$. **(C)** Measurement of a 90:10 film, where PC₇₁BM aggregation is prevented and charge separation is inefficient. **(D)** TA time slices of the 100:0, 90:10, and 60:40 films normalized at 640 nm. The steady-state EA signature, obtained from a device using a steady-state electro-absorption measurement (CW), is proportional to the first derivative of the absorption spectrum.

this system, the nonresonant artefact is not as pronounced as for the p-DTS(FBTTh₂)₂:PC₇₁BM, allowing accurate EA detection at delays as short as 40 fs.

By performing quasi-steady-state electroabsorption measurements, which measure the EA signature induced by an oscillating electric field on p-DTS(FBTTh₂)₂:PC₇₁BM and PCDTBT:PCBM diode devices, we can calibrate the EA amplitude to the electric field present in the semiconductor layer (see supplementary materials for details). Using this calibration, we convert the transient EA amplitude of Fig. 3 to a spatially averaged value of the square of the electric field. We calculate the root mean square field strength, and hence the energy stored in the electric field, as $\int \frac{\epsilon \epsilon_0}{2} E^2 dV$.

Figure 3E shows the energy stored in the electric field per charge pair as a function of time for the various blends studied (taking a value of 3.5 for ϵ and modeling half the field to be present in the donor phase). For the 60:40 p-DTS(FBTTh₂)₂:PC₇₁BM, the energy per charge pair reaches more than half its maximum value by 300 fs, and for the 1:4 PCDTBT:PCBM blends, it attains its saturation value by 40 fs. The energies involved are substantial, well above $k_B T$ (where k_B is the Boltzmann constant and T is

temperature), and provide direct evidence that considerable work must be done to overcome the Coulomb attraction between the separating electron hole pairs in these low-dielectric constant materials. Crucially, most of this work against the Coulomb interaction is done on ultrafast time scales. This requires that charges undergo rapid spatial separation on these time scales.

With simple electrostatic modeling and the assumption that the initial step of photoinduced electron transfer just across the heterojunction causes an average separation of electron and hole by 1.5 nm in the absence of fullerene aggregation, we find that charges reach a separation of 4 to 5 nm in both systems at the earliest times measured (see supplementary materials). The further growth for the 60:40 p-DTS(FBTTh₂)₂:PC₇₁BM blend on time scales greater than 300 fs is most likely due to the diffusive motion of the hole within the crystalline p-DTS(FBTTh₂)₂ domains. For PCDTBT, this is not observed, as the larger fullerene domains lead to an increased initial separation, resulting in the saturation of the EA signal. (This occurs when the separation reaches 5 to 6 nm; see supplementary materials for details.)

The length scales being considered here for the separation of charges, ≈ 4 to 5 nm, are consistent with known OPV morphology in efficient

systems, where the presence of pure domains of fullerene, 5 nm in length (28, 29), is strongly correlated with suppressed geminate recombination and improved device performance. In our measurements, the presence of fullerene aggregates leads to large EA signals and electrostatic energies at short times, strongly suggesting that they are key to enabling ultrafast long-range charge separation.

Our measurements are particularly sensitive to the early-time separation of charge carriers at heterojunctions, due to our direct measurement of $|E|^2$, which is insensitive to the initial direction of charge separation with respect to charge collection electrodes (which we expect to be randomly directed, given the bulk heterojunction morphology of these materials). This initial process is not dependent on the presence of an external electric field. By contrast, other time-resolved techniques, such as electric field-induced second harmonic (EFISH) (30), are sensitive to a change in $|E|$. In such experiments, this change in $|E|$ arises when carriers drift in the field set up by the electrodes and the external circuit. This necessarily builds up at later times. For example, Vithanage *et al.* (30) used EFISH to measure net charge motion due to drift toward the electrodes of 2 nm at 1 ps and 5 nm at 100 ps. This provides complementary information to our measurements of the first

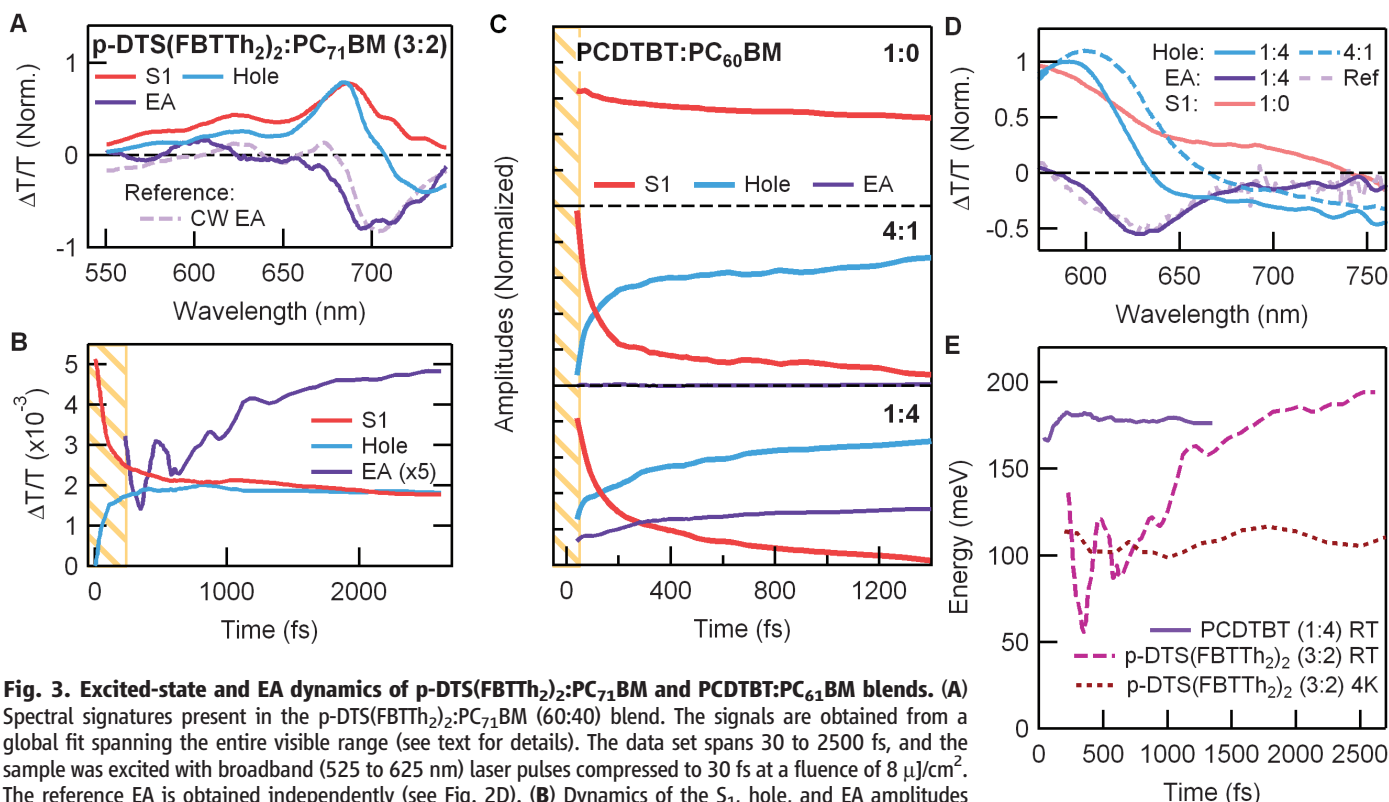


Fig. 3. Excited-state and EA dynamics of p-DTS(FBTTh₂)₂:PC₇₁BM and PCDTBT:PC₆₁BM blends. (A) Spectral signatures present in the p-DTS(FBTTh₂)₂:PC₇₁BM (60:40) blend. The signals are obtained from a global fit spanning the entire visible range (see text for details). The data set spans 30 to 2500 fs, and the sample was excited with broadband (525 to 625 nm) laser pulses compressed to 30 fs at a fluence of 8 $\mu\text{J}/\text{cm}^2$. The reference EA is obtained independently (see Fig. 2D). **(B)** Dynamics of the S₁, hole, and EA amplitudes obtained by fitting the data set with a linear combination of the excited-state signatures shown in (A). The yellow zone indicates the region over which artefacts prevent accurate measurement of the EA. **(C and D)** Spectral signatures and their associated dynamics for three different compositions of PCDTBT:PC₆₁BM blends (see supplementary materials for details of the analysis). The samples were excited at a fluence of 2 $\mu\text{J}/\text{cm}^2$, and the reference EA spectrum was measured on a device. **(E)** Total energy stored in the electric field per electron-hole pair (at room temperature and 4 K). The EA is converted to a spatially integrated electric field square using a calibration from steady-state measurements ($EA = C_{EA} \int |E|^2 dV$, where C_{EA} is the calibration constant for a given system (see supplementary materials for details). The time-resolved energy per hole ($\frac{1}{2} \epsilon \epsilon_0 \int |E|^2 dV$) is obtained assuming that half of the field is in the donor phase. The low temperature (4 K) measurement grows continuously up to 1 ns, where it saturates at ~ 200 meV (see supplementary materials).

steps in charge separation (see supplementary materials for details).

Based on the above results, we propose a simple phenomenological model of the heterojunction interface. Films without aggregated fullerene domains do not exhibit a substantial EA response, which implies that the mobile component of the charge pair is the electron at early times. We model the electron motion on a nano-scale face-centered cubic lattice of acceptor sites, consisting of localized single-electron energy levels that are coherently coupled to their nearest neighbors (a tight binding model), giving rise to a band of delocalized eigenstates with bandwidth B . We include a Gaussian distribution of acceptor-site energies to introduce disorder. As expected, we find that when the static disorder of the on-site energies is within the bandwidth, disorder does not localize the states. The initial excitation is a single exciton on an adjacent donor site.

We include a Coulomb well, of depth W , surrounding the donor to model the presence of the hole, which we assume does not move during the first 200 fs of charge separation. The well lowers the energies of electron states in the local vicinity of the donor (Fig. 4A), introducing a set of bound states and narrowing the energetic width of delocalized states to $\sim B-W$. Typical structures of the emergent eigenstates are illustrated in Fig. 4A ($\phi_{1,2}$), with corresponding examples of the actual states given in fig. S11. We emphasize that our model is only valid for a few hundred femtoseconds after exciton dissociation when delocalized states are briefly accessed; after this, polaron formation will localize the electronic states

and holes and electrons will move via incoherent hopping with comparable mobilities.

If the energy of the electron on the donor site lies within the spread of fullerene eigenstates at the interface, the electron can undergo resonant transfer. When this energy lies below the conduction edge (CE, Fig. 4A), the initial electron wave function can only mix with bound states localized near the hole (ϕ_1), forming a bound charge-transfer state. However, if the initial electron energy lies within the conduction channel above this edge, then the initial state is mixed with states that are fully delocalized across the fullerene lattice (ϕ_2), enabling long-range charge separation to occur.

The model described above assumes spatial coherence between acceptor sites (delocalization). To describe the dynamics of the system, we consider two cases: (i) incoherent transitions between a localized donor site and the delocalized acceptor eigenstates, or (ii) a fully coherent case where the initial electron is described as phase-coherent superposition of these delocalized eigenstates. We perform simulations for both these models on a 5.25 nm by 5.25 nm by 5.25 nm lattice of acceptor sites and for a range of couplings and disorder strengths between 30 and 50 meV and 0.1 and 0.2 eV, respectively (31, 32); all parameters are described in full in the supplementary materials.

Incoherent transitions arise from a perturbative treatment of the D-A coupling [case (i), see supplementary materials]. This generates a set of Fermi golden rule transition rates from the localized donor site into the delocalized states

described earlier. Results are shown in Fig. 4B, yellow curves. We find that charge separation occurs via a single hop of ~ 4 nm. For case (ii), we evolve the coherent superposition under the Schrödinger equation, which generates a wave packet that rapidly propagates across the Coulomb well and into the acceptor crystallite (see supplementary materials for details). Results are shown in Fig. 4B, red curves. Again, for all parameter values considered, electron and hole separate by 3 to 5 nm within 300 fs. For both cases, the separation distance is determined primarily by the size of the acceptor aggregate in our model. Currently, our experiments cannot differentiate between these two separation mechanisms.

We also consider charge dynamics under fully incoherent localized dynamics (Marcus theory)—i.e., in the absence of delocalization—for the same parameters (see supplementary materials for details). This leads to rapid exciton dissociation, with hole and electron on nearest-neighbor sites (Fig. 4B, blue curve), to form tightly bound CT states that are not expected to dissociate rapidly.

Our demonstration and model of short-time charge delocalization and coherent motion is very different from models for exciton coherence and delocalization that have been suggested as being key to efficient OPV performance (33). Within our study, we find no need to invoke such excitonic processes (see supplementary materials for details).

Our results rationalize the apparent asymmetry between efficient electron-hole capture in organic light-emitting diodes (34) and near-unity photo-conversion quantum efficiencies in OPVs (25) by revealing that ultrafast charge separation through delocalized band-like states in fullerene aggregates is key to efficient charge separation. Moreover, the fast time scale for this process indicates that efficient charge separation requires no excess energy beyond that needed to overcome the Coulomb interaction. This is in contrast to Onsager-like models that require excess energy in hot states. Our results suggest that the real energy loss during charge separation lies elsewhere—for instance, in later energetic relaxation of charges through polaron formation or the presence of defect-mediated gap states—and that such energy losses are not fundamental for efficient charge separation.

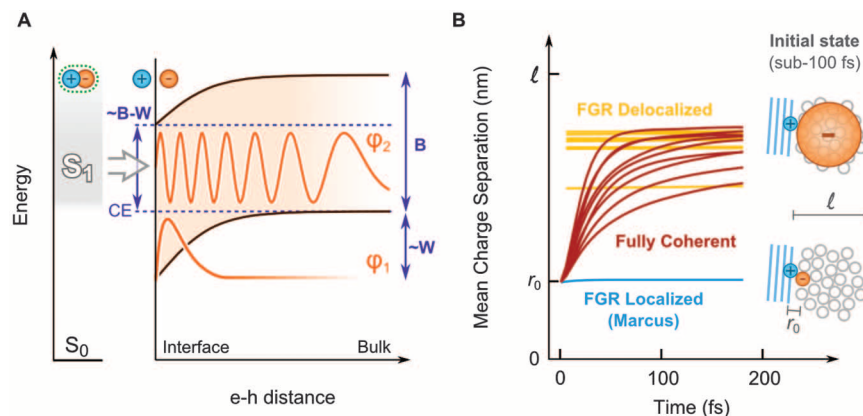


Fig. 4. Model of initially accessible electronic states in fullerene derivatives and calculated electron-hole separation distance. (A) Excited states before and immediately after charge transfer. When excitons (S_1) dissociate at interfaces with aggregated PC₆₁/71BM, the isoenergetic charge transfer places the electrons in delocalized band states, where they undergo wave-like propagation within the PC₆₁/71BM aggregate. In this model, the hole at the interface induces a well of depth W , reducing the width of the band from its bulk value B to $\sim B-W$. This system can sustain two typical electron wave functions represented as $\phi_{1,2}$. The electron is either trapped at the interface (ϕ_1) or propagating through the band (ϕ_2). **(B)** Calculation of electron-hole separation dynamics per charge pair for (i) injection of a fully coherent electron wave packet; (ii) tunneling of the electron into delocalized states (Fermi golden rule, FGR); and (iii) tunneling of the electron into localized states (i.e., Marcus-type electron transfer). The multiple lines represent different values of disorder and couplings, spanning 100 to 200 meV and 30 to 50 meV, respectively (31, 32). r_0 is the separation distance of the initial next-neighbor charge-transfer state [typically 1.5 nm (9)], and l is the length of the PC₆₁/71BM aggregate over which the wave function is delocalized (5.25 nm for the calculation shown).

Reference and Notes

1. J. J. M. Hallis *et al.*, *Nature* **376**, 498–500 (1995).
2. G. Yu, J. Gao, J. C. Hummelen, F. Wudl, A. J. Heeger, *Science* **270**, 1789–1791 (1995).
3. T. M. Clarke, J. R. Durrant, *Chem. Rev.* **110**, 6736–6767 (2010).
4. J.-L. Brédas, J. E. Norton, J. Cornil, V. Coropceanu, *Acc. Chem. Res.* **42**, 1691–1699 (2009).
5. X.-Y.-Y. Zhu, Q. Yang, M. Muntwiler, *Acc. Chem. Res.* **42**, 1779–1787 (2009).
6. A. E. Jaijlaubekov *et al.*, *Nat. Mater.* **12**, 66–73 (2013).
7. S. Gellinas *et al.*, *J. Phys. Chem. C* **115**, 7114–7119 (2011).
8. R. D. Pensack, J. B. Asbury, *J. Phys. Chem. Lett.* **1**, 2255–2263 (2010).
9. A. A. Bakulin *et al.*, *Science* **335**, 1340–1344 (2012).
10. G. Grancini *et al.*, *Nat. Mater.* **12**, 29–33 (2013).
11. P. W. M. Blom, V. D. Mihailescu, L. J. A. Koster, D. E. Markov, *Adv. Mater.* **19**, 1551–1566 (2007).

12. D. Caruso, A. Troisi, *Proc. Natl. Acad. Sci. U.S.A.* **109**, 13498–13502 (2012).
13. J. Cabanillas-Gonzalez *et al.*, *Phys. Rev. B* **75**, 045207 (2007).
14. A. Devizis, A. Serbenta, K. Meerholz, D. Hertel, V. Gulbinas, *Phys. Rev. Lett.* **103**, 027404 (2009).
15. J. Cabanillas-Gonzalez *et al.*, *Phys. Rev. Lett.* **96**, 106601 (2006).
16. L. Sebastian, G. Weiser, H. Bässler, *Chem. Phys.* **61**, 125–135 (1981).
17. I. H. Campbell, T. W. Hagler, D. L. Smith, J. P. Ferraris, *Phys. Rev. Lett.* **76**, 1900–1903 (1996).
18. Y. Sun *et al.*, *Nat. Mater.* **11**, 44–48 (2011).
19. T. S. van der Poll, J. A. Love, T.-Q. Nguyen, G. C. Bazan, *Adv. Mater.* **24**, 3646–3649 (2012).
20. N. Blouin, A. Michaud, M. Leclerc, *Adv. Mater.* **19**, 2295–2300 (2007).
21. J. A. Love *et al.*, *Adv. Funct. Mater.* **23**, 5019–5026 (2013).
22. A. A. Bakulin, J. C. Hummelen, M. S. Pshenichnikov, P. H. M. van Loosdrecht, *Adv. Funct. Mater.* **20**, 1653–1660 (2010).
23. C. Mayer *et al.*, *Adv. Funct. Mater.* **19**, 1173–1179 (2009).
24. L. G. Kaake, Y. Sun, G. C. Bazan, A. J. Heeger, *Appl. Phys. Lett.* **102**, 133302 (2013).
25. S. H. Park *et al.*, *Nat. Photonics* **3**, 297–302 (2009).
26. Z. He *et al.*, *Adv. Mater.* **23**, 4636–4643 (2011).
27. N. C. Miller *et al.*, *Nano Lett.* **12**, 1566–1570 (2012).
28. B. Collins *et al.*, *Adv. Energy Mater.* **3**, 65–74 (2013).
29. F. Liu, Y. Gu, J. W. Jung, W. H. Jo, T. P. Russell, *J. Polym. Sci. B Polym. Phys.* **50**, 1018–1044 (2012).
30. D. Amarasinghe Vithanage *et al.*, *Nat. Commun.* **4**, 2334 (2013).
31. R. C. I. MacKenzie, J. M. Frost, J. Nelson, *J. Chem. Phys.* **132**, 064904 (2010).
32. H. Tamura, M. Tsukada, *Phys. Rev. B* **85**, 054301 (2012).
33. L. G. Kaake, D. Moses, A. J. Heeger, *J. Phys. Chem. Lett.* **4**, 2264–2268 (2013).
34. A. C. Morteani *et al.*, *Adv. Mater.* **15**, 1708–1712 (2003).

Acknowledgments: We thank the Engineering and Physical Sciences Research Council, and the Winton Programme (Cambridge) for the Physics of Sustainability for funding.

S.G. acknowledges funding from the Fonds québécois de recherche sur la nature et les technologies; A.R. thanks Corpus Christi College for a Research Fellowship; A.K. thanks National Research Foundation Singapore for a scholarship; J.C. thanks the Royal Society for a Dorothy Hodgkin Fellowship; and T.S.v.d.P. acknowledges funding from the Center for Energy Efficient Materials, an Energy Frontier Research Center funded by the U.S. Department of Energy, Office of Science, Basic Energy Sciences under Award DC0001009.

Supplementary Materials

www.sciencemag.org/content/343/6170/512/suppl/DC1
Supplementary Text
Figs. S1 to S14
References (35–44)

20 September 2013; accepted 25 November 2013
Published online 12 December 2013;
10.1126/science.1246249

Sound Isolation and Giant Linear Nonreciprocity in a Compact Acoustic Circulator

Romain Fleury,¹ Dimitrios L. Sounas,¹ Caleb F. Sieck,^{1,2} Michael R. Haberman,^{2,3} Andrea Alù^{1*}

Acoustic isolation and nonreciprocal sound transmission are highly desirable in many practical scenarios. They may be realized with nonlinear or magneto-acoustic effects, but only at the price of high power levels and impractically large volumes. In contrast, nonreciprocal electromagnetic propagation is commonly achieved based on the Zeeman effect, or modal splitting in ferromagnetic atoms induced by a magnetic bias. Here, we introduce the acoustic analog of this phenomenon in a subwavelength meta-atom consisting of a resonant ring cavity biased by a circulating fluid. The resulting angular momentum bias splits the ring's azimuthal resonant modes, producing giant acoustic nonreciprocity in a compact device. We applied this concept to build a linear, magnetic-free circulator for airborne sound waves, observing up to 40-decibel nonreciprocal isolation at audible frequencies.

Reciprocity refers to the symmetric wave transmission between two points in space. It is a basic property observed in many wave phenomena because it is directly associated to the symmetry of physical laws under time reversal (*1*). Reciprocal transmission is not always desirable—for example, when one wants to isolate or protect a region of space allowing wave transmission in one direction yet blocking it in the opposite one. For electromagnetic waves, several approaches are available to break reciprocity and achieve isolation by using both linear (*2–10*) and nonlinear (*11–14*) techniques, the most common being based on magnetic biasing. In contrast, nonreciprocal isolation of acoustic waves has so far been based on nonlinear mechanisms (*15–17*), which introduce inherent signal distortions and limitations on the amplitude of operation. Recently, proposals to achieve unidirectional sound propagation in linear components have been discussed (*18–24*), but they rely on devices

that are strictly symmetric to time-reversal, being therefore completely reciprocal (*25, 26*) and not attaining the highly desirable functionality of a nonreciprocal linear acoustic isolator. However, nonreciprocal acoustic wave propagation can occur in linear media, by using magneto-acoustic effects (*27*), or in moving fluids (*28*). These possibilities are typically associated with weak effects that are only observable over large volumes and often require bulky and impractical biasing equipment.

Inspired by the way magnetic bias produces electromagnetic nonreciprocity in magneto-optical media based on the electronic Zeeman effect, we introduce here an acoustic meta-atom able to realize a nonreciprocal, linear, compact acoustic isolator. In magneto-optical media, such as ferromagnetic materials or atomic vapors, an applied static magnetic field \vec{B}_0 splits the energy levels corresponding to countercirculating electronic orbitals (Fig. 1A), inducing different refractive properties for right- and left-handed circularly polarized waves that depend nonreciprocally on the direction of propagation. An analogous phenomenon can be obtained for acoustic waves in our macroscopic meta-atom (Fig. 1B). Imparting a circular motion to the fluid filling a subwavelength acoustic resonant ring cavity splits the degenerate counterpropagating azimuthal resonant modes and, for a

proper velocity and cavity design, induces giant nonreciprocity via modal interference. In this scenario, the angular momentum vector imparted by the circular flow takes the role of the static magnetic bias, and the proposed meta-atom experiences the acoustic analog of Zeeman splitting and therefore displays a nonreciprocal response.

It is possible to qualitatively explain this phenomenon by considering the effective wavelength change for sound propagating in a moving medium. We assume that the azimuthally symmetric cavity is filled with a fluid on which we apply a circular motion with velocity v along the azimuthal direction \vec{e}_ϕ (Fig. 1B). In absence of rotation ($v = 0$), the ring resonates when its average circumference approximately equals an integer number m of wavelengths, supporting degenerate counterpropagating eigenmodes with azimuthal dependence $e^{\pm im\phi}$ and frequencies $\omega_m = mc/R_{av}$, where c is the speed of sound and R_{av} is the mean radius. For $v \neq 0$, the sound effectively circulates with different velocities $c + v$ and $c - v$ in the moving fluid, depending on whether it travels with or against the flow. As a consequence, the resonant frequencies of the $e^{\pm im\phi}$ modes split according to

$$\omega_m^\pm = \omega_m \pm \frac{mv}{R_{av}} \quad (1)$$

The splitting is linear with respect to the biasing flow velocity, in perfect analogy to the electronic Zeeman effect (*29*)—an analogy that becomes even more apparent when the phenomenon is more rigorously studied with the quantum-mechanical approach developed in the supplementary materials (*30*). If the circulation is right-handed (RH), the RH mode $e^{im\phi}$ shifts to a higher frequency, whereas the left-handed (LH) mode $e^{-im\phi}$ shifts down by the same amount. In order to validate this model, we numerically solve the eigenvalue problem for the dominant mode $m = 1$, for which the ring diameter is smaller than the wavelength, for a range of biasing fluid velocity. The cavity, whose geometry is detailed in (*30*), is designed to resonate around 800 Hz, and the corresponding eigenvalues (Fig. 1C) are found in perfect agreement with Eq. 1.

To demonstrate the possibility of getting large nonreciprocity through the proposed concept, we

¹Department of Electrical and Computer Engineering, The University of Texas at Austin, Austin, TX 78712, USA. ²Applied Research Laboratories, The University of Texas at Austin, Austin, TX 78758, USA. ³Department of Mechanical Engineering, The University of Texas at Austin, Austin, TX 78712, USA.

*Corresponding author. E-mail: alu@mail.utexas.edu

consider a three-port generalization of the isolator, also known in the microwave community as a circulator (Fig. 1D). Such a device allows acoustic power incident in port 1 to only be transmitted to port 3. From port 3, however, power only flows to port 2 and, likewise, from 2 to 1. The scattering matrix S of the acoustic circulator is nonsymmetrical

$$S = \begin{pmatrix} 0 & 1 & 0 \\ 0 & 0 & 1 \\ 1 & 0 & 0 \end{pmatrix} \quad (2)$$

which is a symptom of its inherently nonreciprocal nature. An isolator is a subsystem of a circulator

and can be readily obtained by impedance matching one of the circulator ports.

We realized such a device by coupling the proposed acoustic Zeeman meta-atom to three acoustic waveguides symmetrically placed at 120° intervals via small holes (Fig. 1D). As a result of mode splitting, an acoustic wave incident at port 1 unevenly couples to both RH and LH modes, in general with different amplitudes a^+ and a^- . Their interference supports different outputs at ports 2 and 3 despite the geometrical symmetry of the cavity. Using temporal coupled-mode theory, the power transmission coefficients at ports 2 and 3 are (2)

$$T_{1 \rightarrow 2} = \left| \frac{2}{3} \left(\frac{e^{-i4\pi/3}}{1 - i(\omega - \omega^-)/\gamma^-} + \frac{e^{-i2\pi/3}}{1 - i(\omega - \omega^+)/\gamma^+} \right) \right|^2 \quad (3)$$

$$T_{1 \rightarrow 3} = \left| \frac{2}{3} \left(\frac{e^{-i2\pi/3}}{1 - i(\omega - \omega^-)/\gamma^-} + \frac{e^{-i4\pi/3}}{1 - i(\omega - \omega^+)/\gamma^+} \right) \right|^2 \quad (4)$$

where γ^\pm are the decay rates associated with RH and LH modes, with $\gamma^+ = \gamma^- = \gamma$ owing to symmetry. It follows that we can obtain $T_{1 \rightarrow 2} = 0$ and $T_{1 \rightarrow 3} = 1$ at frequency $\omega = \omega_r$ if the cavity modes are split so that $\omega^\pm = \omega_r \pm \gamma/\sqrt{3}$. As seen in Eq. 1, this condition is directly satisfied for $\omega_r = \omega_0$ at the optimal bias velocity $v_{opt} = \gamma R_{av}/\sqrt{3}$. After considering that $\omega_0 = c_0/R_{av}$ and $Q = \omega_0/(2\gamma)$ —where c_0 and Q are the sound velocity and the cavity quality factor, respectively—we obtain the optimal fluid velocity $v_{opt} = c_0/(2Q\sqrt{3})$. Therefore, by choosing a sufficiently high Q-factor the proposed acoustic meta-atom can realize an ideal linear circulator (Eq. 2) within a subwavelength volume using arbitrarily low bias velocities.

We performed full-wave numerical simulations in order to investigate the behavior of the proposed device, assuming an acoustic wave incident from port 1. The magnitude of the pressure transmission coefficient at ports 2 and 3 in the absence of biasing motion is shown in Fig. 2A. In this case, the transmission coefficients at the two output ports are identical, which is due to symmetry. The unbiased cavity simply forms a power divider, which at resonance sends 4/9 of the power to each of the output ports, and the remaining 1/9 is reflected. The altered transmission spectrum when the device is appropriately biased with optimal fluid velocity $v_{opt} = 0.5 \text{ m/s}$ is shown in Fig. 2B. As predicted by our model, the transmission to port 2

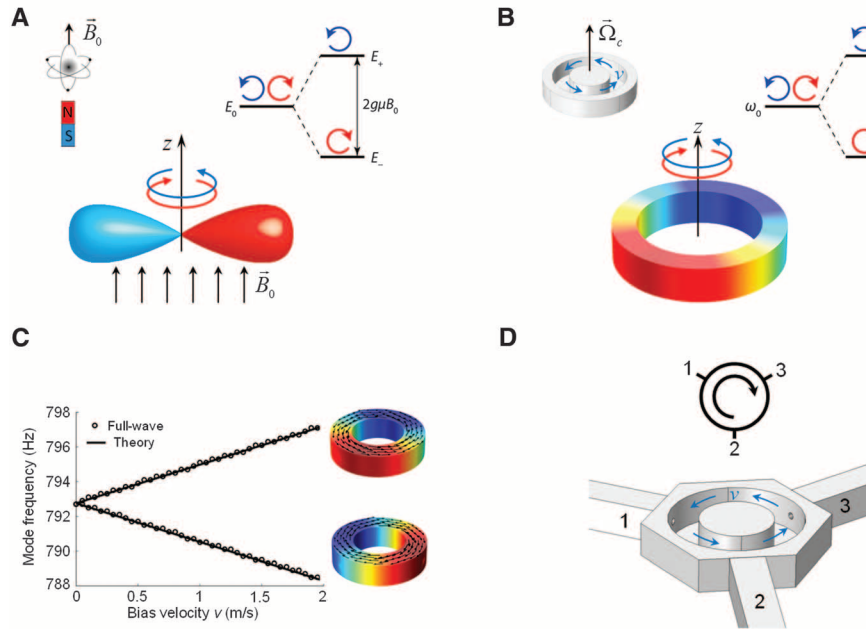
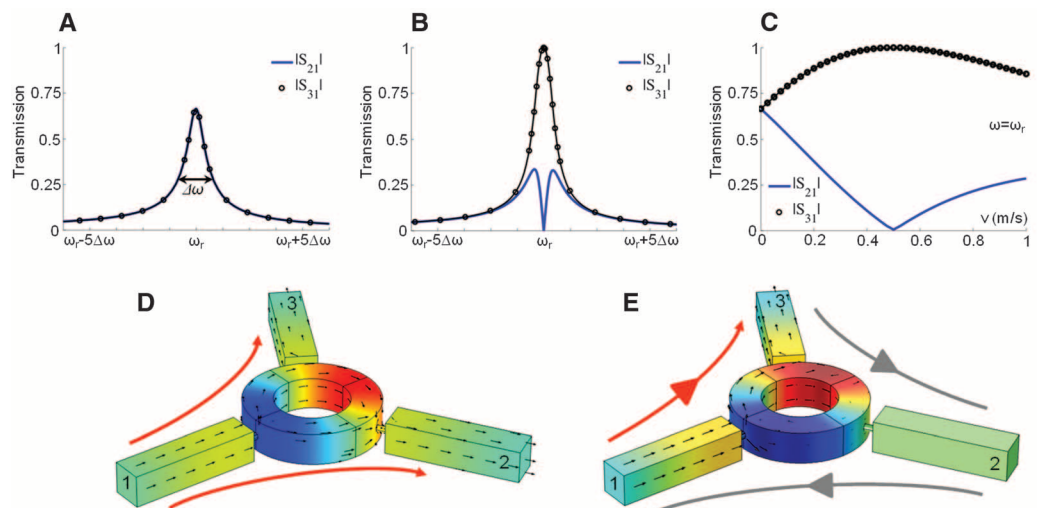


Fig. 1. The acoustic Zeeman effect. (A) The classical electronic Zeeman effect involves an atom biased by an external magnetic field \vec{B}_0 . The magnetic bias lifts the degeneracy of electronic eigenstates (here, $p_\pm = p_x \pm ip_y$ orbitals, with energies E_\pm) with a splitting proportional to \vec{B}_0 . (B) The proposed acoustic Zeeman effect involves an acoustic meta-atom (here, a ring cavity, with degenerate counterpropagating modes) internally biased by a circulating fluid with angular momentum \vec{Q}_c . The modes split in a similar fashion (30). (C) Frequency splitting as a function of the bias velocity. (D) A circulator as a three-port generalization of an isolator, its schematic model (top) and its implementation by using a Zeeman acoustic meta-atom coupled via small holes to three acoustic waveguides (bottom). Sound propagates from port 1 to 3, 3 to 2, and 2 to 1.

Fig. 2. Full-wave simulations for excitation at port 1. (A) Case of no bias. Transmission at ports 2 and 3 is identical. (B) Case of optimal biasing velocity for maximum nonreciprocity, with zero transmission to port 2 and total transmission to port 3 at ω_r . (C) Effect of varying the biasing fluid velocity on the nonreciprocal transmission properties of the device at $\omega = \omega_r$. (D) Acoustic pressure field distribution inside the unbiased device. (E) Same as (D), but when the circulator is optimally biased. Black arrows represent the average acoustic power flow.



is dramatically reduced at the operating frequency ω_r , whereas transmission to port 3 reaches unity, indicating that all energy is now directed there. On the contrary, when the excitation is incident on port 3 the acoustic wave flows to port 2 instead of port 1. The effect of varying the biasing fluid velocity on the transmission from port 1 to ports 2 and 3 is shown in Fig. 2C. When $v = 0$ (unbiased device), the amplitude transmission coefficients are equal to $2/3$. As the velocity increases, the transmission to port 2, $|S_{21}|$, gradually goes down to zero, whereas the transmission to port 3, $|S_{31}|$, increases to reach unity for the specific value of bias velocity used in Fig. 2B. This value coincides with the optimal bias velocity v_{opt} calculated above and provides the correct amount of acoustic Zeeman splitting to obtain an ideal acoustic circulator. Beyond this value, $|S_{21}|$ increases again, whereas $|S_{31}|$ decreases. The proposed effect is quite robust to fluctuations in the mean velocity, and our simulations predict a large degree of isolation $|S_{31}|/|S_{21}|$ over a moderately broad range of velocities around the optimal value.

To gain further insights into the response of the proposed device, we show the acoustic pressure field distribution for unbiased operation (Fig. 2D) and for optimal biasing velocity (Fig. 2E). In the first case, the resonant modes are degenerate and evenly excited, resulting in a field distribution inside the cavity that is totally symmetric with respect to the axis of port 1. Ports 2 and 3, which are symmetrically placed, are therefore evenly excited, and the response is fully reciprocal. The average power flow, represented by the black arrows, is split evenly between the two output ports. When the device is biased, on the contrary, the mode splitting is perfectly balanced to produce an asymmetric field distribution with respect to port 1 and create, by destructive interference between the two modes, a null of pressure field at port 2 and conversely, through constructive interference, a maximum at port 3. In this scenario, the power flow is routed exclusively toward the output port on the left of the input (the direction opposite to the velocity bias), independent of the feeding port.

These theoretical and full-wave simulation results are confirmed by our experimental investigations. Photographs of the fabricated device are presented in Fig. 3, A and B. The device consists of a ring cavity that resonates in the audible range at $\omega_r = 800$ Hz and contains three low-noise central processing unit (CPU) cooling fans, placed at 120° intervals so as to generate the desired circulating air flow. Details of the setup are provided in (30). The ring cavity, with the top cover removed to show the fan positions, is presented in Fig. 3A, and the closed cavity connected to the three acoustic waveguides is presented in Fig. 3B. By varying the input current at the fans, we are able to control the air velocity in the cavity and the corresponding biasing angular momentum. Shown in Fig. 3, C and D, are the measured transmission spectrum at ports 2 and 3 normalized to the no-bias case (Fig. 3C). As expected,

when the fans are not operating (Fig. 3C) transmission at ports 2 and 3 is equal, and the system is fully reciprocal. On the other hand, for an input current to the fans $I = 130$ mA (Fig. 3D), nonreciprocity is clearly observed, which is in excellent agreement with our theory. The effect of varying the fan input current, directly correlated with the fan speed, on the measured transmission coefficients is shown in Fig. 3E. Our measurements corroborate the theoretical predictions of Fig. 2C, showing the evolution from a fully reciprocal system for $I = 0$ to a close-to-ideal acoustic circulator for $I = 130$ mA. To quantify the performance of the realized device, the measured isolation $|S_{31}|/|S_{21}|$ is shown as a function of the input current (Fig. 3F). Around the optimal bias value, this device produces very large values of isolation, up to 40 dB. During the experiments, we have tested the device response at all ports, confirming its nonreciprocal operation and circulation of the input acoustic signal. Because the bias is electrically controlled, our design provides a large degree of tunability, with the possibility of switching from reciprocal to nonreciprocal oper-

ation and reversing the handedness of the circulator by simply changing the polarity of the input current. In our experiments, narrowband signals with carrier frequency ω_r were transmitted through the realized device, and acoustic nonreciprocity, isolation, and circulation could be directly verified by ear.

A similar effect may be realized in liquids by using cylindrical cavities biased with magnetic stirrers. The fluid motion is a convenient way to impart the desired angular momentum to the resonant cavity, but other solutions, such as involving spatially modulated micromechanical resonators, may be considered in order to realize this effect in a fully integrated design and at higher frequencies. Our realized prototype is moderately subwavelength, but even smaller dimensions may be obtained by loading the resonant cavity. The proposed effect is largely tunable and scalable from audible to ultrasonic frequencies and provides a compact solution to realize acoustic switching, energy rectification, isolation, and circulation. Targeting higher frequencies may result in impractically small cavity sizes; however, it is possible to work with higher-

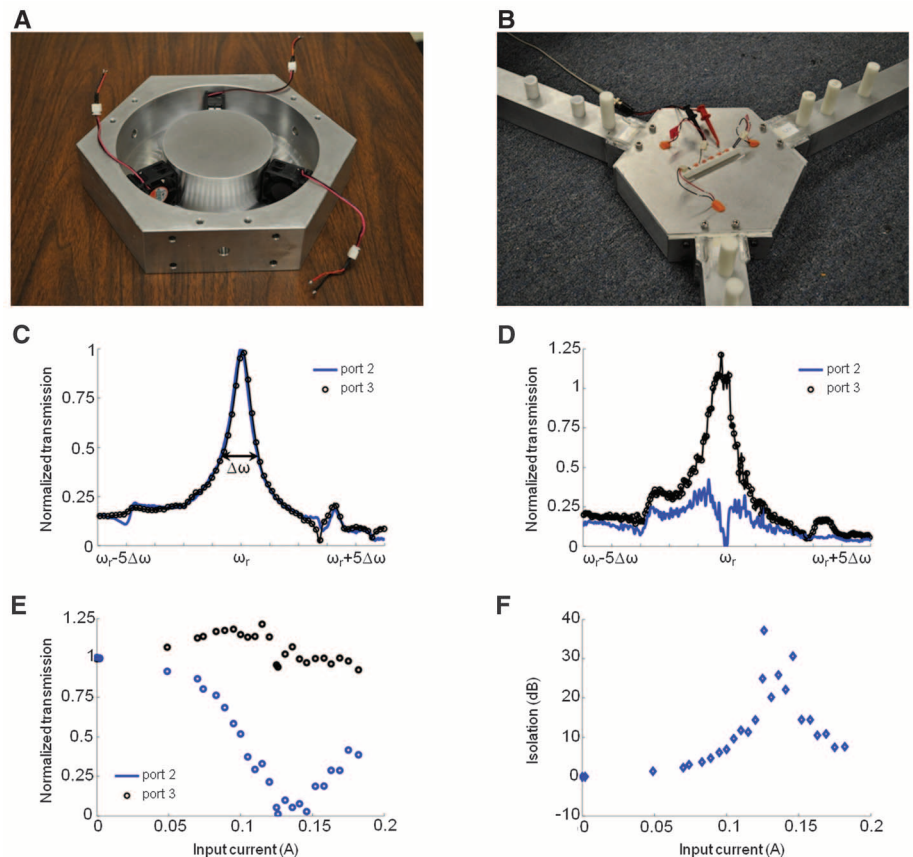


Fig. 3. Experimental results. (A) Photograph of the fabricated cavity (without the top cover). The ring cavity is biased by using three low-noise CPU fans connected to a current source. (B) Photograph of the fabricated device. The biased cavity is closed and connected to three acoustic waveguides. Sound is incident from port 1, and transmission to ports 2 and 3 is measured. (C and D) Measured pressure transmission spectrum normalized to the unbiased case when (C) the fans are not powered and (D) the fan velocity is adjusted to produce optimal nonreciprocal behavior. (E) Measured transmission spectrum at ω_r normalized to the peak transmission in the unbiased case as a function of the input current. (F) Measured isolation in decibels as a function of input current at the fans.

order modes to circumvent this issue. We envision that this concept may open new directions in acoustics research, including advances in noise control, transducer technologies, energy harvesting systems, acoustic imaging, and sensing.

References and Notes

- H. B. G. Casimir, *Rev. Mod. Phys.* **17**, 343–350 (1945).
- Z. Wang, S. Fan, *Appl. Phys. B* **81**, 369–375 (2005).
- Z. Yu, S. Fan, *Nat. Photonics* **3**, 91–94 (2009).
- L. Bi et al., *Nat. Photonics* **5**, 758–762 (2011).
- A. Kamal, J. Clarke, M. H. Devoret, *Nat. Phys.* **7**, 311–315 (2011).
- T. Koderer, D. L. Sounas, C. Caloz, *Appl. Phys. Lett.* **99**, 031114, 031114–3 (2011).
- M. S. Kang, A. Butsch, P. S. J. Russell, *Nat. Photonics* **5**, 549–553 (2011).
- D.-W. Wang et al., *Phys. Rev. Lett.* **110**, 093901 (2013).
- H. Lira, Z. Yu, S. Fan, M. Lipson, *Phys. Rev. Lett.* **109**, 033901 (2012).
- D. L. Sounas, C. Caloz, A. Alù, *Nat. Commun.* **4**, 2407 (2013).
- S. Lepri, G. Casati, *Phys. Rev. Lett.* **106**, 164101 (2011).
- M. Soljačić, C. Luo, J. D. Joannopoulos, S. Fan, *Opt. Lett.* **28**, 637–639 (2003).
- I. V. Shadrivov, V. A. Fedotov, D. A. Powell, Y. S. Kivshar, N. I. Zheludev, *New J. Phys.* **13**, 033025 (2011).
- L. Fan et al., *Science* **335**, 447–450 (2012).
- B. Liang, B. Yuan, J. C. Cheng, *Phys. Rev. Lett.* **103**, 104301 (2009).
- B. Liang, X. S. Guo, J. Tu, D. Zhang, J. C. Cheng, *Nat. Mater.* **9**, 989–992 (2010).
- N. Boechler, G. Theoharis, C. Daraio, *Nat. Mater.* **10**, 665–668 (2011).
- X.-F. Li et al., *Phys. Rev. Lett.* **106**, 084301 (2011).
- X. Zhu, X. Zou, B. Liang, J. Cheng, *J. Appl. Phys.* **108**, 124909, 124909–5 (2010).
- Z. He et al., *Appl. Phys. Lett.* **98**, 083505, 083505–3 (2011).
- H. Sun, S. Zhang, X. Shui, *Appl. Phys. Lett.* **100**, 103507, 103507–4 (2012).
- A. Cicek, O. Adem Kaya, B. Ulug, *Appl. Phys. Lett.* **100**, 111905, 111905–4 (2012).
- J. Hwan Oh, H. Woong Kim, P. Sik Ma, H. Min Seung, Y. Young Kim, *Appl. Phys. Lett.* **100**, 213503, 213503–213504 (2012).
- B. Yuan, B. Liang, J. Tao, X. Zou, J. Cheng, *Appl. Phys. Lett.* **101**, 043503, 043503–043504 (2012).
- D. Jalas et al., *Nat. Photonics* **7**, 579–582 (2013).
- A. A. Maznev, A. G. Every, O. B. Wright, *Wave Motion* **50**, 776–784 (2013).
- C. Kittel, *Phys. Rev.* **110**, 836–841 (1958).
- L. M. Brekhovskikh, I. P. Lysanov, *Fundamentals of Ocean Acoustics* (Springer, Berlin, 2003).
- C. Cohen-Tannoudji, B. Diu, F. Laloë, *Quantum Mechanics*, vol. 1 (Hermann, Wiley, NY, 1991).
- Materials and methods are available as supplementary materials on Science Online.

Acknowledgments: This work has been supported by the Defense Threat Reduction Agency Young Investigator Program (YIP) award HDTRA1-12-1-0022 and the Air Force Office of Scientific Research YIP award FA9550-11-1-0009. A provisional U.S. patent has been filed with title “Non-reciprocal acoustic devices based on angular momentum bias” (61/868,178). R.F., D.L.S., and A.A. developed the concept presented in this paper. R.F. and D.L.S. carried out the analytical and numerical modeling and built the device. R.F. and C.F.S. conducted the measurements. M.R.H. contributed to the design and realization of the experimental set-up. A.A. supervised the entire project. All authors discussed the results and commented on the article.

Supplementary Materials

www.sciencemag.org/content/343/6170/516/suppl/DC1
Materials and Methods
Fig. S1
References (31–35)

8 October 2013; accepted 3 December 2013
10.1126/science.1246957

Unlocking the Potential of Cation-Disordered Oxides for Rechargeable Lithium Batteries

Jinhyuk Lee,¹ Alexander Urban,^{1*} Xin Li,^{1*} Dong Su,² Geoffroy Hautier,¹ Gerbrand Ceder^{1†}

Nearly all high-energy density cathodes for rechargeable lithium batteries are well-ordered materials in which lithium and other cations occupy distinct sites. Cation-disordered materials are generally disregarded as cathodes because lithium diffusion tends to be limited by their structures. The performance of $\text{Li}_{1.211}\text{Mo}_{0.467}\text{Cr}_{0.3}\text{O}_2$ shows that lithium diffusion can be facile in disordered materials. Using ab initio computations, we demonstrate that this unexpected behavior is due to percolation of a certain type of active diffusion channels in disordered Li-excess materials. A unified understanding of high performance in both layered and Li-excess materials may enable the design of disordered-electrode materials with high capacity and high energy density.

Rechargeable lithium-ion batteries enable increasingly capable portable electronics and are the crucial factor in the deployment of electric vehicles. Cathodes with high energy density are desirable for high-performance lithium batteries, as they make up a substantial part of the cost, weight, and volume of a battery. Cathode compounds operate by reversibly releasing (de-intercalation) and reinserting (intercalation) lithium ions during charge and discharge, respectively. This process must occur without causing permanent change to the crystal structure because the battery must endure hundreds of charge-discharge cycles. Traditionally, cathodes have been sought from well-ordered close-packed oxides—in

particular, layered rocksalt-type lithium–transition metal oxides (Li-TM oxides) (1–3) and ordered spinels (4, 5)—whereas nonordered materials have received limited attention (6–9). In these ordered compounds, Li sites and pathways (a 2D slab in the layered oxides and a 3D network of tetrahedral sites in the spinels) are separated from the TM sublattice, which provides stability and electron storage capacity. Having well-ordered structures where there is little or no intermixing between the Li and the TM sublattice is generally considered important for obtaining high-capacity cathode materials with good cycle life (10, 11). In some cases, improvements in ordering have led to notable increases in power or energy density (3, 12–14). Here, we show that this “ordering paradigm” may have led the community to overlook a large class of cathode materials in which Li and TM share the same sublattice in a random (disordered) fashion; some of these materials may offer higher capacity and better stability relative to the layered oxides.

We chose the $\text{Li}_{1.211}\text{Mo}_{0.467}\text{Cr}_{0.3}\text{O}_2$ (LMCO) compound because of our interest in metals that can exchange multiple electrons, such as Mo and Cr. In addition, both Mo and Cr have been shown to migrate in layered materials (15, 16). LMCO was synthesized through standard solid-state procedures as described (17). The material forms as a layered rocksalt but transforms to a disordered rocksalt after just a few charge-discharge cycles, as seen in the x-ray diffraction (XRD) patterns in Fig. 1A. The (003) reflection, characteristic of the layered structure, starts to disappear after one cycle and is essentially gone at the 10th cycle. From Rietveld refinement, we estimate 34 to 52% of the TM ions to be in Li layers after 10 cycles, indicating substantial cation mixing in LMCO (17). The evolution of LMCO to a disordered structure was confirmed in real space with scanning transmission electron microscopy (STEM) (Fig. 1B). The bright and dark columns in the “before” image correspond to atomic columns of mixed Li-Mo-Cr ions and Li ions, respectively. The Z-contrast decreases after one cycle and is very weak after 10 cycles, indicating increased cation mixing. This substantial structural evolution is consistent with the change in voltage profile (Fig. 1C) between the first charge and all subsequent cycles.

The reversible Li capacity of carbon-coated LMCO (LMCO/C) is remarkably high, even after disordering (17). As seen in Fig. 1C, approximately one lithium ($= 265.6 \text{ mAh g}^{-1}$) per formula unit can be reversibly cycled at C/20 rate [$= 16.4 \text{ mA g}^{-1}$; the C/n rate denotes the rate of cycling the theoretical capacity of LMCO (327.5 mAh g^{-1}) in n hours], delivering an energy density of $\sim 660 \text{ Wh/kg}$ ($\sim 3100 \text{ Wh/liter}$) at $\sim 2.5 \text{ V}$. Such high capacity is rarely achieved even in layered Li-TM oxides (18–20) and is counterintuitive because cation mixing has been argued to markedly degrade the cyclability of layered oxides, primarily by reducing the Li layer spacing

¹Department of Materials Science and Engineering, Massachusetts Institute of Technology, Cambridge, MA 02139, USA.

²Center for Functional Nanomaterials, Brookhaven National Laboratory, Upton, NY 11973, USA.

*These authors contributed equally to this work.

†Corresponding author. E-mail: gceder@mit.edu

(Li slab distance), resulting in limited Li diffusion (3, 12, 14, 21–24). Indeed, given that the oxygen-interlayer (slab) distance around the Li layer of LMCO decreases considerably from ~ 2.63 Å to ~ 2.39 Å after disordering (17), negligible Li mobility would be expected (3, 14, 23).

In a disordered rocksalt, both Li and TM occupy a cubic close-packed lattice of octahedral sites, and Li diffusion proceeds by hopping from one octahedral site to another octahedral site via an intermediate tetrahedral site (*o-t-o* diffusion; Fig. 2A) (17, 23, 25). Li in the intermediate tetrahedral site is the activated state in Li diffusion. The activated tetrahedral Li^+ ion shares faces with four octahedral sites: the site previously occupied by the ion itself; the vacancy it will move into; and two sites that can be occupied by Li, TM, or a vacancy. The energy in this state, which reflects the Li migration barrier, is largely determined by electrostatic repulsion between the activated Li^+ ion and its face-sharing species, and thus depends on (i) the valence of the face-sharing species and (ii) the available space for relaxation between the activated Li^+ ion and the face-sharing species. This space is measurable as the Li slab distance in layered structures (3, 14, 23), or more generally as the height of the tetrahedron along which the relaxation occurs (Fig. 2A).

As electrostatic repulsion on an activated Li^+ ion is too strong when there are two face-sharing cations, Li dominantly diffuses with the divacancy mechanism, involving a second vacancy beside the vacancy the migrating Li will move into (3, 23, 25). In rocksalt-type Li-TM oxides, two kinds of diffusion channels support this mechanism: 0-TM channels, involving no face-sharing TM ion (Fig. 2B), and 1-TM channels, involving one face-sharing TM ion (Fig. 2C). Note that 1-TM channels are responsible for Li diffusion in typical layered Li-TM oxides. To investigate which channels in disordered LMCO allow for reasonable hopping rates, we calculated Li migration barriers for 1-TM and 0-TM channels using density functional theory (DFT), according to the divacancy mechanism (17).

The red and blue dashed lines in Fig. 3 show the mean migration barriers along a 1-TM channel as a function of the average tetrahedron height of model disordered structures (disordered Li_2MoO_3 , disordered LiCrO_2) when the face-sharing octahedral species is Mo^{4+} and Cr^{3+} , respectively (17). Note that migration barriers in disordered structures vary with the local atomic environment, which accounts for a distribution of migration barriers. The mean barrier increases as the tetrahedron height (h) decreases, reaching ~ 510 meV along a 1- Mo^{4+} channel and ~ 490 meV along a 1- Cr^{3+} channel at $h \sim 2.39$ Å, the average tetrahedron height in disordered LMCO (17). Note that these barriers tend to increase as the transition metal becomes oxidized in charge. Considering that typical 1-TM barriers in layered oxides are ~ 300 meV (23), such high barriers in disordered LMCO indicate very limited Li diffusion along 1-TM channels. This is because the small

tetrahedron height in disordered LMCO confines the activated Li^+ ion close to a face-sharing high-valent octahedral TM ion in 1-TM channels, resulting in strong electrostatic repulsion on the Li^+ ion.

The black dashed line in Fig. 3 shows the mean migration barriers along 0-TM channels. In

contrast to the high barriers in 1-TM channels, the low barrier at $h \sim 2.39$ Å (~ 290 meV) indicates that Li migration along 0-TM channels will still be facile in disordered LMCO, with a hopping rate higher than that along 1-TM channels by a factor of ~ 4400 [$\exp(-290 \text{ meV}/kT)/\exp(-500 \text{ meV}/kT)$] at room temperature. The low valence of a face-

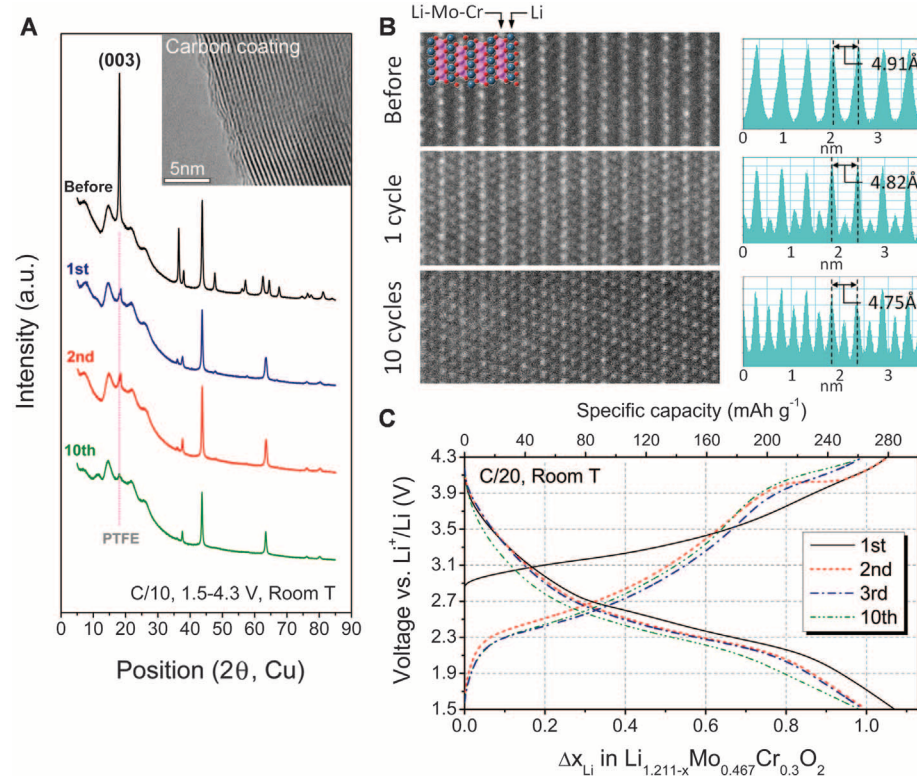


Fig. 1. $\text{Li}_{1.211}\text{Mo}_{0.467}\text{Cr}_{0.3}\text{O}_2$ shows high Li cycling capacity even after substantial cation disordering. (A) XRD patterns of C-coated $\text{Li}_{1.211}\text{Mo}_{0.467}\text{Cr}_{0.3}\text{O}_2$ (LMCO/C) electrodes before and after 1, 2, and 10 cycles, 1.5 to 4.3 V, C/10. The inset image shows the C-coating layer. (B) Left: STEM images along the [010] zone axis in a LMCO/C particle before cycling and after 1 and 10 cycles, 1.5 to 4.3 V, C/20. Right: Corresponding line profiles of the Z-contrast information with the measured spacing of Li-Mo-Cr layers. (C) Voltage profile of LMCO/C, 1.5 to 4.3 V, C/20.

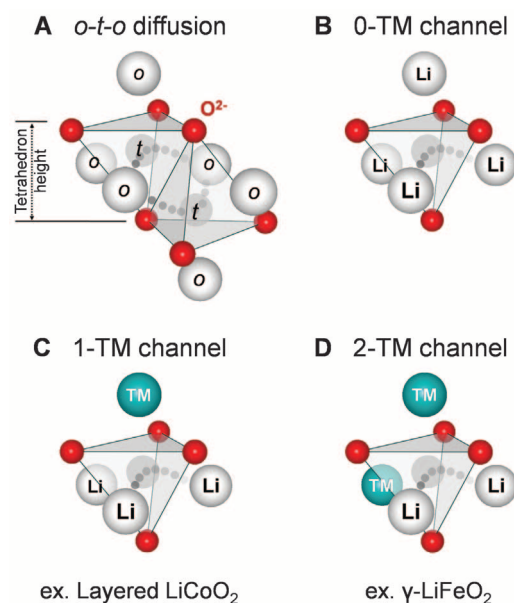


Fig. 2. Possible environments for an *o-t-o* Li hop in rocksalt-like Li-TM oxides. (A) *o-t-o* diffusion: Two tetrahedral paths connect each pair of neighboring octahedral sites. (B to D) The activated state can share faces with no octahedral transition metals (0-TM channel) (B), one transition metal (1-TM channel) (C), or two transition metals (2-TM channel) (D).

sharing octahedral Li^+ ion (versus Mo^{4+} or Cr^{3+}) results in much weaker electrostatic repulsion on the activated Li^+ ion in 0-TM channels. At highly charged states, tetrahedral Li may form in some 0-TM channels because high delithiation should leave no face-sharing octahedral Li at all (26). However, the mean migration barrier between two 0-TM tetrahedral sites was calculated to be ~ 15 meV, indicating that Li can easily escape from these sites.

Herein lies the real issue of (cation) disordered structures: 1-TM channels, which account for the excellent Li mobility in the layered intercalation oxides that currently dominate the battery industry, become nearly inactive in disordered materials as a result of their small tetrahedron heights. In contrast, 0-TM channels are active in disordered rocksalts but are much less frequent than 1-TM channels. Nonetheless, as we show below, 0-TM channels start to enable facile

macroscopic diffusion in disordered structures once enough Li excess is introduced.

For 0-TM channels to dominate macroscopic Li diffusion, they must be continuously connected through the entire material, forming a percolating network uninterrupted by 1-TM and 2-TM channels. To establish a general understanding of 0-TM percolation, we studied (i) when 0-TM channels percolate in a rocksalt-type Li-TM oxide and (ii) which fraction of the Li ions become part of a percolating network of 0-TM channels.

Figure 4A shows the probability of finding a percolating network of 0-TM channels (0-TM network) in a rocksalt-type Li-TM oxide as a function of Li content (x in $\text{Li}_x\text{TM}_{2-x}\text{O}_2$) and cation mixing ($\text{TM}_{\text{Li layers}}/\text{TM}_{\text{TM layers}} \times 100\%$), as obtained by Monte Carlo simulations (17). The probability (color-coded) steeply increases from 0 (red) to 1 (blue) across the black line in Fig. 4A (percolation threshold), varying from x

~ 1.13 for layered oxides to $x \sim 1.09$ for fully disordered oxides. Because 0-TM channels require a locally Li-rich environment, excess Li ($x \geq \sim 1.09$) is essential to open the percolating 0-TM network.

To estimate the contribution of a percolating 0-TM network to macroscopic Li diffusion, we investigated how Li excess and cation mixing affect the Li content in the network (Fig. 4B), which we refer to as accessible Li. This Li can diffuse through the network without traversing 1-TM or 2-TM channels, whereas “inaccessible” Li must traverse 1-TM or 2-TM channels to reach the percolating 0-TM network. The three black lines in Fig. 4B are the contour lines where the accessible Li content is 0.8 Li, 1 Li, and 1.2 Li per $\text{Li}_x\text{TM}_{2-x}\text{O}_2$. For $x \leq 1$, no percolating 0-TM network exists (Fig. 4A) and hence there is no accessible Li content, which explains why stoichiometric LiTMO_2 compounds have low capacity when cation-disordered (7, 9, 21, 24). However, the accessible Li content gradually increases as x exceeds ~ 1.09 (percolation threshold), and becomes as high as 1 Li as x exceeds ~ 1.22 regardless of cation mixing. Increasing Li excess adds more 0-TM channels to a percolating 0-TM network, improving the network’s connectivity.

The above results explain how Li diffusion can be facile in disordered LMCO. LMCO is a Li-excess material with $x = 1.233$ in $\text{Li}_x\text{TM}_{2-x}\text{O}_2$. With this Li content, 0-TM channels will be percolating (Fig. 4A), accessing as high as ~ 1 Li per formula unit (Fig. 4B). Therefore, even as 1-TM channels become nearly inactive after disordering (Fig. 3), a large fraction of Li in the material can still be cycled through the percolating active 0-TM network.

The principle of creating a percolating 0-TM network can be applied to the design of other high-performing disordered Li-TM oxides for two reasons. First, the 0-TM activated state is surrounded only by Li sites, making the effect of the TM species on the activation energy less pronounced. Second, as shown in table S1 (17), the tetrahedron height of most disordered rocksalts is such that 0-TM channels are calculated to be active (Fig. 3). Therefore, a percolating 0-TM network will likely enable facile Li diffusion in other disordered materials, assuming that no other kinetic barriers become limiting. Note that the few cation-disordered materials in the literature that were electrochemically active are indeed Li-excess materials, whereas stoichiometric disordered materials are usually not electrochemically active, which is consistent with our understanding (7–9, 16, 21, 24).

Disordered Li-excess rocksalts have considerable advantages over layered materials. We find that the changes in lattice parameters and volume, as a function of Li concentration, are very small in disordered materials ($<1\%$ in LMCO), which will lead to less mechanical stress and capacity loss in an electrode (fig. S8). Furthermore, as they have more homogeneous cation distribution, they tend to experience less change in local environment

Fig. 3. Li hopping through 0-TM channels can still be facile in cation-disordered materials. Calculated Li migration barriers along 1-TM (Mo^{4+}) channels (red squares), 1-TM (Cr^{3+}) channels (blue triangles), and 0-TM (Li^+) channels (black circles) as a function of the average tetrahedron height of model disordered structures (disordered Li_2MoO_3 , disordered LiCrO_2). Error bars denote SD. The shaded area highlights typical tetrahedron heights of disordered materials (17).

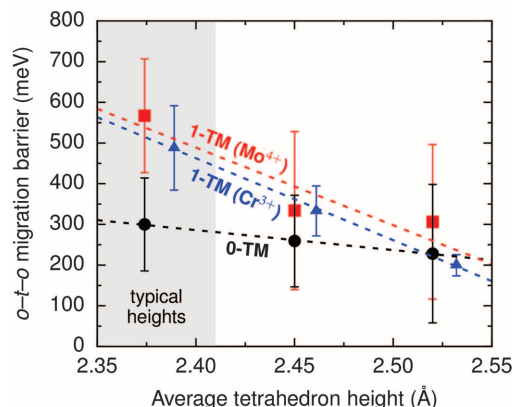
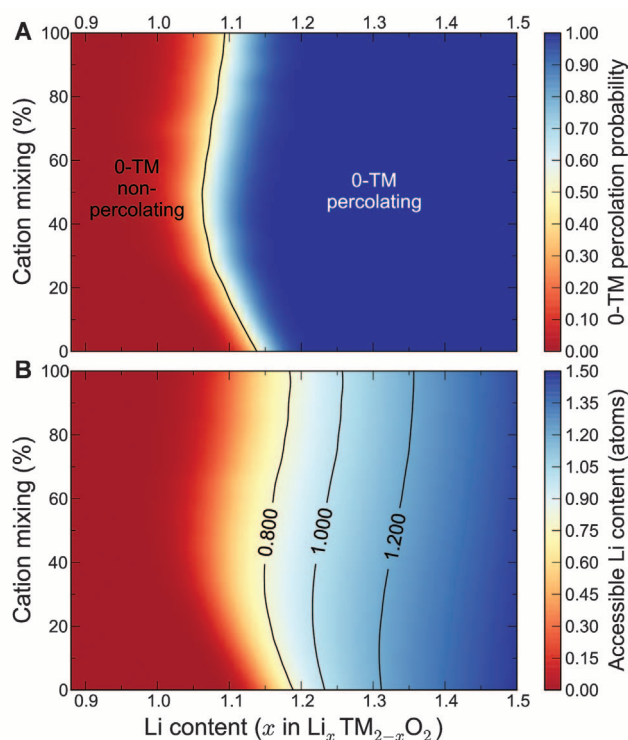


Fig. 4. Li excess opens a percolating network of 0-TM channels in rocksalt-type Li-TM oxides. (A) Computed probability of finding a percolating network of 0-TM channels (color) versus Li content (x in $\text{Li}_x\text{TM}_{2-x}\text{O}_2$) and cation mixing ($\text{TM}_{\text{Li layers}}/\text{TM}_{\text{TM layers}} \times 100\%$). (B) Accessible Li content by a percolating 0-TM network (color) versus Li content and cation mixing. In the simulation, cations were randomly distributed at each cation-mixing level (17).



of the lithium ions as a function of state of charge. This change in environment is particularly problematic in layered structures where the slab spacing decreases considerably when large amounts of Li are removed, leading to a substantial reduction of Li mobility (25, 27, 28). However, in cation-disordered structures, homogeneously distributed cations should lead to a Li diffusivity that is more independent of the Li concentration, as is the case for electrode materials with the spinel- and olivine-type structures. One issue that requires more investigation is whether cation disordering will lead to a more sloped voltage profile than for well-ordered materials, as one would expect from the wider distribution of Li-site energies in a disordered material. However, this variance in the Li-site energy may be counteracted by a less effective Li-Li interaction, which is responsible for the slope of the voltage curve in layered materials (29). Hence, careful tailoring of the TM-Li to Li-Li ion interaction may mitigate this effect. Given the insights presented above, it may not be surprising that the highest-capacity layered materials are highly Li-excess materials (18–20) that become more disordered in the first few cycles because of a particular overcharge mechanism (30).

Our results may explain why disorder has not been pursued as a strategy before: Most materials synthesized are near stoichiometry (LiTMO_2), which is well below the percolation threshold for 0-TM diffusion. Therefore, these materials quickly lose their capacity upon disorder as it renders typical 1-TM channels inactive, while 0-TM channels are not percolating (7, 9, 21, 24). As a result, disorder may have appeared to be a counterintuitive strategy. In contrast, our analysis points

to cation-disordered materials as a class of materials that can exhibit high capacity and high energy density, thereby offering hope for substantial improvements in the performance of rechargeable Li batteries.

References and Notes

1. K. Mizushima, P. C. Jones, P. J. Wiseman, J. B. Goodenough, *Mater. Res. Bull.* **15**, 783–789 (1980).
2. T. Ohzuku, A. Ueda, M. Nagayama, *J. Electrochem. Soc.* **140**, 1862–1870 (1993).
3. K. Kang, Y. S. Meng, J. Br  ger, C. P. Grey, G. Ceder, *Science* **311**, 977–980 (2006).
4. M. M. Thackeray, P. J. Johnson, L. A. De Picciotto, P. G. Bruce, J. B. Goodenough, *Mater. Res. Bull.* **19**, 179–187 (1984).
5. K. M. Shaju, P. G. Bruce, *Dalton Trans.* **2008**, 5471–5475 (2008).
6. A. J. Jacobson, R. R. Chianelli, S. M. Rich, M. S. Whittingham, *Mater. Res. Bull.* **14**, 1437–1448 (1979).
7. M. N. Obrovac, O. Mao, J. R. Dahn, *Solid State Ion.* **112**, 9–19 (1998).
8. V. Pralong, V. Gopal, V. Caignaert, V. Duffort, B. Raveau, *Chem. Mater.* **24**, 12–14 (2012).
9. Y. Sakui, H. Arai, J.-i. Yamaki, *Solid State Ion.* **113–115**, 29–34 (1998).
10. M. S. Whittingham, *Chem. Rev.* **104**, 4271–4302 (2004).
11. J. B. Goodenough, Y. Kim, *Chem. Mater.* **22**, 587–603 (2010).
12. A. Rougier, I. Saadoune, P. Gravereau, P. Willmann, C. Delmas, *Solid State Ion.* **90**, 83–90 (1996).
13. Z. Lu, D. D. MacNeil, J. R. Dahn, *Electrochem. Solid State Lett.* **4**, A200–A203 (2001).
14. A. Rougier, P. Gravereau, C. Delmas, *J. Electrochem. Soc.* **143**, 1168–1175 (1996).
15. A. C. W. P. James, J. B. Goodenough, *J. Solid State Chem.* **76**, 87–96 (1988).
16. L. Zhang, H. Noguchi, *J. Electrochem. Soc.* **150**, A601–A607 (2003).
17. See supplementary materials on Science Online.
18. C. S. Johnson *et al.*, *Electrochem. Commun.* **6**, 1085–1091 (2004).
19. M. Sathija *et al.*, *Nat. Mater.* **12**, 827–835 (2013).

20. Z. Lu, J. R. Dahn, *J. Electrochem. Soc.* **149**, A815–A822 (2002).
21. K. Kang *et al.*, *Chem. Mater.* **15**, 4503–4507 (2003).
22. J. Peres *et al.*, *J. Phys. Chem. Solids* **57**, 1057–1060 (1996).
23. K. Kang, G. Ceder, *Phys. Rev. B* **74**, 094105 (2006).
24. K. Ozawa *et al.*, *J. Power Sources* **174**, 469–472 (2007).
25. A. Van der Ven, G. Ceder, *Electrochem. Solid State Lett.* **3**, 301–304 (2000).
26. J. Br  ger *et al.*, *Chem. Mater.* **18**, 4768–4781 (2006).
27. A. Van der Ven, M. K. Aydinol, G. Ceder, G. Kresse, J. Hafner, *Phys. Rev. B* **58**, 2975–2987 (1998).
28. G. G. Amatucci, J. M. Tarascon, L. C. Klein, *J. Electrochem. Soc.* **143**, 1114–1123 (1996).
29. A. Van der Ven, M. K. Aydinol, G. Ceder, *J. Electrochem. Soc.* **145**, 2149–2155 (1998).
30. N. Yabuuchi, K. Yoshii, S. T. Myung, I. Nakai, S. Komaba, *J. Am. Chem. Soc.* **133**, 4404–4419 (2011).

Acknowledgments: Supported by the Robert Bosch Corporation, by Umicore Specialty Oxides and Chemicals, and by a Samsung Scholarship (J.L.). Computational resources from the National Energy Research Scientific Computing Center (NERSC) and from the Extreme Science and Engineering Discovery Environment (XSEDE) are gratefully acknowledged. The STEM work carried out at the Center for Functional Nanomaterials, Brookhaven National Laboratory, was supported by the U.S. Department of Energy, Office of Basic Energy Sciences, under contract DE-AC02-98CH10886. We thank N. Twu, S. Kim, and J. Kim for valuable discussions.

Supplementary Materials

www.sciencemag.org/content/343/6170/519/suppl/DC1
Materials and Methods
Supplementary Text
Figs. S1 to S8
Table S1
References (31–46)

25 September 2013; accepted 24 December 2013
Published online 9 January 2014;
10.1126/science.1246432

Low Core-Mantle Boundary Temperature Inferred from the Solidus of Pyrolite

Ryuichi Nomura,^{1*} Kei Hirose,^{1,2,3*} Kentaro Uesugi,⁴ Yasuo Ohishi,⁴ Akira Tsuchiyama,⁵ Akira Miyake,⁵ Yuichiro Ueno^{1,2}

The melting temperature of Earth's mantle provides key constraints on the thermal structures of both the mantle and the core. Through high-pressure experiments and three-dimensional x-ray microtomographic imaging, we showed that the solidus temperature of a primitive (pyrolitic) mantle is as low as 3570 ± 200 kelvin at pressures expected near the boundary between the mantle and the outer core. Because the lowermost mantle is not globally molten, this provides an upper bound of the temperature at the core-mantle boundary (T_{CMB}). Such remarkably low T_{CMB} implies that the post-perovskite phase is present in wide areas of the lowermost mantle. The low T_{CMB} also requires that the melting temperature of the outer core is depressed largely by impurities such as hydrogen.

The core-mantle boundary (CMB), located at a depth of 2900 km inside Earth, is the interface between molten metal and rock. The temperature jump across the thermal boundary layer (TBL) above the CMB has been believed to be about 1500 K (1), which has important con-

sequences for the dynamics and thermal evolution in the mantle and the core. The temperature at the top of the core should be lower than the solidus temperature of a primitive mantle to avoid global melting above the CMB. Conventionally, the temperature at the CMB (T_{CMB}) has

been estimated to be about 4000 K, primarily based on the melting temperature of iron at the inner core boundary (ICB), where solid and liquid cores coexist (1–3). Such high T_{CMB} implies that MgSiO_3 -rich post-perovskite, a primary mineral in the lowermost mantle, changes back into perovskite with steeply increasing temperature near the CMB (4), which allows detailed modeling of the thermal structure in the CMB region and the heat flux from the core into the mantle (5). Previous experiments using laser-heated diamond-anvil cell (DAC) techniques showed that the solidus temperature of a primitive mantle is about 4200 K at the CMB, supporting the high T_{CMB} around 4000 K (6–8). The

¹Department of Earth and Planetary Sciences, Tokyo Institute of Technology, Meguro, Tokyo 152-8551, Japan. ²Earth-Life Science Institute, Tokyo Institute of Technology, Meguro, Tokyo 152-8551, Japan. ³Institute for Research on Earth Evolution, Japan Agency for Marine-Earth Science and Technology, Yokosuka, Kanagawa 237-0061, Japan. ⁴Japan Synchrotron Radiation Research Institute, Sayo, Hyogo 679-5198, Japan. ⁵Division of Earth and Planetary Sciences, Kyoto University, Kyoto, Kyoto 606-8502, Japan.

*Corresponding author. E-mail: nomura.r.ab@m.titech.ac.jp (R.N.); kei@elsi.jp (K.H.)

determination of solidus temperature using the DAC is, however, challenging because detecting a small amount of partial melt is difficult.

We determined the solidus temperature of the lower mantle on the basis of the textural and chemical characterizations of quenched samples after subjecting them to a high-pressure environment like that of the CMB. Our starting material possessed a natural primitive mantle (pyrolite) composition, with about 400 parts per million (ppm) H_2O (SM text). It was heated to 2100 to 3900 K at 25 to 169 GPa in a DAC (9), which covers the entire pressure range of the lower mantle (table S1).

We subsequently collected x-ray microtomographic images to explore the three-dimensional (3D) internal structure of all samples (9). Additionally we prepared cross sections of heated samples in order to examine more-detailed melting texture and composition in two dimensions.

Comparison between images collected with two different x-ray energies, 7 and 8 keV, showed iron enrichment in the sample, because the K-absorption edge of Fe is 7.11 keV. Some of the samples exhibited an iron-rich pocket at the center, corresponding to the hottest part during laser heating (Fig. 1). Electron microprobe analyses revealed

that such iron-rich regions represented quenched partial melt with nonstoichiometric composition, which was enclosed by MgSiO_3 -rich perovskite (Fig. 2 and fig. S1) (10, 11). We thus bracketed the solidus curve of pyrolite by monitoring the iron-rich pocket in the tomographic images (Fig. 3). With synchrotron x-rays, we successfully detected a melt pool as small as 3 μm , formed by ~ 3 volume % partial melting at 142 GPa (Fig. 1A).

The solidus curve obtained in this study is consistent with the results of multi-anvil experiments performed below 25 GPa (12, 13) but is lower than those of recent laser-heated DAC studies combined with *in situ* x-ray diffraction measurements (7, 8) (Fig. 3). Although earlier experiments contained little water (6–8), our experiments included ~ 400 ppm H_2O , which may represent the lower bound of the range of geochemical estimates of water concentrations in the lower mantle (14, 15). The lower solidus temperature found in our study is therefore attributed to both the effect of water and the difference in criteria for the onset of melting. The diffuse scattering used in (7) certainly indicates the presence of melt but is hardly observed for silicate when a melt fraction is minor (8). In contrast, a small amount of partial melt in the DAC sample is best evidenced by the *ex situ* characterization using microtomography techniques. The solidus curves found in (6–8) might represent a certain degree of partial melting, which explains their steeper temperature/pressure slopes, because the liquidus temperature increases more rapidly with increasing pressure than the solidus temperature (Fig. 3).

A lower solidus temperature helps explain the present-day thermal and chemical structure of the mantle and the core. The seismic evidence of ultralow velocity zones (ULVZs) may suggest the presence of partial melt above the CMB; however, ULVZs are local, not global, features. Because the CMB temperature is isothermal, such local occurrence indicates that regions where the ULVZ is observed have distinct chemical compositions with lower melting temperatures (16). The upper bound of T_{CMB} should therefore be 3570 ± 200 K from the solidus temperature of a typical lower mantle including 400 ppm H_2O (Fig. 3), which is much lower than the conventional estimate of around 4000 K (1). These previous estimates assumed that the liquidus temperature of the core alloy is depressed by 600 to 700 K at the ICB by the effect of impurities (2, 3). Such an impurity effect is, however, strongly variable depending on the unidentified light elements present in the core. On the other hand, the lower limit of T_{CMB} is given by the melting temperature of the Fe-H alloy, which is lower than those of other possible core constituents (17). Earlier experiments demonstrated that pure Fe and FeH [Fe with 1.8 weight % (wt %) H] melt at 4190 and 2600 K, respectively, at the CMB (3, 17), although the latter was estimated by extrapolation and may thus include relatively

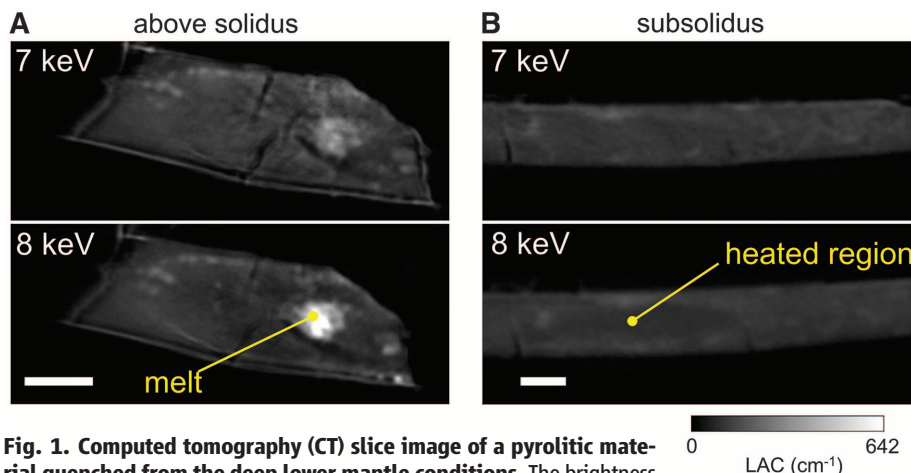


Fig. 1. Computed tomography (CT) slice image of a pyrolitic material quenched from the deep lower mantle conditions. The brightness contrast is based on the x-ray linear attenuation coefficient (LAC) of an object. Comparison between the images obtained with 7- and 8-keV energies shows an Fe-rich melt pocket at the hottest part of the sample in (A) but not in (B), bracketing a solidus curve between (A) 142 GPa/3690 K and (B) 151 GPa/3680 K (Fig. 3). Scale bars, 5 μm .

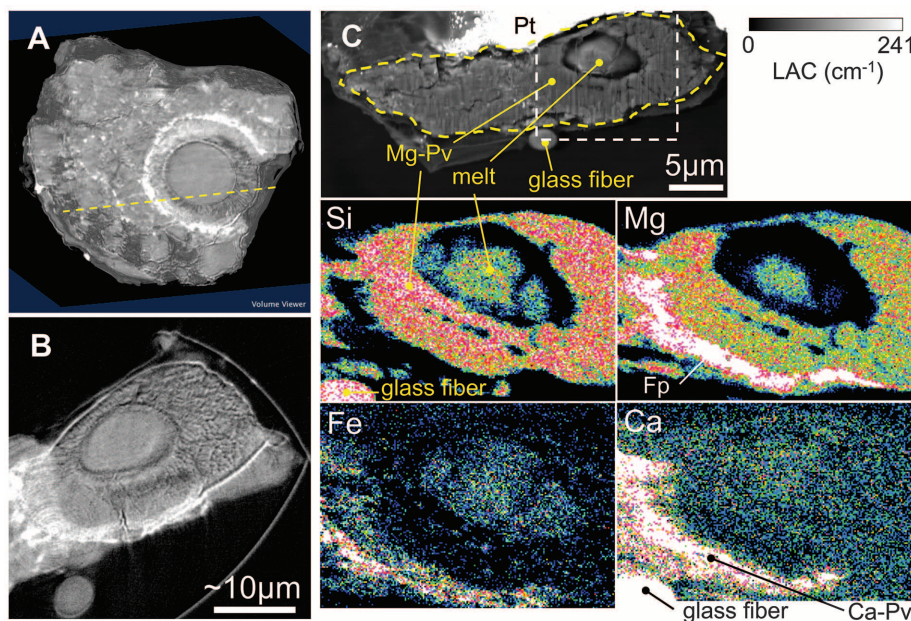


Fig. 2. Melt pocket revealed by both tomographic imaging and microprobe analyses. (A and B) CT images of the sample quenched from 42 GPa/3200 K for two different slices [the yellow line in (A) corresponds to (B)]. The cross section of this sample was prepared by a focused ion beam and examined by a microprobe (C). The x-ray maps for Si, Mg, Fe, and Ca were obtained for the area marked by white in a backscattered electron image. Pv, perovskite; Fp, ferropericlase.

large uncertainty. Considering that the 10% core density deficit is reconciled with 1.2 wt% H (18), T_{CMB} could be as low as 3100 K (Fig. 4).

Seismological analysis shows the pairs of positive and negative velocity discontinuities in the lowermost mantle, which have been attributed to the double-crossing of the post-perovskite phase transition boundary by the geotherm (4). Earlier experimental work (7) demonstrated that perovskite is formed above 3500 ± 150 K at the CMB pressure in a natural mantle material. Considering the upper bound of T_{CMB} (3570 ± 200 K) found in this study, the stability of perovskite at the base of the mantle is therefore marginal.

Alternatively, the low T_{CMB} suggests that post-perovskite occurs not only in cold subducted slabs but also in wider regions of the lowermost mantle.

The temperature extrapolated along an adiabat from the transition zone is 2500 to 2800 K at the CMB (5), indicating a temperature jump of 300 to 1100 K across the TBL developed near the base of the mantle. The thermal conductivity of the lowermost mantle, a mixture of (Mg,Fe)SiO₃ post-perovskite and (Mg,Fe)O ferropericlase, has been estimated to be 7.4 to 11.0 W/m/K at 136 GPa and 3600 K (19, 20). Recent theoretical predictions of high thermal conductivity of the core sug-

gest the adiabatic heat flux of 14 to 20 TW at the top of the core (21, 22), which should be comparable to the heat flux across the CMB unless the topmost core is thermally stratified in a wide depth range (22). In this case, the TBL thickness is limited to less than 130 km (fig. S2). Such thin TBL gives an alternative explanation for the seismic velocity reduction observed ~100 km above the CMB (23).

We also calculated the temperature at the ICB (T_{ICB}) from T_{CMB} and the isentropic gradient across the outer core given by $(\text{dln } T/\text{dln } \rho) = \gamma$, where ρ is density and γ is the Grüneisen parameter. With uniform $\gamma = 1.51$ in the core (24) and $\sim 3100 \text{ K} < T_{\text{CMB}} < 3570 \pm 200 \text{ K}$, we obtain $\sim 4200 \text{ K} < T_{\text{ICB}} < 4860 \pm 270 \text{ K}$ (Fig. 4). The core must be fully molten at both the CMB and the ICB. Recent density and sound velocity measurements proposed Fe₉₀O_{0.5}S_{9.5} (in weight ratio) as a liquid core composition (25). However, the liquidus temperature of Fe₉₀O_{0.5}S_{9.5} should be higher than that of Fe₈₅O₂S₁₃ (3600 K at the CMB and 5630 K at the ICB) (26) and thus exceeds the outer core temperatures estimated above. On the other hand, geochemical models based on Si isotope data suggest 6 wt % Si in the core (27). Nevertheless, even the eutectic (solidus) temperatures of Fe_{90.35}Si_{7.35}S_{2.3} and Fe_{80.07}Si_{10.36}S_{2.57} were reported to be 3750 and 3600 K at the CMB, respectively (28), and their liquidus temperatures should therefore be higher than T_{CMB} .

Recent DAC experiments revised the melting temperature of pure Fe upward to be 4190 and 6230 K at CMB and ICB pressures, respectively (3), which is consistent with both ab initio calculations and shock-wave experiments. The upper bounds of T_{CMB} and T_{ICB} found in this study require that the liquidus temperature of the outer core alloy is depressed by >600 K at 136 GPa and >1400 K at 329 GPa from that of pure Fe (Fig. 4). Such a large depression would be impossible without H in the core as discussed above (2, 17). Given that the incorporation of 6 wt % Si contributes to diminishing the liquidus temperature by ~150 K (29) and the density by ~5% (30), Fe_{93.4}H_{0.6}Si₆ (in weight ratio) may be compatible with the low T_{CMB} as well as the 10% core density deficit, although a more precise estimate requires knowledge about liquid density and melting behavior in the Fe-H-Si system. A large amount of H may have been incorporated into metals from a hydrous magma ocean at the time of core formation (31).

Fig. 3. Solidus curve of a pyrolitic lower mantle. Solid and open circles indicate the presence and the absence of partial melt, respectively, based on x-ray tomography. The melting curve is based on the Simon and Glatzel equation. The experimental temperature in this study represents the maximum value, whereas pressure uncertainty is $\pm 10\%$ (9). Light green (7) and purple (8) curves with squares show the solidus temperature of primitive mantle determined by previous in situ measurements in a DAC. The orange band illustrates a possible range of pyrolite solidus reported by (6). The results of earlier multi-anvil experiments are shown by crosses (above solidus, red; subsolidus, blue) (12, 13).

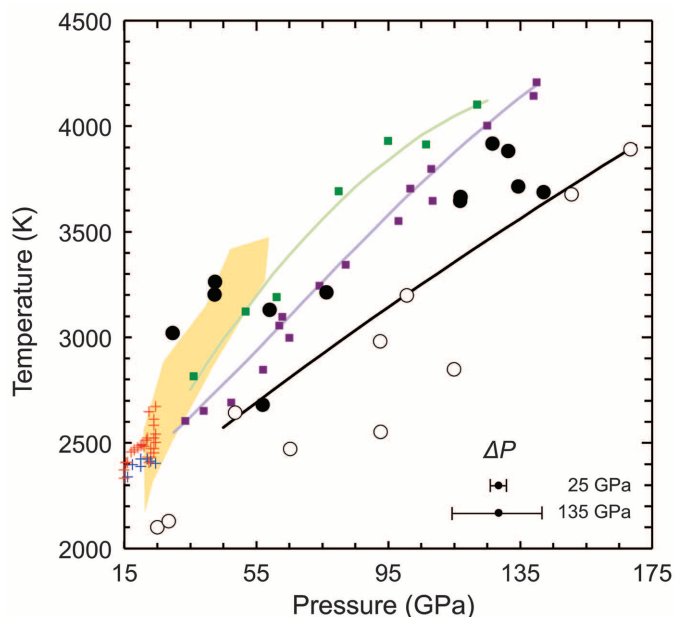
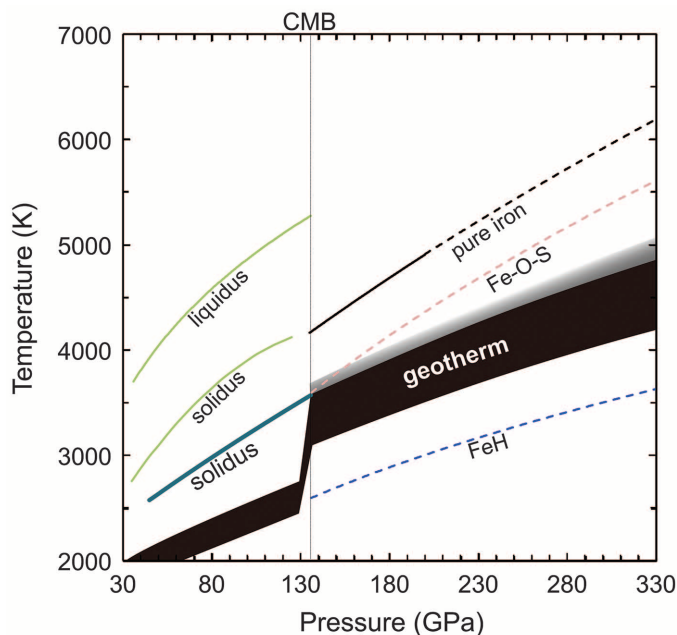


Fig. 4. Temperature profile (geotherm) in the lower mantle and the outer core. Dark blue curve, solidus of pyrolite (this study); light green curves, liquidus and solidus of pyrolite (7). Melting (liquidus) temperatures of pure Fe (3), Fe-O-S alloy (26), and FeH (17) are shown by black, pink, and blue lines, respectively. The dashed curves represent extrapolations of experimental data.



References and Notes

1. R. Boehler, *Annu. Rev. Earth Planet. Sci.* **24**, 15–40 (1996).
2. D. Alfè, M. J. Gillan, G. D. Price, *Contemp. Phys.* **48**, 63–80 (2007).
3. S. Anzellini, A. Dewaele, M. Mezouar, P. Loubeyre, G. Morard, *Science* **340**, 464–466 (2013).
4. J. W. Hernlund, C. Thomas, P. J. Tackley, *Nature* **434**, 882–886 (2005).
5. T. Lay, J. Hernlund, B. Buffett, *Nat. Geosci.* **1**, 25–32 (2008).
6. A. Zerr, A. Diegeler, R. Boehler, *Science* **281**, 243–246 (1998).
7. G. Fiquet et al., *Science* **329**, 1516–1518 (2010).
8. D. Andrault et al., *Earth Planet. Sci. Lett.* **304**, 251–259 (2011).

9. Materials and methods are available as supplementary materials on Science Online.
10. R. Nomura *et al.*, *Nature* **473**, 199–202 (2011).
11. D. Andraut *et al.*, *Nature* **487**, 354–357 (2012).
12. J. Zhang, C. Herzberg, *J. Geophys. Res.* **99**, 17729 (1994).
13. R. G. Trønnes, D. J. Frost, *Earth Planet. Sci. Lett.* **197**, 117–131 (2002).
14. J. E. Dixon, L. Leist, C. Langmuir, J.-G. Schilling, *Nature* **420**, 385–389 (2002).
15. B. Marty, *Earth Planet. Sci. Lett.* **313–314**, 56–66 (2012).
16. A. K. McNamara, E. J. Garnero, S. Rost, *Earth Planet. Sci. Lett.* **299**, 1–9 (2010).
17. K. Sakamaki *et al.*, *Phys. Earth Planet. Inter.* **174**, 192–201 (2009).
18. H. Terasaki *et al.*, *Phys. Earth Planet. Inter.* **194–195**, 18–24 (2012).
19. K. Ohta *et al.*, *Earth Planet. Sci. Lett.* **349–350**, 109–115 (2012).
20. G. M. Manthilake, N. de Koker, D. J. Frost, C. A. McCammon, *Proc. Natl. Acad. Sci. U.S.A.* **108**, 17901–17904 (2011).
21. N. de Koker, G. Steinle-Neumann, V. Vlček, *Proc. Natl. Acad. Sci. U.S.A.* **109**, 4070–4073 (2012).
22. M. Pozzo, C. Davies, D. Gubbins, D. Alfè, *Nature* **485**, 355–358 (2012).
23. T. Lay, J. Hernlund, E. J. Garnero, M. S. Thorne, *Science* **314**, 1272–1276 (2006).
24. J. W. Hernlund, S. Labrosse, *Geophys. Res. Lett.* **34**, L05309 (2007).
25. H. Huang *et al.*, *Nature* **479**, 513–516 (2011).
26. H. Terasaki *et al.*, *Earth Planet. Sci. Lett.* **304**, 559–564 (2011).
27. A. Shahar *et al.*, *Earth Planet. Sci. Lett.* **288**, 228–234 (2009).
28. G. Morard *et al.*, *Phys. Chem. Miner.* **38**, 767–776 (2011).
29. R. A. Fischer *et al.*, *Earth Planet. Sci. Lett.* **373**, 54–64 (2013).
30. J. Li, Y. Fei, in *The Mantle and Core*, R. W. Carlson, Ed., vol. 2 of *Treatise on Geochemistry*, H. Holland, K. K. Turekian, Eds. (Elsevier-Pergamon, Oxford, 2003), pp. 521–546.
31. T. Okuchi, *Science* **278**, 1781–1784 (1997).

Acknowledgments: We thank M. Ishikawa, Y. Kudo, and T. Tomomasa for their assistance in the experiments at BL10XU and BL47XU, SPring-8 (proposals no. 2012B0087 and 2012B1706). Discussions with E. Takahashi and Y. Nakajima were helpful. T. Kawamoto and F. Tomiyasu supported the Fourier transform infrared and thermal conversion elemental analyzer measurements, respectively. R.N. was supported by a Japan Society for the Promotion of Science Fellowship for Young Scientists. Data are available in the supplementary materials.

Supplementary Materials

www.sciencemag.org/content/343/6170/522/suppl/DC1
Materials and Methods
Supplementary Text
Figs. S1 to S7
Tables S1 and S2
References (32–55)

6 November 2013; accepted 30 December 2013
10.1126/science.1248186

A Mechanosensory Pathway to the *Drosophila* Circadian Clock

Alekos Simoni,^{1,†} Werner Wolfgang,^{1,*} Matthew P. Topping,² Ryan G. Kavlie,³
Ralf Stanewsky,^{1,4,‡} Joerg T. Albert^{2,3,4,‡}

Circadian clocks attune the physiology of virtually all living organisms to the diurnal cycles of their environments. In metazoan animals, multiple sensory input pathways have been linked to clock synchronization with the environmental cycle (entrainment). Extrinsic entrainment cues include light and temperature. We show that (12-hour:12-hour) cycles of vibration and silence (VS) are sufficient to synchronize the daily locomotor activity of wild-type *Drosophila melanogaster*. Behavioral synchronization to VS cycles required a functional clock and functional chordotonal organs and was accompanied by phase-shifts of the daily oscillations of PERIOD protein concentrations in brain clock neurons. The feedback from mechanosensory—and particularly, proprioceptive—organs may help an animal to keep its circadian clock in sync with its own, stimulus-induced activities.

The neurocellular network that adjusts an organism's physiological needs to the diurnal fluctuations of its environment is summarily referred to as the “circadian clock” (1). The tasks associated with the operation of circadian clocks are computationally challenging. In metazoan animals, clock synchronization requires integration of inputs from different sensory modalities, of which light and temperature changes provide major cues.

Chordotonal organs (ChOs) have been linked to temperature entrainment of the circadian clock in adult flies (2). ChOs are internal mechano-

receptors mediating proprioception and the detection of air- and substrate-borne vibrations (3, 4). If signaling from ChOs provides sensory input for the entrainment of the fly's circadian clock to temperature cycles (2), we reasoned that exposure to a rhythmic mechanical stimulus (Fig. 1, A and B, stimulus details) that excites the fly's ChOs (fig. S1, response details) might phenocopy temperature entrainment (5) and be sufficient to synchronize the clock and clock-controlled locomotor behavior. To test this, we first entrained adult wild-type flies to 12-hour:12-hour light-dark (LD) cycles (6). Flies were then transferred to constant darkness (DD) and constant temperature (7). One group remained in silence to serve as controls (Fig. 1C, top), whereas a second group was exposed to 12-hour:12-hour vibration:silence (VS) cycles (Fig. 1C, bottom). In the first, 4-day-long VS regime (VS1), vibration onset was delayed by 6 hours from light onset in the preceding LD cycles (L+6h). In a second, 5-day-long vibration regime (VS2), vibration onset was then delayed by another 6 hours (thus now L+12h). At the end of VS2, the flies were released into the final free running (FR) conditions—that is, darkness and silence—in which they were kept for another 5 days (Fig. 1C).

During VS1, wild-type flies showed an initial activity peak after vibration onset, which decreased throughout the remaining vibration part (Fig. 1C and fig. S2). During VS2, flies again showed increased activity immediately after vibration onset, which declined rapidly (Fig. 1, C and D, and fig. S2). In contrast to VS1, flies now also exhibited increased activity several hours before vibration onset, which is reminiscent of anticipatory behavior in LD cycles (Fig. 1D and fig. S2). To quantify the behavioral activity occurring before vibration onset (the anticipatory activity component), we determined the ratio of the activity in the 4-hour time window before the V-phase and the total activity in the S-phase [compare with (8)]. The resulting entrainment index (EI) revealed that anticipatory activity was significantly increased (Fig. 2B). To further probe whether the activity patterns during the VS cycles resulted from a clock-controlled synchronization of behavioral activity, as indicated by the EI calculation, we conducted a phase analysis of the activity peaks in the final FR conditions between flies exposed to VS cycles and controls (fig. S3) (7, 9). The FR activity peaks were in phase with those of the last VS cycle, demonstrating that the circadian clock driving these rhythms had indeed been stably synchronized (Figs. 1, C and D, and 2C). In the control group, activity peaks free-ran from the synchronized phase set during the initial LD cycle and hence occurred significantly earlier (mean difference, 4.9 hours; $P < 0.001$, Watson-Williams-Stevens test) (Figs. 1, C and D, and 2C; fig. S3; and table S1) than those of the experimental group.

Not all flies synchronized their activity to the vibration cycles (fig. S4). We therefore assessed each fly's synchronization by inspecting individual actograms without any knowledge about the experimental treatments of the particular fly under investigation. This “observer-blind” analysis revealed that across eight independent experiments, ~53% of all flies ($n = 312$) synchronized to vibration cycles (table S1). The reasons for this incomplete synchronization are unclear. The vibration stimulus used across our experiments

¹School of Biological and Chemical Science, Queen Mary, University of London, London E1 4NS, UK. ²Centre for Mathematics and Physics in the Life Sciences and Experimental Biology (CoMPLEX), University College London, Gower Street, London WC1E 6BT, UK. ³The Ear Institute, University College London, 332 Gray's Inn Road, London WC1X 8EE, UK. ⁴Department of Cell and Developmental Biology, University College London, London WC1E 6DE, UK.

*These authors contributed equally to this work.

†Present address: Department of Life Science, Division of Cell and Molecular Biology, Imperial College London, South Kensington, London SW7 2AZ, UK.

‡Corresponding author. E-mail: r.stanewsky@ucl.ac.uk (R.S.); joerg.albert@ucl.ac.uk (J.T.A.)

was chosen for its experimental reliability [easy quantifiability and reproducibility (7)] and was not optimized for behavioral efficacy. Two-frequency vibration as used in this study may only excite a certain fraction of the animals' ChOs, and other, spectrally more complex stimuli might prove behaviorally more efficient. Indeed, ablating the animal's antennae, which changes the stimulus perceived by the flies, was already sufficient to increase synchronization rates to ~74% (Fig. 2, B and C; fig. S5; and table S1).

To test whether behavioral entrainment to VS cycles requires a functional clock, we performed the above experiment in the background of the *per*⁰¹ mutation—a loss-of-function allele of the central clock gene *period* (10). On average, *per*⁰¹ mutant flies displayed higher activity during the silent phase and lower activity during the vibration phase (fig. S6), but individual actograms revealed a “noisy” activity pattern during the entire vibration part compared with constitutively high or low activity in silence (fig. S4). The *per*⁰¹ flies did not show anticipatory behavior during VS cycles (fig. S6), suggesting that this anticipation requires a functional clock. We tried to

rescue the VS entrainment in *per*⁰¹ flies by introducing a *period* construct (*per*⁰¹ 13.2) that restores behavioral and molecular rhythms (8, 11, 12). EI calculation and observer-blind actogram classification showed that *per*⁰¹ 13.2 flies synchronized to the VS cycles (Fig. 2, A and B; figs. S4 and S6; and table S1) with the phase difference between the VS-exposed and control flies differing significantly ($P < 0.01$) (fig. S3). Although on average *per*⁰¹ 13.2 flies show a 24-hour period (table S1), the silent control flies do show a lengthened period during the part of the experiment corresponding to VS2 (Fig. 2A, DD days 8 to 12). They thereby acquire a later phase as compared with that of the VS-exposed flies before entry into the final 5 experimental days (used to calculate the phase differences between silence and VS-exposed flies); as a result, the phase relation between the activity curves of experimental and control flies is reversed as compared with that of CantonS flies (Fig. 2C and fig. S3).

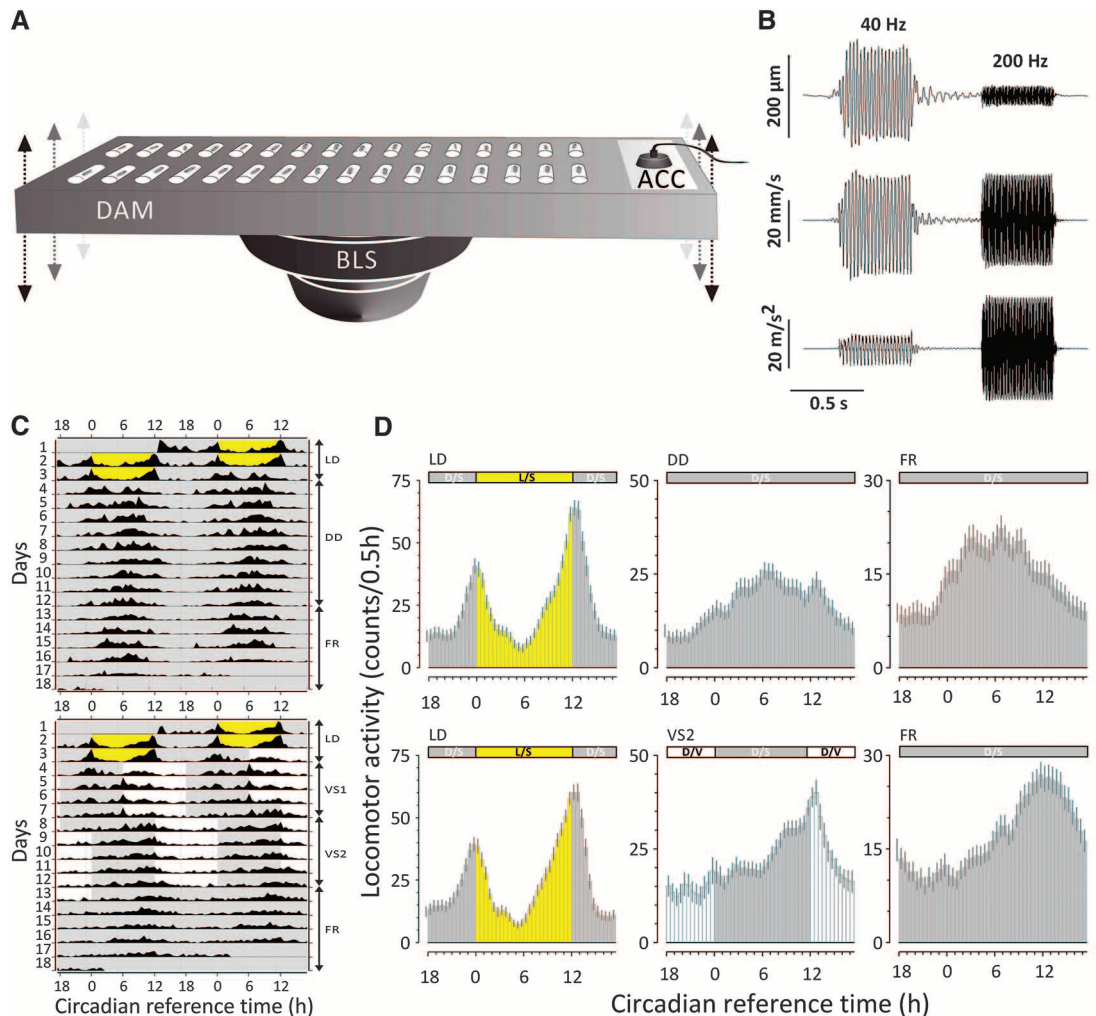
To explore the molecular requirements of vibration-dependent entrainment, we tested flies with mutations in *tilB* (13) and *nocte* (14), two genes important for both temperature synchro-

nization of the fly's circadian clock and structural integrity of ChOs (2, 13). Flies carrying either the loss-of-function allele *tilB*¹ or the hypomorphic allele *nocte*^P failed to synchronize to vibration cycles and instead free-ran throughout the experiment (Fig. 2, figs. S5 and S7, and table S1).

If VS cycles synchronize clock-controlled behavior, they should also synchronize the oscillations of clock gene products in the neurons driving this behavior. We therefore compared the FR bioluminescence oscillations in brain clock neurons of two groups of flies initially synchronized to the same LD cycle and expressing a PER-LUCIFERASE (PER-LUC) fusion protein in subsets of their clock neurons (8, 15): experimental flies that had been exposed to 12-hour:12-hour VS cycles and control flies that had not been exposed to VS cycles (Fig. 3). Both experimental and control flies displayed circadian oscillations of PER-LUC protein levels in constant conditions ($\tau = 22.7 \pm 0.2$ hours) (Fig. 3). In flies exposed to VS cycles, however, the phase of the molecular oscillation was shifted compared with that of flies kept in silence. The observed mo-

Fig. 1. Synchronization of *Drosophila* locomotor activity by VS cycles.

(A) Experimental set-up showing a *Drosophila* activity monitor (DAM) mounted on top of a bass loudspeaker (BLS). Vibrations were monitored by using an accelerometer (ACC). **(B)** Example of vibratory stimulus sequence played in loop (bottom, acceleration; middle, velocity; top, displacement). **(C)** (top) Locomotor activity (actogram) of wild-type (CantonS; $n = 15$ flies) control flies that were exposed to initial 12-hour:12-hour, light-dark (LD) cycles, followed by complete darkness (DD). (bottom) Actogram of experimental flies (CantonS; $n = 15$ flies) that were exposed to initial 12-hour:12-hour LD cycles, followed by two phase-delayed 12-hour:12-hour VS cycles (VS1-VS2) in DD, followed by DD without VS (free-run, FR). Gray areas, darkness; yellow areas, light; white areas, vibration in darkness. The final 5 days in DD were used to compare the phase of the peak activity during FR between experimental and control groups. Circadian reference time is given relative to the initial LD entrainment (Lights ON = 0). **(D)** Histograms showing the daily activity averages during three different phases for (bottom) experimental flies (LD, VS2, and FR, $n = 75$ flies) and (top) control flies (LD, DD, and FR, $n = 72$ flies). Error bars represent SEM.



lecular phase shift was sensitive to the phase of the VS entrainment regime: If the VS cycles were delayed [time shift $\Delta t_{\text{vib}} = +6$ hours] relative to the initial LD entrainment, the molecular oscillations appeared to be shifted to the left, with the peaks occurring ~ 5 hours before those of the FR control group (Fig. 3, left); if the VS cycles were advanced ($\Delta t_{\text{vib}} = -6$ hours), however, the peaks appeared shifted to the right, occurring ~ 3.5 hours after those of the controls (Fig. 3, right). Thus, mechanical stimulation can change the phase of the *Drosophila* molecular clock and function as Zeitgeber.

The phenotypes of *nocte^P* and *tilB¹* mutants, together with the crucial role of chordotonal organs for both mechanical and temperature-dependent circadian entrainment, suggest that both modes of entrainment share a common molecular, cellular, and potentially mechanistic basis. When directly comparing the activities of wild-type flies synchronized to the two different Zeitgebers, the activity peaks in relation to the entraining stimuli acquired similar phases (fig. S2). At the end of two phase-delayed temperature cycles (TCs), wild-type flies exhibited their main activity peak at the late cold/early warm phase, whereas after com-

parable VS cycle shifts, the main activity peak occurred during the late silent or early vibration phase (Fig. 1, C and D, and fig. S2).

Our results reveal a mechanosensory input pathway to the fly's circadian clock that requires signaling from ChOs. Although external, diurnally fluctuating mechanical stimuli can also act as extrinsic Zeitgebers, a circadian pattern of mechanoreceptor activation will inevitably result from every locomotor activity that is patterned in a circadian way. ChOs act as proprioceptors and are located at almost every joint of the insect body (3). The summary output of an animal's ChOs would

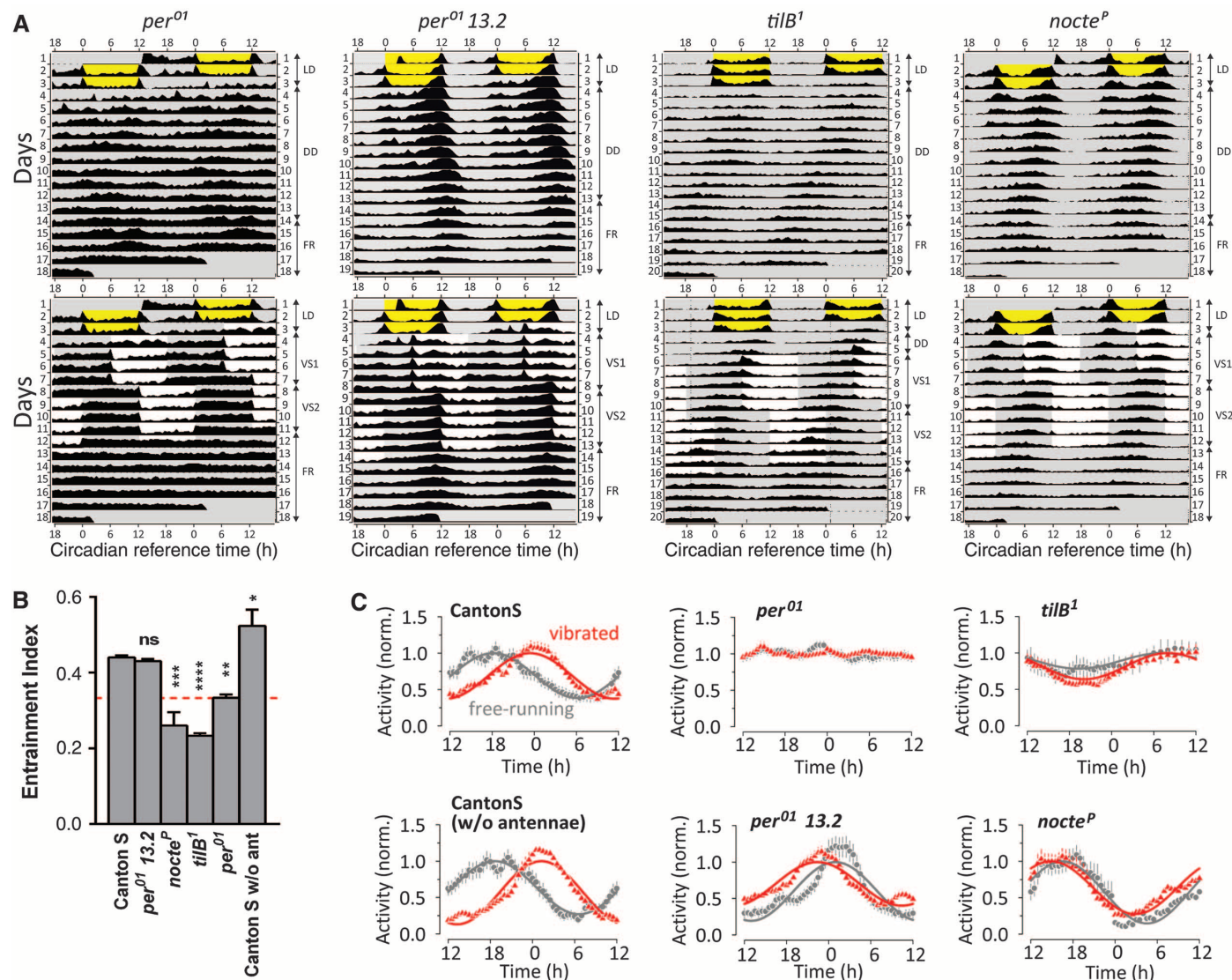


Fig. 2. Requirement of a functional clock and chordotonal organs for synchronization to VS cycles. (A) Average locomotor actograms (top, control flies; bottom, experimental flies) for *per⁰¹*, *per⁰¹ 13.2*, *tilB¹*, and *nocte^P* mutant flies. Quantification is provided in (B) and table S1. Stimulus sequence and actogram shadings are provided in Fig. 1. (B) Entrainment Index: quantification of behavioral activity anticipating the V-onset as a measure for entrainment. Red dotted line indicates random distribution of activity in the 4-hour window (* $P < 0.05$, ** $P < 0.01$, *** $P < 0.001$, **** $P < 0.0001$, one-way analysis of variance) (7). (C) Average locomotor activities for final 5 days in FR conditions of experimental flies exposed to VS cycles (vibrated, red) and control flies not exposed to VS cycles

(FR, gray). Solid lines represent sinusoidal fits to the average locomotor data (circles, control flies; triangles, experimental flies). To facilitate appreciation of phase differences, both data and corresponding fit values have been normalized to the maximum of the fit function. The arrhythmic activities of *per⁰¹* flies have been normalized to their respective mean value. Raw behavioral data of all genotypes in (C) are provided in (A), Fig. 1C, and figs. S4 and S7. CantonS, $n = 75$ flies (vibrated), $n = 72$ flies (FR); CantonS without antennae: $n = 28$ flies (vibrated), $n = 30$ flies (FR); *per⁰¹*: $n = 32$ flies (vibrated), $n = 32$ flies (FR); *per⁰¹ 13.2*: $n = 21$ flies (vibrated), $n = 22$ flies (FR); *tilB¹*: $n = 24$ flies (vibrated), $n = 25$ flies (FR); *nocte^P*: $n = 16$ flies (vibrated), $n = 16$ flies (FR). Error bars represent SEM.

Marine Tubeworm Metamorphosis Induced by Arrays of Bacterial Phage Tail–Like Structures

Nicholas J. Shikuma,^{1*} Martin Pilhofer,^{1,2*} Gregor L. Weiss,¹ Michael G. Hadfield,^{3†} Grant J. Jensen,^{1,2†} Dianne K. Newman^{1,2†}

Many benthic marine animal populations are established and maintained by free-swimming larvae that recognize cues from surface-bound bacteria to settle and metamorphose. Larvae of the tubeworm *Hydroides elegans*, an important biofouling agent, require contact with surface-bound bacteria to undergo metamorphosis; however, the mechanisms that underpin this microbially mediated developmental transition have been enigmatic. Here, we show that a marine bacterium, *Pseudoalteromonas luteoviolacea*, produces arrays of phage tail–like structures that trigger metamorphosis of *H. elegans*. These arrays comprise about 100 contractile structures with outward-facing baseplates, linked by tail fibers and a dynamic hexagonal net. Not only do these arrays suggest a novel form of bacterium-animal interaction, they provide an entry point to understanding how marine biofilms can trigger animal development.

Environmentally selective settlement of swimming larvae that are the propagules of most benthic invertebrate species is a critical life-cycle stage achieved by recognizing specific physicochemical cues (1, 2). This process is of fundamental importance to the fields of developmental biology and marine benthic community ecology—for example, the recruitment of new larval animals is essential to sustain and disperse coral reef populations (1). Economically, larval settlement is necessary for the supply of products for fisheries and aquaculture industries

worldwide (3) and is responsible for millions of dollars of increased fuel consumption per year due to the biofouling of ships (4). Bacteria resident in surface biofilms are now recognized as the sources of metamorphosis-inducing cues for many invertebrates from most phyla (2). Indeed, the importance of microbes to the development and health of diverse animals is becoming increasingly appreciated (5). Yet our understanding of how these microbes interact with their hosts is only in its infancy.

The relation between the marine tubeworm *Hydroides elegans* and the bacterium *Pseudoalteromonas luteoviolacea* is a model for the study of invertebrate metamorphosis (2, 6, 7). Bacteria from the genus *Pseudoalteromonas* are commonly isolated from marine water, sediment, biofilms, or marine eukaryotes (8, 9). *P. luteoviolacea* strain HI1, used in this study, was isolated from a ma-

rine biofilm (8). Recently, Huang *et al.* (7) identified a set of genes in *P. luteoviolacea* whose products are essential to metamorphosis of *H. elegans*. However, the specific cue that triggers this bacterium-mediated developmental transition remained unknown.

In the vicinity of the *P. luteoviolacea* genes identified as essential to the induction of *H. elegans* metamorphosis (7) (Fig. 1, A and B), we identified a cluster of open reading frames (ORFs) predicted to encode components of phage tail–like structures, known as bacteriocins (fig. S1). Bacteria typically use bacteriocins to kill other bacteria by puncturing their membrane, causing depolarization (10, 11). R-type bacteriocins resemble contractile phage tails, similar to type VI secretion systems (T6SS) of Gram-negative bacteria (12). Phage tail–like bacteriocins have a contractile sheath, inner tube, baseplate components and tail fibers, but lack a DNA-filled head and are therefore not replicative. Bacteriocin-like structures can mediate several bacterial pathogen-animal interactions, for example, by causing antifeeding activity in grass grubs (13) and insecticidal activity against wax moths (14). No phage tail–like structures are currently known to mediate an interaction that is beneficial for the animal. On the basis of their predicted role in inducing metamorphosis, we named the ORFs surrounding those identified by Huang *et al.* (7) the metamorphosis-associated contractile structure (*mac*) genes.

To determine whether the *mac* genes play a role in tubeworm metamorphosis, we made in-frame deletions of genes encoding putative sheath (*macS*), tube (*macT1* and *macT2*), and baseplate (*macB*) [previously identified by Huang *et al.* (7)] proteins (fig. S1). These deletion strains grew identically in rich medium (Fig. 1C) but were unable to induce metamorphosis (Fig. 1D).

¹Division of Biology, California Institute of Technology, Pasadena, CA 91125, USA. ²Howard Hughes Medical Institute, Pasadena, CA 91125, USA. ³Kewalo Marine Laboratory, University of Hawai'i at Mānoa, Honolulu, HI 96813, USA.

*These authors contributed equally to this work.

†Corresponding author. E-mail: hadfield@hawaii.edu (M.G.H.); jensen@caltech.edu (G.J.); dkn@caltech.edu (D.K.N.)

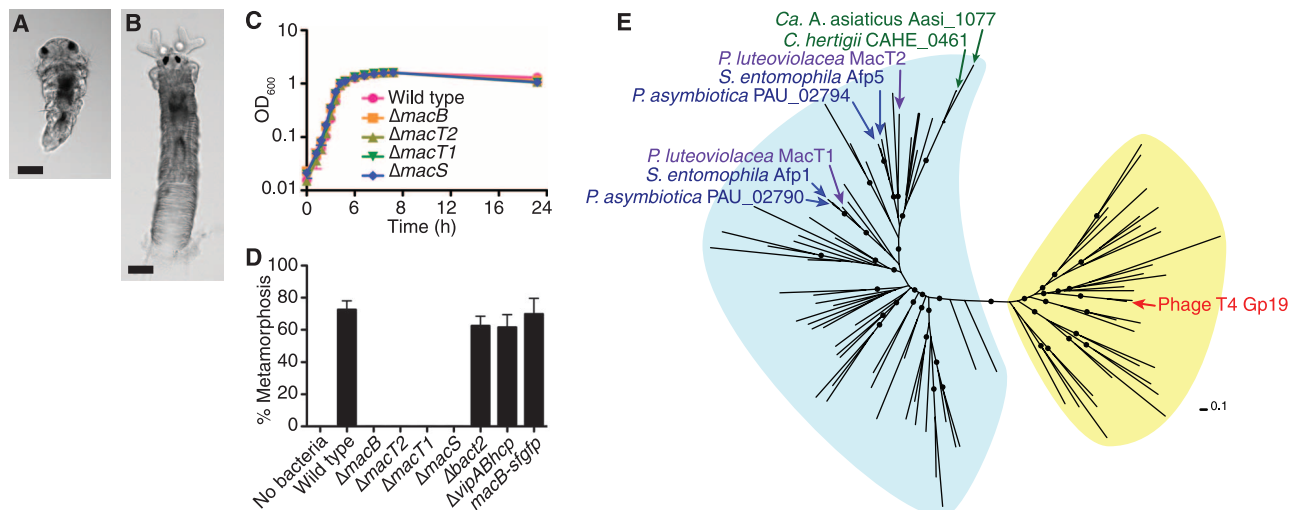


Fig. 1. *P. luteoviolacea mac* genes are required for metamorphosis of *H. elegans* and are similar to genes encoding phage tail–like structures. (A and B) Metamorphically competent *H. elegans* larva (A) and juvenile adult (B) 12 hours after exposure to a *P. luteoviolacea* biofilm. Scale bars, 50 μ m. (C) Growth of *P. luteoviolacea* wild type and mutants containing in-frame deletions of *mac* genes. OD, optical density, a measure of absorbance. (D) Metamorphosis (%) of *H. elegans* in response to biofilms of *P. luteoviolacea* wild

type; and $\Delta macB$, $\Delta macT1$, $\Delta macT2$, $\Delta macS$, $\Delta bact2$, and $\Delta vipABhcp$ mutants; and *macB-sfgfp* fusion strains. Sterile artificial seawater (no bacteria) was used as a negative control. Error bars represent standard deviations ($n = 4$). (E) Maximum likelihood unrooted phylogeny of the Gp19 protein family. Gp19-like protein domains originating from bacteria and phages are highlighted in blue and yellow, respectively. Nodes with approximate likelihood-ratio test (aLRT) (29) values ≥ 0.8 are marked with a black circle. Scale bar indicates amino acid substitutions per site.

Complementation of mutant strains in trans with *mac* genes resulted only in modest restoration of metamorphosis (fig. S2A). When the *mac* genes were replaced in their native chromosomal loci, metamorphosis induction was restored (fig. S2B). In addition to the *mac* gene cluster, we identified a second phage tail-like bacteriocin locus (bacteriocin-2) containing two genes predicted to encode putative tube and sheath proteins and a third gene cluster predicted to encode proteins similar to tube (Hcp) and sheath proteins (VipA/B) from a T6SS (table S1). In contrast to the Δmac mutants, strains containing in-frame deletions of genes predicted to encode tube and sheath proteins of bacteriocin-2 ($\Delta bact2$) or T6SS ($\Delta vipABhcp$) still induced metamorphosis of *H. elegans* similarly to wild type (Fig. 1D).

To test whether the *mac* gene-cluster is responsible for producing phage tail-like structures, we compared negatively stained electron micrographs of cultures of *P. luteoviolacea* wild type—producing MAC, bacteriocin-2, and T6SS—and mutants producing only MACs ($\Delta vipABhcp\Delta bact2$), producing only bacteriocin-2 ($\Delta vipABhcp\Delta macS\Delta macB$), or lacking T6SS, bacteriocin-2, and MACs ($\Delta vipABhcp\Delta bact2\Delta macS\Delta macB$). Contracted and disassembled phage tail-like bacteriocins, as well as aggregated sheaths, were observed in the extracellular space of wild-type cells (Fig. 2A). Cultures producing only MACs ($\Delta vipABhcp\Delta bact2$) contained dense aggregates of contracted sheaths (length 135 ± 4 nm, $n = 13$) and possibly tube structures (Fig. 2B), whereas cultures producing only bacteriocin-2 ($\Delta vipABhcp\Delta macS\Delta macB$) contained contracted and disassembled individual

phage tail-like structures, with shorter contracted sheaths (94 ± 3 nm, $n = 13$) (Fig. 2C). No sheath or phage tail-like structures were detected in the strain lacking MACs, bacteriocin-2, and T6SS ($\Delta vipABhcp\Delta bact2\Delta macS\Delta macB$) (Fig. 2D). Similarly, we observed sheaths or bacteriocins in purifications from the same strains, except that dense aggregates of MACs were not observed (fig. S3, A to D). Mass spectrometry of two bands present in an SDS–polyacrylamide gel electrophoresis (SDS–PAGE) gel of purified proteins from the strain producing only MAC ($\Delta vipABhcp\Delta bact2$)—not seen in the sample from the strain lacking MAC, bacteriocin-2, and T6SS ($\Delta vipABhcp\Delta bact2\Delta macS\Delta macB$) (fig. S4)—revealed three peptides matching the putative MAC sheath protein (MacS) and one peptide matching a putative MAC tube protein (MacT2).

To determine the phylogenetic placement of MACs, we compared sequences of domains from MacT1 and MacT2 to similar domains from the phage T4 Gp19 tail tube (PF06841) protein family (e-value = 2.1×10^{-32} and 3.1×10^{-13} , respectively). MacT1 and MacT2 grouped with bacterial Gp19 proteins within distinct clades (Fig. 1E) and are closely related to the phage tail-like bacteriocin tube proteins from *Serratia entomophila* (13) and *Photobacterium asymbiotica* (14). Comparative genomics also revealed that multiple genes in the *P. luteoviolacea* gene cluster are homologous to genes from the *S. entomophila* *apf* locus, with some conservation of synteny (fig. S1, table S1), which suggested a common evolutionary origin. It is noteworthy that MacT1 and MacT2 are related to tube proteins predicted to function as part

of T6SSs (15) in the parasitic wasp symbiont, *Cardinium hertigii* (16), and the amoeba symbiont, *Candidatus Amoebophilus asiaticus* (17) (Fig. 1E).

Given the relatedness of MACs to phage and phage tail-like structures, we investigated whether *P. luteoviolacea* produces and releases MACs extracellularly. To track MAC localization in vivo, we constructed a strain encoding a C-terminal fusion of MacB with superfolder green fluorescent protein (sfGFP) (18). When the native chromosomal *macB* gene was replaced with one encoding MacB-sfGFP, the recombinant strain induced metamorphosis to levels comparable with that of wild type (Fig. 1D). Fluorescence light microscopy revealed that the MacB-sfGFP fusion protein localized extracellularly when broth cultures reached stationary phase and produced approximately 0.5- to 1.0- μ m-wide ringlike signals, whereas the untagged strain showed no fluorescence (Fig. 2, E and F). MacB-sfGFP expression was observed by using three different marine media [ASWT, NSWT, and 2216 (fig. S5)], which suggests that extracellular release is dependent neither on soluble factors present in natural seawater nor on a specific nutrient-rich medium. Of the cells in a population, 2.4% ($n = 1244$) showed intracellular GFP expression, many of them seemingly in the process of cell lysis. Time-lapse microscopy revealed that lysis of a subset of cells precedes the appearance of extracellular MacB-sfGFP (movie S1).

Electron cryomicroscopy (19) of a strain producing only MACs ($\Delta vipABhcp\Delta bact2$) allowed us to visualize these structures at high resolution in a near-native state. Four out of 162 cells (2.5%) showed intracellular phage tail-like bacteriocins.

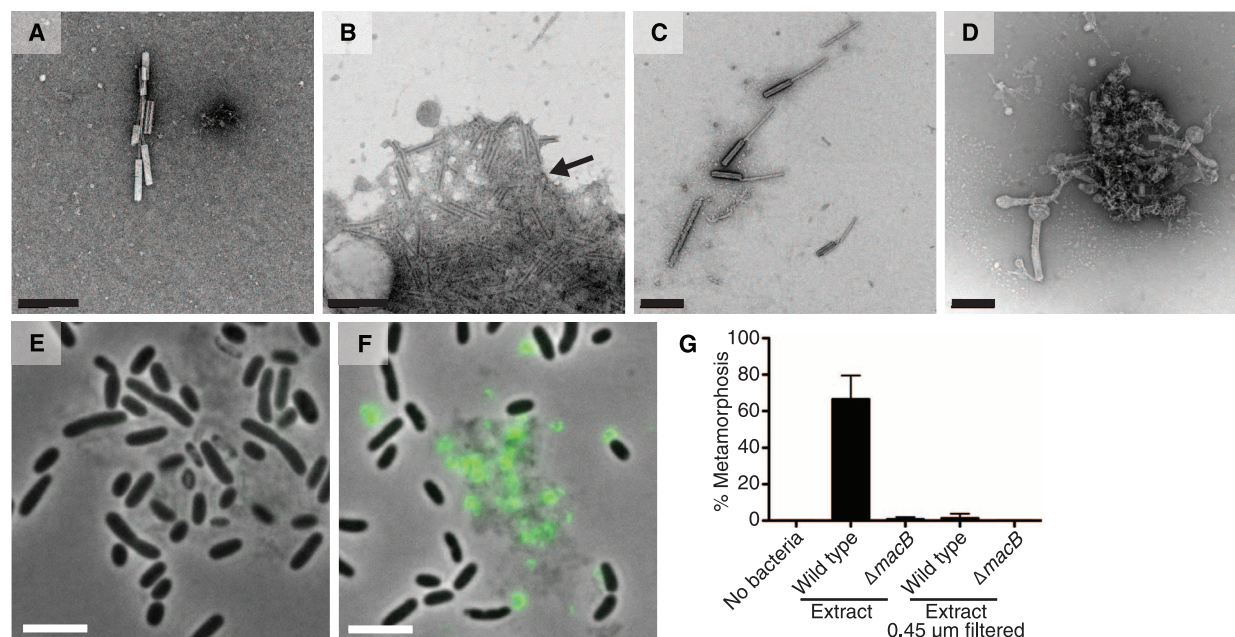


Fig. 2. MACs are phage tail-like structures, are released by cell lysis, and mediate metamorphosis of *H. elegans*. (A to D) Negative stain EM of *P. luteoviolacea* (A) wild type, (B) $\Delta vipABhcp\Delta bact2$, (C) $\Delta vipABhcp\Delta macS\Delta macB$, and (D) $\Delta vipABhcp\Delta bact2\Delta macS\Delta macB$. Aggregated sheaths are indicated by an arrow in (B). Scale bars, 200 nm. (E and F) Micrographs of merged phase-contrast and fluorescence images of *P. luteoviolacea* (E) wild-type and (F)

macB-sfgfp strains (see movie S1). Fluorescence of MacB-sfGFP is shown in green. Scale bar, 5 μ m. (G) Metamorphosis (%) of *H. elegans* in response to cell-free extracts from *P. luteoviolacea* wild type and $\Delta macB$ mutant. Extracts unfiltered and 0.45- μ m filtered are indicated. Sterile artificial seawater (no bacteria) was used as a negative control. Error bars represent standard deviation ($n = 4$).

This percentage of MAC-containing cells matches the percentage of cells harboring MacB-sfGFP. Electron cryotomography (ECT) of these four cells revealed that the entire cytoplasm was packed with clusters of MACs, which in some cases appeared to be connected by a filamentous mesh (white arrow in Fig. 3A, movie S2). The shape and membrane structures of MAC-producing cells indicated that they were about to undergo lysis (fig. S6).

We then asked whether enriched MAC preparations were sufficient to induce metamorphosis in the absence of bacterial cells. MAC preparations obtained by standard bacteriocin purification protocols (12) failed to induce *H. elegans* metamorphosis. MACs likely contract upon purification, and the arrays fall apart, consistent with our observation that MACs were almost exclusively in a contracted state when visualized by

negative-stain electron microscopy (EM). A gentle purification from wild-type *P. luteoviolacea* resulted in a MAC preparation that induced metamorphosis of *H. elegans* (Fig. 2G), whereas extracts from a MAC mutant ($\Delta macB$) did not. Assays were performed with extract concentrations derived from the equivalent of 10^7 cells/ml ($100\times$ dilution). Filtering extracts from wild-type cells through a $0.45\text{-}\mu\text{m}$ filter abolished the metamorphic effect, consistent with the observation that MacB-sfGFP forms $>0.45\text{-}\mu\text{m}$ aggregates. Concentrated bacteriocin extracts (derived from the equivalent of 10^8 cells/ml, $10\times$ dilution) caused 100% larval death after 24 hours, which indicated that MACs or copurifying constituents can have toxic effects at high doses. We do not know the concentration of MACs in laboratory or natural marine biofilms.

To address whether another factor present in the MAC lysate was responsible for inducing metamorphosis independent of MACs, we constructed *macB-sfgfp* strains in mutants lacking the MAC sheath protein ($\Delta macS$), or MAC tube proteins ($\Delta macT1$ or $\Delta macT2$). We observed extracellular MacB-sfGFP fluorescence in all mutants (fig. S7, C to E). Levels of MacB-sfGFP were comparable between a *macB-sfgfp* strain and strains with deletions of *macS*, *macT1*, or *macT2*, as determined by immunoblot analysis with antibodies against GFP (fig. S7, F and G), which suggested that the expression and stability of MacB-sfGFP is not dependent on other MAC components. These results indicate that other biomolecules derived from lysed cells are insufficient to promote metamorphosis of *H. elegans* in the absence of functional MACs. Although MACs

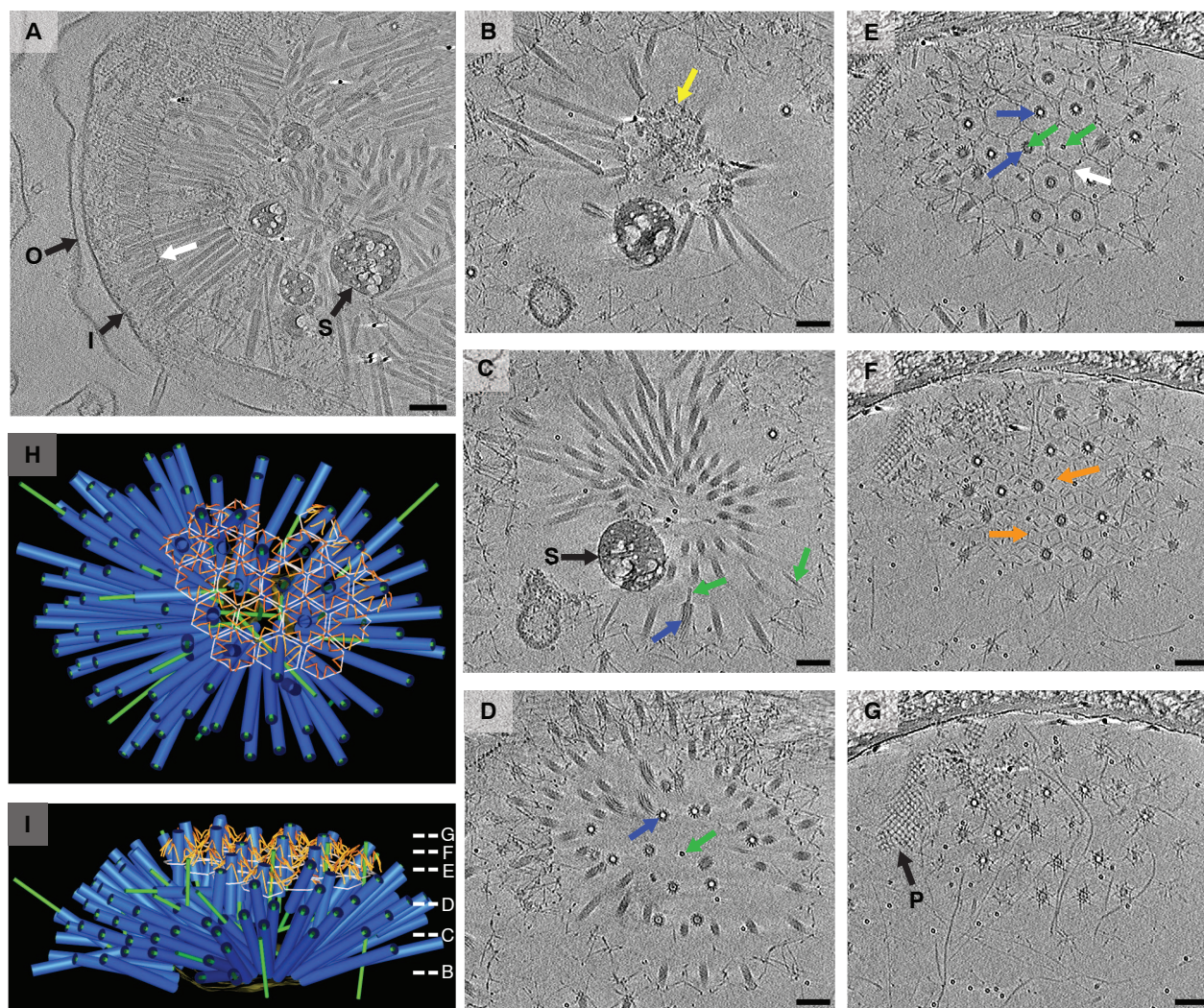


Fig. 3. MACs are assembled intracellularly and expand as an ordered array upon cell lysis. *P. luteoviolacea* $\Delta vipABhcp\Delta bact2$ mutant cells and extracellular aggregates were imaged by ECT (shown are 16.8-nm-thick slices). (A) The cytoplasm of a subset of cells (4 in 162) was packed with MAC aggregates, and cells appeared in the process of lysis (see movie S2). I, inner membrane; O, outer membrane; S, storage granule; white arrow, filamentous connections. (B to G) Extracellular MAC arrays are highly ordered (shown are 2D slices through a tomogram at different z-heights) (see movies S3 and S4).

Yellow arrow, amorphous core; green arrow, inner tube; blue arrow, sheath; white arrow, filamentous hexagonal net; orange arrow, tail fibers; P, presumably polymerized sheath protein. (H and I) MAC arrays were hemispherical with MACs coalescing in an amorphous core and the baseplates hexagonally arranged on the surface. Individual MACs were connected by tail fibers and surrounded by a hexagonal net. Different views of a segmented model of the array are shown. Slice z-heights in (B) to (G) are indicated with the corresponding panel letter. Scale bars, 100 nm.

are necessary for metamorphosis, whether they are sufficient remains to be determined. Additional ORFs in the *mac* gene cluster, such as those identified by Huang *et al.* (7) (i.e., ORF2, ORF3, and ORF4A/B/C) (fig. S1), might also contribute to the MAC structure or the direct induction of metamorphosis.

We used the same MAC extracts shown to promote metamorphosis of *H. elegans* in bacteriocidal activity assays with closely related *P. luteoviolacea* strains and species (*P. luteoviolacea* strain ATCC 33492, *P. piscicida*, and *P. haloplanktis*). These MAC extracts did not kill close relatives of *P. luteoviolacea* H11 (fig. S8), unlike bacteriocins produced by other bacteria (20, 21). It remains to be determined whether these or other types of MACs can kill bacterial species under different conditions.

We characterized MAC aggregates using ECT to compare their structure with that of other phage tail-like bacteriocins. In a frozen, near-native state, we observed MACs forming arrays of multiple contractile phage tail-like structures

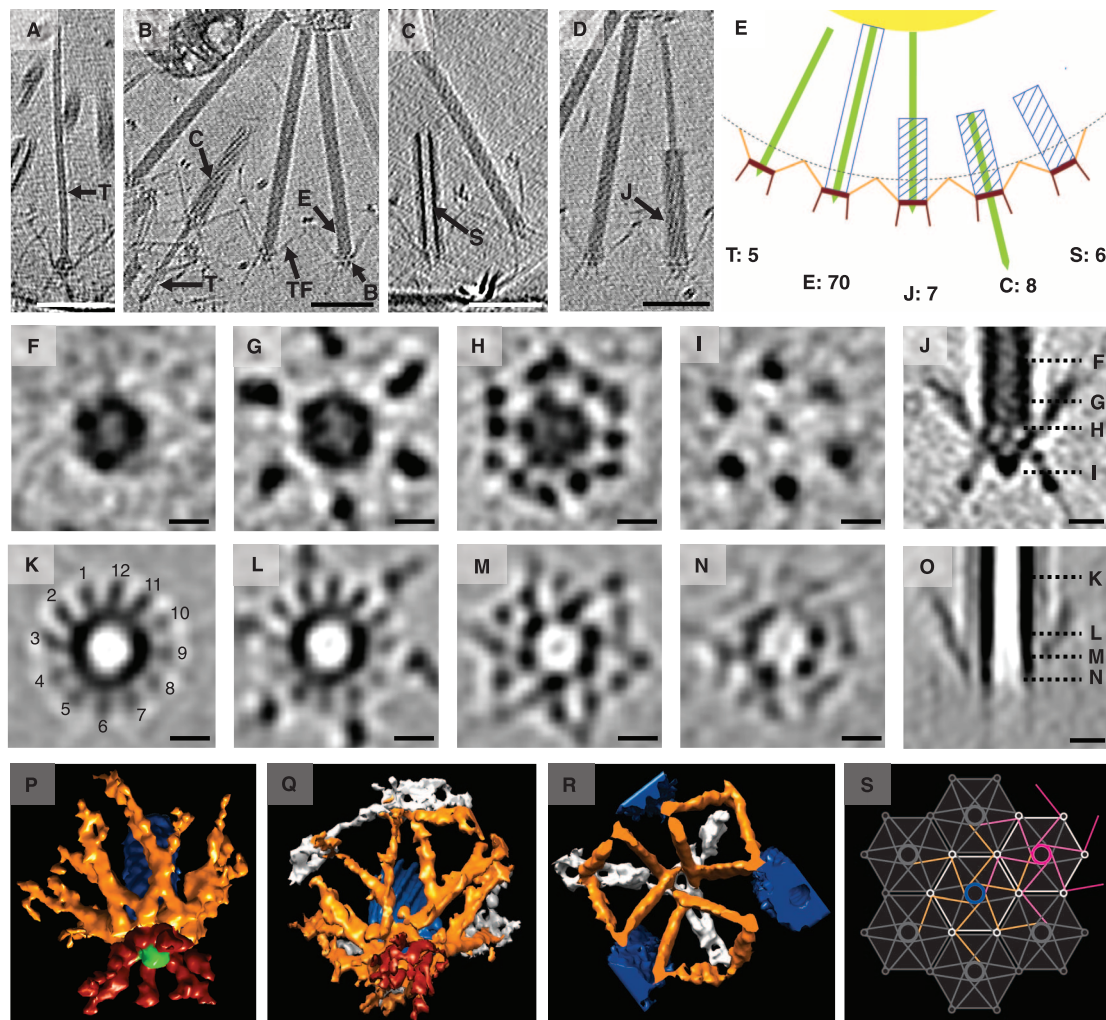
(Fig. 3 and movies S3 and S4). A typical MAC array contained close to 100 individual phagelike tails (96 for the one shown in Fig. 3, B to I), with dimensions matching the size of MacB-sfGFP fluorescence (fig. S9 and table S2). Intracellular MACs were more tightly packed than their extracellular counterparts (table S2), which suggested that MAC arrays expand upon cell lysis. MACs radiate into a hemisphere, originating from an amorphous center (yellow arrow in Fig. 3B). Distal MAC ends were arranged into a regular array, surrounded by a filamentous hexagonal net (white arrow in Fig. 3E). MACs were oriented with their baseplates ("B" in Fig. 4B) outward, with filamentous structures (probably tail fibers; orange arrows in Fig. 3F) emanating from the baseplates and appearing to connect individual MACs to each other ("TF" in Fig. 4B; see also movie S3). To our knowledge, such ordered multitailed arrays have not previously been observed for other types of phagelike structures.

Individual MACs resembled contractile phage tail-like structures (Fig. 4). Sheaths were ob-

served in extended ("E" in Fig. 4B, table S2) and contracted ("C" in Fig. 4B, table S2) forms, with homogeneous and helical surface patterns, respectively. In some cases, the inner tube ("T" in Fig. 4, A and B, and table S2) was observed. We classified the observed MAC conformations into "tube only" (T), "extended" (E), "contracted with jammed tube" (J), "contracted with fired tube" (C) and "contracted without tube" (S) (Fig. 4, A to E, and movie S5). The "extended" conformation represented 73% of MACs within the aggregate shown (Fig. 3). These different structural classes likely represent different states in a functional sequence. In analogy to phage tail-like structures, the "tube only" state may be a partially assembled MAC, whereas the "extended" MAC is in a ready-to-fire configuration (12, 22). "Contracted with fired tube" and "contracted without tube" are likely MACs that have fired. "Contracted with jammed tube" could represent fired MACs that failed to propel the tube. In this conformation, the sheath is contracted as indicated by the helical ridges [assembling T6SS sheaths are in

Fig. 4. MACs are observed in different functional states and connected by tail fibers. (A) Side view of a MAC in the tube only T state. (B) Side views of MACs in extended, E, and contracted, C, states. B, baseplate; TF, tail fibers; T, inner tube. (C) Side view of a MAC in the contracted sheath without tube S state. (D) Side view of a MAC in the contracted state with jammed tube J. Scale bars in (A) to (D), 100 nm.

Tomographic slices that are 16.8 nm thick are shown in (A) to (D). (E) Schematic of different functional states. Numbers indicate the quantity of each state found in the MAC array shown in Fig. 3, (B) to (I). (F to J) Subtomogram average of extended MACs. Cross-sectional slices at different z-heights are shown in (F) to (I) and their positions are indicated in the side view (J). Slices that are 8.4 nm thick are shown. Scale bars, 10 nm. (K to O) Subtomogram average of contracted MACs. Cross-sectional slices at different z-heights are shown in (K) to (N), and their positions are indicated in the side view (O). Slices that are 8.4 nm thick are shown. Scale bars, 10 nm. (P to R) Isosurface of subtomogram averages (see movies S6 to S8) of an extended (P) and a contracted (Q) MAC and of the tail fiber junction (R). Tail pins and baseplate, red; tail fibers, orange; inner tube and spike, green; sheath, blue; hexagonal net, white. (S) Schematic model of tail fiber connections in the MAC array. Each MAC unit contributes six tail fibers that connect to neighboring MAC units. The central MAC unit is colored in the color code used in (P) to (R). A second MAC unit is colored magenta.



white. (S) Schematic model of tail fiber connections in the MAC array. Each MAC unit contributes six tail fibers that connect to neighboring MAC units. The central MAC unit is colored in the color code used in (P) to (R). A second MAC unit is colored magenta.

the extended conformation (12)], and the sheath length of 5 of 7 structures matches the length of a fired MAC (table S2).

We averaged 20 and 25 subtomograms of MACs in the “extended” (Fig. 4P, movie S6) and “contracted without tube” (Fig. 4Q, movie S7) states, respectively. Averages of subtomograms show the different sheath diameters, helical surface ridges on contracted sheath (ridges indicated in Fig. 4K), baseplate symmetry and tail fibers in longitudinal (Fig. 4, J and O) and cross-sectional views (Fig. 4, F to I and K to N). In both the extended and contracted forms twelve fibers emerge from the baseplate, cross paths, and separate to meet at the ring-shaped vertices of the hexagonal net surrounding individual MACs (Fig. 4R, movie S8). We speculate that six of the tail fibers originate from a single MAC, with the remaining six fibers stemming from neighboring MACs to connect the array (Fig. 4, P to S, orange). This six-tail fiber per MAC model (Fig. 4S) is supported by the fact that the two arms of a phage tail fiber have a length ratio of 1:1 (23) and that the length is similar to the tail fiber connections in MACs (fig. S10). The model also predicts the presence of an as-yet-unidentified protein that forms the hexagonal net. A set of six tail pins (Fig. 4P, red) face outwards. Because the tail pins are the most distal structure in the arrays, they are likely the first structure to engage and sense MAC targets.

We have shown that an ordered array of contractile phage tail-like structures produced by an environmentally occurring bacterium induces metamorphosis of a marine invertebrate larva. This discovery begins to explain how marine biofilms can trigger metamorphosis of benthic animals. Our data suggest that MAC arrays are synthesized intracellularly by *P. luteoviolacea*, released by cell lysis, and expand extracellularly into an ordered multi-MAC array. How these arrays engage with larvae of *H. elegans* is an open question. In the arrays imaged, all contracted MACs were clustered together, which suggests that their linkages might support cooperative firing. Array formation might also multiply the total payload delivered per interaction or favor specific engagement sites and/or geometries with MAC targets. The evolutionary pressure to produce MACs is probably strong, given that MAC production leads to the lysis and death of a subpopulation of cells. Whether this represents an instance of altruistic behavior that facilitates group selection, or a neutral lytic event with a set frequency remains to be determined. Although MAC production is beneficial for tubeworm larvae by inducing metamorphosis, it is currently unclear how larval settlement and metamorphosis might benefit the bacterium. It is equally possible that MACs evolved for a completely different purpose. Note that *P. luteoviolacea* has been found to induce the metamorphosis of coral and sea-urchin larvae (24, 25). Other bacterial species also induce metamorphosis of *H. elegans* larvae (8, 26, 27), and *mac*-like gene clusters have

been identified in the genomes of other marine bacteria (28). Future research into how MACs interact with larvae might yield new insights into the mechanisms underpinning marine animal development and ecology, with potentially important practical applications for aquaculture and biofouling.

References and Notes

- M. G. Hadfield, V. J. Paul, in *Marine Chemical Ecology*, J. B. McClintock and B. J. Baker, Eds. (CRC Press, Boca Raton, FL, 2001), pp. 431.
- M. G. Hadfield, *Annu. Rev. Mar. Sci.* **3**, 453–470 (2011).
- Food and Agriculture Organization of the United Nations, *The State of World Fisheries and Aquaculture 2012* (FAO, Rome, 2012).
- M. P. Schultz, J. A. Bendick, E. R. Holm, W. M. Hertel, *Biofouling* **27**, 87–98 (2011).
- M. McFall-Ngai et al., *Proc. Natl. Acad. Sci. U.S.A.* **110**, 3229–3236 (2013).
- B. T. Nedved, M. G. Hadfield, *Marine Indust. Biofouling* **4**, 203–217 (2009).
- Y. Huang, S. Callahan, M. G. Hadfield, *Sci. Rep.* **2**, 228 (2012).
- S. Y. Huang, M. G. Hadfield, *Mar. Ecol. Prog. Ser.* **260**, 161–172 (2003).
- C. Holmström, S. Kjelleberg, *FEMS Microbiol. Ecol.* **30**, 285–293 (1999).
- Y. Michel-Briand, C. Baysse, *Biochimie* **84**, 499–510 (2002).
- Y. Uratani, T. Hoshino, *J. Bacteriol.* **157**, 632–636 (1984).
- M. Basler, M. Pilhofer, G. P. Henderson, G. J. Jensen, J. J. Mekalanos, *Nature* **483**, 182–186 (2012).
- M. R. Hurst, T. R. Glare, T. A. Jackson, *J. Bacteriol.* **186**, 5116–5128 (2004).
- G. Yang, A. J. Dowling, U. Gerike, R. H. French-Constant, N. R. Waterfield, *J. Bacteriol.* **188**, 2254–2261 (2006).
- S. Pukatzki et al., *Proc. Natl. Acad. Sci. U.S.A.* **103**, 1528–1533 (2006).
- T. Penz et al., *PLOS Genet.* **8**, e1003012 (2012).
- T. Penz, M. Horn, S. Schmitz-Esser, *Virulence* **1**, 541–545 (2010).
- J. D. Pédelacq, S. Cabantous, T. Tran, T. C. Terwilliger, G. S. Waldo, *Nat. Biotechnol.* **24**, 79–88 (2006).
- M. Pilhofer, M. S. Ladinsky, A. W. McDowell, G. J. Jensen, *Methods Cell Biol.* **96**, 21–45 (2010).
- T. Köhler, V. Donner, C. van Delden, *J. Bacteriol.* **192**, 1921–1928 (2010).
- D. Gebhart et al., *J. Bacteriol.* **194**, 6240–6247 (2012).
- P. G. Leiman et al., *Virol. J.* **7**, 355 (2010).
- M. E. Cerritelli, J. S. Wall, M. N. Simon, J. F. Conway, A. C. Steven, *J. Mol. Biol.* **260**, 767–780 (1996).
- C. Tran, M. G. Hadfield, *Mar. Ecol. Prog. Ser.* **433**, 85–96 (2011).
- M. J. Huggett, J. E. Williamson, R. de Nys, S. Kjelleberg, P. D. Steinberg, *Oecologia* **149**, 604–619 (2006).
- C. R. C. Unabia, M. G. Hadfield, *Mar. Biol.* **133**, 55–64 (1999).
- S. C. Lau, K. K. Mak, F. Chen, P.-Y. Qian, *Mar. Ecol. Prog. Ser.* **226**, 301–310 (2002).
- O. P. Persson et al., *Environ. Microbiol.* **11**, 1348–1357 (2009).
- N. Anisimova, O. Gascuel, *Syst. Biol.* **55**, 539–552 (2006).

Acknowledgments: We thank B. Pernet for help with locating and identifying tubeworms and for giving us the algal strain used in this work; A. McDowell for help with EM; Y. Huang, who created the Str^R-strain (7); A. Asahina and S. Wilbur for laboratory assistance; J. Levine for help with time-lapse microscopy; J. Ricci for help with phylogenetic analyses; and members of the Newman group for discussions and comments on the manuscript. The Howard Hughes Medical Institute, Z. Yu, and J. de la Cruz are acknowledged for providing access to the FEI Titan Krios at Janelia Farm and support in data collection. N.J.S. was supported by a California Institute of Technology (Caltech) Division of Biology Postdoctoral Fellowship. This collaboration was supported by the Caltech Center for Environmental Microbiology Interactions, the Howard Hughes Medical Institute (D.K.N. and G.J.J.), Office of Naval Research grants N00014-08-1-0413 and N00014-05-1-0579 (M.G.H.), NIH grant GM094800B (G.J.J.), and a gift from the Gordon and Betty Moore Foundation (Caltech). D.K.N. and G.J.J. are Investigators of the Howard Hughes Medical Institute. Strains obtained from the American Type Culture Collection listed in table S2 (ATCC 33492, ATCC 14393, ATCC 15057). DNA sequences encoding for *mac*, T6SS, and bacteriocin-2 genes are deposited under GenBank accession numbers KF724687, KF724688, and KF724689, respectively. Subtomogram averages were deposited in the Electron Microscopy Data Bank (accession numbers EMD-2543, EMD-2544, and EMD-2545). Author contributions: All authors designed research. N.J.S., M.P. and G.L.W. performed research. All authors wrote the paper.

Supplementary Materials

www.sciencemag.org/content/343/6170/529/suppl/DC1
Materials and Methods
Figs. S1 to S10
Tables S1 to S4
References (30–46)
Movies S1 to S8

3 October 2013; accepted 23 December 2013
Published online 9 January 2014;
10.1126/science.1246794

Reversal of Female Infertility by *Chk2* Ablation Reveals the Oocyte DNA Damage Checkpoint Pathway

Ewelina Bolcun-Filas,¹ Vera D. Rinaldi,¹ Michelle E. White,¹ John C. Schimenti^{1*}

Genetic errors in meiosis can lead to birth defects and spontaneous abortions. Checkpoint mechanisms of hitherto unknown nature eliminate oocytes with unrepaired DNA damage, causing recombination-defective mutant mice to be sterile. Here, we report that checkpoint kinase 2 (*Chk2* or *Chek2*), is essential for culling mouse oocytes bearing unrepaired meiotic or induced DNA double-strand breaks (DSBs). Female infertility caused by a meiotic recombination mutation or irradiation was reversed by mutation of *Chk2*. Both meiotically programmed and induced DSBs trigger CHK2-dependent activation of TRP53 (p53) and TRP63 (p63), effecting oocyte elimination. These data establish CHK2 as essential for DNA damage surveillance in female meiosis and indicate that the oocyte DSB damage response primarily involves a pathway hierarchy in which ataxia telangiectasia and Rad3-related (ATR) signals to CHK2, which then activates p53 and p63.

Fertility, offspring health, and species success depend on production of gametes with intact genomes. Particularly crucial is the

proper synapsis and segregation of homologous chromosomes at the first meiotic division, processes requiring homologous recombination (HR),

a high-fidelity DNA double-strand break (DSB) repair process. Meioocytes initiate HR by producing proteins (namely SPO11) that create DSBs. In mice, ~10% of the >200 induced DSBs are repaired as crossovers (COs), and the rest by non-crossover (NCO) recombination (1).

Aberrant homolog synapsis or DSB repair trigger checkpoints that eliminate defective meocytes (2–4). Either defect causes apoptotic elimination of mouse spermatocytes at mid-pachynema of meiotic prophase I (5, 6). In contrast, loss of oocytes defective for both DSB repair and synapsis occurs earlier (within a few days postpartum) than those defective for synapsis alone (~2 months postpartum), suggesting that mammalian oocytes have distinct DNA damage and synapsis checkpoints (2, 7) (fig. S1). Mutations preventing DSB formation (*Spo11* and *Mei1*) are epistatic to those affecting DSB repair (2). The DNA damage checkpoint acts around the time oocytes enter meiotic arrest (dictyate, or resting stage) and presumably persists, because resting primordial follicles are highly sensitive to ionizing radiation (IR) (8).

We focused on checkpoint kinase 2 (CHK2) as a candidate component of the meiotic DNA damage checkpoint. It is a downstream effector of the ataxia telangiectasia mutated (ATM) kinase that responds primarily to DSBs and can also be activated by the ataxia telangiectasia and Rad3-related (ATR) protein kinase that responds primarily to single-stranded DNA (ssDNA) (9, 10). Unlike *Atm* and *Atr*, *Chk2* is dispensable for fertility and viability. To determine whether *Chk2* is required for the meiotic DNA damage checkpoint, we bred mice doubly deficient for *Chk2* and *Dmc1*, a RecA homolog required for inter-homolog repair of meiotic DSBs (11). *Dmc1* deficiency also prevents synapsis, which is HR-dependent. Whereas 3-week-postnatal wild-type or *Chk2*^{-/-} ovaries contain primordial through antral follicles (Fig. 1, A and B, and fig. S2), *Dmc1*^{-/-} ovaries are devoid of follicles (Fig. 1D). Deletion of *Chk2* enabled survival of developing oocytes in DMC1-deficient 3-week-old ovaries (Fig. 1, E and F). However, primordial follicles were absent, leading to a nearly complete oocyte depletion by 2 months postpartum (figs. S2 and S3). This pattern of oocyte loss resembles that of *Spo11* or *Spo11*^{-/-} *Dmc1*^{-/-} mice (fig. S1) (2), suggesting that *Chk2* ablation compromises the DSB repair but not synapsis checkpoint.

To test this, we exploited an allele of *Trip13* (*Trip13*^{Gt/Gt}) that causes male and female meiotic failure. *Trip13*^{Gt/Gt} chromosomes undergo synapsis and CO formation but fail to complete NCO DSB repair (12), causing elimination of the entire primordial follicle pool and nearly all developing oocytes by 3 weeks postpartum (Fig. 1G), coinciding with the oocyte DNA damage checkpoint (fig. S1) (12, 13). *Chk2*^{-/-} *Trip13*^{Gt/Gt} ovaries had a large oocyte pool at 3 weeks postpartum (Fig. 1,

H and I, and fig. S2), and they retained high numbers of all follicle types after 2 months (fig. S3), indicating that the rescue of surviving oocytes from checkpoint elimination was permanent or nearly so (see below). The rescue was not attributable to activation of an alternative DSB repair pathway during pachynema, a consideration because the *Chk2* yeast ortholog *MEK1* influences pathway choice (14); all dictyate *Chk2*^{-/-} *Trip13*^{Gt/Gt} oocytes (*n* = 54), like *Trip13*^{Gt/Gt} oocytes, exhibited abundant histone γH2AX staining, indicative of persistent unrepaired DSBs (versus 7% of *Chk2*^{-/-} dictyate oocytes; *n* = 45) (Fig. 2, A and B).

Despite bearing DSBs into late meiotic prophase I, the rescued oocytes proved to be functional. All tested *Chk2*^{-/-} *Trip13*^{Gt/Gt} females produced multiple litters (Fig. 2C). Litter sizes were smaller than those of controls (Fig. 2D), attributable to fewer ovulated oocytes and implanted embryos (fig. S4). *Chk2*^{-/-} *Trip13*^{Gt/Gt} females sustained fertility for many months, yielding four to seven litters each (Fig. 2C) and over 160 pups collectively. Progeny showed no visible abnormalities up to 1 year of age (*n* = 28). The results suggested that all or most DSBs persisting into late meiosis were eventually repaired. Indeed, there was no evidence of persistent DNA damage (as indicated by γH2AX) in 2-month-old primordial, growing, or germinal vesicle stage preovulatory *Chk2*^{-/-} *Trip13*^{Gt/Gt} oocytes (fig. S5). Thus, repair of DSBs occurred after birth by unknown mechanisms.

Canonically, CHK2 signals to p53 in mitotic cells. In *Drosophila melanogaster*, CHK2-dependent p53 activation occurs in response to SPO11-induced breaks (3). We therefore tested whether p53 deficiency could rescue *Trip13*^{Gt/Gt} oocytes. Three-week-old *p53*^{-/-} *Trip13*^{Gt/Gt} ovaries had significantly more oocytes than *Trip13*^{Gt/Gt} single mutants (Fig. 3, B and C, and fig. S2); however, they contained far fewer primordial follicles than *Chk2*^{-/-} *Trip13*^{Gt/Gt} ovaries at 3 weeks postpartum, and almost no oocytes remained after 2 months (fig. S3). Therefore, CHK2-mediated elimination of *Trip13*^{Gt/Gt} oocytes does not occur exclusively

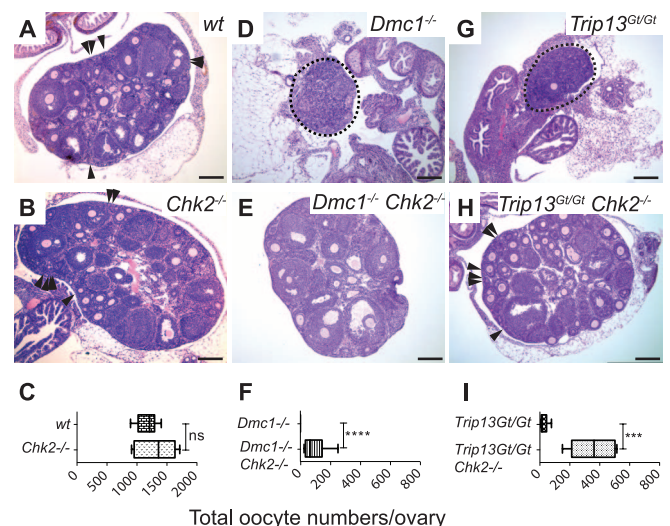
via signaling to p53, indicating the existence of another downstream effector(s) that acts perinatally in primordial follicles.

One candidate is *p63*, a *p53* paralog. A predominant isoform called TAp63 (TA, transactivation) appears perinatally in late pachytene and diplotene oocytes, approximately coinciding with DNA damage checkpoint activation. Because TAp63 was implicated in the elimination of dictyate oocytes subjected postnatally to DSB-causing IR (15, 16) and it contains a CHK2 consensus substrate motif LxRxxS (L, Leu; R, Arg; S, Ser; x, any amino acid) (17), we speculated that CHK2 might activate TAp63 in response to DSBs. Indeed, whereas IR induces phosphorylation in wild-type ovaries (15, 16), TAp63 remained unphosphorylated in CHK2-deficient ovaries (Fig. 3D). Moreover, mutating serine to alanine in the CHK2 phosphorylation motif in p63 also prevented IR-induced TAp63 phosphorylation in cultured cells (Fig. 3E). We next tested whether CHK2 is required for the elimination of DSB-bearing dictyate oocytes, presumably via TAp63 activation. Whereas the entire primordial follicle pool was eradicated 1 week after IR treatment of wild-type ovaries, CHK2 deficiency prevented oocyte elimination despite the presence of p63 protein (Fig. 3F). Furthermore, irradiated *Chk2*^{-/-} females remained fertile, with an average litter size (6.3 ± 1.8 , *n* = 7) similar to that of unirradiated controls (6 ± 2.3 , *n* = 3). If this rescue of fertility was due entirely to abolition of TAp63 activation, then deletion of TAp63 should also restore fertility to irradiated females. Previous studies (15, 16) found that *p63*^{-/-} and *TAp63*^{-/-} oocytes survived 5 days after 0.45 to 5 gray (Gy) of IR, but longer-term survival was not evaluated. We found that 0.45 Gy IR completely eradicated primordial oocytes after 7 days in females homozygous for a viable, TA domain-specific deletion allele of *p63* (*TAp63*⁻) (18, 19), identical to wild type (Fig. 4, A and B).

These results suggested IR-induced DSBs (and perhaps meiotic DSBs) stimulate CHK2 sig-

Fig. 1. Evidence of a specific DNA damage checkpoint in mouse oocytes. (A, B, D, E, G, H) Histology of 3-week postpartum ovaries. Follicle-devoid ovaries are denoted by dotted outline. Arrowheads in (A), (B), and (H) indicate primordial follicles. Scale bars indicate 200 μm; wt, wild type. (C, F, I) Oocyte quantification in mutants. Box plots show 25th and 75th percentiles (box), median (the line in the center of the box), and minimum and maximum values (whiskers).

P values are as follows: ns, not significant; ***, 0.0004; ****, < 0.0001.



¹Department of Biomedical Sciences, Cornell University, Ithaca, NY 14850, USA.

*Corresponding author. E-mail: jcs92@cornell.edu

naling to a protein(s) in addition to Tap63. Suspecting p53, we found that, whereas irradiated $p53^{-/-}$ ovaries were essentially devoid of oocytes (Fig. 4C) (15, 16), $p53^{-/-}$ $Tap63^{-/-}$ oocytes (including those in primordial follicles) were rescued (Fig. 4D) to a degree similar to $Chk2$ mutants (Fig. 3F). Irradiated $p53^{-/-}$ $Tap63^{-/-}$ (Fig. 4E) but not $p53^{-/-}$ $Tap63^{+/+}$ oocytes were partially rescued, indicating that CHK2 signals to both p53 and p63 and that they act in a partially redundant fashion to eliminate DSB-bearing resting oocytes. The marked effects of p53 haploinsufficiency, and

the possible inconsistencies with earlier reports showing that deletion of p63 alone could rescue primordial follicles from IR over the short term, indicate that checkpoint responses may be sensitive to quantitative variation.

Because $Chk2$ but not $p53$ deficiency reversed $Tripl3^{Gt/Gt}$ female infertility, an outcome similar to the results with postnatal ovary irradiation, we hypothesized that the same DNA damage checkpoint was operative in both pachytene/diplotene and dictyate oocytes. To test this, we first examined patterns of p53 and Tap63 activation

Fig. 2. DSBs in $Tripl3^{Gt/Gt}$ $Chk2^{-/-}$ newborn oocytes are eventually repaired and yield offspring.

(A) Co-immunolabeling of neonatal oocytes. (B) $Tripl3^{Gt/Gt}$ $Chk2^{-/-}$ oocytes progress to dictyate ("D") with DSBs. P, pachytene. SYCP3 labels SC axial element. (Right) Boxed nuclei magnified. Female reproductive (C) longevity and (D) fecundity. P values are as follows: ***, 0.0002; ****, <0.0001.

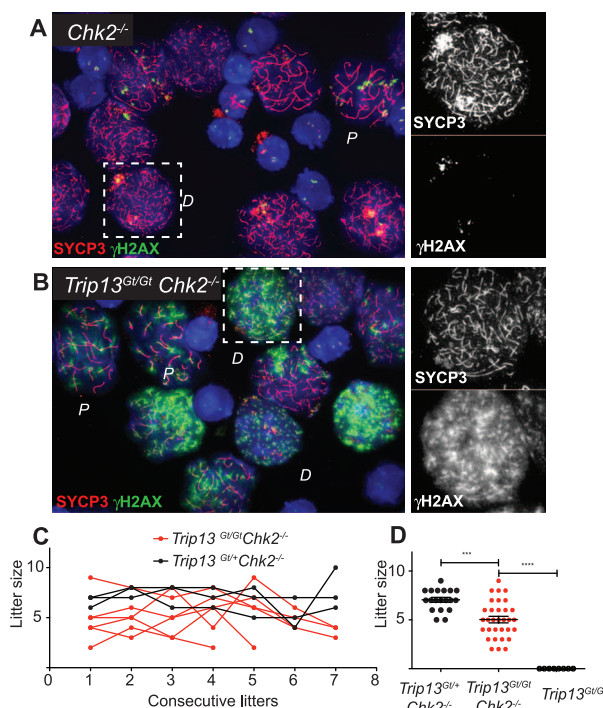
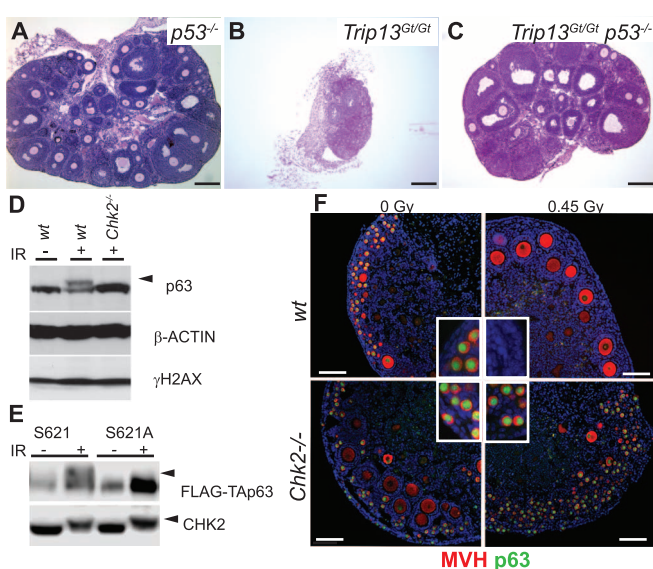


Fig. 3. Genetic and molecular analysis of the oocyte DNA damage checkpoint.

(A to C) $Tripl3^{Gt/Gt}$ oocyte depletion is partially rescued by p53 deficiency. Scale bars, 200 μ m. (D) DNA damage-induced Tap63 phosphorylation in newborn ovaries is CHK2-dependent. Neonatal ovaries (four) received 3 Gy IR before protein extraction 2 hours later. Increased p63 in $Chk2^{-/-}$ is likely due to increased oocytes in this genotype. (E) p63 contains a CHK2 phosphorylation site. HeLa cells bearing FLAG-tagged Tap63 with wild-type (WT) (LxRxxS) or mutant (LxRxxA; A, Ala) CHK2 motifs. Shifted CHK2 (arrowhead) is phosphorylated. IR dose = 3 Gy. (F) Depletion of p63-positive primordial follicles by IR is CHK2-dependent. Ovaries were cultured 7 days after irradiation. Scale bars, 100 μ m. MVH marks oocytes. (Insets) Ovary cortical regions containing primordial follicles.



variation in different genotypes of ovaries, with or without IR exposure. As expected for wild type, Tap63 phosphorylation and p53 stabilization and/or expression occurred only after exposure to IR (Fig. 4F). Importantly, we observed p53 protein in unirradiated $Tripl3^{Gt/Gt}$ neonatal ovaries but not in wild type (Fig. 4F), implying a role for p53 in the elimination of mutant oocytes with unrepaired meiotic DSBs (and consistent with partial rescue of $Tripl3^{Gt/Gt}$ $p53^{-/-}$ oocytes; Fig. 3C). Stabilization of p53 in response to unrepaired meiotic DSBs is CHK2-dependent, because we did not detect p53 in $Chk2^{-/-}$ $Tripl3^{Gt/Gt}$ ovaries (Fig. 4F). Tap63 was absent from neonatal $Tripl3^{Gt/Gt}$ ovaries bearing residual oocytes (Fig. 4F). Normally, Tap63 appears in late meiotic prophase I, when meiotic DSBs have been repaired, and is robustly activated in resting oocytes in response to exogenous DNA damage (15, 16). Nevertheless, the absence of Tap63 in $Tripl3^{Gt/Gt}$ oocytes predicts that it is not responsible for their death. Indeed, no oocyte rescue was observed in wean-age $Tap63^{-/-}$ $Tripl3^{Gt/Gt}$ ovaries (Fig. 4I). A potential explanation for Tap63 repression in $Tripl3^{Gt/Gt}$ oocytes was suggested by our observation (Fig. 4F) that unphosphorylated Tap63 was present in $Chk2^{-/-}$ $Tripl3^{Gt/Gt}$ ovaries lacking detectable p53. These results suggest a regulatory relationship between p53 and Tap63 in the meiotic DNA damage response.

The mutual exclusivity of Tap63 and p53 in $Tripl3^{Gt/Gt}$ oocytes gives insight into the failure of either single mutant to rescue fertility. We hypothesized that unrepaired DSBs that persist into late pachynema trigger CHK2-dependent p53 activation and oocyte elimination independent of Tap63 but that, in the absence of p53, Tap63 can be expressed and activated by CHK2 to drive oocyte elimination. This predicts that removal of both proteins would abolish the CHK2-dependent checkpoint. Indeed, we found that $p53$ heterozygosity could rescue $Tap63^{-/-}$ $Tripl3^{Gt/Gt}$ oocytes (Fig. 4J). This rescue included primordial follicles (Fig. 4J, inset; nullizygosity for all three genes is embryonically semilethal). These and previous results with single mutants indicate that the DNA damage checkpoint pathway that monitors repair of SPO11-induced DSBs involves CHK2 signaling to both p53 and Tap63 and that this pathway also operates in postnatal resting oocytes (fig. S6).

A remaining question concerns the upstream activator(s) of CHK2. Canonically, ATM phosphorylates CHK2 in response to DSBs, whereas ATR responds to ssDNA by activating CHK1 (20, 21). However, ATR and ATM have other activities in mouse meiosis. ATM negatively regulates SPO11, causing $Atm^{-/-}$ oocytes to sustain extensive DSBs and triggering elimination by the meiotic DNA damage checkpoint (fig. S1) (2, 22). Therefore, CHK2 is likely activated by a different kinase. Indeed, $Chk2$ deficiency rescued $Atm^{-/-}$ oocyte depletion (fig. S7) to a degree similar to the rescue of DMC1-deficient ovaries. The facts that (i) CHK2 can trigger apoptosis in the

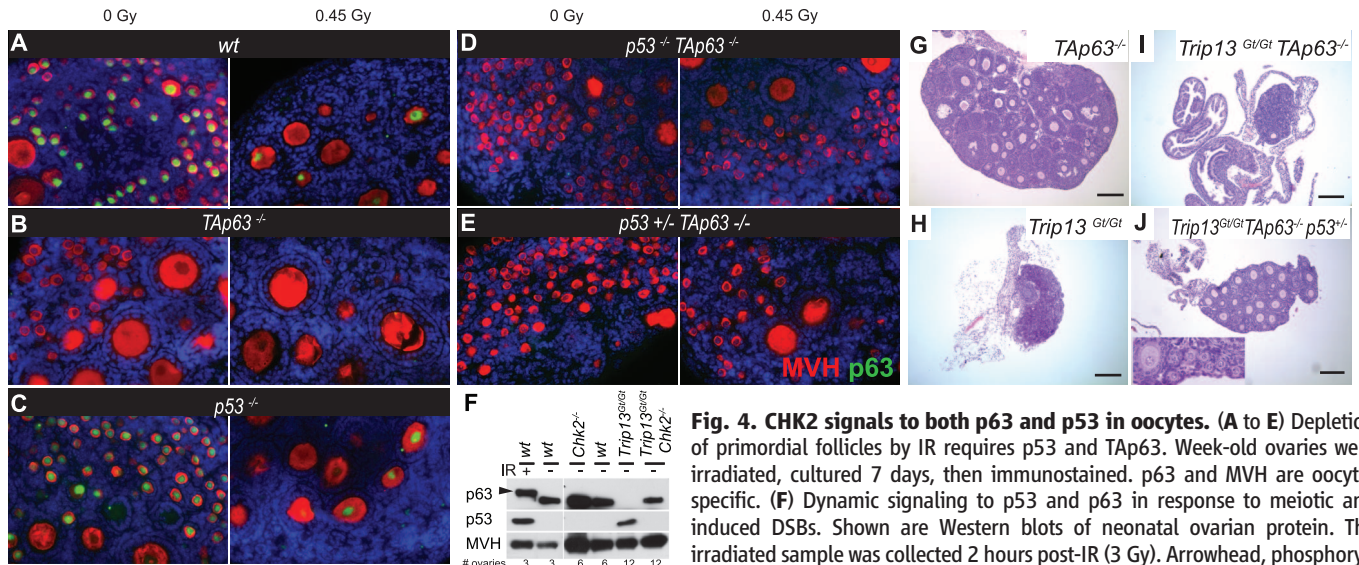


Fig. 4. CHK2 signals to both p63 and p53 in oocytes. (A–E) Depletion of primordial follicles by IR requires p53 and Tap63. Week-old ovaries were irradiated, cultured 7 days, then immunostained. p63 and MVH are oocyte-specific. (F) Dynamic signaling to p53 and p63 in response to meiotic and induced DSBs. Shown are Western blots of neonatal ovarian protein. The irradiated sample was collected 2 hours post-IR (3 Gy). Arrowhead, phosphorylated p63 (15, 16). *Trip13* mutants are undergoing oocyte elimination (reflected

by MVH), hence use of more ovaries. (G to J) p53 and *Tap63* are required for complete elimination of DSB repair–defective oocytes. Ovaries are 3 weeks postpartum. (J) Inset) Primordial follicles. Scale bars, 200 μ m.

absence of ATM in somatic cells (9), (ii) CHK2 can be activated in an ATR-dependent manner (10), and (iii) ATR localizes to sites of meiotic DSBs in mice (23) prompt us to propose that the DNA damage checkpoint pathway in mouse oocytes involves signaling of ATR to CHK2, which in turn signals to p53 and Tap63 (fig. S6). Additionally, spermatocytes may have a distinct DNA damage response pathway; we did not observe histological evidence for rescue of DSB repair-defective but synapsis-proficient spermatocytes by deletion of *Chk2* or *p53* (fig. S8).

Our results are of biomedical interest with respect to the primordial follicle pool depletion and premature ovarian failure that can occur after cancer radiotherapy or chemotherapy. CHK2 is an attractive target because chemical inhibitors are available, and *Chk2* insufficiency is of minor phenotypic consequence in mice (24).

References and Notes

1. F. Cole *et al.*, *Nat. Cell Biol.* **14**, 424–430 (2012).
2. M. Di Giacomo *et al.*, *Proc. Natl. Acad. Sci. U.S.A.* **102**, 737–742 (2005).
3. W. J. Lu, J. Chapo, I. Roig, J. M. Abrams, *Science* **328**, 1278–1281 (2010).
4. N. Bhalla, A. F. Dernburg, *Science* **310**, 1683–1686 (2005).
5. P. S. Burgoyne, S. K. Mahadevaiah, J. M. Turner, *Nat. Rev. Genet.* **10**, 207–216 (2009).
6. M. Barchi *et al.*, *Mol. Cell. Biol.* **25**, 7203–7215 (2005).
7. L. G. Reinholdt, J. C. Schimenti, *Chromosoma* **114**, 127–134 (2005).
8. T. G. Baker, *Mutat. Res.* **11**, 9–22 (1971).
9. A. Hirao *et al.*, *Mol. Cell. Biol.* **22**, 6521–6532 (2002).
10. X. Q. Wang, J. L. Redpath, S. T. Fan, E. J. Stanbridge, *J. Cell. Physiol.* **208**, 613–619 (2006).
11. D. L. Pittman *et al.*, *Mol. Cell* **1**, 697–705 (1998).
12. X. C. Li, J. C. Schimenti, *PLOS Genet.* **3**, e130 (2007).
13. I. Roig *et al.*, *PLOS Genet.* **6**, e1001062 (2010).
14. H. Niu *et al.*, *Mol. Cell* **36**, 393–404 (2009).
15. G. Livera *et al.*, *Reproduction* **135**, 3–12 (2008).
16. E. K. Suh *et al.*, *Nature* **444**, 624–628 (2006).

17. G. J. Seo *et al.*, *Biochem. Biophys. Res. Commun.* **304**, 339–343 (2003).
18. X. Guo *et al.*, *Nat. Cell Biol.* **11**, 1451–1457 (2009).
19. A. A. Mills *et al.*, *Nature* **398**, 708–713 (1999).
20. J. Smith, L. M. Tho, N. Xu, D. A. Gillespie, *Adv. Cancer Res.* **108**, 73–112 (2010).
21. K. A. Cimprich, D. Cortez, *Nat. Rev. Mol. Cell Biol.* **9**, 616–627 (2008).
22. J. Lange *et al.*, *Nature* **479**, 237–240 (2011).
23. D. Perera *et al.*, *Mol. Biol. Cell* **15**, 1568–1579 (2004).
24. H. Takai *et al.*, *EMBO J.* **21**, 5195–5205 (2002).

Acknowledgments: This work was supported by NIH grant GM45415 to J.C.S. and contract CO26442 from the NY State Stem Cell Program. We thank A. Mills for providing p63 mutant mice and M. A. Handel for critical reading of the manuscript.

Supplementary Materials

www.sciencemag.org/content/343/6170/533/suppl/DC1
Materials and Methods

Figs. S1 to S8

References (25–31)

24 October 2013; accepted 20 December 2013
10.1126/science.1247671

Mating Induces Shrinking and Death in *Caenorhabditis* Mothers

Cheng Shi and Coleen T. Murphy*

Interactions between the germ line and the soma help optimize reproductive success. We discovered a phenomenon linking reproductive status to longevity: In both hermaphroditic and gonochoristic *Caenorhabditis*, mating leads to female shrinking and death, compressing postreproductive life span. Male sperm induces germline- and DAF-9/DAF-12–dependent shrinking, osmotic stress susceptibility, and subsequent life-span decrease, whereas seminal fluid induces DAF-16–dependent life-span decrease and fat loss. Our study provides insight into the communication between males and the female germ line and soma to regulate reproduction and longevity, revealing a high-reproduction, low-life-span state induced by mating. Postmating somatic collapse may be an example of the sexually antagonistic influence that males in many species exert on female behavior to maximize their own reproductive success.

Mating is an elaborately regulated process with critical individual and population consequences (1, 2). The development of sexual mating resulted in a now ancient conflict: Although the mother's genome is always propagated, the father is driven to maximize his genomic contribution to the exclusion of other

males, often effected through manipulation of the mother's behavior or physiology. This tension leads to a war between the sexes that plays out in different ways in different species; for example, many insects display sexual antagonism, in which males receive benefits of mating (increased offspring, decreased chance of female remating) by inflicting damage on the female (3).

Reproduction and longevity are intimately linked, with signals between the germ line and soma coordinating the rate of aging of both tissues (4–8). Reproductive aging is regulated by

Lewis-Sigler Institute for Integrative Genomics and Department of Molecular Biology, Princeton University, Princeton, NJ 08544, USA.

*Corresponding author. E-mail: ctmurphy@princeton.edu

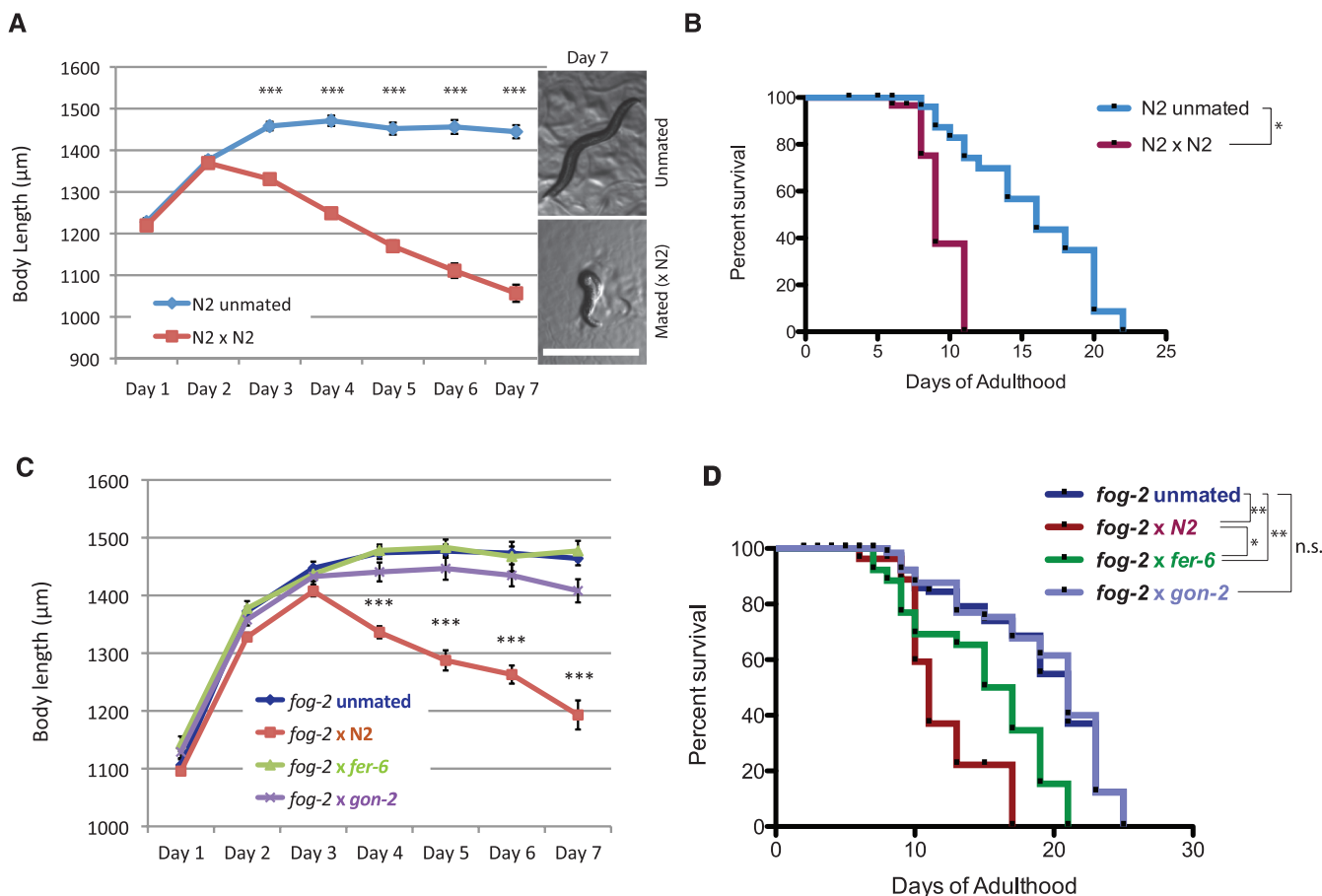


Fig. 1. Postmating somatic collapse: Hermaphrodites shrink and die after mating. Statistical analysis: survival curves, log-rank test, body size, and others. *t* test, $*P < 0.05$, $**P < 0.01$, $***P < 0.001$ for all graphs. Error bars represent SEM unless noted. n.s., not significant. (A) Length of unmated and mated N2 worms. (Inset) Representative pictures of unmated and mated N2 on day 7. Scale bar, 1 mm. (B) Life spans of unmated and mated N2 worms.

Unmated N2: 16.0 ± 1.0 days, $n = 30$ worms; mated N2: 9.6 ± 0.2 days, $n = 36$, $P < 0.05$. (C) Length of unmated *fog-2*(*q71*) hermaphrodites ($n = 35$), and *fog-2*(*q71*) mated with N2 ($n = 42$), *fer-6*(*hc6*) ($n = 24$), and *gon-2*(*q362*) males ($n = 29$). (D) Mean life spans of unmated and mated *fog-2*. Unmated: 19.0 ± 0.6 days ($n = 94$); *fog-2* x N2: 12.0 ± 0.8 days ($n = 83$); *fog-2* x *fer-6*: 15.0 ± 0.9 days ($n = 28$); *fog-2* x *gon-2*: 19.2 ± 0.6 days ($n = 73$).

many of the same pathways that control somatic aging (7, 9, 10), via signals from the soma that coordinate sensing of nutrient conditions with reproductive status (7, 8). Conversely, signals from the reproductive system regulate somatic aging through DAF-16/FOXO and the nuclear hormone DAF-12, extending life span when germline proliferation is arrested (5, 6).

Caenorhabditis elegans hermaphrodites can reproduce either by self-fertilization or by mating with males (11), whose sperm outcompete hermaphroditic sperm (12). Mating increases brood size, extends reproductive span, exacerbates matricide ("bagging," or internal hatching), and shortens life span (9, 10, 13) (fig. S1; see supplementary materials and methods). While studying reproductive aging, we discovered a drastic change in *C. elegans* hermaphrodite physiology after mating that results in shrinking and death of the mother shortly after completion of reproduction. Although unmated worms continued to grow through day 4 of adulthood, mated N2 [wild-type (WT)] hermaphrodites began to shrink 2 days after mating and shrank by up to 30% by day 7 of adulthood (Fig. 1A and figs.

S2 and S3). Unsupervised clustering by percent body-size change separated the worms into two distinct groups, unmated and mated N2 worms (fig. S4A), suggesting that mating is tightly correlated with shrinking. The mean life span of mated WT worms also decreased significantly (>40%) (Fig. 1B and fig. S4C) (13, 14), and experiments modulating mating efficacy indicated that shrinking is a good predictor of postmating death (fig. S4, B and C). Direct resource utilization, mechanical tension, and matricide were eliminated as the cause of postmating shrinking and death (figs. S5 to S7).

To identify signals triggered by mating, we tested the roles of male sperm and seminal fluid. *gon-2*(*q362*) males lack gonads and, therefore, have no seminal fluid or sperm, but they copulate normally (15), whereas *fer-6*(*hc6*) males do not transfer sperm (13, 16), *spe-9*(*hc88*) males' sperm fail to fertilize oocytes (17), and *glp-1*(*e2141*) males lack germ line, but these three mutants have normal seminal fluid and copulation. Mating spermless *fog-2* hermaphrodites with *gon-2* males prevented both shrinking and life-span decrease (Fig. 1, C and D), sug-

gesting that physical copulation plays no role. By contrast, *fog-2* hermaphrodites mated with *fer-6* (13), *spe-9*, or *glp-1* males lived for a significantly shorter time than unmated worms but did not shrink (Fig. 1, C and D, and fig. S8), indicating that functional sperm, but not seminal fluid, is required for shrinking, whereas seminal fluid contributes to postmating death.

The somatic breakdown of worms after mating is slowed but ultimately not prevented by reduced insulin-like signaling: As in the wild type, *daf-2*(*e1370*) hermaphrodites shrank significantly (25%) after mating with N2 males and lived 45% shorter than unmated *daf-2* worms (Fig. 2, A and B, and fig. S9A) (14). Germline proliferation (*glp-1*) mutants are long-lived in a *daf-16* and *daf-9*/*daf-12*-dependent manner (5, 6). Like *daf-2* worms, *glp-1*(*e2141*) hermaphrodites lived ~55% shorter lives after mating (Fig. 2B), but they did not shrink (Fig. 2A), suggesting that the germ line is required for shrinking but not for life-span decrease. Similarly, the steroid hormone receptor DAF-12 and the cytochrome P450 that synthesizes DAF-12's ligand, DAF-9, which are both required for germline-

mediated longevity (5, 6), are required for post-mating shrinking, but less so (16%) for life-span shortening (Fig. 2, A and B). [Shrinking is not mediated by the *sma-9* transforming growth factor- β (TGF- β) body-size pathway (fig. S9B).] Mating decreased *Pdaf-9::daf-9::gfp* expression in the spermatheca in a sperm-dependent manner (Fig. 2C and fig. S10). Thus, shrinking acts through sperm-induced reduction of DAF-9 levels and requires DAF-12 nuclear hormone signaling and a functional germ line.

Using 4',6-diamidino-2-phenylindole (DAPI) staining and GLD-1::GFP (GFP, green fluorescent protein) to identify the distal proliferative mitotic region (18), we found that mating reduced

mitotic zone size and nuclei number (by 30 and 40%, respectively) (fig. S11, A to E). Adult treatment with the DNA replication inhibitor 5-fluorodeoxyuridine (FUdR), which has little effect on un- or self-mated life span or meiosis at low doses (50 μ M) (10) (fig. S11, F and G), reduced the number of germ cell nuclei but had no effect on self-mated brood size (fig. S11, H to J), suggesting that self-mated worms do not require newly proliferating germline cells for progeny production. By contrast, there was a further reduction in the mitotic zone when treated with FUdR after mating (fig. S11D). Adult FUdR treatment prevented shrinking after mating, as in *glp-1* mutants (Fig. 2D), but these worms still

died prematurely (27%) (Fig. 2E). Shifting worms onto FUdR 4 days after mating prevented further shrinking (Fig. 2D), and movement off of FUdR plates delayed the onset but did not prevent shrinking (fig. S11K). Thus, shrinking is actively regulated throughout the postmating period and is tightly coupled with DNA synthesis in the germ line, implicating the sperm-stimulated proliferation of germline stem cells in generating the signal that induces shrinking.

Longevity of *daf-2* and *glp-1* worms requires DAF-16/FOXO (5, 6, 19). Mating *daf-16(mu86)* mutants with N2 males caused shrinking (Fig. 2F) but had a smaller effect on life span (15%) (Fig. 2E) than that observed for WT or *daf-2*

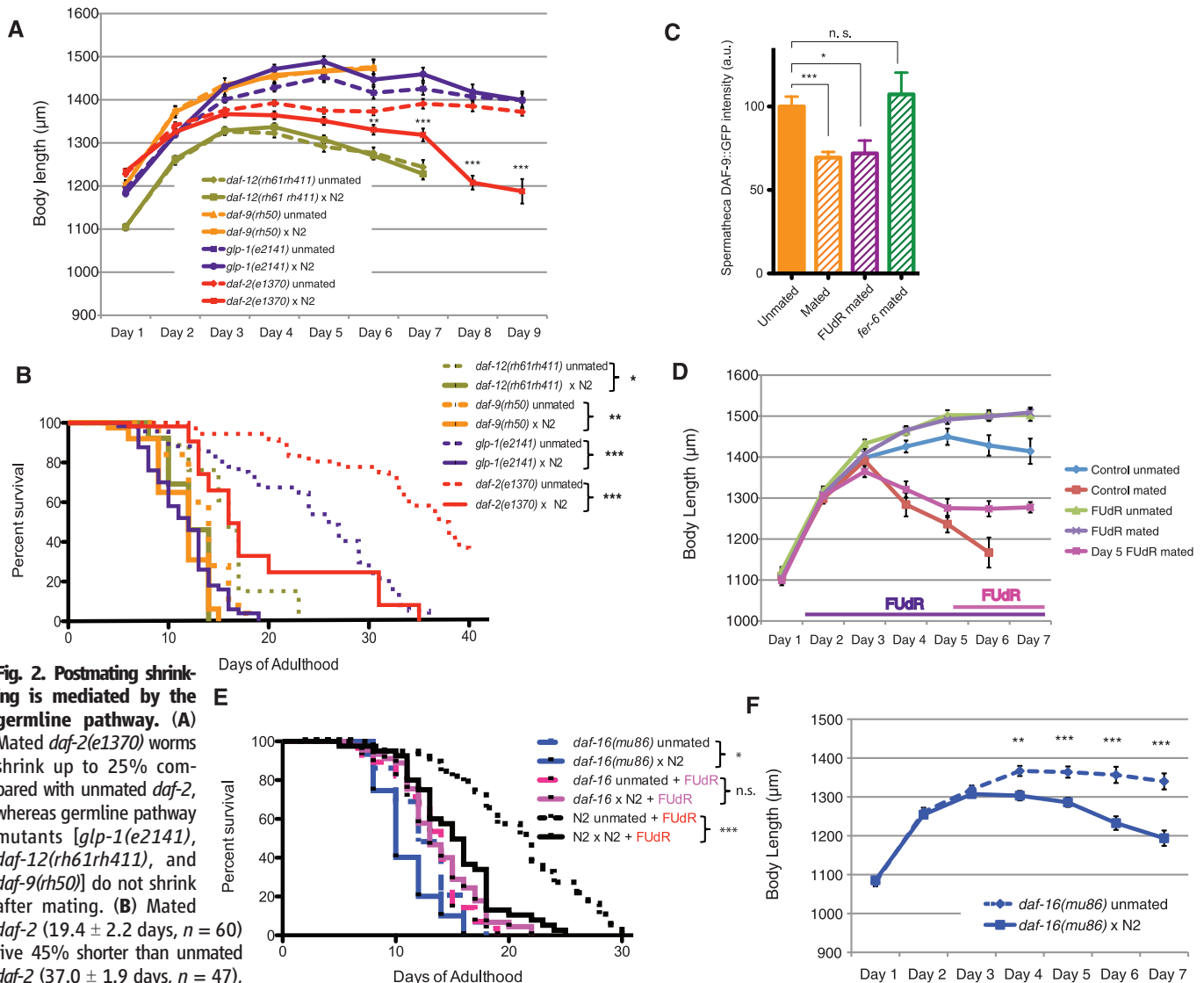


Fig. 2. Postmating shrinking is mediated by the germline pathway. (A) Mated *daf-2(e1370)* worms shrink up to 25% compared with unmated *daf-2*, whereas germline pathway mutants [*glp-1(e2141)*, *daf-12(rh61rh411)*, and *daf-9(rh50)*] do not shrink after mating. (B) Mated *daf-2* (19.4 ± 2.2 days, $n = 60$) live 45% shorter than unmated *daf-2* (37.0 ± 1.9 days, $n = 47$), $P < 0.001$. Mated *glp-1* (11.6 ± 0.5 days, $n = 60$) live 55% shorter than unmated *glp-1* (24.1 ± 1.3 days, $n = 48$), $P < 0.001$. Mated *daf-12* (12.1 ± 1.0 days, $n = 26$) live 20% shorter than unmated *daf-12* (16.0 ± 1.4 days, $n = 20$), $P < 0.05$; mated *daf-9* (11.3 ± 0.4 days, $n = 45$) live 16% shorter than unmated *daf-9* (13.4 ± 0.5 days, $n = 36$), $P < 0.01$. (C) *Pdaf-9::daf-9::gfp* expression in the spermatheca is decreased after mating with N2 males, but not with *fer-6* males, and is not affected by FUdR. Error bars denote SD. a.u., arbitrary units. (D) 50 μ M FUdR treatment dynamically prevents shrinking in mated N2s. (E) Mated *daf-16* (10.83 ± 0.6

days, $n = 53$) live 15% shorter than unmated (12.62 ± 0.5 days, $n = 40$), $P < 0.05$. Adult treatment with FUdR eliminates the difference between mated and unmated *daf-16(mu86)* life span [unmated, 13.2 ± 0.6 days ($n = 36$); mated, 13.8 ± 0.5 days ($n = 48$), $P = 0.385$]. By contrast, FUdR does not prevent postmating life-span decrease in the wild type. Unmated, 21.0 ± 0.9 days ($n = 41$); mated, 15.3 ± 0.7 days ($n = 43$), $P < 0.001$. (F) Mated *daf-16(mu86)* worms shrink by 15%. * $P < 0.05$, ** $P < 0.01$, *** $P < 0.001$ for all graphs. Error bars represent SEM unless noted. n.s., not significant.

worms (45%). FUDR treatment or loss of *daf-12* eliminated *daf-16*'s life-span decrease altogether (Fig. 2E and fig. S12), suggesting that germline-mediated shrinking itself causes significant *daf-16*-independent life-span shortening.

In both *daf-2* and *glp-1* mutants, DAF-16 localizes to the nucleus, where it activates the expression of longevity-promoting genes (5, 6, 19, 20). Mating counteracts this effect, inducing a notable DAF-16::GFP translocation out of the nucleus of both *glp-1* and *daf-2* hermaphrodites (Fig. 3A and fig. S13, A to C), explaining their delayed but significant life-span decreases. Intestinal expression of *Pins-7::gfp*, a reporter for the INS-7 insulin-like peptide DAF-2 agonist that regulates FOXO-to-FOXO signaling (21), increased significantly after mating (Fig. 3B and fig. S13, D and E), likely promoting cytoplasmic localization of DAF-16.

Fat levels increase in *daf-2* and *glp-1* mutants; this increase is associated with germline-mediated longevity (22–25). Mating induced ~50% fat decrease but was independent of shrinking (figs. S14 and S15). By contrast, hypertonic stress susceptibility correlated well with shrinking (correlation coefficient $r^2 = 0.76$) (Fig. 3C and fig. S16): Worms that shrink after mating (N2, *daf-2*, *daf-16*) die earlier than their unmated counterparts when placed on high-salt plates on day 4, whereas nonshrinking worms (*daf-12*, *daf-9*) do not, implying that water loss causes shrinking. Although *daf-16* is required for osmotic stress resistance through its regulation of osmotic stress protection genes (20, 26), *daf-16* mutants are even shorter-lived

on high salt after mating, suggesting that there is a second, *daf-16*-independent, *daf-9/daf-12*-dependent regulation of osmotic stress resistance that correlates with shrinking (Fig. 3C). *daf-12* also regulates osmotic stress resistance genes (27, 28). Although DAF-16 regulates osmotic stress resistance (20, 26), mating induces cytoplasmic localization of DAF-16 in *daf-2*- and *glp-1*-mated animals, decreasing survival on high salt plates (Fig. 3C and fig. S16).

Together, our data suggest that an active signaling process in mothers originates from males, causing an endocrine signaling decision in mated hermaphrodites that causes shrinking and death (Fig. 4A). Sperm both decreases DAF-9 levels and enhances a signal from the germ line through increased mitotic stem cell proliferation. This signal controls a *daf-12*-dependent pathway that induces water loss, shrinking, osmotic stress sensitivity, and life-span shortening. A separate, germline-independent decrease in life span that is mediated by DAF-16 cytoplasmic localization and reinforced by INS-7 feedback may be induced by seminal fluid. Together, the two branches shorten life span by up to 40% after mating. Eliminating both the *daf-12* and *daf-16* pathways removes the effect of mating on both body size and life span (fig. S12). Sperm and seminal fluid maximally activate pathways that are blocked under low-reproduction, high-longevity conditions, resulting in shrinking, fat loss, and death.

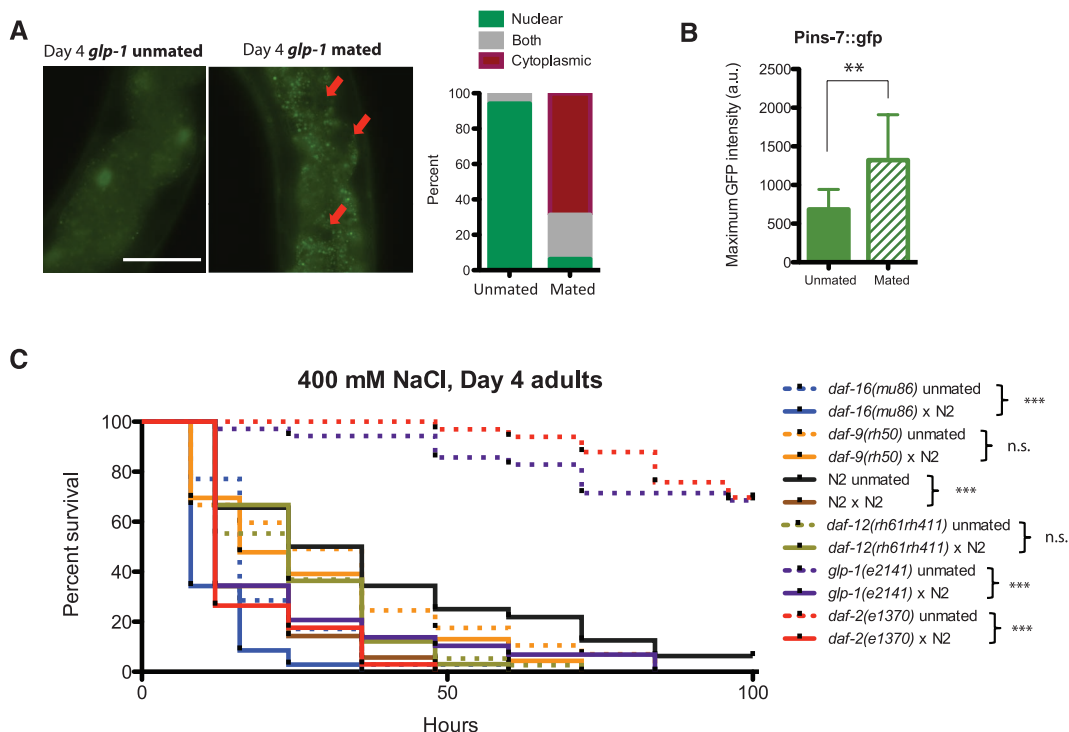
Our data argue against direct resource exhaustion or a life span-versus-reproduction trade-

off (14), because (i) brood size does not correlate with shrinking, (ii) mated *daf-12* mutants have more progeny than unmated *daf-12* but do not shrink, and (iii) animals with no germ line (and, thus, no progeny) are also short-lived after mating. The fact that mutants without a germ line also lose fat in response to mating suggests that fat depletion is a programmed response anticipating future resource allocation.

Like *C. elegans*, the females of the gonochoristic (male or female) species *C. remanei* and *C. sp9* JU1422 shrank significantly and died prematurely after mating (Fig. 4, B and C). However, *C. elegans* hermaphrodites crossed with *C. remanei*, which are not cross-fertile, did not shrink or die early (Fig. 4, C and D). Thus, postmating somatic collapse is evolutionarily conserved, but its signals are species-restricted.

Mating increases reproductive span and decreases life span, eliminating the postreproductive life span of mated mothers (Fig. 4E). *C. elegans* are hermaphroditic, and the male population is normally low (0.1%). Under stress, however, male offspring production increases (7), and mating results in 50% male production, increasing the male population and thus the possibility of sperm competition. Mating also causes a sperm-dependent decrease in attractiveness to males (fig. S17), suggesting that a programmed response to sperm levels modulates a signal from the hermaphrodites that affects male attraction, increasing the chances of successful mating (29). The mother's death immediately after the last eggs are laid prevents

Fig. 3. Postmating life-span decrease is mediated by DAF-16, and shrinking correlates with osmotic stress sensitivity. (A) DAF-16::GFP in *glp-1* translocates from the nucleus to the cytoplasm after mating. GFP channel images of *glp-1* unmated (left) and mated worms (middle); red arrows point to dark nuclei. Scale bar, 100 μ m. (Right) Quantification of GFP localization. **(B)** *Pins-7::gfp* expression [maximum \pm SD (error bars)] increases significantly in the intestine postmating. a.u., arbitrary units. **(C)** Survival curves under osmotic stress (400 mM NaCl): Day 1 mated N2 and *daf-16(mu86)* died faster than the unmated controls put under osmotic stress starting on day 4. Unmated N2: 40.3 ± 6.0 hours, $n = 31$; mated N2: 18.5 ± 1.8 hours, $n = 35$, $P < 0.001$. Unmated *daf-16*: 19.2 ± 1.9 hours, $n = 35$; mated *daf-16*: 11.8 ± 1.1 hours, $n = 35$, $P < 0.001$. Mated *daf-9(rh50)* and *daf-12(rh61rh411)* survived as long as the unmated controls under osmotic stress. Unmated *daf-9*: 31.2 ± 4.3 hours, $n = 30$; mated *daf-9*: 25.7 ± 3.8 hours, $n = 23$, $P = 0.3242$. Unmated *daf-12*: 25.6 ± 2.5 hours, $n = 38$; mated *daf-12*: 26.2 ± 2.3 hours, $n = 33$, $P = 0.9714$. *glp-1* and *daf-2* mated worms survive longer than wild type on NaCl, but still die prematurely.



glp-1 unmated ($n = 35$): 131.7 ± 10.4 hours; *glp-1* mated ($n = 29$): 23.2 ± 3.8 hours; $P < 0.0001$. *daf-2* unmated ($n = 33$): 250.5 ± 30.0 ; *daf-2* mated ($n = 34$): 17.7 ± 1.8 hours; $P < 0.0001$. * $P < 0.05$, ** $P < 0.01$, *** $P < 0.001$ for all graphs.

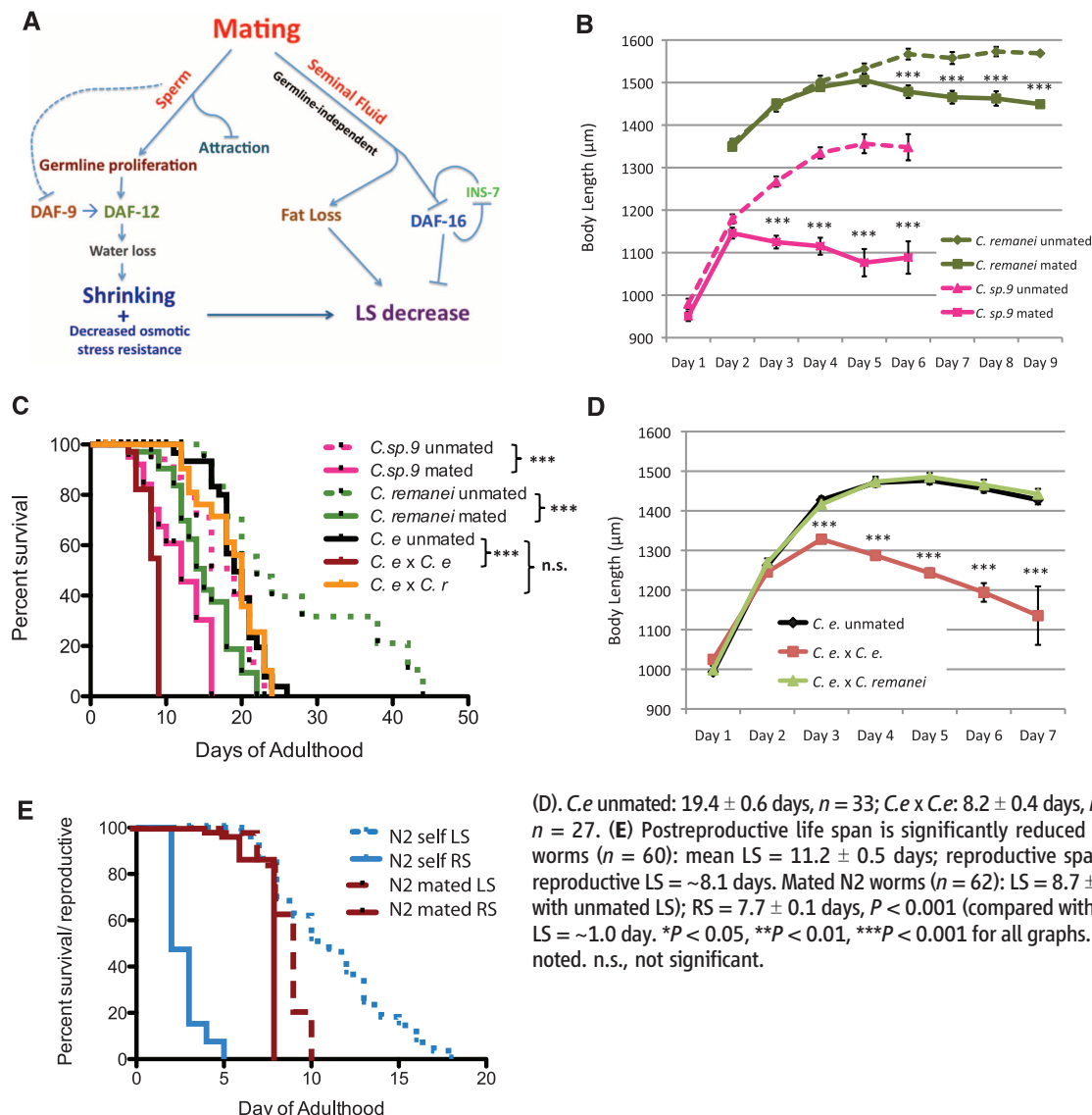


Fig. 4. Evolutionary conservation of mating-induced shrinking and death. (A) Sperm decreases DAF-9 activity and induces germline proliferation, which in turn emits a DAF-12-dependent signal that results in shrinking and subsequent life-span shortening, probably due to reduced osmotic stress resistance. Seminal fluid induces a germline-independent signal that causes both fat loss and DAF-16 cytoplasmic translocation (possibly amplified by INS-7), further reducing life span (LS). (B to D) Mated *C. remanei* and *C. sp.9* shrink (B) and die prematurely (C). *C. remanei*: unmated: 26.9 ± 2.8 days, $n = 48$; mated: 15.1 ± 0.8 days, $n = 48$, $P < 0.001$. *C. sp.9*: unmated: 17.3 ± 1.2 days, $n = 42$; mated: 11.9 ± 0.8 days, $n = 41$, $P < 0.01$. An interspecies cross between *C. remanei* (*C. r.*) males and *C. elegans* (*C. e.*) hermaphrodites does not reduce life span (C) or induce shrinking

(D). *C. e.* unmated: 19.4 ± 0.6 days, $n = 33$; *C. e. x C. e.*: 8.2 ± 0.4 days, $n = 36$; *C. e. x C. r.*: 18.8 ± 0.9 days, $n = 27$. (E) Postreproductive life span is significantly reduced in mated worms. Unmated N2 worms ($n = 60$): mean LS = 11.2 ± 0.5 days; reproductive span (RS) = 3.1 ± 0.1 days; post-reproductive LS = ~ 8.1 days. Mated N2 worms ($n = 62$): LS = 8.7 ± 0.3 days; $P = 0.131$ (compared with unmated LS); RS = 7.7 ± 0.1 days, $P < 0.001$ (compared with unmated RS); postreproductive LS = ~ 1.0 day. * $P < 0.05$, ** $P < 0.01$, *** $P < 0.001$ for all graphs. Error bars represent SEM unless noted. n.s., not significant.

subsequent mating, maximizing the father's reproductive success. *C. elegans* males hijack the very pathways that the hermaphrodite employs to slow down reproduction and aging in times of low nutrients, reversing these processes to accelerate the mother's death, perhaps for the male's benefit.

References and Notes

- H. Kokko, R. Brooks, M. D. Jennions, J. Morley, *Proc. Biol. Sci.* **270**, 653–664 (2003).
- A. Vellella, J. C. Hall, *Adv. Genet.* **62**, 67–184 (2008).
- M. F. Wolfner, *Soc. Reprod. Fertil. Suppl.* **65**, 183–199 (2007).
- C. J. Kenyon, *Nature* **464**, 504–512 (2010).
- H. Hsin, C. Kenyon, *Nature* **399**, 362–366 (1999).
- J. R. Berman, C. Kenyon, *Cell* **124**, 1055–1068 (2006).
- S. Luo, G. A. Kleemann, J. M. Ashraf, W. M. Shaw, C. T. Murphy, *Cell* **143**, 299–312 (2010).
- S. Luo, C. T. Murphy, *Genesis* **49**, 53–65 (2011).
- S. E. Hughes, K. Evason, C. Xiong, K. Kornfeld, *PLoS Genet.* **3**, e25 (2007).
- S. Luo, W. Shaw, J. Ashraf, C. Murphy, *PLoS Genet.* **5**, e1000789 (2009).
- S. Brenner, *Genetics* **77**, 71–94 (1974).
- C. W. LaMunyon, S. Ward, *Proc. Biol. Sci.* **265**, 1997–2002 (1998).
- D. Gems, D. L. Riddle, *Nature* **379**, 723–725 (1996).
- D. Wu, P. M. Tedesco, P. C. Phillips, T. E. Johnson, *Exp. Gerontol.* **47**, 759–763 (2012).
- A. Y. Sun, E. J. Lambie, *Genetics* **147**, 1077–1089 (1997).
- Y. Argon, S. Ward, *Genetics* **96**, 413–433 (1980).
- A. Singson, K. B. Mercer, S. W. L'Hernault, *Cell* **93**, 71–79 (1998).
- J. Kimble, S. L. Crittenden, "Germline proliferation and its control," in *WormBook*, The *C. elegans* Research Community, Ed. (WormBook, 2005); doi: 10.1895/wormbook.1.13.1; www.wormbook.org/.
- C. Kenyon, J. Chang, E. Gensch, A. Rudner, R. Tabtiang, *Nature* **366**, 461–464 (1993).
- C. T. Murphy et al., *Nature* **424**, 277–283 (2003).
- C. T. Murphy, S. J. Lee, C. Kenyon, *Proc. Natl. Acad. Sci. U.S.A.* **104**, 19046–19050 (2007).
- M. Hansen, T. Flatt, H. Aguilaniu, *Cell Metab.* **17**, 10–19 (2013).
- E. J. O'Rourke, A. A. Soukas, C. E. Carr, G. Ruvkun, *Cell Metab.* **10**, 430–435 (2009).
- L. R. Lapierre, S. Gelino, A. Meléndez, M. Hansen, *Curr. Biol.* **21**, 1507–1514 (2011).
- K. Yen et al., *PLOS ONE* **5**, e12810 (2010).
- S. T. Lamitina, K. Strange, *Am. J. Physiol. Cell Physiol.* **288**, C467–C474 (2005).
- A. L. Fisher, G. J. Lithgow, *Aging Cell* **5**, 127–138 (2006).
- M. McCormick, K. Chen, P. Ramaswamy, C. Kenyon, *Aging Cell* **11**, 192–202 (2012).
- N. S. Morsci, L. A. Haas, M. M. Barr, *Genetics* **189**, 1341–1346 (2011).

Acknowledgments: We thank the *Caenorhabditis* Genetics Center for strains, J. Ashraf for assistance, M. Barr for useful discussion, and Z. Gitai and members of the Murphy laboratory for critically reading the manuscript. This work was supported by an NIH Innovator award (DP2OD004402) to C.T.M.

Supplementary Materials

www.sciencemag.org/content/343/6170/536/suppl/DC1
Materials and Methods
Figs. S1 to S17
Tables S1 and S2
References

9 July 2013; accepted 11 December 2013
Published online 19 December 2013;
10.1126/science.1242958

Males Shorten the Life Span of *C. elegans* Hermaphrodites via Secreted Compounds

Travis J. Maures,¹ Lauren N. Booth,¹ Bérénice A. Benayoun,¹ Yevgeniy Izrayelit,² Frank C. Schroeder,² Anne Brunet^{1,3*}

How an individual's longevity is affected by the opposite sex is still largely unclear. In the nematode *Caenorhabditis elegans*, the presence of males accelerated aging and shortened the life span of individuals of the opposite sex (hermaphrodites), including long-lived or sterile hermaphrodites. The male-induced demise could occur without mating and required only exposure of hermaphrodites to medium in which males were once present. Such communication through pheromones or other diffusible substances points to a nonindividual autonomous mode of aging regulation. The male-induced demise also occurred in other species of nematodes, suggesting an evolutionary conserved process whereby males may induce the disposal of the opposite sex to save resources for the next generation or to prevent competition from other males.

In species ranging from worms to nonhuman primates, the life span of individuals is nearly always assessed in conditions where males and females are kept separate. Yet in the wild, the opposite sexes coexist, at least during attraction and mating. In flies and worms, the presence of males decreases longevity in the opposite sex (1, 2). In *Drosophila*, males shorten the life span of females after mating through peptides present in seminal fluid (2). In *Caenorhabditis elegans*, male-induced life-span shortening of the opposite sex (hermaphrodites) has been proposed to result

from physical damage caused by copulation (1). Whether additional mechanisms of male-induced killing exist in *C. elegans*, and the extent to which such mechanisms may be evolutionarily conserved, is largely unknown.

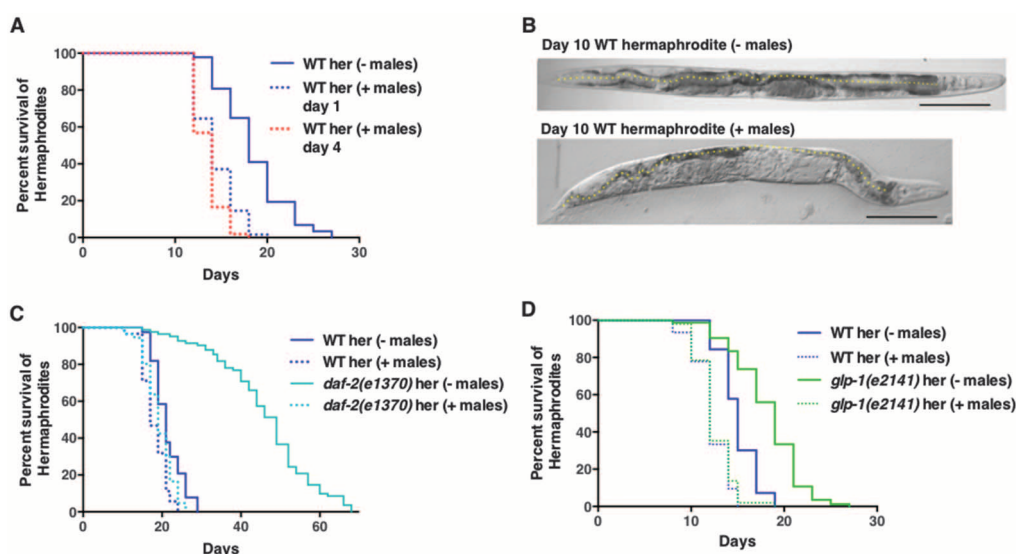
The continuous presence of young males significantly shortened the life span of hermaphrodites (>20% decrease) (Fig. 1A and table S1). The male-induced shortening of life span was seen whether males were placed with hermaphrodites at the beginning of their life (day 1) or at sexual maturity (day 4) (Fig. 1A). This life-span shortening was not a result of crowding, because the total numbers of worms were the same in all conditions. Males also induced behavioral and morphological phenotypes characteristic of an advanced age in these hermaphrodites: Movement was slowed, paralysis increased, and a general decrepitude was observed, as exemplified

by increased incidence of vacuole-like structures and structural decline within the cuticle, muscle, pharynx, and intestine (Fig. 1B; fig. S1, A to I; and movies S1 to S3) (3–6). We termed this phenomenon male-induced demise (MID).

Long-lived hermaphrodites, such as insulin receptor mutants *daf-2*, germline-deficient mutants *glp-1*, and wild-type worms subjected to dietary deprivation (DD), also exhibited a shortened life span (Fig. 1, C and D, and fig. S1J). *daf-2* mutant hermaphrodites displayed a large (>60%) reduction in median life span in the presence of wild-type males (Fig. 1C). *glp-1* mutant hermaphrodites exhibited shortening of life span in response to males, even though they are sterile (Fig. 1D), in agreement with observations that sterile hermaphrodites are equally susceptible to male-induced life-span shortening (1). Thus, the deterioration of hermaphrodites in the presence of males is not a simple result of increased progeny production from sexual reproduction (7), and extension of life span through several well-known longevity pathways is not sufficient to alleviate this form of demise.

To understand how males restrict the life span of the opposite sex, we assessed genome-wide changes in hermaphrodite gene expression triggered by males. To avoid expression changes due to fertilized embryos in the mother, we used sterile hermaphrodites (*glp-1*). We placed *glp-1* young adult hermaphrodites with wild-type young males for 8 days, then removed the males and collected the hermaphrodites' RNA for microarray analysis (Fig. 2A). As a control, we collected RNA from *glp-1* hermaphrodites that were not placed in the presence of males but were grown at the same density with other hermaphrodites (Fig. 2A). Unbiased clustering of the microarray data revealed that the presence of males induced large changes in gene expression

Fig. 1. Reduced life span and increased hallmarks of aging in hermaphrodites exposed to males. (A) Shortened life span of wild-type hermaphrodites when kept in the constant presence of young mating-competent males added at the beginning of the hermaphrodite's life (day 1, log rank $P < 0.0001$) or when hermaphrodites reached young adulthood (day 4, log rank $P < 0.0001$). (B) Representative images of the male-induced deterioration of hermaphrodites at day 10. The dotted yellow line traces the center of the intestine, which is irregular and often appears discontinuous in hermaphrodites undergoing MID. Scale bar, 200 μm . (C) Shortened life span of long-lived *daf-2(e1370)* mutant hermaphrodites (log rank $P < 0.0001$) kept in the constant presence of young males. As a control, wild-type males also shorten the life span of wild-type hermaphrodites (log rank $P < 0.0001$). Note the difference in scale with Fig. 1A. (D) Shortened life span of long-lived and sterile *glp-1(e2141)* mutant hermaphrodites (log rank $P < 0.0001$) in the



constant presence of young males. As a control, wild-type males also shorten the life span of wild-type hermaphrodites (log rank $P < 0.0001$). Note the difference in scale with Fig. 1A. (D) Shortened life span of long-lived and sterile *glp-1(e2141)* mutant hermaphrodites (log rank $P < 0.0001$) in the

constant presence of young males. As a control, wild-type males also shorten the life span of wild-type hermaphrodites (log rank $P < 0.0001$). Statistics are included in table S1.

in hermaphrodites (Fig. 2B, fig. S2A, and table S2). Genes whose expression was increased in response to males were enriched for insulin signaling ($P = 4.3 \times 10^{-3}$) [e.g., insulin peptides

(*ins-4*, *ins-11*, *ins-23*, and *ins-31*), which are expressed in neurons], transthyretin-related family members ($P = 4.3 \times 10^{-3}$) [which are involved in neurodegenerative diseases in mammals

(8)], and G protein-coupled chemoreceptors ($P = 1.9 \times 10^{-3}$) (which are expressed in sensory neurons) (fig. S2B). In contrast, genes whose expression was decreased in response to males were

Fig. 2. Male-induced changes in gene expression in hermaphrodites and attenuation of male-induced demise in *ins-11* mutants. (A) Schematic of the microarray design. (B) Unbiased clustering of the genes whose mRNAs show increased (red) (341) or decreased (blue) (289) abundance in hermaphrodites in response to males (three independent experiments). (C) RNAi to *ins-11* specifically ameliorates the male-induced shortening of life span in hermaphrodites from a strain that is sensitized for neuronal RNAi (log rank $P < 0.0001$). (D) RNAi to *F11A5.3* reduces the male-induced shortening of life span in hermaphrodites from a strain that is sensitized for neuronal RNAi (log rank $P < 0.0001$). (E) RNAi to *utx-1* reduces the male-induced shortening of life span in hermaphrodites from a strain that is sensitized for neuronal RNAi (log rank $P < 0.0001$). (F) *ins-11(tm1053)* hermaphrodite mutants exhibit partial protection from the demise induced by wild-type males (log rank $P < 0.0001$), although they are able to successfully mate. Statistics are included in table S1.

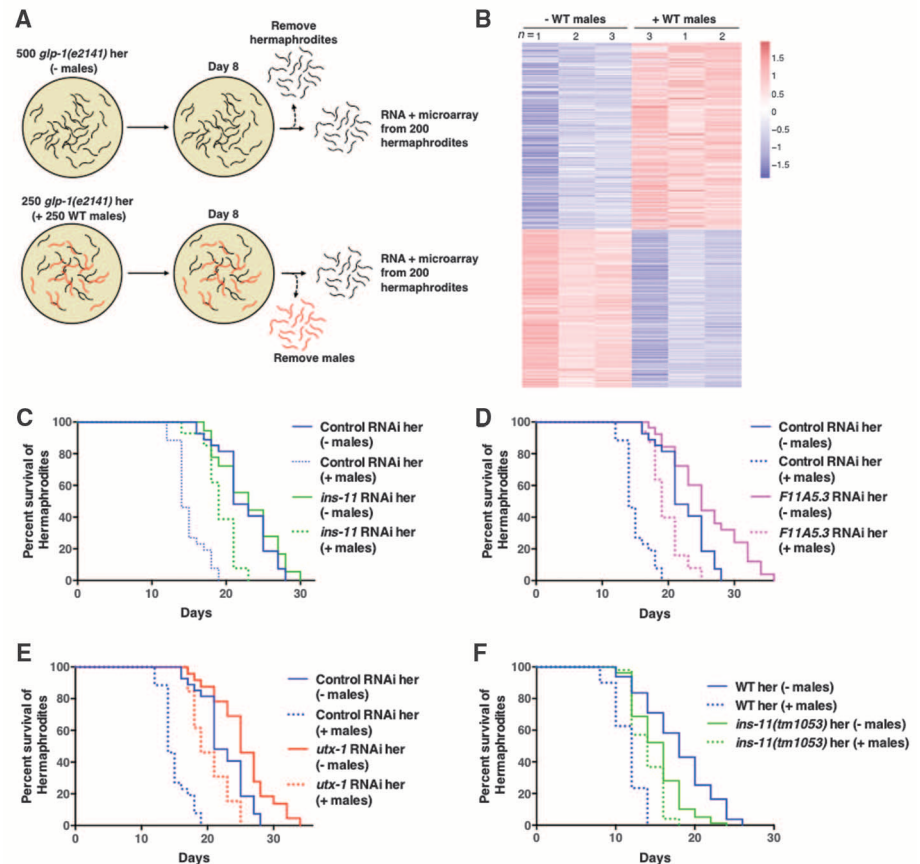
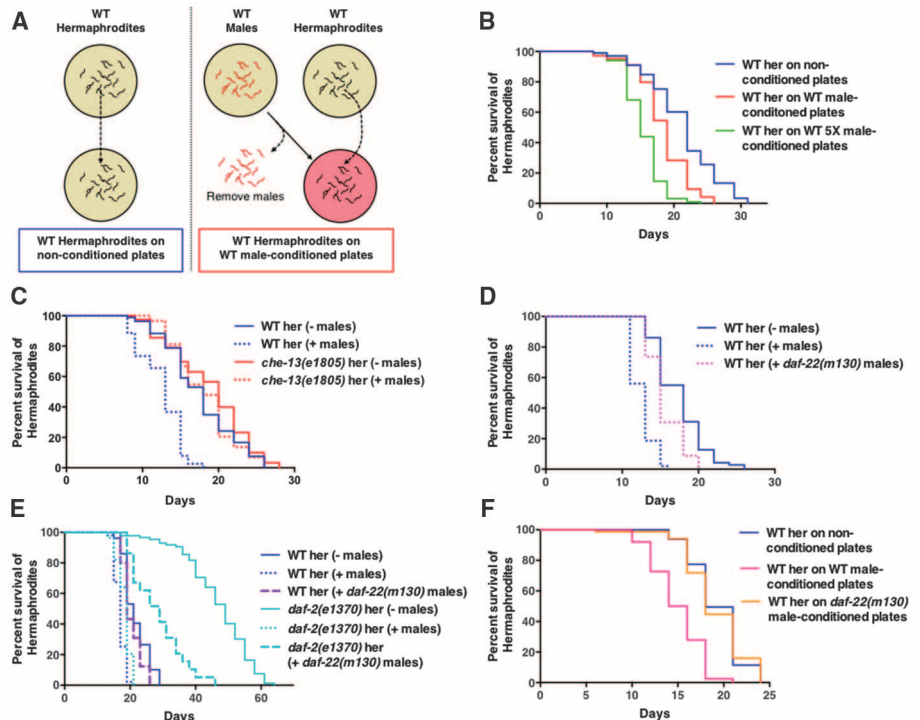


Fig. 3. Role of diffusible substances secreted by males in shortening the life span of hermaphrodites. (A) Schematic for male-conditioned plates. (B) Shortened life span of wild-type hermaphrodites exposed to secreted substances from males [log rank $P < 0.0001$ when plates were conditioned with 30 males/plate or 150 males/plate (5X)]. (C) *che-13(e1805)* hermaphrodites are resistant to male-induced shortening of life span (fig. S3, A and B) (log rank $P < 0.5038$). (D) *daf-22(m130)* males do not shorten the life span of wild-type hermaphrodites, as well as wild-type males (fig. S3, A and B) (statistically significant difference by log rank, $P < 0.0001$). (E) *daf-22(m130)* males do not shorten the life span of *daf-2(e1370)* hermaphrodites, as well as wild-type males (statistically significant difference by log rank, $P < 0.0001$). (F) Medium conditioned by *daf-22(m130)* males does not significantly shorten the life span of wild-type hermaphrodites (log rank $P = 0.9177$). Statistics are included in table S1.



enriched for C-type lectins and the cuticle (fig. S2B). That the presence of males triggered changes in the expression of neuronally expressed genes suggests that mechanisms in addition to structural damage resulting from copulation also contribute to MID.

We next tested whether modulating the expression of genes whose expression was increased in hermaphrodites in response to males and expressed in neurons could rescue MID. We used RNA interference (RNAi) to decrease expression of 10 hand-picked genes that are expressed in neurons and either belong to a significant functional annotation enrichment category or undergo large changes in message abundance in response to males. We used a strain of *C. elegans* that is sensitized for RNAi in neurons *Punc-119::sid-1*. Depletion of mRNA from three of these genes (*ins-11*, *F11A5.3*, and *utx-1*) partially rescued MID (Fig. 2, C to E, and fig. S2, C to L). *ins-11* encodes an insulin-like peptide that is expressed primarily in sensory neurons (9). *F11A5.3* encodes a conserved small guanine triphosphatase (GTPase) of the Rab family of little-known function in worms but whose human ortholog (*RAB2A*) functions in vesicular trafficking (10). *utx-1* encodes a histone H3 demethylase (H3K27me3 demethylase), depletion of which increases longevity in *C. elegans* (11, 12). Whereas decreased expression of *F11A5.3* and *utx-1* also extended the life span of hermaphrodites without males, decreased expression of *ins-11* specifically ameliorated MID without affecting the life span of hermaphrodites kept in the absence of males. The specific rescue of MID after depletion of *ins-11* likely results from the action of this gene in the hermaphrodites themselves and not in the males because *ins-11* mutant hermaphrodites were also partially resistant to demise induced by wild-type males (Fig. 2F). Thus, the shortening of life span induced by males can be ameliorated by depletion of the insulin peptide INS-11.

Because MID could be rescued by manipulating a single gene in the hermaphrodites, the phenomenon seems unlikely to result solely from structural damage caused by copulation. To test more directly whether males could shorten the life span of hermaphrodites without being in physical contact with them, we placed males on plates for 2 days, removed these males, and then added hermaphrodites to the male-conditioned plates (Fig. 3A). Conditioning the plates with

males shortened the life span of wild-type hermaphrodites, in a manner that depended on the number of males used to make the conditioned medium (Fig. 3B). Hermaphrodites placed on male-conditioned plates underwent signs of MID (movies S4, to S6). Although there may be a physical component to MID, one or more diffusible substances secreted or released by males on the plate is sufficient to decrease life span of hermaphrodites.

C. elegans secrete small molecules called ascarosides, which act as pheromones to regulate various processes, including development, behavior, and life span (13–18). Ascaroside production has been primarily studied in the context of hermaphrodites, but males also excrete a sex-specific blend of ascarosides (19). We therefore tested whether pheromone sensing by hermaphrodites and pheromone production by males were required for MID. Hermaphrodites deficient for processing a range of sensory signals, including those from pheromones (20, 21) (*che-13*), were not susceptible to MID (Fig. 3C and table S1), even though they mated normally with wild-type males (fig. S3, A and B). Males deficient in ascaroside pheromone biogenesis (*daf-22*) triggered MID less effectively in both wild-type or long-lived hermaphrodites (Fig. 3, D and E), although these *daf-22* males mated normally with wild-type hermaphrodites (fig. S3, A and B). Conditioned medium from males that are defective in pheromone production (*daf-22*) did not trigger MID in wild-type hermaphrodites (Fig. 3F). Thus, the ability to secrete and sense pheromones appears to be necessary for males to induce shortening of life span in hermaphrodites.

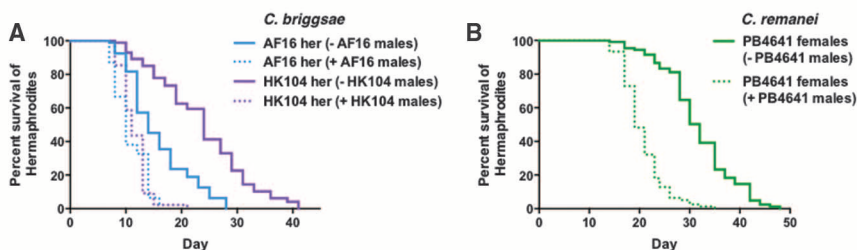
Is the male-induced demise a more general, conserved phenomenon? The genus *Caenorhabditis* includes several distantly related species, each of them with different strains (fig. S4A). Similar to what we observed in the long-domesticated strain of *C. elegans* (N2), males from a wild *C. elegans* strain, AB1, also shortened the life span of hermaphrodites of that strain (fig. S4B). Males from the species *C. briggsae*, which diverged from *C. elegans* about 20 to 30 million years ago (22), decreased the life span of hermaphrodites of two different *C. briggsae* isolates (Fig. 4A). Males from the species *C. remanei*, which has obligate males and females, led to life-span shortening of females (Fig. 4B). Together, these results indicate that MID is conserved at least over 20 to 30 million years of evolution and is not linked to

hermaphroditism. The evolutionary conservation of MID raises the possibility that this phenomenon has adaptive value and may be caused by conserved mechanisms.

We find that continuous presence of mating-competent males shortens the life span of the opposite sex and triggers a phenotype that resembles progeria. In our study, *C. elegans* hermaphrodites were exposed to an unnaturally high percentage of males for the duration of their life spans. The percentage of male *C. elegans* is usually low (0.01 to 0.1%), although this percentage can be increased in response to stress stimuli. However, MID does not appear to be solely due to an artificially high percentage of males, as *C. remanei* females, which naturally exist in a 1:1 ratio with males, also displayed MID in our experimental setting. Males shorten the life span of the opposite sex in part by releasing one or more diffusible substances, possibly a pheromone. Thus, while male secretions promote reproduction under normal circumstances, they might also accelerate demise, especially when these secretions are concentrated. In addition to male pheromones, the male-conditioned plates are also likely to contain sperm and seminal fluid from male-to-male copulation attempts (23). Copulation may help male secretions to be produced or act efficiently. Although male sperm has been previously ruled out as a cause of the male-induced shortening of life span in *C. elegans* (1), seminal fluid, which may itself contain pheromones, cannot be excluded as a causal agent.

In both worms and flies, sensory deficiencies in olfactory and gustatory neurons extend life span (24–26). Although the exact sensory neurons and specific chemoreceptors responsible for pheromone perception are just beginning to be identified (16, 18, 27, 28), pheromones activate conserved downstream signaling pathways, including those activated by transforming growth factor (TGF)- β and insulin (29). Male-induced demise could be influenced by similar neuronal circuits and signaling pathways. Indeed, interfering with the gene encoding the insulin peptide INS-11, which is expressed in sensory neurons, specifically rescued the male-induced demise of hermaphrodites. INS-11 and other genes identified in our microarray analysis could provide a handle on the dissection of sensory or intersexual interactions. If males in wild worm populations shortened life span of the opposite sex after reproduction occurred, this might have the

Fig. 4. Males also shorten the life span of individuals of the opposite sex in other species of nematode. (A) Males from the *C. briggsae* strains AF16 and HK104 shorten the life span of hermaphrodites from the respective strains (log rank $P < 0.0001$). **(B)** Males from the *C. remanei* strain PB4641 shorten the life span of PB4641 females (log rank $P < 0.0001$). Statistics are included in table S1.



evolutionary advantage of preserving limited resources for the offspring (30) or preventing competition from other males.

References and Notes

- D. Gems, D. L. Riddle, *Nature* **379**, 723–725 (1996).
- T. Chapman, L. F. Liddle, J. M. Kalb, M. F. Wolfner, L. Partridge, *Nature* **373**, 241–244 (1995).
- L. A. Herndon *et al.*, *Nature* **419**, 808–814 (2002).
- C. F. Glenn *et al.*, *J. Gerontol. A Biol. Sci. Med. Sci.* **59**, 1251–1260 (2004).
- D. K. Chow, C. F. Glenn, J. L. Johnston, I. G. Goldberg, C. A. Wolkow, *Exp. Gerontol.* **41**, 252–260 (2006).
- M. D. McGee *et al.*, *Aging Cell* **10**, 699–710 (2011).
- J. Hodgkin, T. M. Barnes, *Proc. Biol. Sci.* **246**, 19–24 (1991).
- K. C. Kiontke *et al.*, *BMC Evol. Biol.* **11**, 339 (2011).
- S. B. Pierce *et al.*, *Genes Dev.* **15**, 672–686 (2001).
- E. J. Tisdale, J. R. Bourne, R. Khosravi-Far, C. J. Der, W. E. Balch, *J. Cell Biol.* **119**, 749–761 (1992).
- T. J. Maures, E. L. Greer, A. G. Hauswirth, A. Brunet, *Aging Cell* **10**, 980–990 (2011).
- C. Jin *et al.*, *Cell Metab.* **14**, 161–172 (2011).
- R. A. Butcher, M. Fujita, F. C. Schroeder, J. Clardy, *Nat. Chem. Biol.* **3**, 420–422 (2007).
- P. Y. Jeong *et al.*, *Nature* **433**, 541–545 (2005).
- S. Srinivasan *et al.*, *Nature* **454**, 1115–1118 (2008).
- P. T. McGrath *et al.*, *Nature* **477**, 321–325 (2011).
- E. Z. Macosko *et al.*, *Nature* **458**, 1171–1175 (2009).
- A. H. Ludewig *et al.*, *Proc. Natl. Acad. Sci. U.S.A.* **110**, 5522–5527 (2013).
- Y. Izrayelit *et al.*, *ACS Chem. Biol.* **7**, 1321–1325 (2012).
- L. A. Perkins, E. M. Hedgecock, J. N. Thomson, J. G. Culotti, *Dev. Biol.* **117**, 456–487 (1986).
- B. van Swinderen, L. B. Metz, L. D. Shebest, C. M. Crowder, *Genetics* **161**, 109–119 (2002).
- A. D. Cutter, *Mol. Biol. Evol.* **25**, 778–786 (2008).
- D. Gems, D. L. Riddle, *Genetics* **154**, 1597–1610 (2000).
- J. Apfeld, C. Kenyon, *Nature* **402**, 804–809 (1999).
- J. Alcedo, C. Kenyon, *Neuron* **41**, 45–55 (2004).
- S. Libert *et al.*, *Science* **315**, 1133–1137 (2007).
- C. I. Bargmann, H. R. Horvitz, *Science* **251**, 1243–1246 (1991).
- A. H. Ludewig, F. C. Schroeder, *WormBook* **2013**, 1–22 (2013).
- P. Ren *et al.*, *Science* **274**, 1389–1391 (1996).
- T. B. Kirkwood, *Nature* **270**, 301–304 (1977).

Acknowledgments: We thank members of the Brunet laboratory, S. Kim, A. Fire, and A. Villeneuve for helpful suggestions and J. Lim and S. Zimmerman for critical reading of the manuscript. We thank N. Kosovik and the Protein and Nucleic Acid Facility facility for the microarray experiments and T. Sternagle from the Caenorhabditis Genetics Center. Supported by R01AG031198, DP1AG044848, the Glenn Foundation for Medical Research (A.B.), postdoctoral fellowship F32AG37254 (T.J.M.), T32HG000044 and the Helen Hay Whitney Foundation (L.N.B.), Stanford Dean's Fellowship (BAB), R01GM088290 (F.C.S.), and T32GM008500 (Y.I.).

Supplementary Materials

www.sciencemag.org/content/343/6170/541/suppl/DC1
Materials and Methods

Figs. S1 to S3

Tables S1 and S2

Movies S1 to S6

References (31–37)

2 August 2013; accepted 11 November 2013

Published online 28 November 2013;

10.1126/science.1244160

Drosophila Life Span and Physiology Are Modulated by Sexual Perception and Reward

Christi M. Gendron,^{1*} Tsung-Han Kuo,^{2*} Zachary M. Harvanek,^{1,3} Brian Y. Chung,¹ Joanne Y. Yew,^{4,5} Herman A. Dierick,² Scott D. Pletcher¹

Sensory perception can modulate aging and physiology across taxa. We found that perception of female sexual pheromones through a specific gustatory receptor expressed in a subset of foreleg neurons in male fruit flies, *Drosophila melanogaster*, rapidly and reversibly decreases fat stores, reduces resistance to starvation, and limits life span. Neurons that express the reward-mediating neuropeptide F are also required for pheromone effects. High-throughput whole-genome RNA sequencing experiments revealed a set of molecular processes that were affected by the activity of the longevity circuit, thereby identifying new candidate cell-nonautonomous aging mechanisms. Mating reversed the effects of pheromone perception; therefore, life span may be modulated through the integrated action of sensory and reward circuits, and healthy aging may be compromised when the expectations defined by sensory perception are discordant with ensuing experience.

Sensory perception can modulate aging and physiology in multiple species (1–6). In *Drosophila*, exposure to food-based odorants partially reverses the anti-aging effect of dietary restriction, whereas broad reduction in olfactory function promotes longevity and alters fat metabolism (2, 4). Even the well-known rela-

tion between body temperature and life span may have a sensory component (7, 8).

To identify sensory cues and neuronal circuitry that underlie the effects of sensory perception on aging, we focused on the perception of potential mates. Social interactions are prevalent throughout nature, and the influence of social context on health and longevity is well known in several species, including humans (9). Such influences include behavioral interactions with mates and broader physiological “costs of reproduction,” which often form the basis for evolutionary models of aging (10, 11).

In *Drosophila*, the presence of potential mates is perceived largely through nonvolatile cuticular hydrocarbons, which are produced by cells called oenocytes and are secreted to the cuticular surface, where they function as pheromones (12, 13). To test whether differential pheromone

exposure influenced life span or physiology, we housed “experimental” flies of the same genotype with “donor” animals of the same sex that either expressed normal pheromone profiles or were genetically engineered to express pheromone profiles characteristic of the opposite sex (Fig. 1A). Donor males with feminized pheromone profiles were generated by targeting expression of the sex determination gene, *transformer*, to the oenocytes [via *OK72-GAL4* or *Prom-E800-GAL4* (14) (fig. S1)], whereas masculinization of female flies was accomplished by expressing *tra*-RNAi in a similar way (15). This design allowed manipulation of the experimental animals’ perceived sexual environment without introducing complications associated with mating itself.

In *Drosophila*, sensory manipulations can affect life span, fat storage [as determined by baseline measures of triacylglyceride (TAG)], and certain aspects of stress resistance (2, 4). We found that flies exposed to pheromones of the opposite sex showed differences in these phenotypes. Experimental male flies exposed to male donor pheromone had higher amounts of TAG, were substantially more resistant to starvation, and exhibited a significantly longer life span than genetically identical male siblings exposed to female donor pheromone (Fig. 1, B to D). Females exhibited similar phenotypes in response to male donor pheromone, but the magnitude of the effects was smaller (fig. S2). Subsequent experiments were therefore focused on males.

The characteristics of pheromone exposure were indicative of a mechanism involving sensory perception. Effects were similar in several genetic backgrounds, including a strain recently collected in the wild (fig. S3), and were largely unaffected by cohort composition (fig. S4). Pheromone-induced phenotypes were detected after as little as 2 days’ exposure to donor animals (Fig. 1, B and C), persisted with longer manipulations (Fig. 1D), and were progressively

¹Department of Molecular and Integrative Physiology and Geriatrics Center, Biomedical Sciences and Research Building, University of Michigan, Ann Arbor, MI 48109, USA. ²Department of Molecular and Human Genetics, Baylor College of Medicine, Houston, TX 77030, USA. ³Medical Scientist Training Program, Taubman Medical Library, University of Michigan, Ann Arbor, MI 48109, USA. ⁴Temasek Life Sciences Laboratory, National University of Singapore, Singapore 117604. ⁵Department of Biological Sciences, National University of Singapore, Singapore 117543.

*These authors contributed equally to this work.
†Corresponding author. E-mail: sletcher@umich.edu

reversed when female donor pheromone was removed (Fig. 1, E and F, and fig. S5). Pheromone effects appeared not to be mediated by aberrant or aggressive interactions with donor flies, because (i) we did not observe significant differences in such behaviors and (ii) continuous, vigorous agitation of the vials throughout the exposure period, which effectively disrupted observed behaviors, had no effect on the impact of donor pheromone (fig. S6). Furthermore, exposure of experimental males to the purified female pheromone 7,11-heptacosadiene (7,11-HD) produced physiological changes in the absence of donor animals (mean survival time during starvation, 51.1 ± 1.7 hours and 45.4 ± 1.2 hours for control and 7,11-HD exposure, respectively; $P = 0.007$, log-rank test).

To explore the sensory modality through which donor pheromone exerts its effects, we tested whether the broadly expressed olfactory co-receptor *Or83b*, whose loss of function renders flies largely unable to smell (16), was required for pheromone effects. *Or83b* mutant flies and controls exhibited similar changes in starvation resistance (fig. S7) in response to donor pheromone, indicating that olfaction was not required. To test whether taste

perception was involved, we used flies mutant for the gene *Pox neuro* (*Poxn*), a null mutation that putatively transforms all chemosensory neurons into mechanosensory neurons. *Drosophila* taste neurons are present in the mouthparts and distributed on different body parts, including the wings, legs, and genitals, which allow sensation by contact. When the *Poxn* null mutation is coupled with a partially rescuing transgene, *Poxn*^{ΔM22-B5}-ΔXB, flies are generally healthy but gustatory perception is eliminated in the labelum, the legs, and the wing margins (17). *Poxn*^{ΔM22-B5}-ΔXB flies showed no pheromone-induced changes in starvation resistance, TAG amounts, or life span (Fig. 2, A to C). However, the responses of *Poxn* mutant flies that carried a transgene that restores taste function to the legs and wing margins [but not labelum; *Poxn*^{ΔM22-B5}-*Full1* (17)] were similar to those of control flies (Fig. 2, A to C). Thus, the effects of pheromone exposure appear to be mediated by taste perception through gustatory neurons outside of the mouthparts.

To identify specific gustatory receptors and neurons that might mediate the pheromone effects, we tested candidate pheromone receptors. Of the mutants that we examined, only flies

that carried a loss-of-function mutation in the gene *pickpocket 23* (*ppk23*) were resistant to the effects of pheromone exposure (fig. S8). Further analysis verified that *ppk23* was required for the effects of pheromone exposure on starvation resistance, TAG amounts, and life span (Fig. 2, D to F). Silencing *ppk23*-expressing neurons only during exposure to donor males by expressing a temperature-sensitive dominant-negative allele of the dynamin gene *shibire* (via *ppk23-GAL4;UAS-shi^{ts}*) also eliminated the differential response to pheromones (Fig. 3A). In male *Drosophila*, the transcription factor *fruitless* (*fru*) is expressed with *ppk23* in pheromone-sensing neurons located in the animals' forelegs (18), and silencing *fru*-expressing neurons during exposure (via *fru-GAL4;UAS-shi^{ts}*) abrogated pheromone effects (Fig. 3B). Consistent with a requirement for these neurons, we found that surgical amputation of the forelegs, but not injury alone, was sufficient to reproducibly eliminate the effects of pheromone exposure (Fig. 3C and fig. S9). Moreover, acute targeted activation of *ppk23*-expressing neurons by means of a temperature-sensitive TRPA1 channel (*ppk23-GAL4;UAS-TRPA1*) was sufficient to mimic the effects of female pheromone without exposure

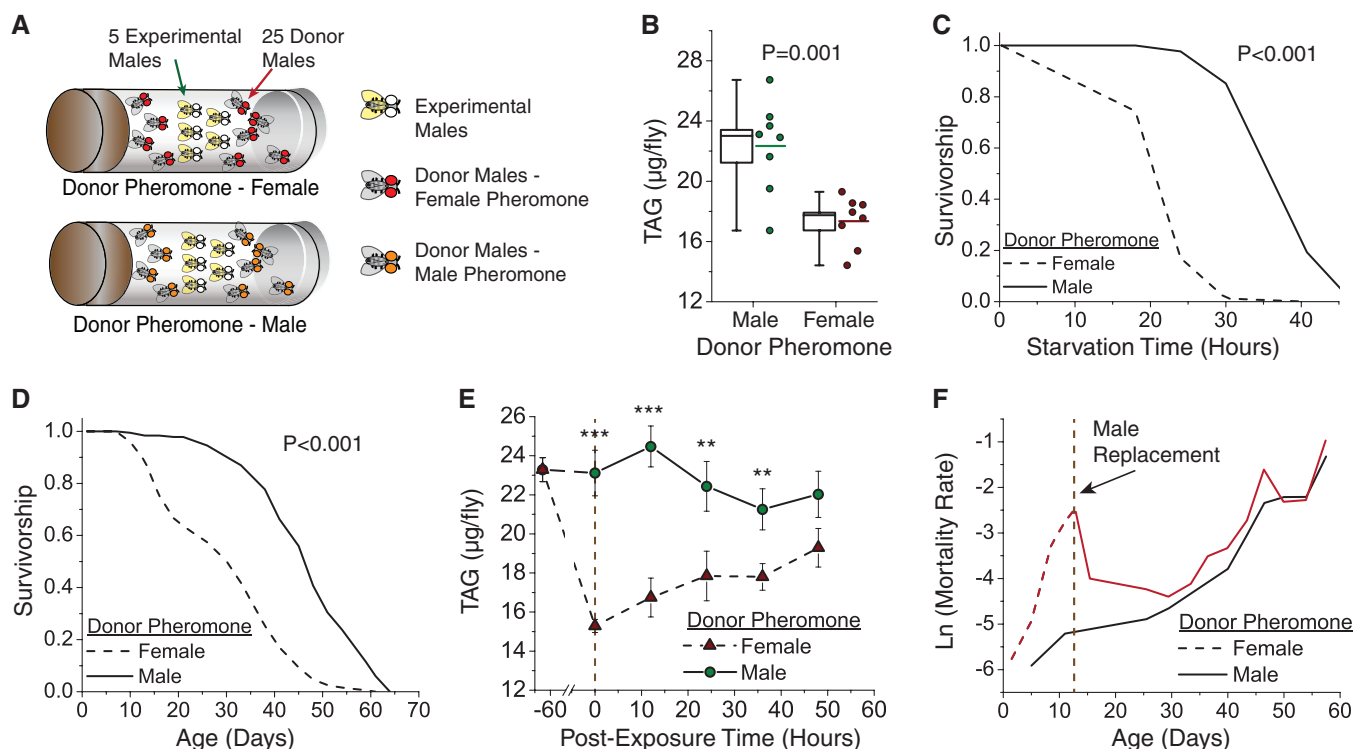


Fig. 1. Exposure to sex-specific pheromones significantly affects physiology, stress resistance, and life span in *Drosophila*. (A) Protocol used to expose male flies to masculine or feminine pheromones. Five experimental males were housed with either 25 control (donor pheromone = male) or feminized (donor pheromone = female) males. (B) Male flies exposed to male donor pheromone exhibit higher TAG amounts than flies exposed to female donor pheromone ($N = 40$ for each treatment). Box plots represent the medians and SEM (box boundaries) for each experimental group. Lines adjacent to the box represent mean values. P value is by t test. (C) Male experimental flies exposed to male donor pheromones exhibit greater star-

vation resistance relative to genetically identical males exposed to female donor pheromones ($N = 88$ and 82 , respectively; P value is by log-rank test). (D) Male experimental flies exposed to male donor pheromones exhibit a longer life span relative to flies that are exposed to female donor pheromones ($N = 184$ and 195 , respectively; P value is by log-rank test). (E) TAG amounts are progressively restored after removal (at $T = 0$) of female donor pheromones ($N = 50$ for each time point). *** $P \leq 0.001$, ** $P \leq 0.01$, other values $P \geq 0.05$ (t test). (F) Differences in age-specific mortality caused by pheromone exposure were reversed within days after feminized males were replaced with control males.

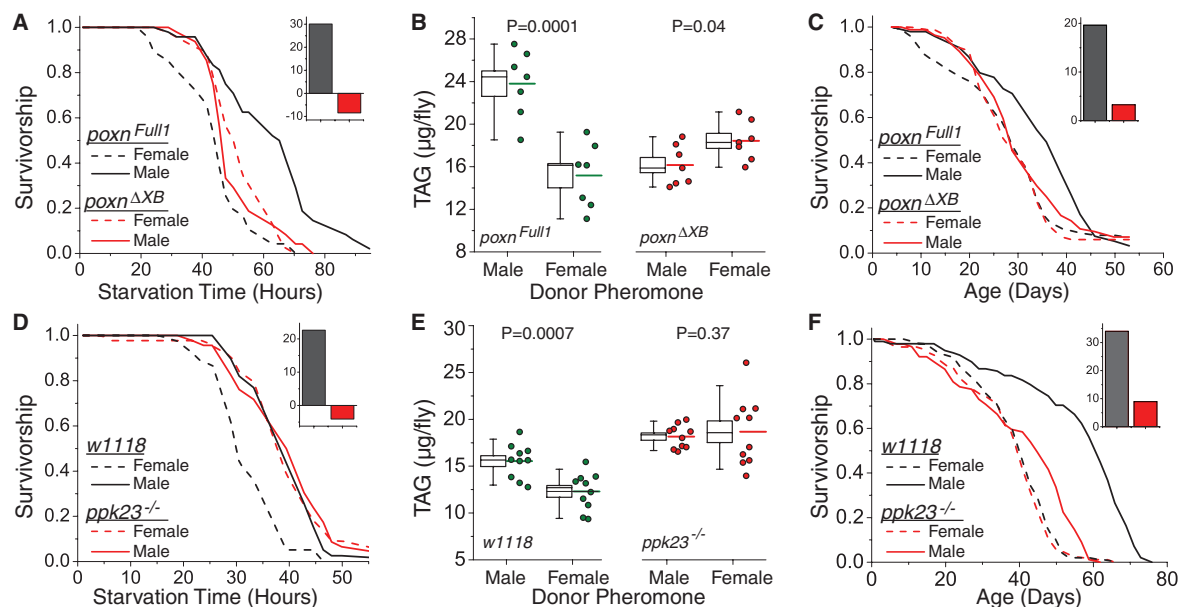


Fig. 2. The effects of pheromone exposure are mediated by taste perception involving gustatory receptor *ppk23*. (A to C) The *Poxn^{ΔXB}* strain lacks taste neurons in the labelum, the legs, and the wing margins, whereas the *Poxn^{Full1}* strain lacks taste neurons in the labelum only. (A) Starvation resistance. $N = 46$ to 48 experimental flies for all treatments. Significance values are $P \leq 0.0001$ for *Poxn^{Full1}* (exposed to control versus feminized donor flies) and $P = 0.56$ for *Poxn^{ΔXB}*. (B) TAG amounts. Box plots are as in Fig. 1. (C) Life span. $N = 100$ to 103 experimental flies for all treatments. Significance values are $P = 0.001$ for *Poxn^{Full1}* exposed to control versus feminized donor flies and $P = 0.30$ for *Poxn^{ΔXB}* exposed to control versus feminized donor flies. (D to F) The gustatory receptor

ppk23 is required for pheromone effects. (D) Starvation resistance. $N = 40$ and 39 for control flies exposed to feminized or control donor males, respectively ($P \leq 0.0001$). $N = 43$ and 46 for *ppk23* mutant flies exposed to female or male donor pheromones, respectively ($P = 0.92$). (E) TAG amounts. Box plots are as in Fig. 1. (F) Life span. $N = 98$ and 99 for control flies exposed to male or female donor pheromones, respectively. $N = 89$ and 86 for *ppk23* mutant flies exposed to male or female donor pheromones, respectively. P values were obtained for life span and starvation resistance by log-rank test and for TAG amounts by t test. Insets in (A), (C), (D), and (F) indicate, for each genotype, the percent change in mean starvation time or mean life span caused by differential pheromone exposure.

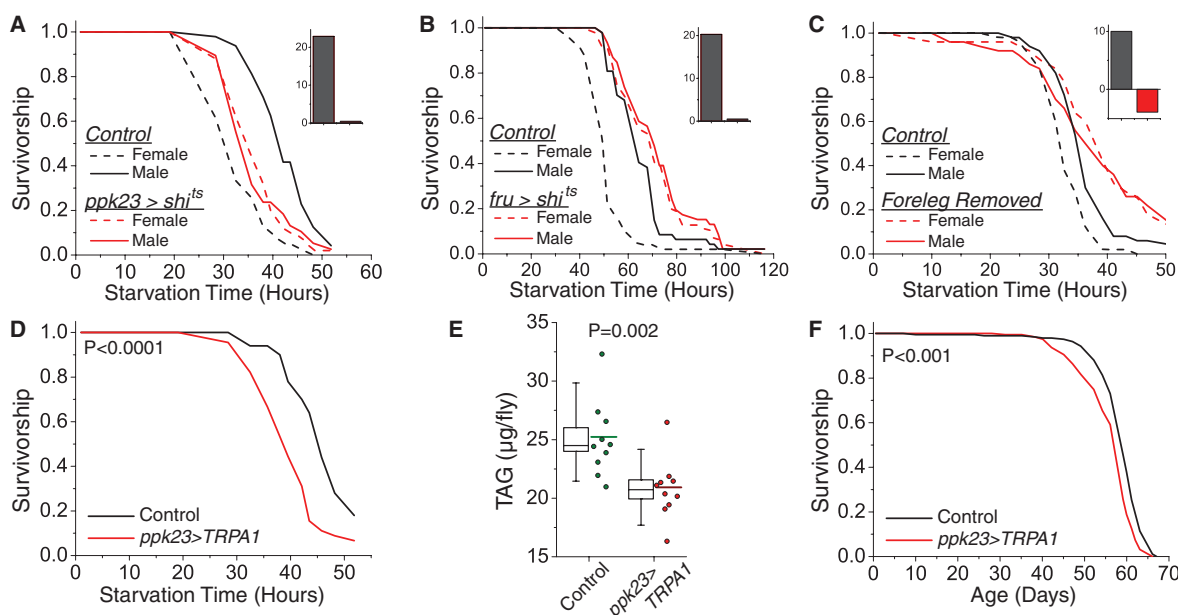


Fig. 3. Activation of *ppk23*-positive pheromone-sensing neurons in the foreleg of male flies is necessary and sufficient for changes in physiology and life span. (A) Targeted inhibition of *ppk23*-expressing neurons abrogates differences in starvation caused by pheromone exposure. $N = 48$ and 39 for control (*ppk23-GAL4* only) flies exposed to male or female donor pheromones, respectively ($P \leq 0.0001$). $N = 38$ and 50 for treatment (*ppk23-GAL4;UAS-shi^{ts}*) flies exposed to male or female donor pheromones, respectively ($P = 0.96$). (B) Targeted inhibition of *fruitless*-expressing neurons abrogates the effect of pheromone exposure on starvation resistance. $N = 47$ and 49 for control (*fru-GAL4* only) flies exposed to male or female donor pheromones, respectively ($P \leq 0.0001$). $N = 46$ and 47 for treatment (*fru-GAL4;UAS-shi^{ts}*) flies exposed to male

or female donor pheromones, respectively ($P = 0.65$). (C) Surgical removal of the forelegs abrogates the effects of pheromone exposure on starvation resistance. $N = 50$ for each genotype or treatment. $P = 0.0008$ for unmanipulated and $P = 0.66$ for amputee flies exposed to either male or female donor pheromones. See also fig. S9. (D to F) Activation of *ppk23*-expressing neurons via heat-activated TRPA1 phenocopies the effects of pheromone exposure. (D) Starvation resistance. $N = 50$ for control (*ppk23-GAL4* only), $N = 45$ for flies with activated neurons (*ppk23-GAL4;UAS-TRPA1*) ($P \leq 0.0001$). (E) TAG amounts. Box plots are as in Fig. 1. (F) Life span. $N = 193$ (*ppk23-GAL4* only) and $N = 191$ (*ppk23-GAL4;UAS-TRPA1*). P values were obtained for life span and starvation resistance by log-rank test and for TAG amounts by t test. Insets are as described in Fig. 2.

(Fig. 3, D to F). Together, these data indicate that pheromone-sensing neurons in the foreleg of the male fly that express the gustatory receptor *ppk23* and the transcription factor *fruitless* influence stress resistance, physiology, and life span in response to perception of female pheromones.

To examine brain circuits that may function in transducing pheromone perception, we selectively expressed *UAS-shi^{ts}* to block synaptic transmission in various neuroanatomical regions with the goal of disrupting the physiological effects of donor pheromone exposure. The effects were abrogated when *UAS-shi^{ts}* was driven in neurons characterized by expression of neuropeptide F (NPF, as represented by *npf-GAL4*) (fig. S10). Further analysis verified that pheromone-induced changes in starvation resistance and TAG abundance were lost after silencing of *npf*-expressing neurons (Fig. 4A). Consistent with a possible role in transducing pheromone information, *npf* expression was significantly increased by 30% in experimental males after exposure to feminized donor males (fig. S11), and activation of *npf*-expressing neurons was sufficient to decrease life span in the absence of pheromone exposure (Fig. 4B).

NPF may function as a mediator of sexual reward in *Drosophila* (19), and its mammalian

counterpart, neuropeptide Y (NPY), has been associated with sexual motivation and psychological reward (20, 21). We tested whether the effects of pheromone perception might be rescued by allowing males to successfully mate with females. Neither a small number of conjugal visits with virgin females nor housing with wild-type females in a 1:1 ratio was sufficient to ameliorate the effects of pheromone exposure (fig. S12). In this context, decreased longevity may be a consequence of pheromone perception and not of mating itself. Male *Drosophila* are willing and able to copulate up to five times in rapid succession before requiring a refractory period (22). We found that supplementing donor cohorts with an excess of mating females (in a 5:1 ratio) was sufficient to significantly reduce the effects on mortality and TAG caused by female donor pheromone early in life (Fig. 4C and fig. S13). The benefits of mating on age-specific mortality decreased with age, which suggests that aging may reduce mating efficiency or may diminish effective mating reward.

To identify how sexual perception and reward may alter physiological responses in peripheral tissues, we used whole-genome RNA sequencing (RNA-seq) technology to examine changes in gene

expression. We found 195 genes with significantly different expression (using an experiment-wise error rate of 0.05) in control male flies that were exposed to feminized or control donor males for 48 hours. Nearly all (188/195 = 96%) of the changes appeared to be due to pheromone perception, because they were not observed in identical experiments using *ppk23* mutant flies (table S1). Males exposed to female pheromones decreased the transcription of genes encoding odorant-binding proteins and increased the transcription of several genes with lipase activity (Fig. 4D). A significant enrichment was observed in secreted molecules, which includes genes encoding proteins that mediate immune and stress responses. Many of these genes and pathways were highlighted in a recent meta-analysis of gene expression changes in response to stress and aging (23).

The activities of insulin and target of rapamycin (TOR) signaling, which modulate aging across taxa, increase sexual attractiveness in flies (24). Our demonstration that perception of sexual characteristics is sufficient to modulate life span and physiology suggests that aging pathways in one individual may modulate health and life span in another (fig. S14). These types of indirect genetic

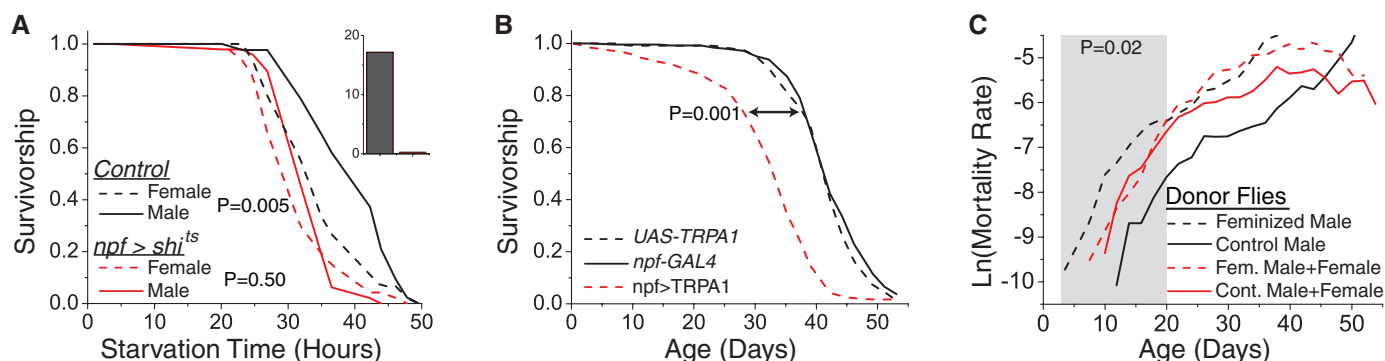


Fig. 4. Aging and physiology are modulated by neural mechanisms of expectation and reward. (A) Inhibition of *npf*-expressing neurons abrogates differences in starvation caused by pheromone exposure. *N* = 43 and 45 for control (*npf-GAL4* only) flies exposed to male or female donor pheromones, respectively (*P* = 0.005, log-rank test). *N* = 48 and 47 for treatment (*npf-GAL4; UAS-shi^{ts}*) flies exposed to male or female donor pheromones, respectively (*P* = 0.50 by log-rank test). Inset as is described in Fig. 2. (B) Activation of *npf*-expressing neurons causes decreased longevity in the absence of pheromone exposure. *npf-GAL4; UAS-shi^{ts}* males (*N* = 239) exhibit significantly shorter life span relative to *UAS-shi^{ts}* only (*N* = 235; *P* ≤ 0.001, log-rank test) and *npf-GAL4* only (*N* = 179; *P* ≤ 0.001, log-rank test) male transgene controls. (C) Mortality rates are reduced when males exposed to female donor pheromone (dashed black line) are given access to excess females (dashed red line; *P* = 0.02 through 20 days of age by Aalen regression). Cohorts consisted of five experimental males together with (i) 30 control donor males (solid black), (ii) 30 feminized donor males (dashed black), (iii) 5 feminized donor males + 25 females (dashed red), or (iv) 5 control donor males + 25 females (solid red); 20 replicate cohorts, totaling 100 experimental flies, were measured for each treatment. (D) Significantly enriched Gene Ontology

pathways and functions whose genes are differentially regulated after pheromone exposure. See table S1 for a complete list of genes with significant changes in expression.

effects have the potential to be influential agents of natural selection (25). Imbalances of expectation and reward may therefore have broad effects on health and physiology in humans and may represent a powerful evolutionary force in nature.

References and Notes

1. J. Apfeld, C. Kenyon, *Nature* **402**, 804–809 (1999).
2. S. Libert *et al.*, *Science* **315**, 1133–1137 (2007).
3. N. J. Linford, T. H. Kuo, T. P. Chan, S. D. Pletcher, *Annu. Rev. Cell Dev. Biol.* **27**, 759–785 (2011).
4. P. C. Poon, T. H. Kuo, N. J. Linford, G. Roman, S. D. Pletcher, *PLOS Biol.* **8**, e1000356 (2010).
5. E. D. Smith *et al.*, *BMC Dev. Biol.* **8**, 49 (2008).
6. J. Alcedo, C. Kenyon, *Neuron* **41**, 45–55 (2004).
7. S. J. Lee, C. Kenyon, *Curr. Biol.* **19**, 715–722 (2009).
8. R. Xiao *et al.*, *Cell* **152**, 806–817 (2013).
9. R. M. Sapolsky, *Science* **308**, 648–652 (2005).
10. L. Partridge, N. H. Barton, *Nature* **362**, 305–311 (1993).
11. L. Partridge, D. Gems, D. J. Withers, *Cell* **120**, 461–472 (2005).
12. J. C. Billeter, J. Atallah, J. J. Krupp, J. G. Millar, J. D. Levine, *Nature* **461**, 987–991 (2009).
13. J. F. Ferveur, *Behav. Genet.* **35**, 279–295 (2005).
14. J. F. Ferveur *et al.*, *Science* **276**, 1555–1558 (1997).
15. M. P. Fernández *et al.*, *PLOS Biol.* **8**, e1000541 (2010).
16. M. C. Larsson *et al.*, *Neuron* **43**, 703–714 (2004).
17. W. Boll, M. Noll, *Development* **129**, 5667–5681 (2002).
18. R. Thistle, P. Cameron, A. Ghorayshi, L. Dennison, K. Scott, *Cell* **149**, 1140–1151 (2012).
19. G. Shohat-Ophir, K. R. Kaun, R. Azanchi, H. Mohammed, U. Heberlein, *Science* **335**, 1351–1355 (2012).
20. S. P. Kalra, J. T. Clark, A. Sahu, M. G. Dube, S. S. Kalra, *Synapse* **2**, 254–257 (1988).
21. M. Heilig, *Neuropeptides* **38**, 213–224 (2004).
22. M. Ashburner, K. Golic, R. S. Hawley, *Drosophila: A Laboratory Handbook* (Cold Spring Harbor Laboratory Press, Cold Spring Harbor, NY, ed. 2, 2004).
23. G. Landis, J. Shen, J. Tower, *Aging* **4**, 768–789 (2012).
24. T. H. Kuo *et al.*, *PLOS Genet.* **8**, e1002684 (2012).
25. J. W. McGlothlin, A. J. Moore, J. B. Wolf, E. D. Brodie 3rd, *Evolution* **64**, 2558–2574 (2010).

Acknowledgments: We thank the members of the Pletcher laboratory for *Drosophila* husbandry, N. Linford for comments on the revision, P. J. Lee for figure illustration, and members of the Dierick and Pletcher laboratories for suggestions on experiments and comments on the manuscript. Supported by NIH grants R01AG030593, TR01AG043972, and R01AG023166, the Glenn Foundation, the American Federation for Aging Research, and the Ellison Medical Foundation (S.D.P.); Ruth L. Kirschstein National Research

Service Award F32AG042253 from the National Institute on Aging (B.Y.C.); NIH grant T32AG000114 (B.Y.C.); NIH grants T32GM007863 and T32GM008322 (Z.M.H.), a Glenn/AFAR Scholarship for Research in the Biology of Aging (Z.M.H.); NSF grant IOS-1119473 (H.A.D.); and the Alexander von Humboldt Foundation and Singapore National Research Foundation grant RF001-363 (J.Y.Y.). This work made use of the *Drosophila* Aging Core of the Nathan Shock Center of Excellence in the Biology of Aging, funded by National Institute on Aging grant P30-AG-013283. RNA-seq expression data are provided in table S1. The funders had no role in study design, data collection and analysis, decision to publish, or preparation of the manuscript. The authors declare that they have no competing interests. C.M.G., T.-H.K., Z.M.H., and S.D.P. conceived and designed the experiments; C.M.G., T.-H.K., Z.M.H., B.Y.C., J.Y.Y., H.A.D., and S.D.P. performed the experiments; C.M.G., T.-H.K., Z.M.H., B.Y.C., J.Y.Y., and S.D.P. analyzed the data; and C.M.G., T.-H.K., J.Y.Y., H.A.D., and S.D.P. wrote the paper.

Supplementary Materials

www.sciencemag.org/content/343/6170/544/suppl/DC1
Materials and Methods
Figs. S1 to S14
Table S1
References (26–28)

16 July 2013; accepted 31 October 2013
Published online 28 November 2013;
10.1126/science.1243339

Savanna Vegetation-Fire-Climate Relationships Differ Among Continents

Caroline E. R. Lehmann,^{1,2*} T. Michael Anderson,³ Mahesh Sankaran,^{4,5} Steven I. Higgins,^{6,7} Sally Archibald,^{8,9} William A. Hoffmann,¹⁰ Niall P. Hanan,¹¹ Richard J. Williams,¹² Roderick J. Fensham,¹³ Jeanine Felfili,¹⁴ Lindsay B. Hutley,¹⁵ Jayashree Ratnam,⁴ Jose San Jose,¹⁶ Ruben Montes,¹⁷ Don Franklin,¹⁵ Jeremy Russell-Smith,¹⁵ Casey M. Ryan,² Giselda Durigan,¹⁸ Pierre Hiernaux,¹⁹ Ricardo Haidar,¹⁴ David M. J. S. Bowman,²⁰ William J. Bond²¹

Ecologists have long sought to understand the factors controlling the structure of savanna vegetation. Using data from 2154 sites in savannas across Africa, Australia, and South America, we found that increasing moisture availability drives increases in fire and tree basal area, whereas fire reduces tree basal area. However, among continents, the magnitude of these effects varied substantially, so that a single model cannot adequately represent savanna woody biomass across these regions. Historical and environmental differences drive the regional variation in the functional relationships between woody vegetation, fire, and climate. These same differences will determine the regional responses of vegetation to future climates, with implications for global carbon stocks.

Savannas cover 20% of the global land surface and account for 30% of terrestrial net primary production (NPP) and the vast majority of annual global burned area (1–3). Savanna ecosystem services sustain an estimated one-fifth of humans, and savannas are also home to most of the remaining megafauna (4). Tropical savanna is characterized by the codominance of C₃ trees and C₄ grasses that have distinct life forms and photosynthetic mechanisms that respond differently to environmental controls (4). Examples include the differing responses of these functional types to temperature and atmospheric CO₂ concentrations, predisposing savannas to altera-

tions in structure and extent in the coming century (4–6).

Tropical savannas are defined by a continuous C₄ herbaceous layer, with a discontinuous stratum of disturbance-tolerant woody species (7). Although savanna tree cover varies greatly in space and time (8, 9), the similarities in structure among the major savanna regions of Africa, Australia, and South America have led to an assumption that the processes regulating vegetation structure within the biome are equivalent (10, 11). Current vegetation models treat savannas as a homogenous entity (12, 13). Recent studies, however, have highlighted differences

in savanna extent across continents (14, 15), and it remains unknown how environmental drivers interact to determine the vegetation dynamics and limits of the biome (10, 14, 15).

We sought universal relationships between savanna tree basal area (TBA, m² ha^{−1}), a key metric of woody biomass within an ecosystem, and the constraints imposed by resource availability (moisture and nutrients), growing conditions (temperature), and disturbances (fire). Ecologists have devoted considerable effort to the identification of universal relationships to describe the structure and function of biomes (16). However, it has not been clear whether such relationships exist. Any such relationships may be confounded by the unique evolutionary and environmental histories of each ecological setting (11).

Across Africa and Australia, TBA scales similarly with rainfall, but the intercepts and the 95th quantile differ substantially (Fig. 1, A to C). On average, at a given level of moisture availability, TBA is higher in Africa and lower in Australia. However, in South America there is almost no relationship between rainfall and TBA, which is probably in part attributable to the narrow range of rainfall that savanna occupies on this continent (Fig. 2). Further, across the observed range of rainfall, the upper limits of TBA increase linearly with effective rainfall for Australian savannas (Fig. 1B) but show a saturating response in African and South American savannas (Fig. 1, A and C). When TBA is used to estimate above-ground woody biomass (AWB) (17), the large differences in intercepts between Africa and Australia are reduced but substantial differences in the limits remain (fig. S1, A to C). By con-

verting TBA to AWB, we attempted to quantify how variation in biomass allometry, modal tree size, maximum tree size, and the mean number of stems per hectare affects our interpretation of the functional relationships between savanna woody vegetation, climate, and fire. These regional differences imply that savanna vegetation dynamics are region-specific and are influenced by both regional climates and the allometric traits specific to the woody species of each region (17). We interpret the fact that so few sites reach the maximum values as being partially a result of variation in soil properties and disturbance processes. Fire is a prevalent agent of vegetation change, as shown by experimental, landscape, and modeling studies (8, 15, 18).

To investigate the drivers underlying the observed continental differences in TBA, we constructed a conceptual model of the determinants of woody vegetation structure based on a priori hypotheses about the direct and indirect effects of climate, soils, and fire on TBA (Fig. 3A) (1, 8, 10, 14). The model estimates the effects of resource availability (moisture availability and soil properties), growing conditions (temperature), and disturbance (fire) on TBA. Globally, data availability on herbivore abundance is sparse and unreliable and, as a result, we could not include herbivore abundance as a predictor (17). We used our conceptual model to develop a series of structural equation models (SEMs) to quantify the response of TBA to functionally related composite

variables (17). Composite variables in our analysis were (i) moisture availability, composed of effective rainfall, rainfall seasonality, and Foley's drought index; (ii) soil properties, composed of percent of organic carbon and percent of sand; and (iii) temperature, composed of mean annual temperature and annual temperature range [described in detail in (17)]. Specifically, our model allowed us to test the extent to which TBA is directly determined by climate and edaphic factors, versus the extent to which TBA is indirectly effected by these factors through their effects on fire.

Our results highlight that interactions among moisture availability, fire, and TBA are a defining characteristic of savannas. Increasing moisture availability simultaneously promotes increases in both TBA and grass-fueled fire frequencies (Fig. 3, B to D). As moisture availability increases, mean TBA can approach a maximum value, which is different in each region (Fig. 1, A to C). Fire, by preventing the accumulation of TBA, generally maintains TBA below a maximum value.

Therefore, on a qualitative level there is universality in savanna vegetation dynamics, evidenced by our analysis of each region identifying the same network of factors influencing TBA. The exception was that soil properties influenced TBA in South America and did not influence fire frequency, in contrast to Africa and Australia.

Interactions between moisture, fire, and TBA are unequal across continents. Moisture availability explains approximately two to three times more of the variation in both TBA and fire frequency in Africa and Australia as compared to South America (Fig. 3). Similarly, the negative effect of fire explains 1.5 to 2.5 times more of the variation in TBA in Africa as compared with South America or Australia, with only a very weak effect of fire on TBA in Australia (Fig. 3). Our findings are consistent with studies that have shown that the importance of the effect of fire on TBA is conditional on seedling and sapling growth rates, fire resilience traits, and fire intensity (10, 18, 19). Woody plant growth rates determine the post-fire rates of TBA accumulation,

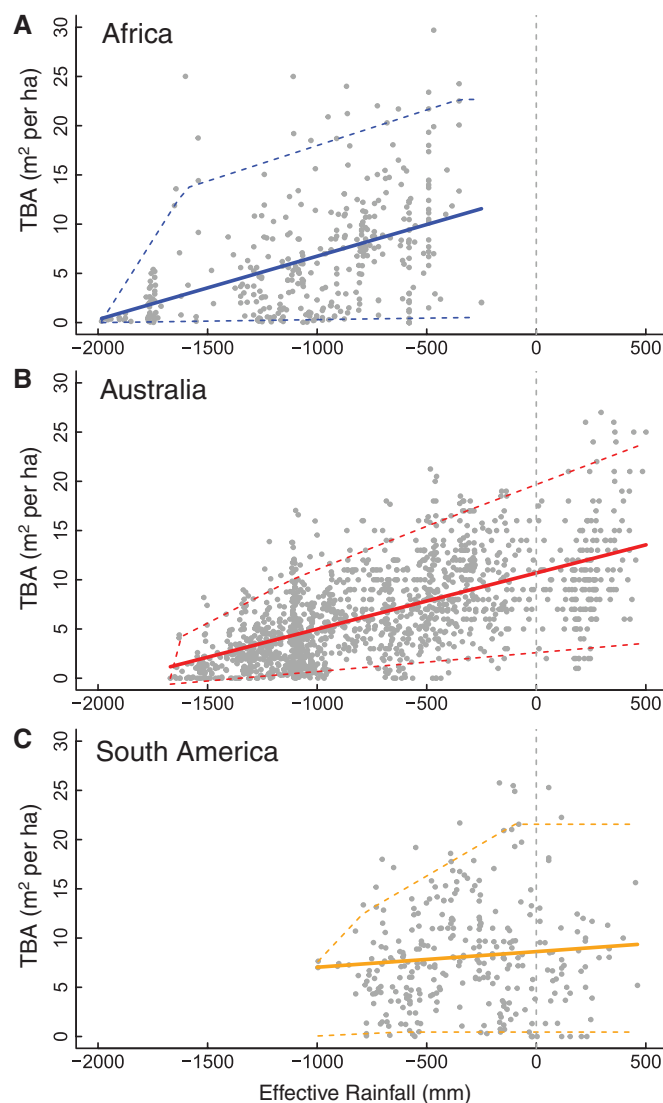


Fig. 1. Change in TBA of savannas relative to effective rainfall. The relationships between TBA and effective rainfall (in millimeters per year) across (A) Africa [$r^2 = 0.203$, $F(1, 363) = 92.4$, P value = <0.001]; (B) Australia [$r^2 = 0.385$, $F(1, 1485) = 930.9$, P value = <0.001]; and (C) South America [$r^2 = 0.008$, $F(1, 300) = 2.6$, P value = 0.111] are shown. Also depicted are the piecewise quantile fits of the 5th and 95th quantiles.

¹Department of Biological Sciences, Macquarie University, New South Wales 2109, Australia. ²School of GeoSciences, University of Edinburgh, Edinburgh EH9 3JN, UK. ³Department of Biology, Wake Forest University, 226 Winston Hall, Box 7325 Reynolda Station, Winston-Salem, NC 27109, USA. ⁴National Centre for Biological Sciences, Tata Institute of Fundamental Research, Gandhi Krishi Vignana Kendra, Bellary Road, Bangalore 560 065, India. ⁵School of Biology, University of Leeds, Leeds LS2 9JT, UK. ⁶Institute for Physical Geography, J. W. Goethe University Frankfurt am Main, Altenhöferallee 1, 60438 Frankfurt, Germany. ⁷Department of Botany, University of Otago, Post Office Box 56, Dunedin 9054, New Zealand. ⁸Natural Resources and the Environment, Council for Scientific and Industrial Research, Post Office Box 395, Pretoria, South Africa. ⁹School of Animal, Plant and Environmental Sciences, University of the Witwatersrand, Post Office WITS, 2050 Johannesburg, South Africa. ¹⁰Department of Plant Biology, North Carolina State University, Raleigh, NC 27695, USA. ¹¹Geographic Information Science Centre of Excellence, South Dakota State University, Brookings, SD 57007, USA. ¹²Commonwealth Scientific and Industrial Research Organisation Ecosystem Sciences, Tropical Ecosystems Research Centre, PMB 44 Winnellie, Northern Territory 0822, Australia. ¹³School of Biological Sciences, University of Queensland, Brisbane, Queensland 4072, Australia. ¹⁴Forestry Department, University of Brasília, Brasília 70919-970, DF—Brazil. ¹⁵Research Institute for Environment and Livelihoods, Charles Darwin University, Casuarina, Northern Territory 0810, Australia. ¹⁶Centro de Ecología, Instituto Venezolano de Investigaciones Científicas, Apartado 21827, Caracas 1020-A, Venezuela. ¹⁷Departamento de Estudios Ambientales, Universidad Simón Bolívar, Apartado 89000, Caracas 1080-A, Venezuela. ¹⁸Laboratório de Ecologia e Hidrologia Florestal, Floresta Estadual de Assis, Instituto Florestal, 19802-970 - Assis - SP Brazil. ¹⁹Géosciences Environnement Toulouse Observatoire Midi-Pyrénées, Université de Toulouse, CNRS 31401, Toulouse, France. ²⁰School of Plant Science, University of Tasmania, Hobart, Tasmania 7001, Australia. ²¹Department of Botany, University of Cape Town, Rondebosch 7700, South Africa.

*Corresponding author. E-mail: c.e.r.lehmann@gmail.com

whereas fire frequency and intensity are a product of grassy fuels (19). Differences among continents in the effect of fire on TBA probably reflect differences in woody plant traits and the fuel loads and flammability of C_4 grasses.

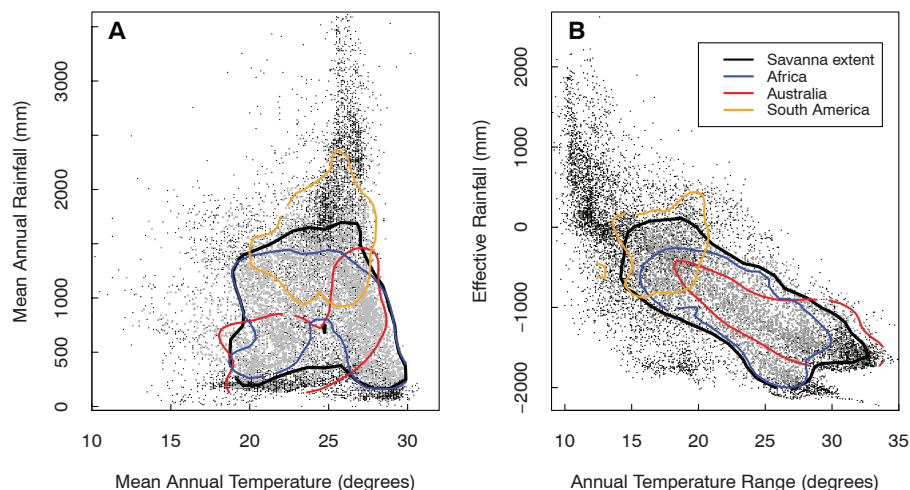
In Africa, moisture availability has a strongly positive relationship with fire, implying that fire and the accumulation of C_4 grasses in African savanna are more tightly controlled by

yearly variation in the timing and amount of rainfall than in either Australia or South America. These cascading relationships appear weaker in Australia, and less so in South America, and can be partially explained by the differences in the climatic domain occupied by the savanna of each region (Fig. 2). Thus, continental differences in TBA and AWB relate to a combination of differences in the climatic drivers of fire fre-

quency and intensity, as well as to differences in the growth and fire resilience traits of woody plants.

In Africa and Australia, temperature has a strong effect on fire (Fig. 3, B to C, and tables S1 and S2), probably determined by a composite of two factors. First, at warmer sites, fuels are more likely to cure, facilitating more frequent fire (3). Second, the physiology of C_4 grasses means

Fig. 2. Climate domain of savannas in Africa, Australia, and South America. The savanna climate domain relative to (A) mean annual rainfall versus mean annual temperature and (B) effective rainfall versus annual temperature range. Black points represent all vegetated 0.5° grid cells within 30° of the equator across Africa, Australia, and South America. Gray points represent all 0.5° grid cells where savanna is present as in (14). Lines represent the 95th quantile of the density of these points for savanna on each continent.



A Conceptual model

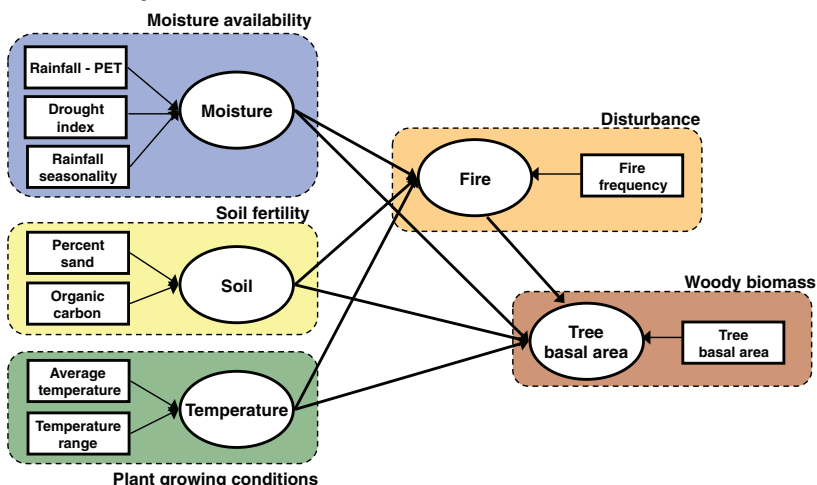
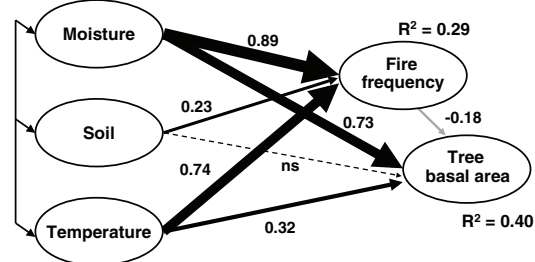
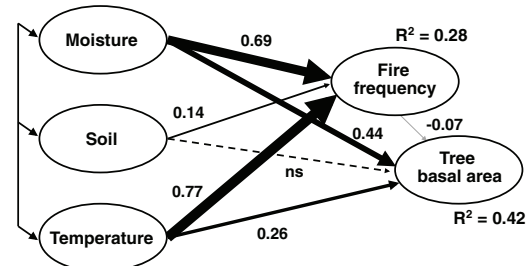


Fig. 3. Structural equation modeling of TBA for Africa, Australia, and South America. Structural equation modeling of TBA for Africa, Australia, and South America. (A) Conceptual model depicting theoretical relationships among moisture availability, soil fertility, plant growing conditions (temperature), and disturbance (fire frequency), and their effects on TBA either directly or indirectly as mediated by fire frequency. (B to D) The final model for each continent. Values associated with arrows are absolute path strengths, which combine positive and negative effects of indicators into a composite effect (17); the arrow thickness is proportional to the absolute path strength. The arrows from fire to TBA represent standardized path coefficients and are depicted in gray to express their negative impacts. Full models results are presented in (17).

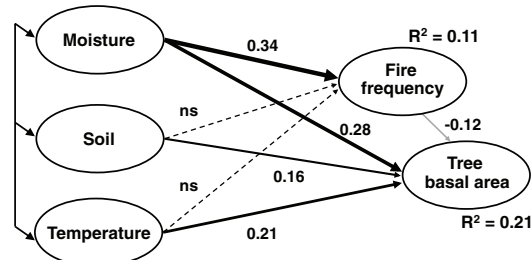
B Africa



C Australia



D South America



that they have a higher temperature optima for photosynthesis and growth (relative to C_3 plants), facilitating the potential for rapid biomass accumulation in hot seasonally dry environments (4, 20), conditions that are more extensively found in the savannas of Africa and Australia (Fig. 2).

In South America, we found a limited explanation of TBA (Fig. 3D). This is consistent with previous studies that have examined savanna extent and found that the limited explanatory power was not simply a product of South American savanna being wetter (14, 15). A previous study found that if the climatic range of South American savanna were projected to Africa or Australia, the global extent of savanna would diminish (14). One potential explanation is that acid and infertile soils may act as constraints on both the distribution and vegetation structure of South American savanna, as discussed in numerous studies (14, 15, 21), although the quality of global soils data limits any ability to detect the regional influence of soils.

Taken together, our findings illustrate how a common set of environmental drivers shape savannas across the globe in qualitatively similar ways. However, the quantitative details of how these factors interact (Fig. 3) and the climatic domains occupied (Fig. 2) differ substantially among continents, so that for practical purposes we must dismiss the use of a single global model relating savanna TBA and AWB to environmental drivers. Instead, we make a case for

regionally calibrated models to investigate the response of savanna vegetation to climate change. For example, we show that our global analysis, in which the role of continent is ignored, fails to capture regional differences in the predicted response to a hypothetical 4°C increase in mean annual temperature (Fig. 4). In particular, for Africa our global analysis predicts a net decrease in woody biomass, whereas the regional model predicts a net increase (Fig. 4) due to fire-temperature interactions within our model. Our regional analyses show that changing climates could set these three savanna regions on different paths of vegetation change.

Why are these structurally similar ecosystems in different geographic regions regulated in different ways by the same environmental drivers? The answer may lie in the evolutionary history of this biome. Tropical savanna is relatively new, originating with the global expansion of C_4 grasses 3 to 8 million years before the present (22). When savannas arose, the southern continents had been separated for >40 million years. C_4 grasses and the coincident increase in fire frequency (and also megaherbivory) exerted novel selective pressures on regional woody floras, while the phylogenetic and geographic distance between savanna regions led to the development of analogous but not identical solutions in woody plants to these new selective pressures. Today, savanna tree canopies are dominated by Myrtaceae in Australia and in Africa by Mimosaceae, Combretaceae, and

Caesalpiniaceae (23). In South America, there is a mix of dominance, with savanna taxa derived from forests in the past 10 million years (24). These distantly related woody taxa are disturbance-tolerant but differ in their phenology (23), growth rates (19), resilience to fire (19), canopy architecture, and biomass allometry (17).

The global ensemble of regions constituting modern savannas has, over millennia, converged on a similar open-canopy vegetation structure due to the evolution and invasion of C_4 grasses (22) and the resulting ubiquity of disturbance (3, 14). The environmental space occupied by modern savanna allows for the multiple interactions among moisture availability, temperature, fire, and vegetation. However, the functional and architectural traits of the woody species dominating each region determine the form and strength of the functional relationships to environmental drivers. Our data indicate that each savanna region may respond differently to changes in climate. Currently, remote sensing evidence suggests differing trajectories of change in Australian and southern African savannas (9, 25). The one climate-one vegetation paradigm is an underpinning of many global vegetation models (12, 13), and these models are a primary tool for anticipating the response of vegetation to future climates (5, 26), but are based on a notion that the same environmental controls will produce the same vegetation structure irrespective of environmental and evolutionary history. We show

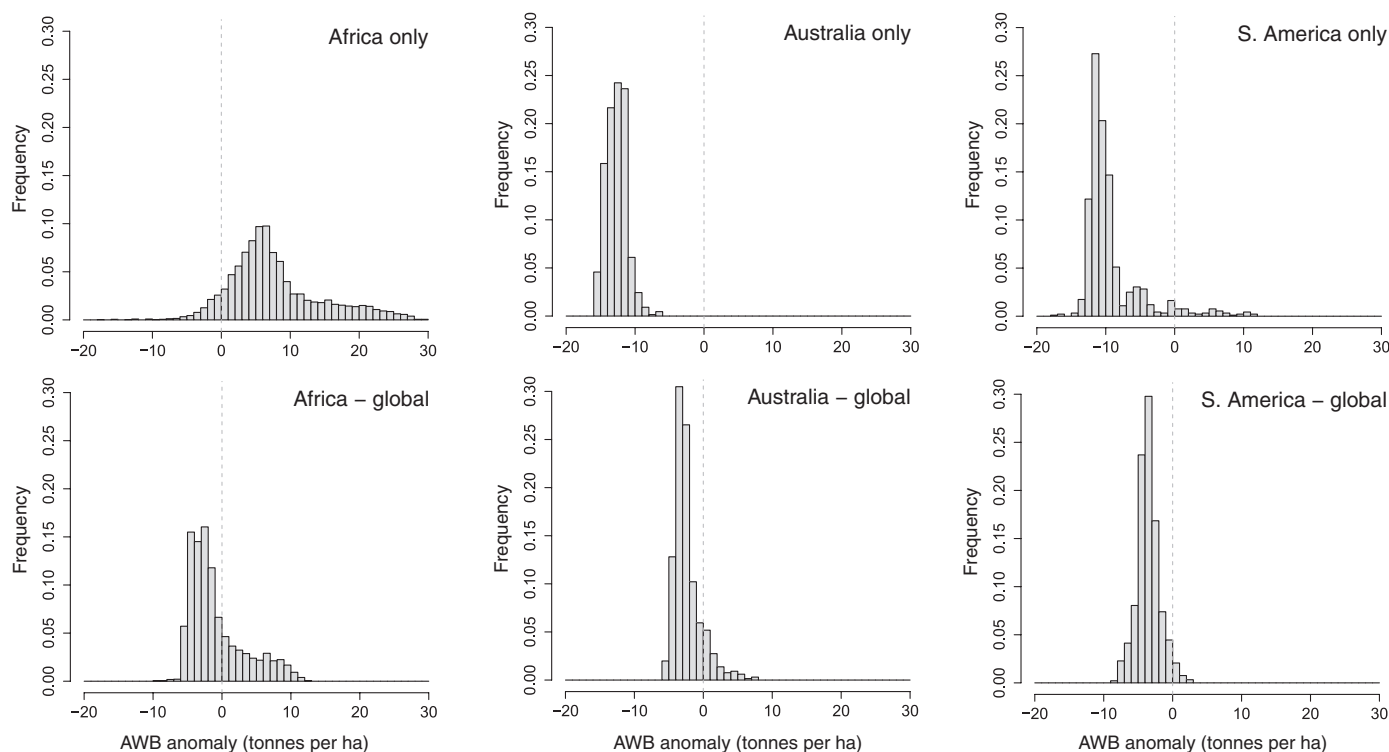


Fig. 4. Hypothetical shifts in AWB on three continents relative to a 4°C increase in mean annual temperature. Frequency distributions of the predicted anomalies in AWB (metric tons per hectare) with a 4°C increase in mean

annual temperature, where a region-specific model and a global model are compared. Distributions are calculated at a 0.5° resolution. The global model shows the results of an analysis where “continent” is ignored (table S4).

that the convergence of structure in savanna conceals substantial differences in the relationships between savanna woody vegetation, climate, and fire. Just as the regional evolutionary and environmental histories underpin differences in these relationships, these same differences will determine the contemporary vegetation response of each region to future climates.

References and Notes

1. R. J. Scholes, S. R. Archer, *Annu. Rev. Ecol. Syst.* **28**, 517–544 (1997).
2. C. B. Field, M. J. Behrenfeld, J. T. Randerson, P. Falkowski, *Science* **281**, 237–240 (1998).
3. S. Archibald, C. E. R. Lehmann, J. L. Gómez-Dans, R. A. Bradstock, *Proc. Natl. Acad. Sci. U.S.A.* **110**, 6442–6447 (2013).
4. W. J. Bond, G. F. Midgley, *Glob. Change Biol.* **6**, 865–869 (2000).
5. S. I. Higgins, S. Scheiter, *Nature* **488**, 209–212 (2012).
6. I. C. Prentice, S. P. Harrison, P. J. Bartlein, *New Phytol.* **189**, 988–998 (2011).
7. J. Ratnam *et al.*, *Glob. Ecol. Biogeogr.* **20**, 653–660 (2011).
8. M. Sankaran *et al.*, *Nature* **438**, 846–849 (2005).
9. B. P. Murphy, C. E. R. Lehmann, J. Russell-Smith, M. J. Lawes, *J. Biogeogr.* **41**, 133–144 (2014).
10. W. J. Bond, *Annu. Rev. Ecol. Evol. Syst.* **39**, 641–659 (2008).
11. A. K. Knapp *et al.*, *Front. Ecol. Environ.* **2**, 483–491 (2004).
12. S. Sith *et al.*, *Glob. Change Biol.* **9**, 161–185 (2003).
13. R. Fisher *et al.*, *New Phytol.* **187**, 666–681 (2010).
14. C. E. R. Lehmann, S. A. Archibald, W. A. Hoffmann, W. J. Bond, *New Phytol.* **191**, 197–209 (2011).
15. A. C. Staver, S. Archibald, S. A. Levin, *Science* **334**, 230–232 (2011).
16. J. H. Lawton, *Oikos* **84**, 177 (1999).
17. Materials and methods and other information are available in the supplementary materials on Science Online.
18. S. I. Higgins, W. J. Bond, W. S. W. Trollope, *J. Ecol.* **88**, 213–229 (2000).
19. W. A. Hoffmann *et al.*, *Ecol. Lett.* **15**, 759–768 (2012).
20. B. Ripley, G. Donald, C. P. Osborne, T. Abraham, T. Martin, *J. Ecol.* **98**, 1196–1203 (2010).
21. M. Haridasan, in *Nature and Dynamics of Forest-Savanna Boundaries*, P. A. Furley, J. Proctor, J. A. Ratter, Eds. (Chapman & Hall, London, 1992), pp. 171–184.
22. E. J. Edwards *et al.*, *Science* **328**, 587–591 (2010).
23. D. M. J. S. Bowman, L. Prior, *Aust. J. Bot.* **53**, 379 (2005).
24. M. F. Simon *et al.*, *Proc. Natl. Acad. Sci. U.S.A.* **106**, 20359–20364 (2009).
25. B. J. Wigley, W. J. Bond, M. T. Hoffman, *Glob. Change Biol.* **16**, 964–976 (2010).
26. G. B. Bonan, *Science* **320**, 1444–1449 (2008).

Acknowledgments: C.L. conceived the project and led the writing; C.L., T.M.A., M.S., S.I.H., W.A.H., N.H., J.F., G.D., and S.A. compiled the data; and C.L., T.M.A., M.S., and S.I.H. analyzed the data. All authors provided new data and contributed to the writing and/or intellectual development of the manuscript. M. Crisp, B. Medlyn, and R. Gallagher provided manuscript feedback. Data used in this study are available in the supplementary materials and at <http://modis.gsfc.nasa.gov/>, <http://www.worldclim.org/>, and www.fao.org/nr/land/soils/harmonized-world-soil-database/en/.

Supplementary Materials

www.sciencemag.org/content/343/6170/548/suppl/DC1
Materials and Methods
Figs. S1 to S4
Tables S1 to S5
References (27–188)
Data Sets S1 and S2

18 October 2013; accepted 18 December 2013
10.1126/science.1247355

Effector Specialization in a Lineage of the Irish Potato Famine Pathogen

Suomeng Dong,¹ Remco Stam,^{1*} Liliana M. Cano,¹ Jing Song,^{2†} Jan Sklenar,¹ Kentaro Yoshida,¹ Tolga O. Bozkurt,¹ Ricardo Oliva,^{1‡} Zhenyu Liu,² Miaoying Tian,^{2§} Joe Win,¹ Mark J. Banfield,³ Alexandra M. E. Jones,^{1||} Renier A. L. van der Hoorn,^{4,5} Sophien Kamoun^{1¶}

Accelerated gene evolution is a hallmark of pathogen adaptation following a host jump. Here, we describe the biochemical basis of adaptation and specialization of a plant pathogen effector after its colonization of a new host. Orthologous protease inhibitor effectors from the Irish potato famine pathogen, *Phytophthora infestans*, and its sister species, *Phytophthora mirabilis*, which is responsible for infection of *Mirabilis jalapa*, are adapted to protease targets unique to their respective host plants. Amino acid polymorphisms in both the inhibitors and their target proteases underpin this biochemical specialization. Our results link effector specialization to diversification and speciation of this plant pathogen.

The potato blight pathogen, *Phytophthora infestans*, is a recurring threat to world agriculture and food security. This funguslike oomycete traces its origins to Toluca Valley, Mexico, where it naturally infects wild *Solanum* plants (1). In central Mexico, *P. infestans* co-occurs with closely related species in a tight phylogenetic clade known as clade 1c. These species evolved through host jumps followed by adaptive specialization on plants belonging to different botanical families (2, 3) (fig. S1). One species, *Phytophthora mirabilis*, is a pathogen of four-o'clock (*Mirabilis jalapa*). It split from *P. infestans* about 1300 years ago (1), and the two species have since specialized on their *Solanum* and *Mirabilis* hosts. Adaptive evolution after the host jump has left marks on the genomes of *P. infestans* and *P. mirabilis* (3). Comparative genomics analyses revealed signatures of accelerated evolution, structural polymorphisms, and

positive selection in genes occurring in repeat-rich genome compartments (3). In total, 345 genes induced within plants show signatures of positive selection between the two sister species (3). These include 82 disease effector genes, rapidly evolving determinants of virulence that act on host target molecules. We lack a molecular framework to explain how plant pathogen effectors adapt and specialize on new hosts, even though this process affects pathogen evolution and diversification (4–6).

To gain insight into the molecular patterns of host adaptation after host jumps, we selected the cystatinlike protease inhibitor EPIC1, an effector protein of *P. infestans* that targets extracellular (apoplastic) defense proteases of the *Solanum* hosts (7, 8). The *epiC1* gene and its paralogs *epiC2A* and *epiC2B* evolved relatively recently in the *P. infestans* lineage, most likely as a duplication of the conserved *Phytophthora*

gene *epiC3* (7) (Fig. 1). To reconstruct the evolution of these effectors in the clade 1c species, we aligned the *epiC* gene cluster sequences, performed phylogenetic analyses, and calculated variation in selective pressure across the phylogeny (Fig. 1, fig. S2, and table S1) (9). We detected a signature of positive selection in the branch of *PmepiC1*, the *P. mirabilis* ortholog of *P. infestans* *epiC1* [nonsynonymous to synonymous ratio (ω) = 2.52] (Fig. 1B). This is consistent with our hypothesis that *PmEPIC1* evolved to adapt to a *M. jalapa* protease after *P. mirabilis* diverged from *P. infestans*.

To test our hypothesis, we first determined the inhibition spectra of the EPIC effectors using DCG-04 protease profiling, a method based on the use of a biotinylated, irreversible protease inhibitor that reacts with the active site cysteine of papainlike proteases in an activity-dependent

¹The Sainsbury Laboratory, Norwich Research Park, Norwich NR4 7UH, UK. ²Department of Plant Pathology, Ohio Agricultural Research and Development Center, The Ohio State University, Wooster, OH 44691, USA. ³Department of Biological Chemistry, John Innes Centre, Norwich Research Park, Norwich NR4 7UH, UK. ⁴The Plant Chemetics Laboratory, Department of Plant Sciences, University of Oxford, Oxford OX1 3RB, UK. ⁵Plant Chemetics Laboratory, Max Planck Institute for Plant Breeding Research, 50829 Cologne, Germany.

*Present address: Division of Plant Sciences, University of Dundee, Invergowrie, Dundee DD2 5DA, UK.

†Present address: Center for Proteomics and Bioinformatics, School of Medicine, Case Western Reserve University, Cleveland, OH 44106 USA.

‡Present address: Plant Breeding, Genetics, and Biotechnology, International Rice Research Institute (IRRI), Los Baños, Laguna, Philippines.

§Present address: Department of Plant and Environmental Protection Sciences, University of Hawaii, Honolulu, HI 96822, USA.

||Present address: School of Life Sciences, Gibbet Hill Campus, The University of Warwick, Coventry, CV4 7AL, UK.

¶Corresponding author. E-mail: sophien.kamoun@tsl.ac.uk

manner (7, 10). We assayed effector activities against the tomato (*Solanum lycopersicum*) papainlike cysteine proteases RCR3, PIP1, and C14, which have been previously implicated in pathogen defense (7, 8, 11, 12). RCR3 was inhibited by effectors EPIC1, PipeEPIC1, and EPIC2B but not by PmEPIC1 (fig. S3). C14 was inhibited by all four effector proteins. PIP1 was inhibited by EPIC2B but not by the three EPIC1 effectors (fig. S3). The reduced activity of PmEPIC1 on RCR3 is not due to instability, given that this protein remained as stable as EPIC1 after a 2-hour incubation in plant apoplastic extracts (fig. S4).

P. infestans originates from central Mexico, where it naturally infects the wild potato species *Solanum demissum*, *S. verrucosum*, and *S. stoloniferum* (2). To challenge our model with ecologically relevant host proteases, we assayed five RCR3 homologs from these three wild potato species for their interactions with pathogen effectors EPIC1 and PmEPIC1 (fig. S5). For all three species, EPIC1 was a better inhibitor of the potato RCR3 proteases than PmEPIC1 (fig. S6). This confirms that the two orthologous effectors have evolved different biochemical activities on *Solanum* RCR3 proteases.

To identify the target of PmEPIC1 in *M. jalapa*, the natural Mexican host of *P. mirabilis*, we co-incubated *M. jalapa* intercellular fluids with the EPIC1 proteins and analyzed the interactions by coimmunoprecipitation and tandem mass spectrometry (fig. S7). We compared the peptides detected with an expressed sequence tag database generated from *P. mirabilis*-infected leaves of *M. jalapa* (tables S2 and S3 and fig. S7). We con-

sistently detected peptides matching two RCR3-related cysteine proteases. We termed the two proteases *Mirabilis* RCR3-like protease 1 and 2 (MRP1 and MRP2). We recovered the full-length proteases and found that they share ~60% amino acid sequence similarity with *Solanum* RCR3 and carry common signatures of the papainlike cysteine protease SAG12 subfamily (13) (fig. S8).

We transiently expressed MRP1 and MRP2 proteins as a fusion to the histidine (His) epitope tag in *M. jalapa* leaves. However, only MRP2-His can be expressed and enriched (fig. S9A). Activity profiling of the MRP2-His protein revealed that it can be labeled with the cysteine protease probe DCG-04 (10), and this labeling can be blocked by preincubation with the irreversible cysteine protease inhibitor E-64, which indicates that MRP2 is an active cysteine protease (fig. S9B).

To independently confirm the interaction, we performed coimmunoprecipitation experiments on enriched MRP2-His incubated with FLAG epitope-tagged EPIC proteins (9). Both PmEPIC1 and EPIC1 coimmunoprecipitated with MRP2-His, and the interaction could be outcompeted by E-64, which suggests that the cystatinlike effectors most likely bind to the active site of the protease (fig. S10). We then determined the extent to which the EPIC proteins inhibit MRP2-His using the DCG-04 activity profiling assay. This revealed that PmEPIC1 is more effective than EPIC1 at inhibiting MRP2-His, results counter to the activity of these effectors on *Solanum* RCR3 proteases (Fig. 2A). To further investigate these

findings, we conducted a time-course DCG-04 labeling experiment. Here too, the effectors showed differential inhibition activities on MRP2-His and *S. demissum* RCR3^{dms3}-His (Fig. 2B). PmEPIC1 reduced DCG-04 labeling of MRP2-His for up to 60 min but had no noticeable effect on RCR3^{dms3}. EPIC1, in contrast, had opposite effects on DCG-04 labeling of the two proteases, as it showed stronger inhibition of RCR3^{dms3}-His than MRP2-His. These findings reveal an adaptive biochemical phenotype, with the effectors displaying increased inhibition of protease targets from their respective host plants.

We resurrected (14) the ancestral EPIC1 gene to test the hypothesis that the activity spectrum of EPIC1 has shifted over time. We inferred the sequence for ancestral EPIC1 using the maximum likelihood method, synthesized the corresponding gene, and determined the inhibition spectrum of the resurrected protein (fig. S11) (9). Ancestral EPIC1 displayed activities similar to those of modern EPIC1, i.e., stronger inhibition of RCR3^{dms3} than MRP2 (fig. S11). This indicates that the ability of PmEPIC1 to inhibit MRP2 and its inability to inhibit *Solanum* RCR3s were not characteristic of the ancestral protein.

To determine which of the variant amino acids underpin the alterations in specificity, we first took advantage of the crystal structure of tarocystatin in complex with a papain protease (Protein Data Bank ID: 3MIA) (fig. S12A). Structure-based sequence alignments of PmEPIC1 or EPIC1 with tarocystatin suggest that the inhibitors share a similar fold and are likely to bind proteases through three regions, two of which are

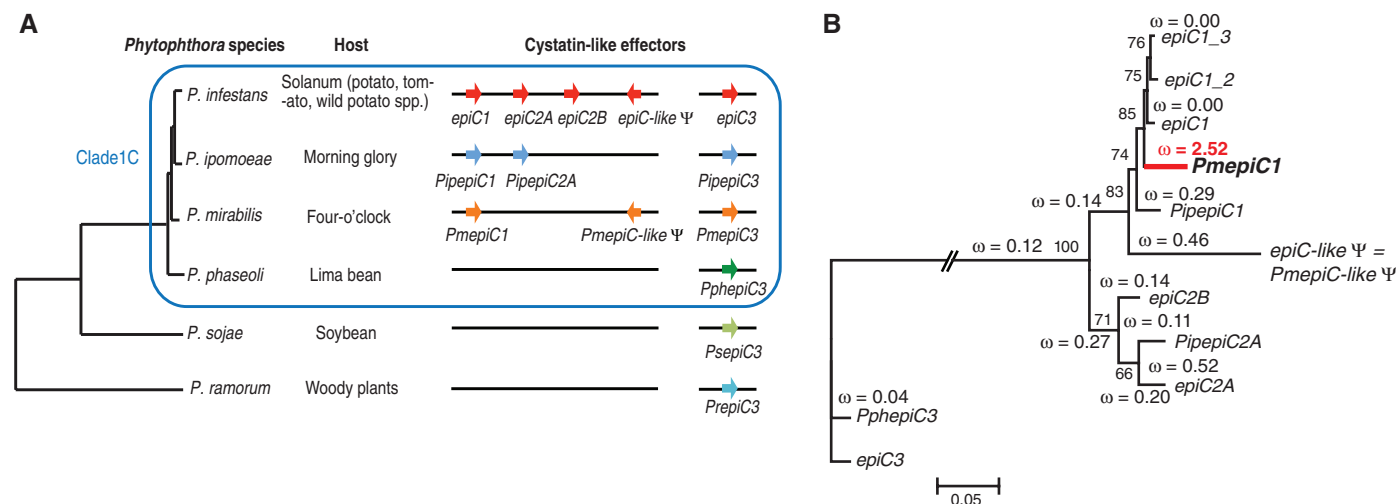
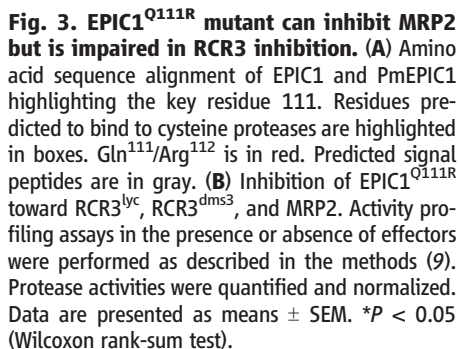


Fig. 1. Evolution of the *epiC1* gene family in *Phytophthora* clade 1c sister species. (A) Phylogeny, host range, and the presence or absence of polymorphisms of the *epiC1* gene family of *Phytophthora* clade 1c sister species. The *Phytophthora* phylogenetic tree was adapted from a previous publication (15). The positions of *P. mirabilis* and *P. ipomoeae* as closest to *P. infestans* remain to be resolved. *P. sojae* and *P. ramorum* are species from remote clades that are shown for comparison and as outgroups. The presence or absence of *epiC* genes in clade 1c is a simplified diagram of fig. S2. Arrows with colors indicate the presence of the *epiC1* homolog in genomes. The polymorphism in *Phytophthora* clade 1c and

other *Phytophthora* species is consistent with the recent emergence of *epiC1* and 2 from duplication of the widespread *epiC3* gene (7). (B) Selection analysis of the *epiC1* family genes in *Phytophthora* clade 1c. The phylogenetic tree was rooted with conserved *P. infestans* gene *epiC3* using PhyML software (9). Rates of nonsynonymous to synonymous ratio (ω) across branches were investigated with the branch model using the codeml function provided by PAML software (9). Note that the PmEPIC1 branch is the only one with a strong signature of positive selection ($\omega = 2.52$). Ψ indicates a pseudogene that has lost its ability to produce the full-length protein.

Inhibition activity of EPIC1 and PmEPIC1 toward *Solanum* RCR3 and *M. jalapa* MRP2 proteases. Activity profiling assays in the presence or absence of effectors revealed that FLAG-EPIC1, but not FLAG-PmEPIC1, inhibits RCR3^{lyc} and RCR3^{dms3}-His and that FLAG-PmEPIC1 exhibits stronger inhibition of MRP2-His than FLAG-EPIC1 does. Equal amounts of *Nicotiana benthamiana* apoplastic fluid containing RCR3^{lyc}-His and RCR3^{dms3}-His or MRP2-His enriched from *M. jalapa* apoplastic fluids were preincubated with excess E-64 (200 μ M) or recombinant EPIC1 or PmEPIC1 (4 μ M) for 1 hour, followed by DCG-04 (100 nM) labeling for 30 min (9). Biotinylated proteases were detected by streptavidin-horseradish peroxidase (Strep. HRP). α -His, antibody against histidine. Protease activities were quantified, normalized, and presented as means \pm SEM. * P < 0.05 (Wilcoxon rank-sum test). (B) Time-course inhibition assay confirms inhibition specificity of EPIC1 and PmEPIC1. Apoplastic fluids containing RCR3^{dms3}-His and enriched MRP2-His proteins were preincubated with an excess of FLAG-EPIC1 and FLAG-PmEPIC1 (4 μ M) for 1 hour, followed by addition of DCG-04 (200 nM) to label the proteases. Reactions were stopped at different time points to record inhibition of protease activity over time.



A

Sequence alignment of PmEPIC1 (120 aa) and E. coli proteins. Domains are indicated: SP (Signal Peptide), N-terminal trunk (residues 20-30), Loop1 (residues 70-80), and Loop2 (residues 100-110). Residues Q111 and R112 are highlighted in red in the Loop2 domain.

B

Protease activity assays. Top: Western blots for Strep-HRP and α-His. Bottom: Bar graphs showing normalized protease activity for MRP2, RCR3^{dms3}, and RCR3^{lyc} strains under various conditions (Buffer, E-64, PmEPIC1, EPIC1, EPIC1^{Q111R}). Error bars represent standard deviation. Asterisks (*) indicate significant differences (p < 0.05).

Strain	Condition	Normalized protease activity
MRP2 (n=6)	Buffer	1.0
	E-64	0.02
	PmEPIC1	0.3
	EPIC1	0.65*
	EPIC1 ^{Q111R}	0.45
RCR3 ^{dms3} (n=4)	Buffer	1.0
	E-64	0.02
	PmEPIC1	0.95
	EPIC1	0.25
	EPIC1 ^{Q111R}	0.9*
RCR3 ^{lyc} (n=6)	Buffer	1.0
	E-64	0.02
	PmEPIC1	0.85
	EPIC1	0.15
	EPIC1 ^{Q111R}	0.75*

polymorphic between the orthologous effectors (fig. S12). Next, we modified the proteins to determine which of the polymorphic residues contribute to the difference in biochemical activity. Protease inhibition assays with chimeric proteins and with single-site mutants revealed that the Gln-Arg polymorphism at position 111 is critical for specificity (Fig. 3 and figs. S13 and S14). In particular, EPIC1^{Q111R}, carrying a Gln-to-Arg mutation, most closely recapitulated the function of PmEPIC1, with more effective inhibition of the *M. jalapa* protease MRP2 and less inhibition of the *Solanum* proteases RCR3^{dms3} and RCR3^{lyc} (*S. lycopersicum*) (Fig. 3). Sequences of *epiC1* or *PmepiC1* alleles from 26 *P. infestans* isolates and 9 *P. mirabilis* isolates indicated that the key Gln or Arg residue is fixed in each population (table S1 and fig. S11).

We also investigated which variant amino acids determine specificity in the proteases. Inspection of the tarocystatin-papain complex identified a protease region that interacts with a tarocystatin residue equivalent to the EPIC1 or PmEPIC1 key Gln or Arg residue (fig. S15A). Structure-based sequence alignments of RCR3 or MRP2 with papain indicated that the inhibitor-binding region overlaps with a seven-amino acid region that is polymorphic between RCR3 and MRP2 (fig. S15, B and C). We constructed proteases altered in this region by swapping the entire seven-amino acid domain or by single-amino acid changes. The results revealed the polymorphic residue His¹⁴⁸ or Asn¹⁴⁷ in RCR3 and

Asp¹⁵² in MRP2 as a key element of specificity (figs. S16 and S17). Unlike wild-type RCR3 proteases, RCR3^{H148D} and RCR3^{N147D} mutants with a single His to Asp or Asn to Asp mutation could be inhibited by PmEPIC1 (fig. S17). This suggests that effector PmEPIC1 adaptation to host protease MRP2 was in part driven by the occurrence of Asp¹⁵² in the *M. jalapa* protease.

Thus, in this case of oomycete infection of potato and four o'clock flower, a single-amino acid polymorphism in the host protease and a reciprocal single-amino acid change in the pathogen effectors underpin the ecological diversification (fig. S18). The arginine substitution found in the *P. mirabilis* effector may enhance effector inhibition of the *M. jalapa* protease. This same substitution would impair interaction with Asn¹⁴⁷ of RCR3^{dms3} and His¹⁴⁸ of RCR3^{lyc} and so provide a molecular explanation for how this effector works on one protease but not the other (fig. S19).

References and Notes

1. K. Yoshida *et al.*, *eLife* **2**, e00731 (2013).
2. N. J. Grünwald, W. G. Flier, *Annu. Rev. Phytopathol.* **43**, 171–190 (2005).
3. S. Raffaele *et al.*, *Science* **330**, 1540–1543 (2010).
4. B. A. Roy, *Evolution* **55**, 41–53 (2001).
5. S. Raffaele, S. Kamoun, *Nat. Rev. Microbiol.* **10**, 417–430 (2012).
6. E. H. Stukenbrock, *New Phytol.* **199**, 895–907 (2013).
7. M. Tian *et al.*, *Plant Physiol.* **143**, 364–377 (2007).

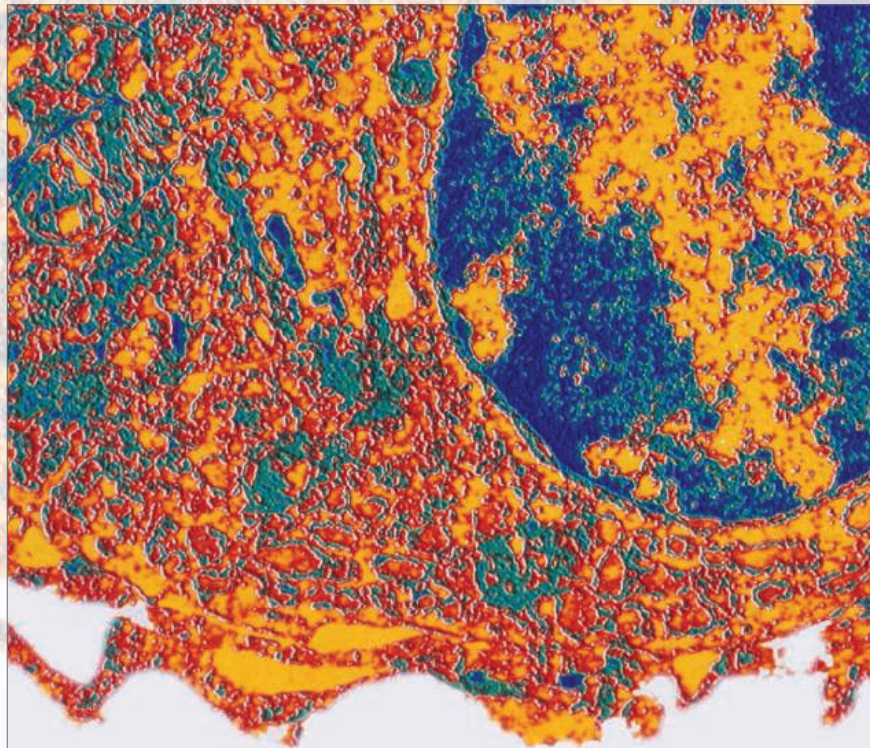
8. J. Song *et al.*, *Proc. Natl. Acad. Sci. U.S.A.* **106**, 1654–1659 (2009).
9. Materials and methods are available as supplementary material on Science Online.
10. R. A. L. van der Hoorn, M. A. Leeuwenburgh, M. Bogyo, M. H. Joosten, S. C. Peck, *Plant Physiol.* **135**, 1170–1178 (2004).
11. F. Kaschani *et al.*, *Plant Physiol.* **154**, 1794–1804 (2010).
12. M. Shabab *et al.*, *Plant Cell* **20**, 1169–1183 (2008).
13. K. H. Richau *et al.*, *Plant Physiol.* **158**, 1583–1599 (2012).
14. J. W. Thornton, *Nat. Rev. Genet.* **5**, 366–375 (2004).
15. J. E. Blair, M. D. Coffey, S. Y. Park, D. M. Geiser, S. Kang, *Fungal Genet. Biol.* **45**, 266–277 (2008).

Acknowledgments: We thank D. G. O. Saunders for comments on drafts of the manuscript and C. Taylor, M. D. Coffey, and V. Vleeshouwers for providing biomaterial. This project was funded by the Gatsby Charitable Foundation, the U.K. Biotechnology and Biological Sciences Research Council, the Ohio Agricultural Research and Development Center at The Ohio State University, and a National Research Initiative of the U.S. Department of Agriculture grant OH000963–SS. Sequences are deposited in GenBank under the submission accession numbers provided in (9).

Supplementary Materials

www.sciencemag.org/content/343/6170/552/suppl/DC1
Materials and Methods
Supplementary Text
Figs. S1 to S19
Tables S1 to S5
References (16–36)

23 September 2013; accepted 11 December 2013
10.1126/science.1246300



The Scientific World Journal

Hindawi Publishing Corporation
<http://www.hindawi.com>

Volume 2014

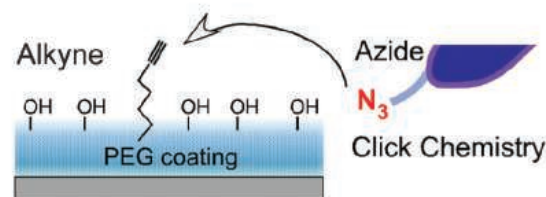
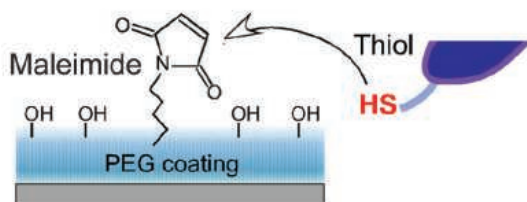
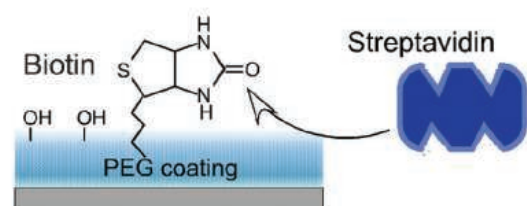
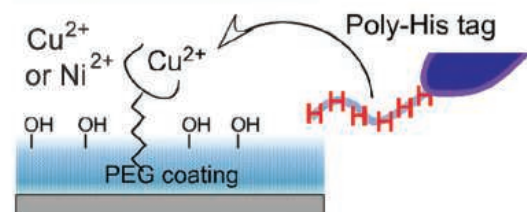
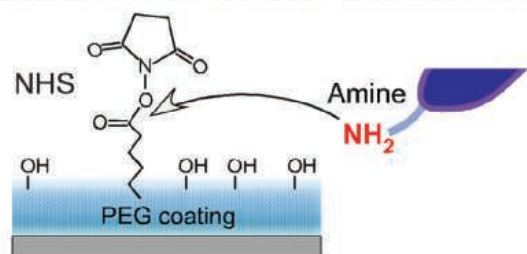
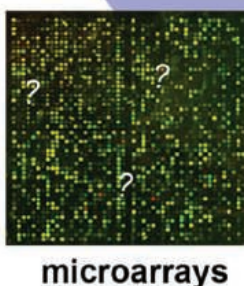
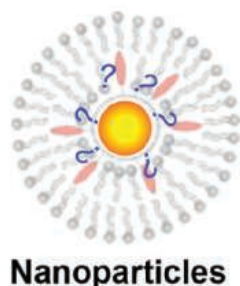
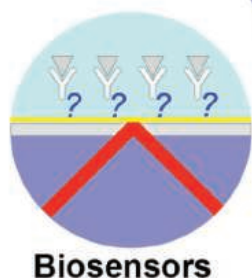
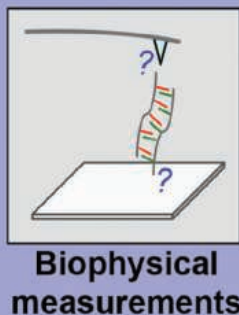
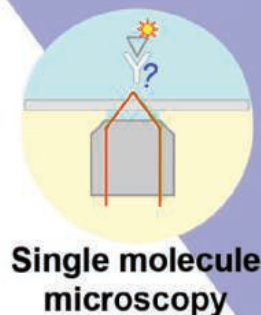


Hindawi

- ▶ Impact Factor **1.730**
- ▶ **28 Days** Fast Track Peer Review
- ▶ All Subject Areas of Science
- ▶ Submit at <http://www.tswj.com>

How do I link bio- or organic molecules to a solid surface?

Save hundreds of hours and quickly turn your ideas into breakthrough results.



Join thousands of researchers who have already discovered the perfect answer from MicroSurfaces' technologies.

Products & Services:

- ZeroBkg® high density poly-ethylene glycol (PEG) brush coatings on a variety of surfaces, including standard glass coverslips & slides, quartz coverslips & slides, gold SPR sensors, ITO slides & chips, silicon wafers & chips, nanoparticles, or any customer surface.
- Surface functionalities include **PEG** for low background, **Biotin** for streptavidin/biotin linkage, **Chelated Cu^{2+} or Ni^{2+}** for His-tags, **NHS** for $-\text{NH}_2$ functional group, **Alkyne** for azide tags via Click chemistry, **Maleimide** for $-\text{SH}$ group, & many more.
- Other customer functionalities, such as **silanes**, **thiols**, **acids**, **amines**, **poly-L-lysine**, **dextran**, supported **lipid bilayers**, etc.

Clone with Confidence.

Whether you are performing your first cloning experiment, or constructing multi-fragment gene assemblies, NEB[®] has the solution for you. Our high quality reagents are available for every workflow, and include specialized enzymes, competent cells, and novel solutions – such as Gibson Assembly[®]. When you are looking to clone with confidence, think of NEB.

Explore the wise choice at
CloneWithNEB.com.

Visit **CloneWithNEB.com** to view online tutorials describing various cloning workflows.



AAAS|2014 ANNUAL MEETING

13-17 FEBRUARY • CHICAGO

MEETING GLOBAL CHALLENGES:
DISCOVERY AND INNOVATION

Final registration reminder!

If you can't make it to Chicago, selected sessions will be available to watch (for a fee) on a live video stream. And to help you tell your story, the Communicating Science seminar will be provided at no cost.

For more information and a list of sessions that will be available by video, visit:

www.aaas.org/AM14video



AAAS, publisher of *Science*, thanks the sponsors and supporters of the 2014 Annual Meeting



the **Lemelson** foundation
improving lives through invention



AAAS thanks
THE KAVLI FOUNDATION
for its generous support of
the Science Journalism Awards

Sponsors as of 15 January 2014

Historical Breakthroughs

Breathtaking Progress



Radical Reinvention



Introducing **NextSeq™**
A Whole Human Genome on Your Desktop

www.illumina.com/nextseq500

illumina®

Sequencing power for every scale.



The HiSeq X Ten contains 10 sequencing systems.

NEW
HiSeq X™ Ten

Population power.

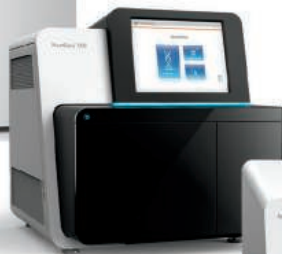
\$1000 human genome and extreme throughput for population-scale sequencing.



HiSeq® 2500

Production power.

Power and efficiency for large-scale genomics.



NEW
NextSeq™ 500

Flexible power.

Speed and simplicity for whole-genome, exome, and transcriptome sequencing.



MiSeq®

Focused power.

Speed and simplicity for targeted and small-genome sequencing.



MiSeqDx™

Focused Dx power.

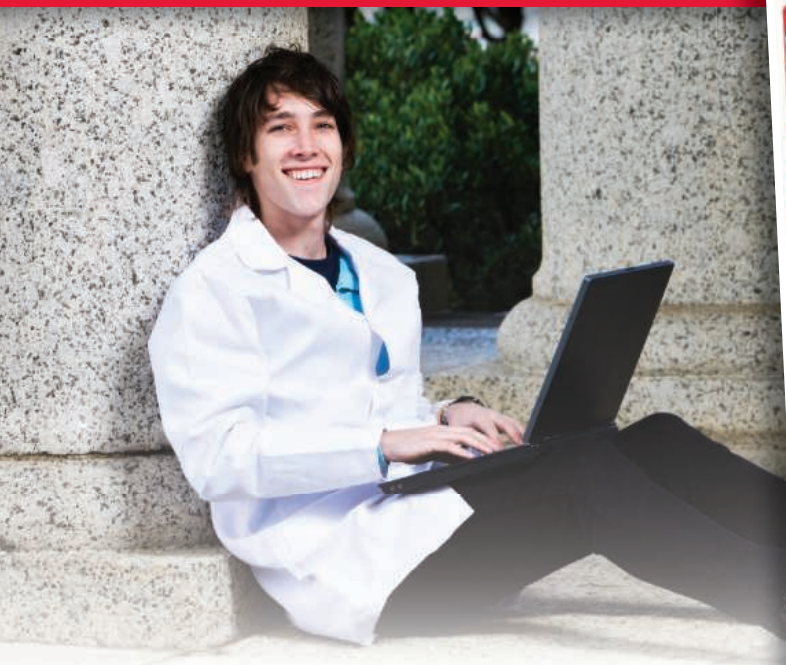
The first and only FDA-cleared *in vitro* diagnostic next-generation sequencing system.

Find the right sequencer to fit your every need. www.illumina.com/power

illumina®

For your career in science, there's only one **Science**

A career plan customized
for you, by you.



myIDP.sciencecareers.org



Recommended by leading professional societies and endorsed by the National Institutes of Health, an individual development plan will help you prepare for a successful and satisfying scientific career.



In collaboration with FASEB, UCSF, and the Medical College of Wisconsin and with support from the Burroughs Wellcome Fund, AAAS and *Science* Careers present the first and only online app that helps scientists prepare their very own individual development plan.

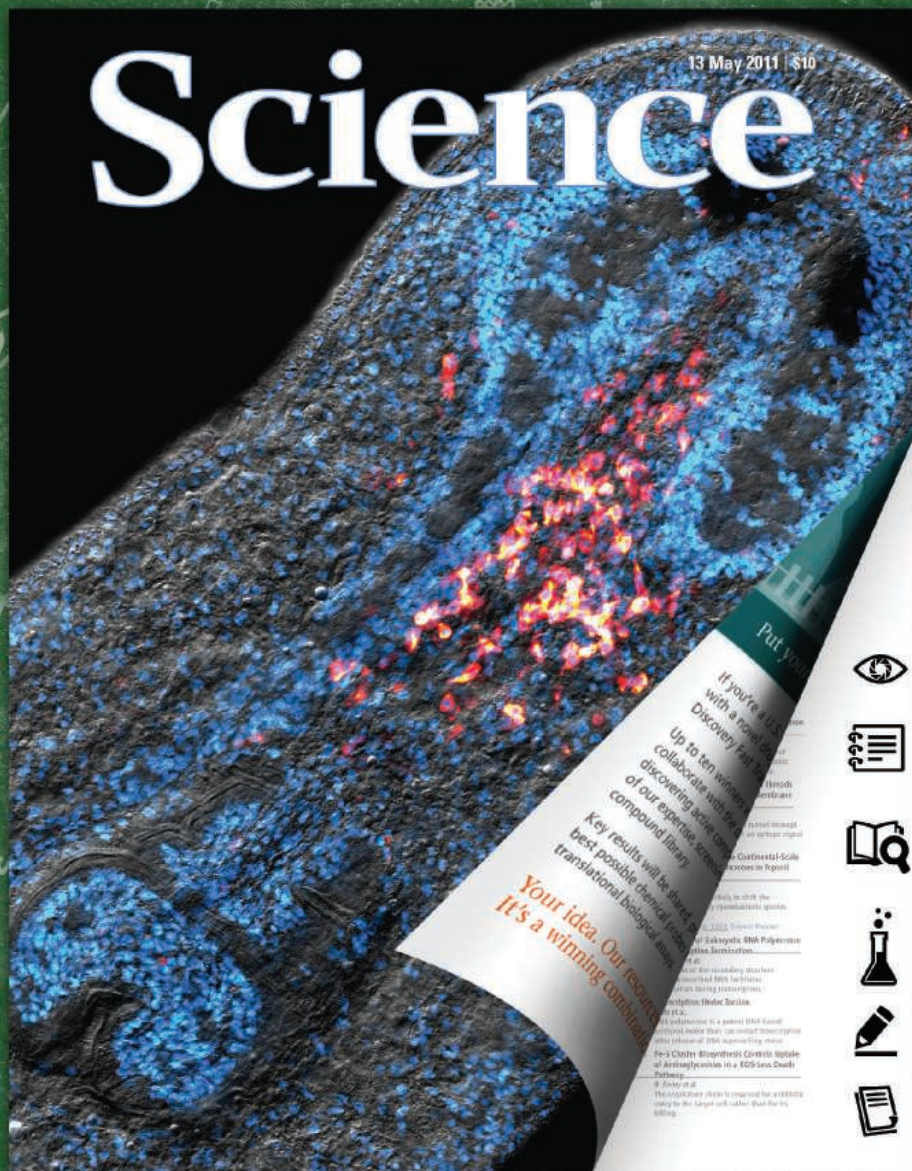
Visit the website and
start planning today!
myIDP.sciencecareers.org

In partnership with:



Science

13 May 2011 | \$10



Learning Lens



Learning Notes



Connect to
Learning Standards



Activities = 0 (2)



Discussion Questions



References



Online tools to help your
students analyze a
professional research paper!

Tell me and I forget. Teach me and I remember. Involve me and I learn. -- Benjamin Franklin

Featuring over 6 research papers at any given time, *Science in the Classroom* is specifically designed to help young researchers understand the structure and workings of professional scientific research.

Learn for yourself how *Science in the Classroom* can help your students deepen their understanding of scientific research. **Visit scienceintheclassroom.org today.**

FLUORESCENT DNA QUANTITATION KIT

The new Fluorescent DNA Quantitation Kit utilizes the fluorescent DNA intercalator, bisBenzimide H33258, otherwise known as Hoechst dye, and a simple method that may be easily scaled for a single cuvette or for high throughput in multiwell plates. The kit includes Fluorescent DNA Dye Solution, Fluorescent DNA Standard, and Fluorescent DNA Assay Buffer, provided at 10X in volumes sufficient to perform up to 750 reactions. Assays are performed by fluorometric reading of a DNA standard series and unknown samples prepared in diluted Fluorescent DNA Dye Solution. The selective binding of the bisBenzimide H33258 dye to A-T base pairs results in significant fluorescent emission at 460 nm in the presence of DNA. The dye has low affinity for RNA, which improves specificity and sensitivity of the assay results when using impure samples. The assay also tolerates protein contamination that may be present in crude extracts and various buffer compositions commonly used in DNA extraction.

AMRESCO

For info: 800-448-4442 | www.amresco-inc.com



FFPE ASSAY KIT

The new OncoScan FFPE Assay Kit is a whole-genome copy number assay for highly degraded formalin-fixed paraffin-embedded (FFPE) solid tumor samples. Despite the growing need of cancer researchers and clinicians, obtaining high-quality, whole-genome copy number data from degraded FFPE-derived tumor DNA has remained extremely challenging due to the limitations of current methods such as FISH, array CGH, and next generation sequencing technologies. The new OncoScan FFPE Assay Kit, utilizing Affymetrix' unique Molecular Inversion Probe technology, is capable of analyzing small amounts of highly degraded DNA from FFPE samples quickly and affordably. This new product provides whole-genome copy number data with specifically enhanced high resolution in approximately 900 known cancer genes, loss of heterozygosity across the whole genome as well as clinically relevant somatic mutation data—all from a single assay. The OncoScan Nexus Express Software enables copy number calls for hundreds of samples in minutes and will be included with the product.

Affymetrix

For info: 888-362-2447 | www.affymetrix.com

NGS DATA ANALYSIS SOFTWARE

BioDT is an open source suite of next generation sequencing (NGS) data analysis software and services. The new platform addresses the shortcomings found with current data analysis offerings by delivering much higher performance and an intuitive interface, thereby enabling genomic and biomedical researchers to more quickly glean meaningful insights from their data. NGS data analysis is now considered an essential tool for basic and clinical genomic research. While the Big Data generated by such research can be acquired more quickly and at a lower cost, it has become increasingly difficult to derive meaningful insights from it. Existing solutions have proven slow, with complex yet inflexible user interfaces, long turnaround times and difficult-to-interpret results. These shortcomings have meant higher costs and delays in potential breakthroughs. BioDT is an open source platform capable of analyzing NGS data up to 100 times faster than similar systems, thanks to a proprietary execution engine and a Hadoop-based architecture.

BioDatomics

For info: 877-249-6660 | www.biodatomics.com

SCREENTAPE ASSAYS

Two new assays are available for the 2200 TapeStation system: the RNA ScreenTape and the D1000 ScreenTape assays. Both assays are essential for the quality control of samples in next generation sequencing (NGS) workflow. They replace Agilent's R6K and D1K ScreenTape assays. The new RNA ScreenTape assay delivers qualitative and quantitative assessment of total RNA for both eukaryotic and prokaryotic samples, with a Bioanalyzer-like electropherogram and RNA Integrity Number equivalent quality score. The new D1000 ScreenTape assay builds on the success of the D1K ScreenTape, with closer alignment in sizing and quantification to the market-leading 2100 Bioanalyzer system. The 2200 TapeStation system is an ideal technology for high-quality NGS, providing a simplified, automated process for nucleic acid quality control. With enhanced performance, these new assays optimize quantification and sizing and improve RNA resolution.

Agilent Technologies

For info: 800-227-9770 | www.agilent.com/genomics/NGS-QC

RNA METHYLATION QUANTIFICATION KIT

A new, breakthrough approach for the identification of the "fifth RNA base," N6-methyladenosine (m6A), has been developed to efficiently study RNA methylation. This technology is based on a high throughput strip-well format and is also incorporated into the first commercially available product, the EpiQuik m6A RNA Methylation Quantification Kit, for rapidly quantifying m6A RNA methylation. Epigentek's new quantification technique can be used for rapidly and accurately identifying m6A in RNA or detecting m6A-specific RNA methylation in a high throughput format, suitable for use in any species including mammals, plants, fungi, bacteria, and viruses in a variety of forms such as cultured cells, fresh and frozen tissues, paraffin-embedded tissues, plasma/serum samples, and body fluid samples. In the assay, RNA is bound to strip wells and the m6A contained in the RNA is then immunospecifically detected using a high-quality m6A antibody.

Epigentek

For info: 877-374-4368 | www.epigentek.com

Electronically submit your new product description or product literature information! Go to www.sciencemag.org/products/newproducts.dtl for more information.

Newly offered instrumentation, apparatus, and laboratory materials of interest to researchers in all disciplines in academic, industrial, and governmental organizations are featured in this space. Emphasis is given to purpose, chief characteristics, and availability of products and materials. Endorsement by Science or AAAS of any products or materials mentioned is not implied. Additional information may be obtained from the manufacturer or supplier.

Science Signaling

The Leading Journal for Cell Signaling

Publishing key findings of broad
relevance in the multidisciplinary
field of cell signaling

Submit your research

ScienceSignaling.org

Recommend to your library

ScienceOnline.org/recommend

Join the ranks of high-profile papers
published in *Science Signaling*:

CANCER BIOLOGY

Vemurafenib Potently Induces Endoplasmic
Reticulum Stress–Mediated Apoptosis in
BRAFV600E Melanoma Cells

D. Beck *et al.* (F. Meier), *Sci. Signal.* **6**, ra7 (2013)

NEUROSCIENCE

Requirement for Nuclear Calcium Signaling in
Drosophila Long-Term Memory

J.-M. Weislogel *et al.* (H. Bading), *Sci. Signal.* **6**, ra33 (2013)

CELL AND MOLECULAR BIOLOGY

A Nontranscriptional Role for HIF-1 α as a Direct
Inhibitor of DNA Replication

M. E. Hubbi *et al.* (G. L. Semenza), *Sci. Signal.* **6**, ra10 (2013)

IMMUNOLOGY

Monovalent and Multivalent Ligation of the
B Cell Receptor Exhibit Differential Dependence
upon Syk and Src Family Kinases

S. Mukherjee *et al.* (A. Weiss), *Sci. Signal.* **6**, ra1 (2013)

COMPUTATIONAL AND SYSTEMS BIOLOGY

Cross-Species Protein Interactome Mapping
Reveals Species-Specific Wiring of Stress
Response Pathways

J. Das *et al.* (H. Yu), *Sci. Signal.* **6**, ra38 (2013)

Chief Scientific Editor

Michael B. Yaffe, M.D., Ph.D.

Massachusetts Institute of Technology

Editor

Nancy R. Gough, Ph.D.

AAAS, Washington, DC

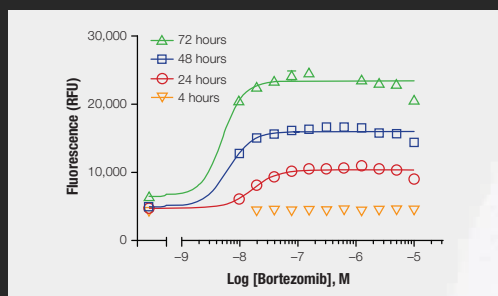


sciencesignalingeditors@aaas.org

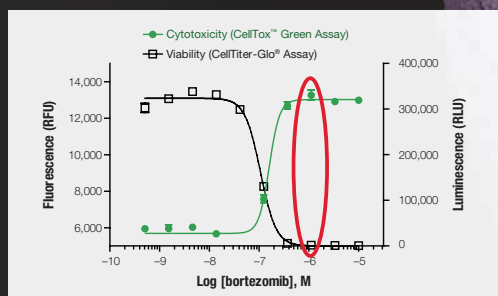
CellTox™ Green

More Biology, Less Work

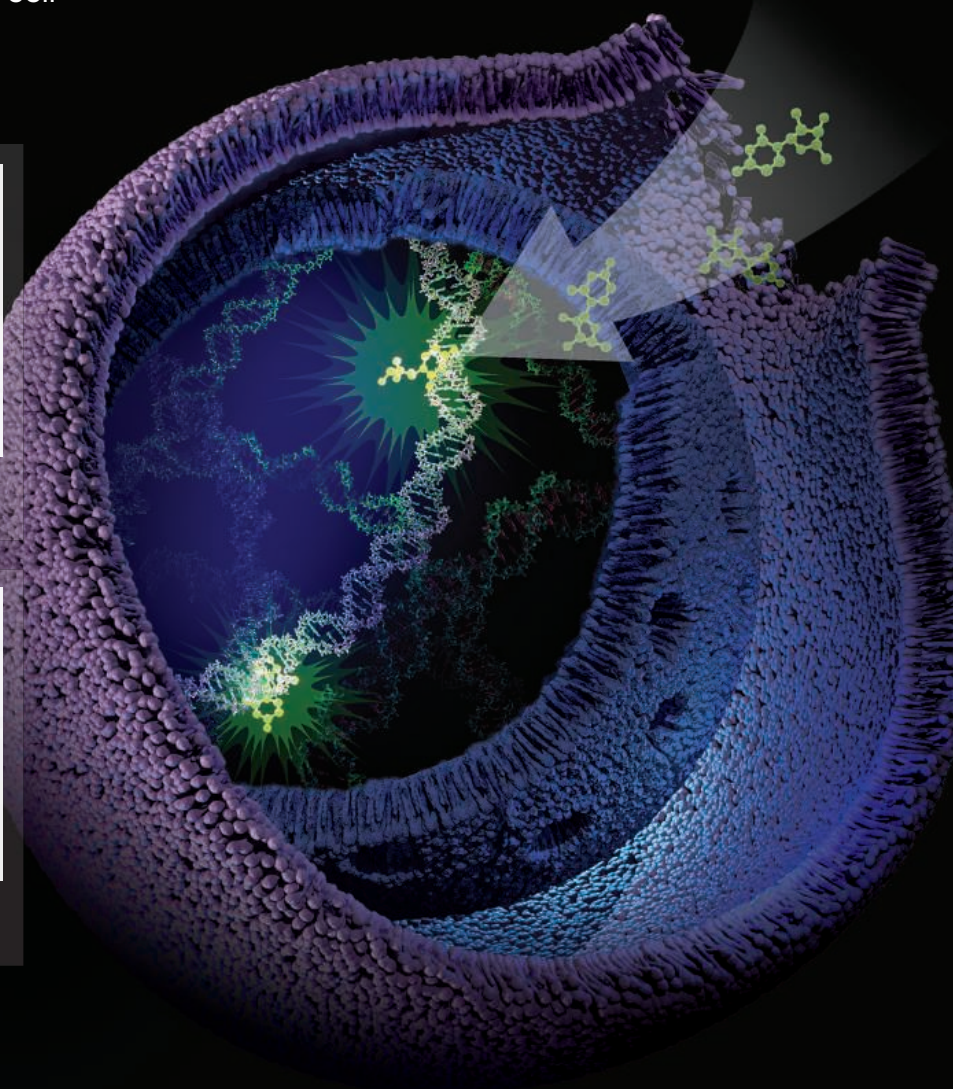
CellTox™ Green enables real-time mechanistic toxicity monitoring with a simple Add & Read protocol. Multiplexing with CellTiter-Glo® allows investigators to monitor temporal changes of membrane-modulated cytotoxicity in parallel with the key cell viability biomarker, ATP.



Easily monitor temporal changes in a key cytotoxicity biomarker for IC_{50} determinations.



Get more informative data from same-well multiplexing of cytotoxicity and viability assays.



To see how easy better biology can be, request a free sample at:
www.promega.com/newcelltox



Science Careers Advertising

For full advertising details, go to ScienceCareers.org and click For Employers, or call one of our representatives.

Tracy Holmes

Worldwide Associate Director
Science Careers
Phone: +44 (0) 1223 326525

THE AMERICAS

E-mail: advertise@sciencecareers.org
Fax: 202-289-6742

Tina Burks

Phone: 202-326-6577

Marci Gallun

Phone: 202-326-6582

Online Job Posting Questions

Phone: 202-312-6375

EUROPE / INDIA / AUSTRALIA / NEW ZEALAND / REST OF WORLD

E-mail: ads@science-int.co.uk
Fax: +44 (0) 1223 326532

Axel Gesatzki

Phone: +44 (0)1223 326529

Sarah Lelarge

Phone: +44 (0) 1223 326527

Kelly Grace

Phone: +44 (0) 1223 326528

JAPAN

Yuri Kobayashi

Phone: +81-(0)90-9110-1719
E-mail: ykobayas@aaas.org

CHINA / KOREA / SINGAPORE / TAIWAN / THAILAND

Ruolei Wu

Phone: +86-1367-1015-294
E-mail: rwu@aaas.org

All ads submitted for publication must comply with applicable U.S. and non-U.S. laws. *Science* reserves the right to refuse any advertisement at its sole discretion for any reason, including without limitation for offensive language or inappropriate content, and all advertising is subject to publisher approval. *Science* encourages our readers to alert us to any ads that they feel may be discriminatory or offensive.

Science Careers

From the journal *Science*



ScienceCareers.org

POSTDOCTORAL POSITIONS in High-Throughput Developmental Lethal Screening at The Jackson Laboratory



**The Jackson
Laboratory**

Leading the search
for tomorrow's cures

www.jax.org

The Jackson Laboratory (JAX) has unique openings for several postdoctoral fellows interested in working collaboratively as part of Phase 2 of the NIH-funded Knockout Mouse Program (KOMP2). JAX is a member of the International Mouse Phenotyping Consortium (IMPC) and is an NIH-funded KOMP2 recipient. We are looking for post-doctoral associates to join in an exciting opportunity to identify and characterize novel embryonic lethal phenotypes, taking advantage of and participating in a high-throughput screen of KOMP2 mice. KOMP2 postdoctoral fellows will work collaboratively to screen and characterize an expected 30% of embryonic lethal mutants from more than 800 mouse strains that JAX is characterizing as part of an international effort to functionally annotate the mouse genome and generate mouse models of human disease. Fellows will be able to devote approximately 50% of their time using individual mutants to develop an independent research program, which is expected to form the foundation of the next stage of their careers.

Postdocs will perform the secondary characterization of mutants in the labs of any of several JAX faculty members, who have research programs in areas such as embryonic development, reproductive biology, neurobiology, stem cell biology and craniofacial and skeletal development.

Applicants must have a Ph.D. in developmental biology, genetics or related fields, with a proven track record of success. Candidates must be highly motivated to take advantage of this unique opportunity. Experience with mouse genetics and high-resolution 3D imaging techniques is preferred.

Applications should include a cover letter, curriculum vitae, and the names of three references.

Application deadline is March 15, 2014. Apply online at www.jax.org/careers/postdoc (select link for Bar Harbor positions, position #4024).

For more information, please contact Robert Braun, Professor and Vice President of Research at bob.braun@jax.org.

The Jackson Laboratory, 600 Main Street,
Bar Harbor, Maine 04609

The Jackson Laboratory is an EOE/AA employer.

DEPARTMENT OF BIOTECHNOLOGY MINISTRY OF SCIENCE & TECHNOLOGY, GOVERNMENT OF INDIA NOMINATIONS / APPLICATIONS FOR THE POST OF DIRECTOR, CDFD, HYDERABAD

Nominations / Applications are invited for the post of Director on deputation (including short term contract), Centre for DNA Fingerprinting & Diagnostics (CDFD), Hyderabad, an autonomous institute under the Department of Biotechnology, Government of India, from Indian citizens including those staying abroad and Non - Resident Indians (NRIs).

The Centre uniquely combines two kinds of activities, the first being those of services in the twin areas of DNA profiling for law - enforcement agencies and diagnostics tests and clinical counseling for genetic disorders, and the second that of cutting - edge basic research in various disciplines of modern biology, in such a way that each supports and in turn is enriched by the other.

The applicants should be below 56 years of age. The post carries HAG Scale of Pay of ₹ 67,000 (annual increment @ 3%) - 79,000/- with usual allowances as per the Government of India Rules.

The applicants should be Scientists from Central / State Governments, research institutes, autonomous bodies etc.

- Holding analogues post on regular basis in the parent Department.
- With 5 years service in post with Grade Pay of ₹ 10,000/- or equivalent in the parent cadre / Department and possess the qualification & experience as below:-

Essential

- Ph.D in any life science discipline / M.D. or equivalent
- Minimum 15 years experience of research in the area of organismal, cellular, molecular or systems biology, or biotechnology.
- Excellent track record, hand in publications, patent and awards.

Desirable

- Experience in successfully running large programme, centre, institution
- Experience of guiding research activities in the area of specialization.

The period of deputation includes period of deputation in other ex - cadre posts, held immediately preceding this appointment in the same or some other organization / Department should ordinarily not exceed 5 years. The maximum age limit for appointment on deputation should not exceed 56 years as on the closing date of receipt of nominations / applications.

The nomination / application along with detailed curriculum vitae including the date of birth, address for correspondence including telephone no., fax and e - mail address, qualifications acquired, professional and research experience, present position and scale of pay with total emoluments, publication details and a 500 words write - up on the candidate's vision of CDFD for the next ten years may be sent to **Smt. Kusum Lata Sharma, Deputy Secretary, Department of Biotechnology, Block - 2, CGO Complex, Lodi Road, New Delhi - 110 003**, superscribing the cover "Nomination / Application for the Post of Director, CDFD" so as to reach her within 30 days from the date of publication of this advertisement. The detailed advertisement and format of application is available at DBT website www.dbtindia.nic.in and at the CDFD website www.cdfd.org.in

The Department reserves the right to relax any of the requirements prescribed above.

Director, Robert H. Lurie Comprehensive Cancer Center of Northwestern University

Northwestern University Feinberg School of Medicine invites applications and nominations for the position of Director, Lurie Cancer Center, an NCI-designated, university-based, matrix cancer center conducting a broad range of multidisciplinary clinical, laboratory, and population science research.

Assuming a leadership appointment at the Feinberg School of Medicine and Northwestern University, the Director will join Feinberg at a crucial point in time with the formation of our national brand called Northwestern Medicine. The Director is not just a center director but also an important figure across the academic medical center and university. He/she will lead the next phase of growth of the cancer center.

Ranked 18th in US News & World Report, principal investigators appointed through the Feinberg School of Medicine are supported by \$374 million of annual research funding. The medical school is embedded among three U.S. News & World Report Honor Roll hospitals; Northwestern Memorial Hospital is ranked 6th, Lurie Children's Hospital 8th, and the Rehabilitation Institute of Chicago 1st.

Reporting to the Vice President of Medical Affairs/Dean of the Feinberg School of Medicine, and accountable to Northwestern Medicine leadership, the Director is responsible for oversight of the academic, research, clinical, and administrative affairs of the cancer center, and will assume responsibility as principal investigator for the recently-renewed comprehensive cancer center grant from the National Cancer Institute.

Successful candidates will possess an M.D. or M.D./Ph.D, be eligible for a faculty appointment as a full-time Professor, and have a record of scholarly accomplishments and national recognition in cancer research.

Please email nominations and CVs of appropriate candidates to Ila Allen at cancerctrsearch@northwestern.edu, recruitment coordinator, Feinberg School of Medicine. Applications will be taken until the position is filled.

Northwestern University is an Affirmative Action, Equal Opportunity Employer. Women and minorities are encouraged to apply. Hiring is contingent upon eligibility to work in the United States.



Science Careers is the forum that answers questions.



Science Careers is dedicated to opening new doors and providing timely answers to the career questions that matter to you.

Science Careers Forum:

- » Relevant Career Topics
- » Timely Advice and Answers
- » Community, Connections, and More!

Visit the forum and join the conversation today!

Your Future Awaits.



Research Positions

Careers Applied Science, Technology, and Engineering Research



INL's Energy and Environment Science and Technology Directorate is seeking outstanding, highly creative and motivated early to mid-level career professionals to join our multi-disciplinary research teams. The Directorate is INL's principal multi-mission organization focused on research to advance clean energy systems, advanced transportation, advanced process technology and related sciences.

Multiple positions are available in the following areas:

- Bioenergy research including biomass characterization, conversion, pre-processing and molecular biology.
- Analytical chemistry specializing in laser spectroscopy and mass spectrometry.
- Materials science and physics with focus on performance in harsh environments, nondestructive evaluation, and radiation based imaging.
- Membrane science with a focus on dense film separation and filtration.
- Geology and Hydrology with a focus on hydraulic fracturing and geothermal evaluation.
- Scientific visualization research in a CAVE environment with a focus on immerse visualization, virtual reality, graphics programming, and large format display technologies.

The Idaho National Laboratory is a science-based, applied engineering national laboratory dedicated to supporting the U.S. Department of Energy's mission in nuclear energy research, science, and national defense. With 3,800 scientists, researchers and support staff, the laboratory works with national and international governments, universities and industry partners to discover new science, develop technologies that underpin the nation's nuclear and renewable energy, national security and environmental missions. The Laboratory is a multi-program national laboratory. It currently performs a range of research and development activities associated with energy and national security. The laboratory currently has more than 150,000 sq. ft. of modern research facilities with a significant amount of wet laboratory space that are supported by a vast array of state-of-the-art research instrumentation. Idaho Falls is conveniently situated near many national treasures such as Yellowstone National Park, Teton National Park, Jackson, WY, etc. For more information about the area, please visit www.visitidahofalls.com and www.visitidaho.org. Interested parties should visit our website at www.inl.gov.

INL is an Equal Opportunity Employer M/F/D/V

There's only one GALILEO GALILEI

Born in 1564, Galileo Galilei once contemplated a career in the priesthood. It's perhaps fortunate for science that upon the urging of his father, he instead decided to enroll at the University of Pisa. His career in science began with medicine and from there he subsequently went on to become a philosopher, physicist, mathematician, and astronomer, for which he is perhaps best known. His astronomical observations and subsequent improvements to telescopes built his reputation as a leading scientist of his time, but also led him to probe subject matter counter to prevailing dogma. His expressed views on the Earth's movement around the sun caused him to be declared suspect of heresy, which for some time led to a ban on the reprinting of his works.

Galileo's career changed science for all of us and he was without doubt a leading light in the scientific revolution, which is perhaps why Albert Einstein called him the father of modern science.

Want to challenge the status quo and make the Earth move? At *Science* we are here to help you in your own scientific career with expert career advice, forums, job postings, and more — all for free. For your career in science, there's only one *Science*. Visit ScienceCareers.org today.

**AAAS**

For your career in science, there's only one **Science**

ScienceCareers.org



大连理工大学
DALIAN UNIVERSITY OF TECHNOLOGY

“人工光合作用研究所” 科研人员招聘

Faculty positions in solar cells and solar fuels

Openings of more than 15 tenure-track positions of Assistant Professor, Associate Professor and Full Professor are now available in the recently established Institute of Artificial Photosynthesis (IAP), Dalian University of Technology (DUT), China. The research fields of these open positions cover dye sensitized solar cells, quantum dots sensitized solar cells, organic polymer solar cells, organic-inorganic hybrid solar cells, catalytic water oxidation, catalytic proton reduction, catalytic CO₂ reduction, functional devices for light driven total water splitting, new type batteries, light to heat conversion at molecular level. Qualified candidates for these open positions should have obtained PhD degree, postdoc research experience, and well documented research achievements in related research fields. DUT will provide for the positions in IAP competitive salaries at international levels. Applicants should send their curriculum vitae, a statement of research plans together with publication list by email to Xue Sun (zhaopin@dlut.edu.cn), indicating in the email subject with “IAP+applicant’s name”. All applications should contain information of related interested positions in certain research fields mentioned above and potential reference persons with corresponding addresses.



首都师范大学
CAPITAL NORMAL UNIVERSITY

Faculty Positions Available at Capital Normal University

Capital Normal University invites applications for full-time positions in research and academics.

Established in 1954, Capital Normal University (CNU) is a comprehensive university offering majors in arts and humanities, sciences, technology, business management, laws, education, foreign languages, and art. CNU is a key university under the administration of Beijing Municipal Government, and a Project 211 institution.

For more detailed information, please visit the website http://www.cnu.edu.cn/pages/info_details.jsp?seq=20433&boardid=71002&classcode=71002

Eligible applicants:

Young scholars with PhDs or postdoctoral research experiences with a specific area of expertise and outstanding research achievements. The applicant must be physically healthy, and demonstrate good teamwork skills.

Professors are required to be under 45 years of age, exceptions can be made for holders of high-level academic titles; PhDs are expected to be under 35 years of age, and post-docs under 40.

Employee benefits:

CNU provides different levels of competitive salaries and start-up research funding. Housing and relocation allowances will be provided for the professors. Post-docs or PhDs from overseas universities with vice senior academic titles who have made significant academic achievements can apply for temporary housing.

To apply:

Please submit the following items to the related colleges or departments, and forward it to the Personnel Department of CNU: Curriculum Vitae; proposed work plan for 3 years; a list of papers and publications in the last 5 years; a list of awards won; a list of research projects participated or led by the applicants; and reference letters from experts in the applicant’s field of study.

Please also sent paper copies of the application package to:

Personnel Department, Capital Normal University, 105 Xisanhuanbeilu, Haidian District, Beijing 100048, P.R. China
Contact: Zhou Quan, Chen Wenxin
Email: cnurse2013@163.com
Tel: 86-10-68902824
Fax: 86-10-68902240

Faculty and Postdoctoral Positions at Peking-Tsinghua Center for Life Sciences



Applications are invited for Principal Investigator (PI) and postdoctoral positions at Peking-Tsinghua Center for Life Sciences (<http://www.cls.edu.cn/english/>).

We look for the best scientists in all areas of life sciences, with emphasis in the following areas: bioinformatics, biochemistry and biophysics, bioengineering, cancer biology, epigenetics, cell biology, chemical biology, computational biology, microbiology and virology, human genetics, genetics, genomics, molecular medicine, molecular neuroscience and cognitive neuroscience, modern imaging, physiology, plant biology, synthetic biology, and systems biology.

Each PI holds a joint (tenure track or tenured) appointment in one of the departments or schools at Peking University (such as Chemistry, Computer Science, Engineering, Life Sciences, Mathematics, Medicine, Physics and Psychology). Peking University provides excellent interdisciplinary research environment and outstanding core research facilities. We offer an internationally competitive package. The kindergarten and the primary school attached to Peking University will be available to the children of all Center PIs and postdocs.

PI application materials (with cover letter, summary of research interests, CV and less than 5 representative publications, all in a single PDF file) should be sent to Ms. Wei Xiao (gsmkyb@pku.edu.cn), to whom you should also ask your references to send in their recommendation letters. Postdoc applicants should indicate in the cover letter 1 or 2 laboratories as your intended host, and send application materials to Ms. Siyuan Gong (clspostdoc-peking@cls.edu.cn). Applications from both Chinese and non-Chinese nationals will be evaluated on an equal opportunity basis.



Faculty Positions Available in Southwest University, Chongqing, China

Southwest University is a national key university of the “211” project directly under the Ministry of Education. It is located in Chongqing, the youngest municipality of China. The university hosts approximately 50,000 students, covering undergraduate, postgraduate and other programs. For more detailed information, please visit the website: <http://www.swu.edu.cn/#>

Applications for full-time professors, associate professors and distinguished scientists are welcome. Competitive salaries and start-up funds will be provided to successful candidates, in line with the national Recruitment Program of Young Experts.

The Recruitment Program of Young Experts (i.e. the Plan for Recruiting 1,000 Professorship for Young Talents): The candidates are required to be under the age of 40 and have obtained a PhD degree in a world-renowned university with at least 3 years of research experience abroad, or have obtained a PhD degree in Mainland China with at least 5 years of research and teaching experience abroad. Special offers will be granted to those who have excellent research achievements during their doctoral study.

Further information is available at <http://renshi.swu.edu.cn/rcgzbggs/> The Talents Recruitment Office, Southwest University, Beibei, Chongqing 400715, P. R. China. 0086-23-68254265.

Please kindly send applications or nominations in the form of an application letter enclosing a current CV to rencai@swu.edu.cn.



AAAS is here – helping scientists achieve career success.

Every month, over 400,000 students and scientists visit ScienceCareers.org in search of the information, advice, and opportunities they need to take the next step in their careers.


A complete career resource, free to the public, *Science* Careers offers a suite of tools and services developed specifically for scientists. With hundreds of career development articles, webinars and downloadable booklets filled with practical advice, a community forum providing answers to career questions, and thousands of job listings in academia, government, and industry, *Science* Careers has helped countless individuals prepare themselves for successful careers.

As a AAAS member, your dues help AAAS make this service freely available to the scientific community. If you're not a member, join us. Together we can make a difference.

To learn more, visit aaas.org/plusyou/sciencecareers




CAREER TRENDS Running Your Lab



Download your free copy today at
ScienceCareers.org/booklets

Science Careers
From the journal *Science* AAAS

Brought to you by the
AAAS/Science Business Office


UNIVERSITY of HAWAII
MĀNOA

**Three Assistant Professors:
Evolutionary Developmental Biology
and Marine Biology**

The Department of Biology at the flagship campus of the University of Hawai'i seeks three new faculty—two in developmental biology and one in marine biology—who will complement existing strengths of its faculty (see <http://manoa.hawaii.edu/biology>). Successful applicants will be expected to establish a vigorous extramurally funded research program, as well as teach and mentor undergraduate and graduate students and postdoctoral scholars.

Areas of interest for the developmental biology positions include, but are not limited to, the integration of evolutionary developmental biology with the fields of ecology, genomics, and/or epigenetics. Teaching expectations for these positions will include undergraduate developmental biology and graduate courses in the successful candidates' fields of study.

For the marine biology position (pending approval), we seek applicants that use modern quantitative approaches in fields such as genomics or experimental ecology to understand patterns of diversity or speciation within natural populations of non-model marine organisms. Applicants with an organismal emphasis on the biology of corals or the ecology and evolution of other commensal/symbiotic systems are particularly encouraged, but all areas of research will be considered. Teaching expectations include leading one of two core courses in the new Marine Biology Graduate Program (www.hawaii.edu/mbiograd), and contributing to our Undergraduate Program in Marine Biology. Applicants must have a Ph.D. in biology or a related field, evidence of significant research accomplishments and a commitment to excellence in teaching. Desirable qualifications include relevant postdoctoral experience, extramural funding, and teaching experience.

To apply, please prepare a single PDF document that includes: a cover letter indicating how you satisfy the minimum and desirable qualifications; statements of research and teaching experience/interests; detailed curriculum vitae; and three representative publications. Also arrange to have three letters of reference submitted electronically. Review of applications will begin **February 14, 2014**. Applications, letters of reference and inquiries for the **developmental biology positions** should be sent to dbsearch@hawaii.edu, **808-956-4706**. For complete job announcements, please refer to <http://workatuh.hawaii.edu>, **Positions #84248 and #82208**. Applications, letters of reference and inquiries for the **marine biology position** should be sent to mbiofacsch@hawaii.edu. For a complete job announcement, please refer to <http://workatuh.hawaii.edu>, **Position #83910**.

The University of Hawai'i is an Equal Opportunity/Affirmative Action Institution and encourages applications from women and minority candidates.

**Creighton
UNIVERSITY
Medical Center**


**School of Medicine
Department of Medical Microbiology
and Immunology**

**Faculty Position in
Microbial Pathogenesis/Host Response**

As part of ongoing expansion, the Department of Medical Microbiology and Immunology in the School of Medicine at Creighton University invites applications for two tenure-track positions at the rank of Assistant Professor. Investigators studying bacterial pathogenesis and host defense are encouraged to apply. Special consideration will be given to those with a research focus in neuropathology and/or neuroimmunology. Appointees will be expected to conduct a vigorous independent research program, and participate in the teaching of graduate and professional students. Generous laboratory space with equipment, competitive start-up funding, and ongoing support with state-of-the-art core facilities will be provided. Applicants should have a Ph.D., M.D., or M.D./Ph.D. degree, postdoctoral training and experience denoting significant research accomplishment and scholarly promise.

Application materials, including a curriculum vitae, brief summary of research plans, statement of teaching interests, reprints of recent publications, and **three** letters of recommendation should be sent to **Chair of Search Committee, Department of Medical Microbiology and Immunology, Creighton University Medical Center, 2500 California Plaza, Omaha, NE 68178**. Materials may also be sent via email to MMIsearchcommittee@creighton.edu. Applications will be screened immediately and will continue to be accepted until the position is filled.

Creighton University is an Affirmative Action/Equal Opportunity Employer.

 **LSUHealth
Shreveport**

**Faculty Positions in
Microbiology and Immunology**

Two tenure track faculty positions at the rank of Assistant Professor or Associate Professor are open for scientists with a Ph.D., M.D. or M.D./Ph.D. and postdoctoral research experience. Responsibilities include teaching graduate and medical students and directing a nationally competitive research program in the areas of microbial pathogenesis and/or host defense mechanisms to infection. Ideal candidates will be those who have extramural funding and whose research integrates molecular aspects of pathogenesis with host defense mechanisms and the immune system. The Department faculty of 16 members directs a training program of 40 doctoral students and postdoctoral fellows and an NIH-funded Center for Molecular and Tumor Virology staffed with 18 interactive principal investigators in several Departments. Both the Department and the Center are well-equipped for molecular research and are augmented by the LSUHSC Research Core Facility that offers BSL-3PLUS laboratories and technologies such as flow cytometry, confocal microscopy, laser capture microdissection, DNA array analysis, proteomics, small animal imaging, and positron emission tomography. Information about the Department is provided at the two websites <http://www.lsuhsbcmicrobiology.com> and <http://www.lsuhsbcmicrobiology.com/cmtv-overview.htm>.

Applicants should send a curriculum vitae, statement of research goals and funding, and three letters of reference to: **Dr. Dennis J. O'Callaghan, Boyd Professor & Head, Department of Microbiology and Immunology, LSU Health Sciences Center, 1501 Kings Highway, Shreveport, LA 71130-3932**.

Louisiana State University is an Affirmative Action/Equal Opportunity Employer.

Women in Science Booklet

Science and the L'Oréal Foundation present



Read inspiring profiles of women
making a difference in biology.

Free download at
ScienceCareers.org/LOrealWIS

Cognition

May 28 - June 2, 2014

Abstracts due March 14, 2014

Topics:

- Motor Systems
- Sensory Processing
- Innate Circuits
- Learning & Memory Systems
- Neuromodulation
- Behavioral Ethology & Evolution
- Perceptual Decision-Making
- Face and Object Recognition
- Language and Communication
- Number Cognition
- Attention
- Cognitive Control
- Probabilistic Brain & Uncertainty
- Neuroeconomics
- Cognitive Genetics
- Dysfunction & Treatment
- Social Neuroscience

Organizers:

Cori Bargmann, The Rockefeller University

Daphne Bavelier, University of Geneva, Switzerland & University of Rochester

Terrence Sejnowski, The Salk Institute for Biological Studies

David Stewart & Bruce Stillman, Cold Spring Harbor Laboratory

Speakers:

David Anderson, HHMI/California Institute of Technology

Dora Angelaki, Baylor College of Medicine

Richard Axel, Columbia University

Cori Bargmann, The Rockefeller University

Daphne Bavelier, University of Geneva, Switzerland &
University of Rochester, NY

Alexander Borst, Max-Planck-Institute of Neurobiology,
Germany

Carlos Brody, Princeton University

Marisa Carrasco, New York University

Marvin Chun, Yale University

Anne Churchland, Cold Spring Harbor Laboratory

Mark Churchland, Columbia University

Patricia Churchland, University of California, San Diego

Yang Dan, University of California, Berkeley

Karl Deisseroth, Stanford University

Robert Desimone, McGovern Institute for Brain Research/MIT

James DiCarlo, McGovern Institute for Brain Research/MIT

Raymond Dolan, UCL/Welcomme Trust Centre, UK

Allison Doupe, University of California, San Francisco

Catherine Dulac, HHMI/Harvard University

Michale Fee, MIT

Russell Fernald, Stanford University

Loren Frank, University of California, San Francisco

Adam Gazzaley, University of California, San Francisco

Paul Glimcher, New York University

Ann Graybiel, MIT

Hopi Hoekstra, Harvard University

Thomas Jessell, Columbia University

Nancy Kanwisher, MIT

Adam Kepecs, Cold Spring Harbor Laboratory

David Kleinfeld, University of California, San Diego

Christof Koch, California Institute of Technology

William Kristan, Jr., University of California, San Diego

Patricia Kuhl, University of Washington

Joseph LeDoux, New York University

Shawn Lockery, University of Oregon

Zachary Mainen, Champalimaud Neuroscience
Programme, Portugal

Eve Marder, Brandeis University

Markus Meister, Harvard University

Tirin Moore, Stanford University

J. Anthony Movshon, New York University

Eric Nestler, Mount Sinai University

Elissa Newport, Georgetown University Medical Center

Yael Niv, Princeton University

Steven Petersen, Washington University

Michael Platt, Duke University

Alexandre Pouget, University of Geneva, Switzerland

John Reynolds, The Salk Institute

Trevor Robbins, University of Cambridge, UK

Ranulfo Romo, Instituto de Fisiologia Celular, Mexico

Matthew Rushworth, University of Oxford, UK

Phillip Sabes, University of California, San Francisco

Terrence Sejnowski, The Salk Institute

Michael Shadlen, Kavli Institute of Brain Science

Eero Simoncelli, New York University

Elizabeth Spelke, Harvard University

Michael Stryker, University of California, San Francisco

Karel Svoboda, HHMI/Janelia Farm Research Campus

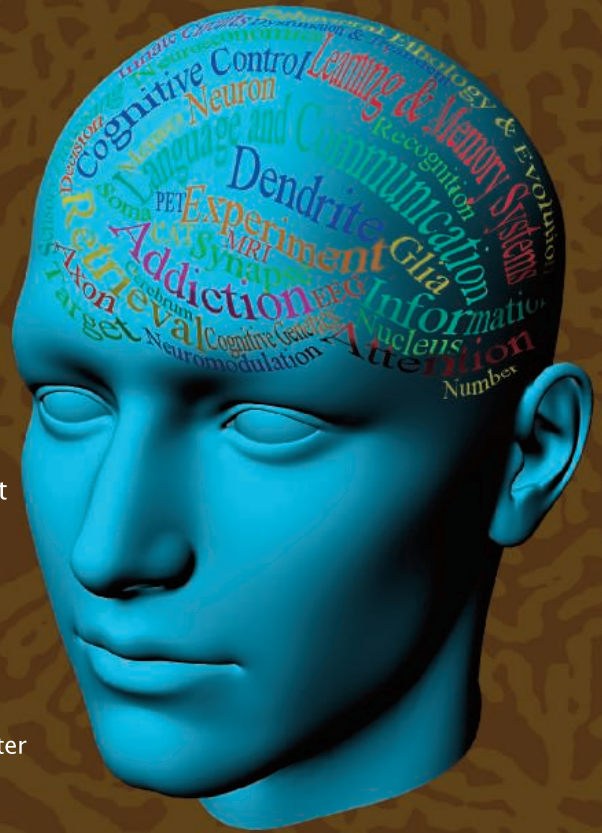
David Tank, Princeton University

Doris Tsao, California Institute of Technology

Michael Wigler, Cold Spring Harbor Laboratory

Daniel Wolpert, University of Cambridge, UK

Tony Zador, Cold Spring Harbor Laboratory



POSITIONS OPEN

FACULTY POSITION

The College of Pharmacy, Washington State University, located on the Riverpoint campus in Spokane, Washington, invites applications for a faculty position in the Section of Clinical Pharmacology, specializing in biostatistics and/or epidemiology. Candidates with a focus in the area of quantitative systems pharmacology are especially encouraged to apply. This is a full-time, 12-month tenure-track position at the **ASSISTANT PROFESSOR** rank. The successful applicant must have a Ph.D. in biostatistics, epidemiology, or a related field before employment start date with an emphasis in statistics, including systems biology and population pharmacokinetic/pharmacodynamic modeling and possess a track record of accomplishment that demonstrates the potential to become an outstanding scholar and educator. Responsibilities will include teaching in both the professional (Doctor of Pharmacy) and graduate (Ph.D.) curricula, maintenance of active, externally funded methodological research in the candidate's area of specialization, and collaborative pharmaceutical/biomedical research.

Screening of all applications is on going and will continue until a suitable applicant pool has been identified. To apply and see complete position description, go online to **website: <http://www.wsujobs.com>**. Applications must include the following materials: (1) a letter of application describing your professional goals, relevant academic preparation, and experience; (2) a current curriculum vitae; and (3) name, title, organization, telephone number, and e-mail address for four people willing to serve as employment references. *Washington State University is an Equal Opportunity/Affirmative Action/ADA Educator and Employer.*

BCMB: BIOCHEMIST beginning August 2014. Visiting (three-year position) Assistant Professor in Biochemistry and Molecular Biology (BCMB) at The College of Wooster to teach introductory courses in cellular and molecular biology, upper level courses in biochemistry and molecular biology, and mentor undergraduates in our nationally recognized senior research program. Ph.D. required; teaching experience preferred. Send resume, undergraduate and graduate transcripts, brief statement of teaching philosophy, description of research program, and three letters of reference electronically to **e-mail: biology@wooster.edu**. Address questions regarding the position to **William Morgan (e-mail: wmorgan@wooster.edu)**, Chair of BCMB. Review of applications begins February 21, 2014, and will continue until the position is filled. The College of Wooster is an independent college of the liberal arts and sciences with a commitment to excellence in undergraduate education. *Wooster seeks to ensure diversity by its policy of employing persons without regard to age, sex, color, race, creed, religion, national origin, disability, veteran status, sexual orientation, or political affiliation. The College of Wooster is an Equal Opportunity/Affirmative Action Employer.*

Find your future here.



Science Careers

From the journal *Science*



www.ScienceCareers.org

Download your free copy today.

ScienceCareers.org/booklets



From technology specialists to patent attorneys to policy advisers, learn more about the types of careers that scientists can pursue and the skills needed in order to succeed in nonresearch careers.

Science Careers

From the journal *Science*

